

# VYSOKÉ UČENÍ TECHNICKÉ V BRNĚ

BRNO UNIVERSITY OF TECHNOLOGY

**FAKULTA STROJNÍHO INŽENÝRSTVÍ**  
FACULTY OF MECHANICAL ENGINEERING

**ÚSTAV AUTOMOBILNÍHO A DOPRAVNÍHO INŽENÝRSTVÍ**  
INSTITUTE OF AUTOMOTIVE ENGINEERING

**NÁVRH ZAVĚŠENÍ KOL FORMULE STUDENT**  
DESIGN OF FORMULA STUDENT WHEEL SUSPENSIONS

**DIPLOMOVÁ PRÁCE**  
MASTER'S THESIS

**AUTOR PRÁCE** Bc. Marek Urban  
AUTHOR

**VEDOUCÍ PRÁCE** doc. Ing. Petr Porteš, Ph.D.  
SUPERVISOR

**BRNO 2020**



# Specification Master's Thesis

Department: Institute of Automotive Engineering  
Student: **Bc. Marek Urban**  
Study programme: Mechanical Engineering  
Study branch: Automotive and Material Handling Engineering  
Supervisor: **doc. Ing. Petr Porteš, Ph.D.**  
Academic year: 2019/20

Pursuant to Act no. 111/1998 concerning universities and the BUT study and examination rules, you have been assigned the following topic by the institute director Master's Thesis:

## Design of Formula Student Wheel Suspensions

### **Concise characteristic of the task:**

The topic of the master's thesis is the modification of the Formula Student wheel suspensions with emphasis on the new tire characteristics and new chassis design.

### **Goals Master's Thesis:**

Comparison of competitive suspension designs with the Dragon X design.  
Analysis of the new tire characteristics.  
Design adjustments of the suspension kinematic points, using kinematic analysis.  
Evaluate the effect of the design changes on vehicle dynamics of the car.

### **Recommended bibliography:**

GILLESPIE, T. D. Fundamentals of vehicle dynamics. Warrendale, PA: Society of Automotive Engineers, c1992. ISBN 15-609-1199-9.

MILLIKEN, W. F., MILLIKEN, D. L.. Race car vehicle dynamics. Warrendale, PA, U.S.A.: SAE International, c1995. ISBN 15-609-1526-9.

Deadline for submission Master's Thesis is given by the Schedule of the Academic year 2019/20

In Brno,

L. S.

---

prof. Ing. Josef Štětina, Ph.D.  
Director of the Institute

doc. Ing. Jaroslav Katolický, Ph.D.  
FME dean

## ABSTRAKT

Tato práce se zabývá návrhem kinematiky zavěšení kol obou náprav. Na základě analýz jízdních dat, multi-body simulací v softwaru Adams Car, simulací v Matlabu a analytických kalkulací v Mathcadu, je navržena řada změn s cílem zlepšit jízdní vlastnosti vozu Formule student, tyto změny jsou následně implementovány do CAD modelu vozu. Jednotlivé změny kinematiky náprav jsou provedeny na základě analýzy konkrétního problému, který se snaží řešit. Jednou z problematik je zástavbová náročnost systému odpružení a zavěšení zadních kol, zde je cílem snížit hmotnost, výšku těžiště a moment setrvačnosti. Další problematikou je geometrie předního kola, kde je cílem zlepšit využití pneumatik a snížit síly v řízení. Dále se práce zabývá simulacemi elastokinematiky zadní nápravy, součástí je také návrh měřicího zařízení. V poslední části je zkoumán vliv provedených změn i elastokinematiky na jízdní dynamiku vozu v ustálených stavech za pomocí MM metody simulované s modelem celého vozu v Adams Car a zpracované v Matlabu.

## KLÍČOVÁ SLOVA

Dynamika vozidel, kinematika, zavěšení kola, náprava, Adams Car, multi-body, Matlab, teplota pneumatik, odpružení, geometrie kola, změna odklonu kola, síly v řízení, síly v zavěšení kol, model pneumatik, elastokinematika, simulace, ovladatelnost, stabilita, kontrola, MM metoda, zpracování jízdních dat, podvozek, závodní vozidlo, Formule Student, TU Brno Racing

## ABSTRACT

This thesis deals with design of suspension kinematics of both axles. Based on analyses of on-track data, multi-body simulations in Adams Car, simulations in Matlab and analytical calculations in Mathcad, various changes of the design are conducted in order to improve the vehicle dynamics of the Formula student car. Individual kinematic changes are made as a response to specific problems that were perceived with the previous car. One of the issues is the packaging of the decoupled roll and heave suspension system and rear suspension links, with the aim to minimize mass, center of gravity height and yawing moment of inertia. Beside packaging, changes of front wheel geometry were conducted to utilize the tire and minimize steering torque. Also, kinematics and compliance simulations of the rear suspension are conducted and a measuring device is designed. Lastly, the effects of kinematic changes and compliance on the steady-state vehicle dynamics are studied using the Force-moment method full-vehicle simulation in Adams, which is then post-processed in Matlab.

## KEYWORDS

Vehicle dynamics, kinematics, wheel suspension, decoupled roll and heave suspension system, roll-heave, Adams Car, multi-body, full-vehicle model, Matlab, tire temperature, wheel geometry, camber change, steering torque, forces in suspension links, tire model, kinematics and compliance, simulations, handling, stability, control, MMM Force-moment diagram, Yaw moment diagram, on-track data post-processing, suspension, racing car, Formula Student, TU Brno Racing

## BIBLIOGRAPHIC CITATION

URBAN, Marek. *Design of Formula Student Wheel Suspensions*. Brno, 2020. Available from: <https://www.vutbr.cz/studenti/zav-prace/detail/124572>. Master's thesis. Brno University of Technology, Faculty of Mechanical Engineering, Institute of Automotive Engineering. 138 p. Supervisor doc. Ing. Petr Porteš, Ph.D.



## **DECLARATION**

I declare this master's thesis to be my own work, I have elaborated this thesis independently under the supervision of doc. Ing. Petr Porteš Ph.D., with the use of listed sources.

In Brno, June 26<sup>th</sup>, 2020 .....

Bc. Marek Urban

## ACKNOWLEDGMENT

I would like to express my deepest gratitude to my supervisor doc. Ing. Petr Porteš Ph.D. for his guidance, valuable advices and clarifications of several vehicle dynamic issues. I would also like to extend my deepest appreciation to Ing. Jan Fojtášek, Ph.D. for his unrelenting willingness to explain and help with various problems in Adams Car. I can not even begin to express my appreciation to the large number of people who have contributed to the project of Formula Student at our university and thereby made it possible. This includes the University, and more than 120 sponsors. Furthermore, I would like to thank the members of TU Brno Racing team, and, of course, I want to thank my girlfriend who has endured and supported me throughout 4 years of my Formula Student participation. And lastly, I want to express my gratitude to my parents and family who have been supporting me throughout my whole education as well as Formula Student participation.



## TABLE OF CONTENTS

<b>Introduction .....</b>	<b>10</b>
<b>1 Bases for the suspension design.....</b>	<b>12</b>
1.1 Comparison of suspension designs .....	12
1.1.1 Space requirements of springs and dampers .....	13
1.1.2 The layout of rear wishbones .....	16
1.2 Tire analysis.....	19
1.2.1 Comparison of the Continental C18 and C19 tires.....	19
1.2.2 Comparison of soft and stiff suspension setups .....	25
<b>2 Design changes of the suspension .....</b>	<b>27</b>
2.1 Springs and dampers .....	28
2.1.1 Definition of static suspension rates for the Roll-Heave system.....	28
2.1.2 Analysis of the Dragon 9 suspension setup .....	30
2.1.3 Dragon X design.....	34
2.1.4 Kinematic simulations in Adams and Matlab.....	44
2.1.5 Algorithm for an automatic optimal coil spring construction design .....	49
2.2 Wheel geometry .....	54
2.2.1 Wheel inclination angle analysis .....	54
2.2.2 Caster angle design.....	57
2.2.3 Steering forces and scrub radius design .....	60
2.2.4 Rear wheel geometry .....	70
2.3 Suspension links .....	71
2.3.1 The geometry of suspension wishbone arms .....	71
2.3.2 Tire forces.....	72
2.3.3 Dynamic wheel bump .....	75
2.3.4 Front suspension .....	78
2.3.5 Rear suspension .....	81
2.3.6 Tie rods and bump steer .....	84
2.4 Effect of kinematic design changes on the vehicle parameters .....	85
<b>3 Kinematics and Compliance .....</b>	<b>90</b>
3.1 Bushing stiffness sensitivity study .....	91
3.2 Compliance analysis based on FEM values.....	94
3.3 New rear tie rod position design .....	98
3.4 Design of suspension compliance measuring device.....	102
<b>4 Effect of kinematic design changes on vehicle dynamics .....</b>	<b>106</b>
4.1 Full vehicle model in Adams .....	107
4.2 Force-Moment diagram (Yaw Moment Diagram).....	109
<b>Conclusion .....</b>	<b>116</b>
<b>Abbreviations and symbols.....</b>	<b>121</b>
<b>List of attachments .....</b>	<b>125</b>

## INTRODUCTION

Formula student competition is a dynamic engineering challenge in which students of mechanical, electrical engineering, or even information technology compete. Each year a new, single-seater, four-wheel, formula-style vehicle must be designed and manufactured. Brno University of Technology has its team TU Brno Racing participating in the Formula Student competition for 10 years now. There is a significant effort to make each year's car slightly better than the previous one and every department of the team is trying their best to do so. **Formula Student rules do not limit minimal weight, therefore it is one of the main goals of the team to minimize the weight of the car, because based on the Newton's Second Law of motion, all other things being equal, lighter car will always be faster.**

This thesis is covering several design changes of the suspension kinematics for the 10<sup>th</sup> car named Dragon X (DX). The main goals of this thesis are to:

- Improve the packaging of the suspension which influences the mass of suspension components and chassis. Mass, center of gravity height, yawing moment of inertia, and creating more space for aerodynamic devices are the main points of interest.
- Utilize the tire, mainly in terms of tire temperature distribution, related to inclination angle of the wheel during cornering.
- Minimize the braking-in-turn steering torque.
- Investigate the suspension kinematics and compliance.
- Improve the vehicle dynamic simulations in Adams Car and Matlab.

To see the potential of suspension packaging solution, a comparison study is made against the previous vehicles of TU Brno Racing and competition vehicles as well. The main emphasis is on the space requirements of the front suspension system and the rear wishbone layout which directly influences the dimensions of chassis.

**To point out problems that occurred during testing, tire analyses of on-track testing data with the use of tire temperature sensors are made.** Main emphasis is on the difference between the camber angle needed by the new tire Continental C19 and the older Continental C18. The tire models are compared as well. **Another point of interest is a suspension stiffness influence on tire temperature.**

**Improvement of the packaging of the springs and dampers is dependent on the suspension characteristics in heave and roll motions.** A study of the Dragon 9 suspension rates, damping and their cooperation with aerodynamics is conducted. Based on the study, design changes of installation ratios and position of suspension system is made. Suspension rate characteristics are calculated in Matlab and implemented into the Adams model.

**Changes of the wheel geometry are based on the tire analyses, the emphasis is to improve camber change of the front wheels.** Study of wheel inclination angle during racing is made from testing data. Scrub radius is changed to lower the steering torque in braking-in-turn states. Steering forces are calculated with the use of tire model in Matlab and then compared to Adams simulations. Rear wheel geometry is changed to accommodate the new wishbones layout and to the new four-wheel steering project.

Wishbones are changed on both axles to cooperate with the outboard pickup points, desired kinematic characteristics, suspension system, aerodynamics, chassis and to prevent collisions

---

with the rim in steering. The main change is done at the rear axle, where the wishbone inner pickup points are moved completely to compromise between chassis dimensions and compliance. Static and dynamic force simulations are made in Adams Car to study the force distribution in the suspension members. For the steady-state simulations, tire model is used to calculate the tire reactions in various longitudinal and lateral accelerations based on data. Dynamic wheel bump is simulated according to strain gauge measurement.

Kinematics and compliance are investigated for the first time. Flexible members are added to the Adams Car vehicle model and compliance studies are conducted including a comparison with the previous wishbone layout of Dragon 9. Moreover, a basic compliance measuring device is designed to validate the simulations.

Force-Moment simulations are made with Adams Car full-vehicle model to get a better understanding of the influence of conducted design changes. The Force-moment diagram is constructed in Matlab.

This thesis contains large number of simulations in Matlab and Adams. An important goal of this thesis is to improve the existing, create new Matlab simulations and improve the Adams model during the design process and after it.

# 1 BASES FOR THE SUSPENSION DESIGN

## 1.1 COMPARISON OF SUSPENSION DESIGNS

The study of the competition is an important part of the development. This applies even more in motorsport and Formula Student competition – although Formula Student is not motorsport, but rather an educational project. This chapter is focused on comparing different suspension designs with an emphasis on areas where optimization is sought after for the new design of Dragon X.



*Figure 1 Spring and dampers in heave and roll decoupled suspension of Dragon 9 including casted hollow bellcranks [1]*

One of the main goals – as already mentioned – is reducing the mass of the vehicle. Each department has its limited area of improvability and the limits are sometimes drawn by the neighbor department. This applies best for the relationship of chassis and suspension. It is known that chassis has to accommodate the suspension pickup points, and so the suspension is superior. Therefore chassis is quite limited in terms of size and consequently mass by the suspension department. From a mechanical point of view it is safe to say that suspension of TU Brno Racing cars which are called Dragons (e.g. Dragon 9 is the 9<sup>th</sup> car, shortly D9), has been of pristine quality in the last years. Meaning that the bellcranks (Figure 1), uprights (Figure 2), wishbones, steering holder (Figure 3), etc. were designed to be very light and stiff, therefore efficient.

In Figure 1 and 2, bellcranks, uprights, and other significant suspension components are designed based on a topology optimization using Ansys software to utilize the use of material. As for the manufacturing, bellcranks in Figure 1 and steering column holder in Figure 2 were made by precision gravity casting using a lost wax method, while the wax was 3D printed by MultiJet printing technology. These are advanced designing and manufacturing techniques and if there was an effort to make these components lighter without changing the kinematic skeleton of the suspension, maybe only a few grams could be saved.

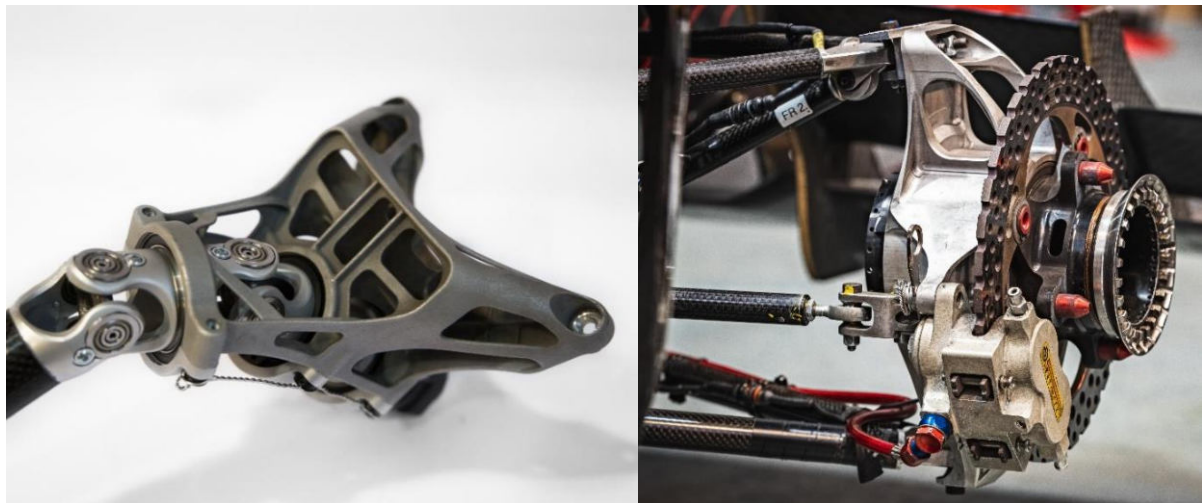


*Figure 2 On the left is a casted steering column holder and on the right a wheel assembly, both of Dragon 9 [1][2]*

### 1.1.1 SPACE REQUIREMENTS OF SPRINGS AND DAMPERS

Much more can be saved if the overall dimensions of the component (the concept) were optimized. This applies especially for the bellcranks as motion ratio can be minimized to reduce the size of the bellcrank. Then a compromise between the dynamics and weight is needed. The front suspension of TU Brno Racing cars has always been a pullrod system. The pullrod solution offers to put the (not negligible) weight of dampers, springs, and anti-roll bars under the car which lowers the center of gravity. On the other hand, there might be some negatives in aerodynamics as the components could disturb the flow of air under the car. In some designs, the position of dampers under the car can influence the shape and even dimensions of the body. Then a compromise of installation ratio – thus the size of the bellcrank and position of dampers

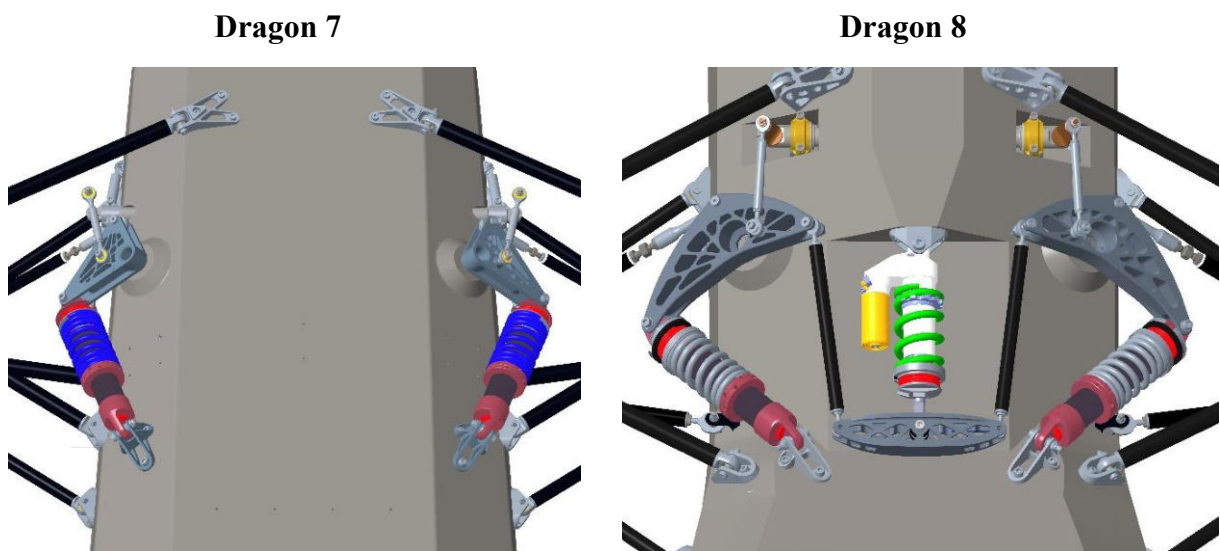


*Figure 3 Bottom view of the front suspensions of Dragon 7 and Dragon 8 respectively*

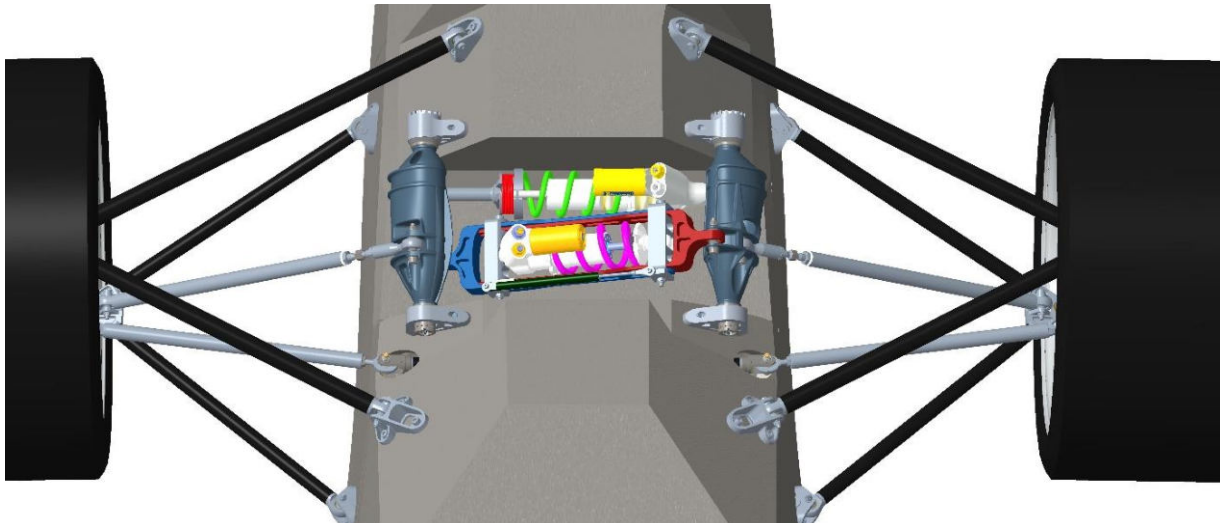


*Figure 4 Bottom view of the front suspension of Dragon 9*

might prove to save not only the weight of the bellcranks themselves but also some weight of the chassis as well as lower the center of gravity of the chassis.

In Figures 3 and 4 there is a noticeable difference in the impact of suspension layout on the chassis monocoque. On Dragon 8 a heave spring and damper were used per each axle to improve the control over heave and pitching motions of the vehicle and therefore the

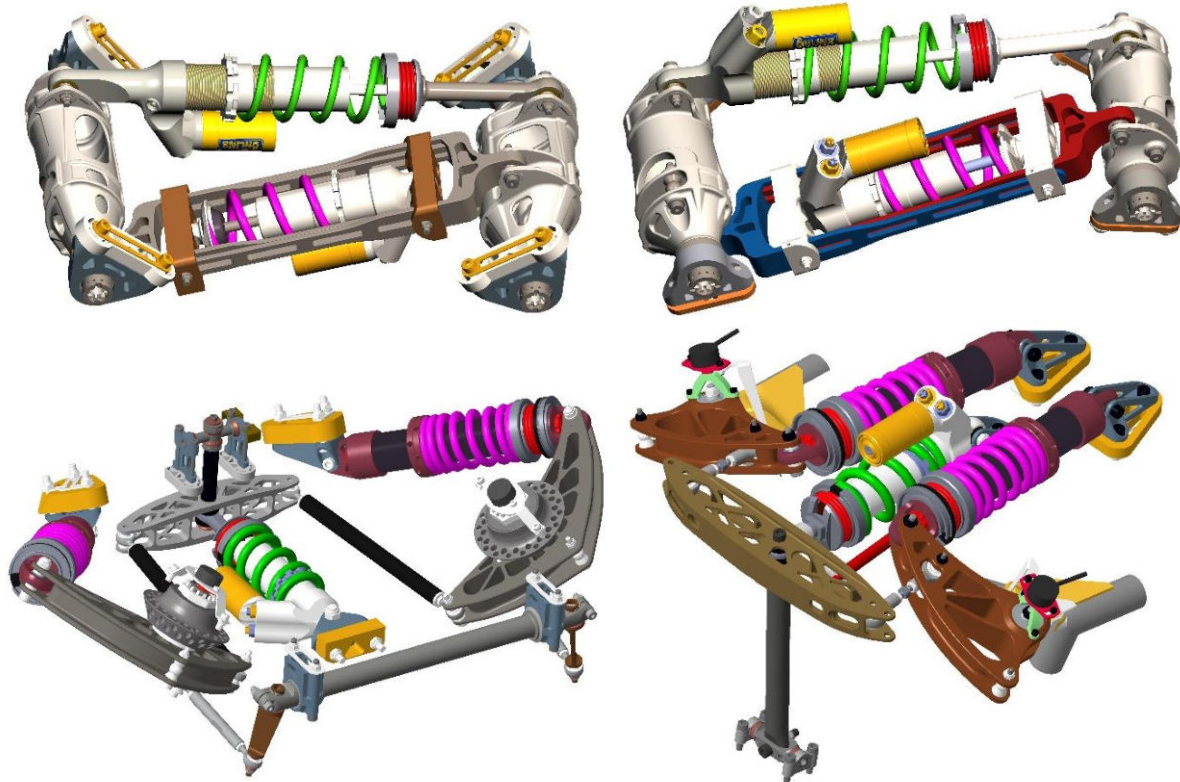


*Figure 5 Comparison of Dragon 9 (upper) and Dragon 8 (lower) suspension concepts, front on the left and rear on the right [3]*

cooperation of the suspension and aerodynamics. For Dragon 9, a completely different concept of suspension was used, that is a decoupling of roll and heave motions into each spring and damper. This means that per each axle there is one spring and damper only acting against rolling motion of the car and second spring and damper for the heave and pitching motions of the car (Figures 1, 4, 5).

The roll spring is equivalent to an anti-roll bar. This system is excellent in the ability to set desired wheel and roll rates (and damping) without the necessity to compromise. As the car has complex aerodynamic devices, including the undertray, the cooperation between the aerodynamics and suspension is needed. The concept of heave spring is inherited from Dragon 8 and has been developed based on aero maps and the sensitivity of the aerodynamics on the ride heights of each axle.

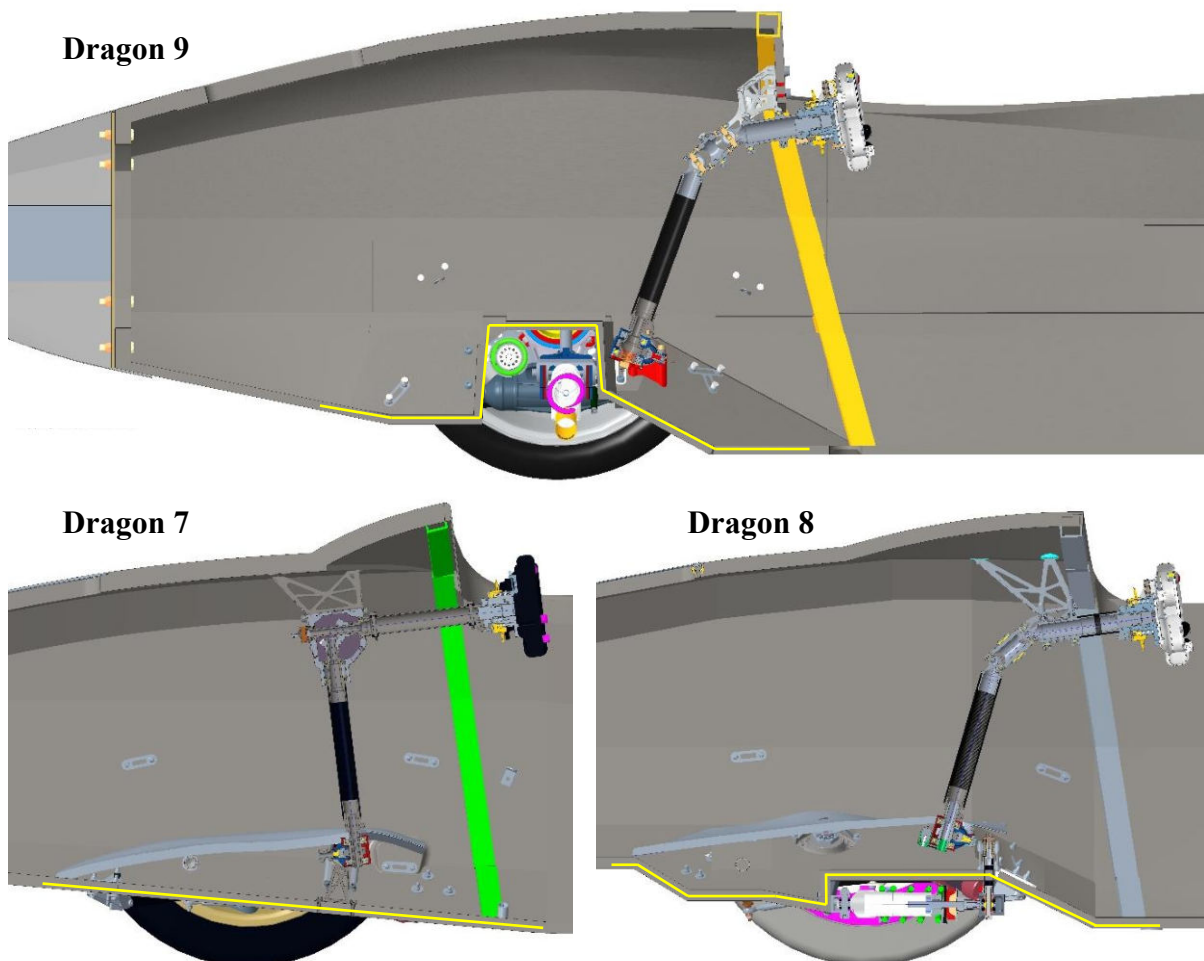


*Figure 6 Comparison of suspension system influence on the monocoque in the side view section among Dragon 9, Dragon 7, and Dragon 8*

With the new suspension concept, much was gained. A damper that only acts in the cornering can provide an improvement in the feedback for the driver. Roll and heave decoupled system was able to replace the Dragon 8 complex design so anti-roll bar, one bellcrank, one damper and spring were removed. In Figure 5 can be seen an obvious difference in the complexity. In

total 3,5 kg was saved. The numbers in Table 1 are weights of the systems as seen in Figure 5, all the related components were taken into consideration.

*Table 1 Comparison of suspension system weights displayed in Figure 5*

Dragon 9			Dragon 8		
Front [kg]	Rear [kg]	Total [kg]	Front [kg]	Rear [kg]	Total [kg]
3.265	2.939	<b>6.204</b>	5.263	4.445	<b>9.703</b>

But there is another aspect of this change that needs to be looked at. The roll and heave decoupled system (hereafter also referred to as roll-heave) connects both wheels of each axle and therefore, it is more space demanding than the Dragon 8 design, mainly in the vertical direction. Because the dampers cannot be placed longitudinally, the system becomes higher. This creates a problem at the front axle, as the dampers are higher the monocoque has to create the space. By lifting a part of the lower wall of the monocoque the upper wall has to be moved as well because of the cross-section template rule. This issue can be seen in Figure 6 where a comparison of the last concepts viewed from the side in a section is pictured. For Dragon X the roll-heave suspension system is chosen. Therefore one of the goals of this thesis is to optimize the suspension system dimensions to save the weight of the monocoque.

### 1.1.2 THE LAYOUT OF REAR WISHBONES

Another idea of possible reduction of weight and the yawing moment of inertia was inspired by the competition. Plenty of very well ranked teams have much shorter chassis at the rear. The

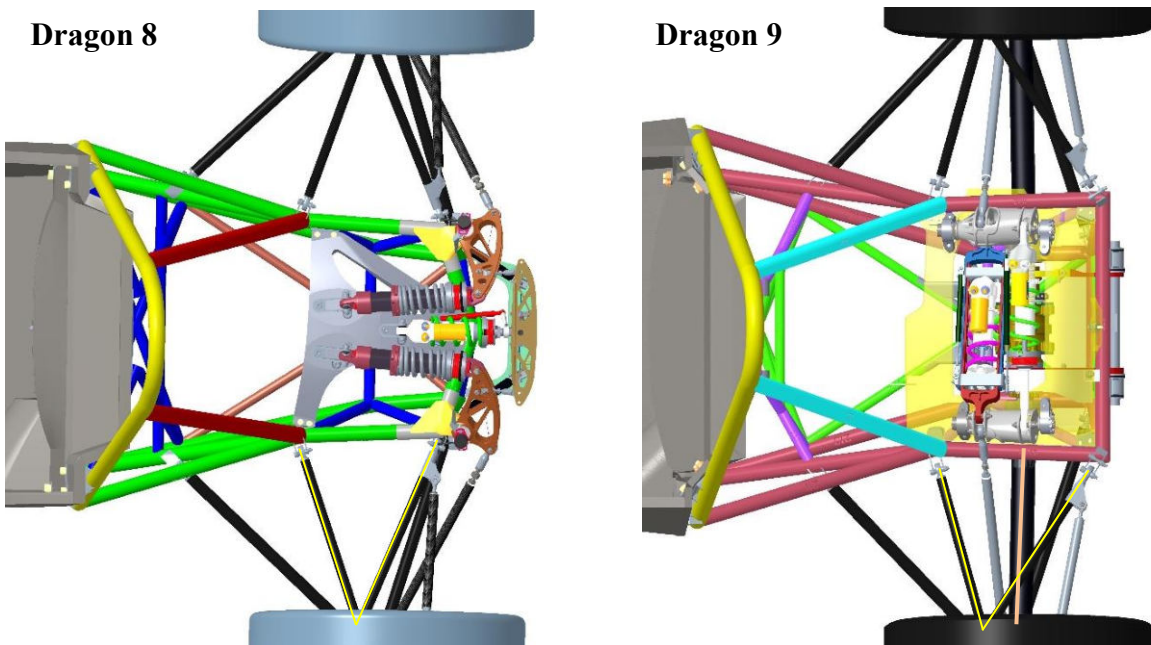


*Figure 7 Top view of rear suspension and chassis of Dragon 8 and Dragon 9*

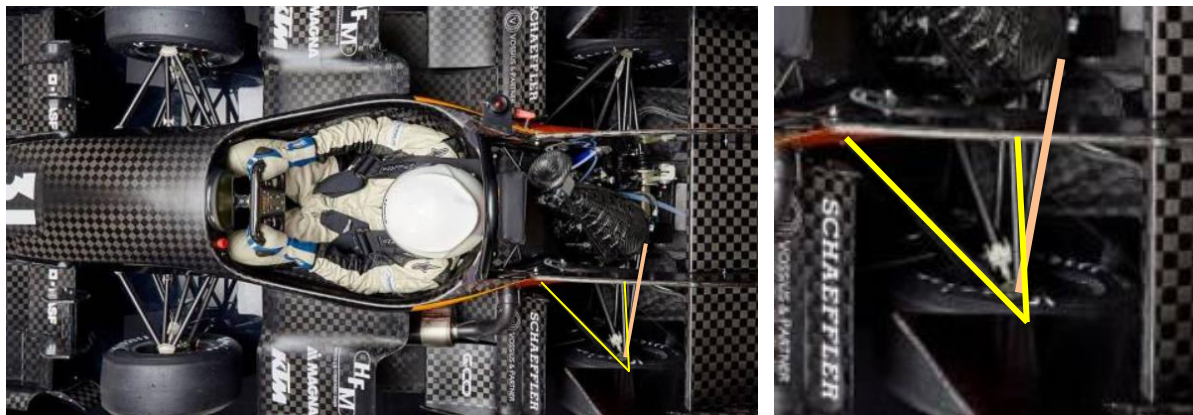


Figure 8 Last combustion car nb017 of TU Fast racing team from Technical University of Munich [4]

length of the chassis is also given by the suspension kinematics, therefore there might be room for optimization if a compromise between compliance and weight was made.

In Figure 7, there is an obvious benefit of the compactness of the roll-heave system. The higher profile of the system is not such an issue at the rear as it is a pushrod system, therefore it does not lift any part of a chassis due to its dimensions. Since the heave spring was first introduced on Dragon 8, only the pushrod system is applicable at the rear as the drivetrain does not allow for any damper to be under the car. In Figure 8 there is a top view of arguably one of the fastest combustion formula student cars ever made – this is most apparent from their lap times in Formula Student Germany competition. Comparing Figure 7 and Figure 8, there is an apparent difference in the wishbone layout of these rear suspensions. Upper a-arms are highlighted with yellow lines to underline the difference. There is also a drivetrain assembly added to Dragon 9

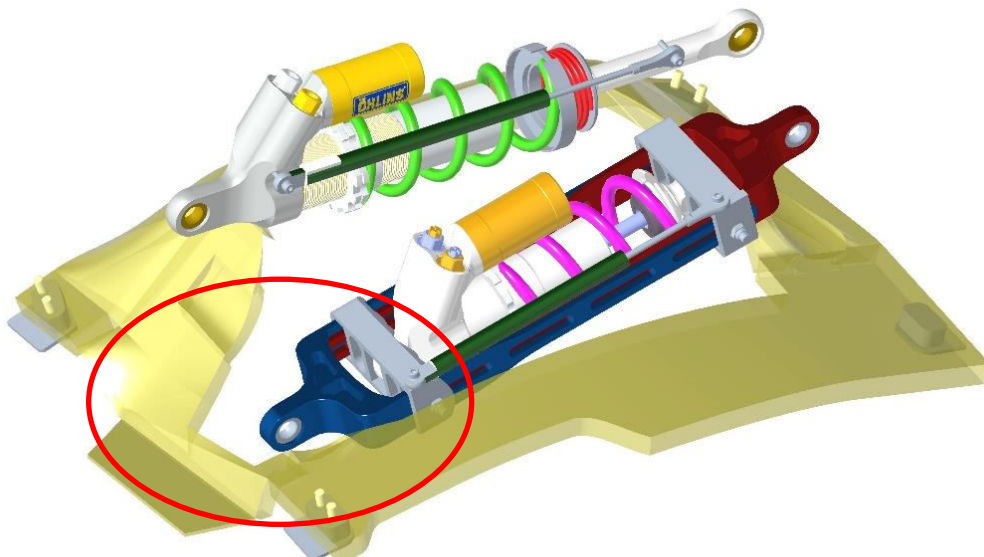
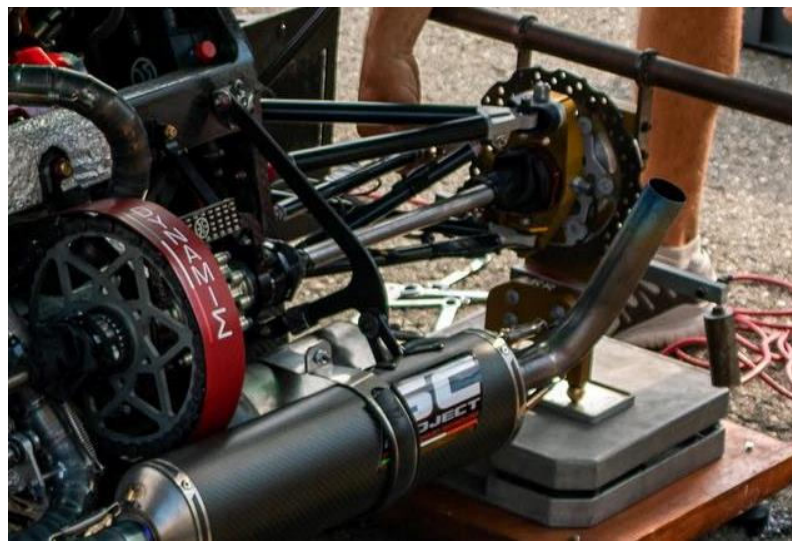
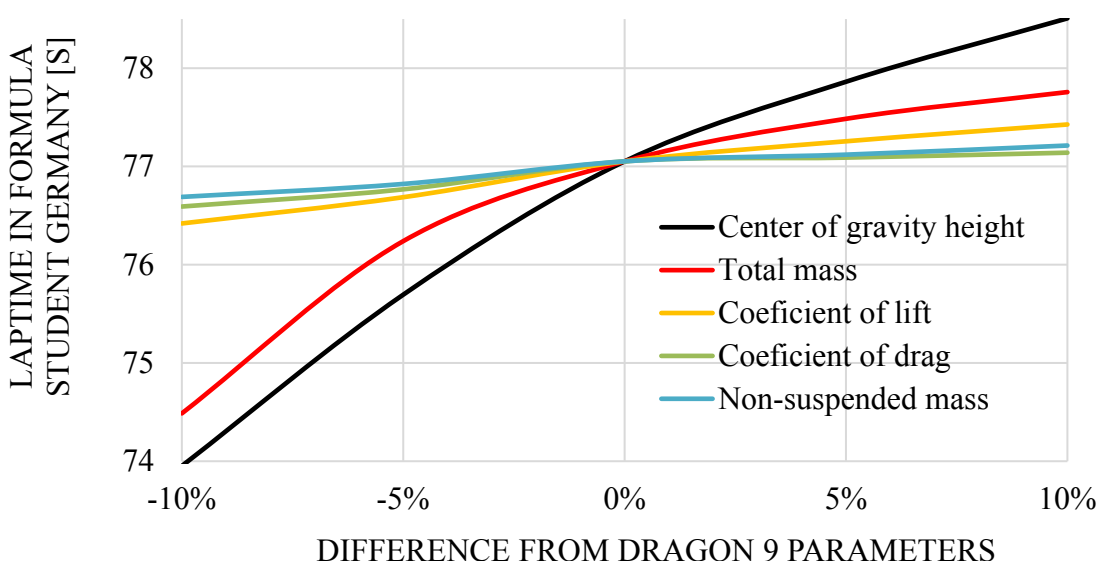


Figure 9 Rear carbon fiber chassis member of Dragon 9 with highlighted problematic area



*Figure 10 Rear suspension of the formula student car DP11 of Dynamis PRC team from Polytechnic University of Milan [5]*

(Figure 7) and driveshafts are highlighted with pink lines to point out the different relationship between the wishbones and driveshafts. As seen in Figure 8, the wishbone pickup points are in front of the driveshaft while in Figure 7 they are behind. There is a direct impact of wishbone layout on the distribution of forces in the wishbones and consequently compliance. Specifically, there is likely to be larger suspension compliance in the layout in Figure 8. Nevertheless, as a full monocoque (i.e. no tubular frame at the rear part of the chassis) is introduced for the Dragon X, the shortening of chassis seems to be of benefit, as it can (besides lowering the weight of the monocoque itself) simplify the mounting (and assembling) of the drivetrain and also simplify the chassis at the roll-heave system mounting. There is a problematic area on the Dragon 9 chassis by the rear roll damper mounting as highlighted in Figure 9. As the roll damper is



*Figure 11 Lap time sensitivity analysis in ChassisSim [6]*

positioned at an angle, space needs to be provided at the lower end of the damper. This created a gap in the chassis where a loss of torsional stiffness might be introduced. Moreover, shorter chassis provides space for larger diffusor.

Another car of similar concept with even shorter chassis, but undeniably higher rear toe and camber compliances, is the DP11 of the team Dynamis PRC from the Polytechnic University of Milan seen in figure 10. To give an idea of the mass difference between the cars, Dragon 9 weights 188 kg, while nb017 and DP11 weight in the range of 150-155 kg. Although the shorter chassis is not the main factor of such mass difference, it is a contributor.

Finally, a decision to try to shorten the chassis at the rear was made for reasons mentioned above, the strongest arguments are the unquestionable reduction of weight and yawing moment of inertia. The problem is that to specifically quantify these values, one needs a detailed CAD model, as the concept influences many related components. These values will be quantified later in this thesis. The disadvantage of this concept change is the increase of compliance so a study of rear suspension compliance needs to be done to evaluate the influence on the car's performance. In Figure 11 is shown how different parameters influence the lap time, this analysis was done in ChassisSim software by colleague Pavel Gellner. The influence of mass is clear.

## 1.2 TIRE ANALYSIS

Some changes in the kinematics were made based mostly as a response to the tire behavior during testing. In this chapter, an analysis of test data with the emphasis on tire temperature will be made as well as analysis of the tire model obtained from Continental AG Flat Track measurement.

### 1.2.1 COMPARISON OF THE CONTINENTAL C18 AND C19 TIRES

TU Brno Racing team has been using the Formula Student tires by Continental AG for many years as the company is one of the main sponsors of the team. Each year new tires are developed and delivered to us in late spring, in the testing period of the year when the car is already designed and built. That is why the suspension is always developed based on the latest tires, although the new tires can be entirely different. Such vast change is not common, but it did occur between the C18 and C19 tires.

Several changes in the tire construction were made but as the information was not publicized, only an idea of the changes is known based on a conversation with the Continental tire engineers. A change of the tire belt was made, instead of glass fibers, steel wires were used and a change in the compound took place. The result which was observed during on-track testing was a difference in the response of the tire as C19 felt leaner for the driver, also a higher grip, and an obvious need for larger camber on the front axle were observed.

## ON-TRACK TEST DATA

These statements can be supported by measured data, as tire temperature was measured on the tire surface by 3 infrared sensors on each wheel mounted in a fixture (see Figure 12). Outer, center, and inner part of the tire are measured. The fixture is mounted to the upright at the upper ball joint, therefore it measures surface temperature at the top part of the tire, even though the heat is generated at the contact patch. The temperatures of the tire surface can change between the heat generation and the moment it is measured, due to airflow. This can also influence the distribution of the heat. To improve the accuracy of this measurement in the future, tire temperature sensors should be placed as close to the contact patch as possible.

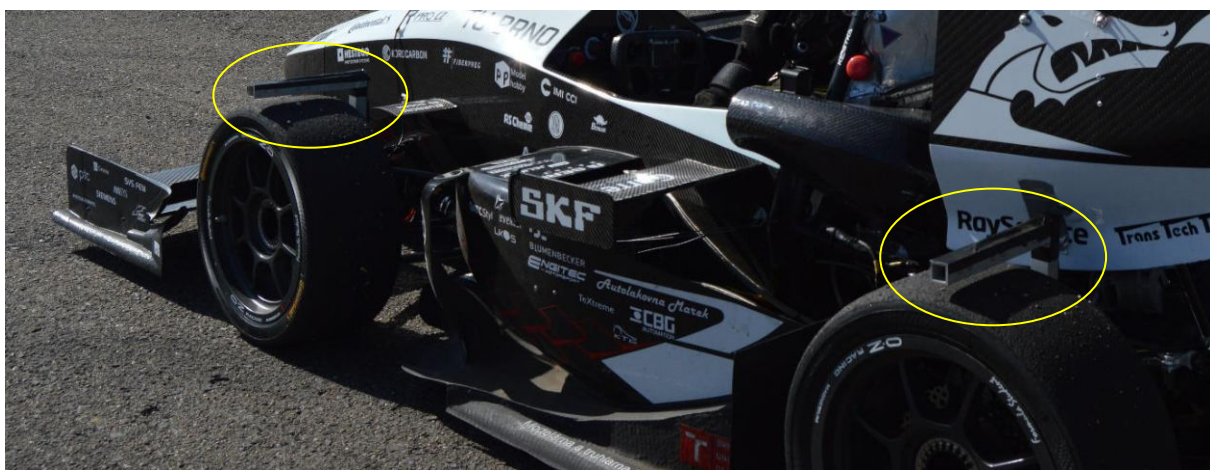


Figure 12 Tire temperature sensors mounted on the vehicle

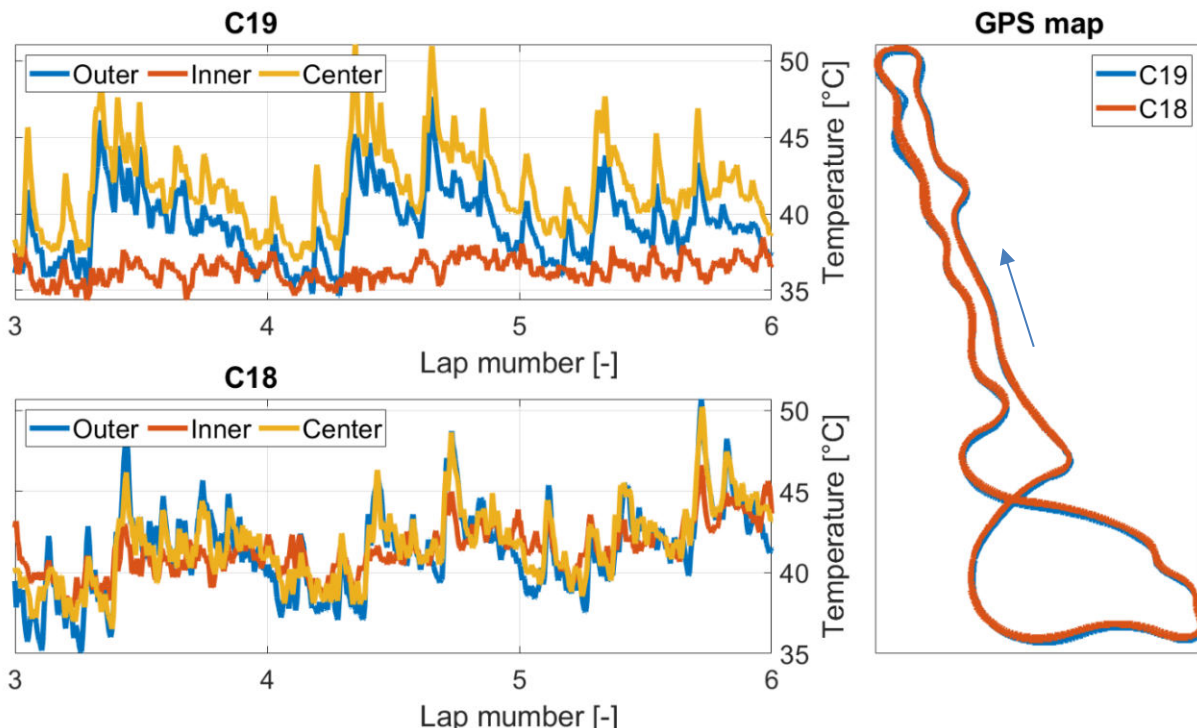


Figure 13 Comparison of **front** right wheel tire temperatures of C18 and C19 tires

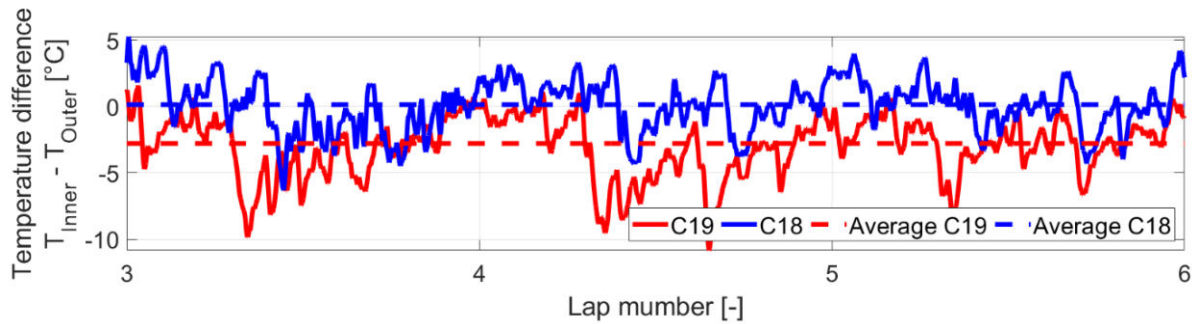


Figure 14 Comparison of the difference between inner and outer tire temperature of C18 and C19



Figure 15 Visible piling up of rubber on the inner part of the C19 tires

During the same day of testing, tires were switched with the same setup, on the same track, and with the same driver for the comparison to be objective. As seen in Figure 13, with C19 a difference between the inner and outer temperature appears. Moreover, it is visibly not responding to the cornering, which might mean that the part of the tire was not fully in contact with the road. A more negative camber is needed for the C19 tires. A plot of the difference between inner and outer temperature is displayed in Figure 14. The inner part is lower in temperature on average of 3,3 °C. The static camber on front wheels was set to -2,6 °. [7]

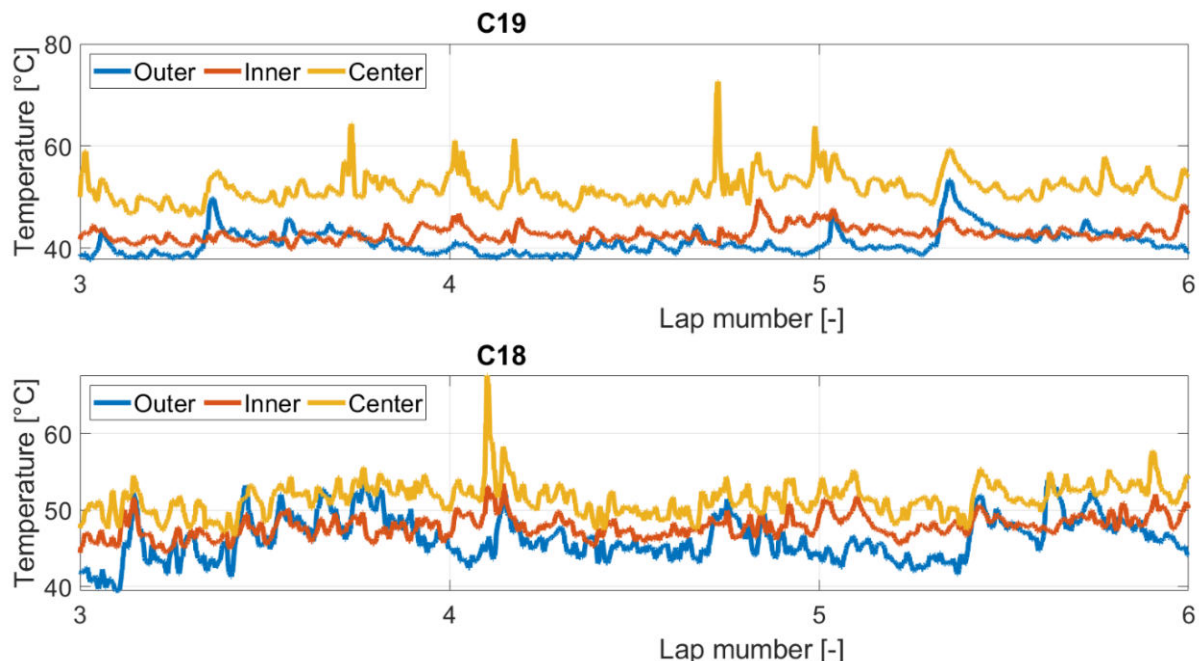


Figure 16 Comparison of rear right wheel tire temperatures of C18 and C19 tires

This effect was visible on the tire surface as well. It seemed as if the rubber was moving toward the inner part of the tire due to lateral graining where it has piled up as seen in Figure 15.

Figure 16 shows a comparison of rear right tire temperatures in the same test track as in Figure 14. Larger camber does not seem to be needed for the rear tires, apparent rise of the tire center temperature is seen. That means that theoretically the pressure of the C19 tire should be lowered to even out the center and the edges of the tire. As the vehicle is rear-wheel driven, the traction force heats the inner side of the tire and therefore larger camber might lead to overheating. The static camber of the rear tires was  $-1,6^\circ$ . [7]

In Figure 17 is shown a comparison of the two tires in terms of lateral and longitudinal acceleration. C19 tires seem to reach higher lateral acceleration, while C18 tires reach higher longitudinal acceleration.

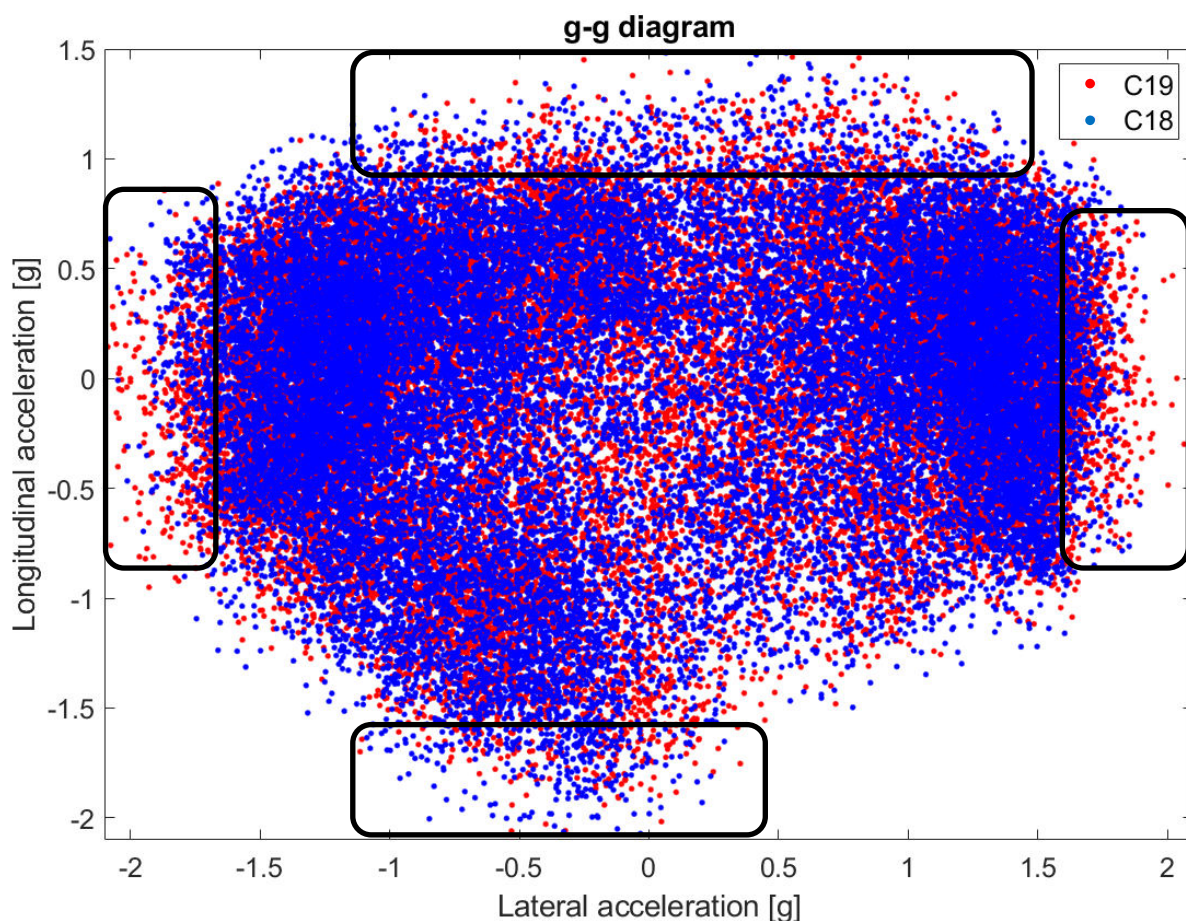


Figure 17 „g-g diagram“ comparing C19 (red) and C18 (blue) tires

## TIRE MODEL

Force and moment characteristics were received from Continental AG engineers as Pacejka MF-Tyre 5.2 tire model. These models were obtained by fitting to measured raw data from the Flat Trac tire testing. For comparison of the two tires, no scaling of the coefficients is done, so the values correspond directly to the Flat Trac measurement. [8]

From Figure 18 it seems that the peak friction coefficient is higher with the C18 tires (for the outer tire) according to the measured data on Flat Track, however, for higher normal loads (1400 N), the peak is shifted in much higher slip angles and the coefficient of friction is approximately even. Cornering stiffness is higher for the C19 tires and the peak lateral force area seems to be smaller (in a lower range of slip angles) in Figure 18 for  $F_z = 1400$  N, which means that the C19 tires require better driving skills (i.e. is harder to drive). On the other hand, C18 tires create a higher slip angle induced power loss. [7]

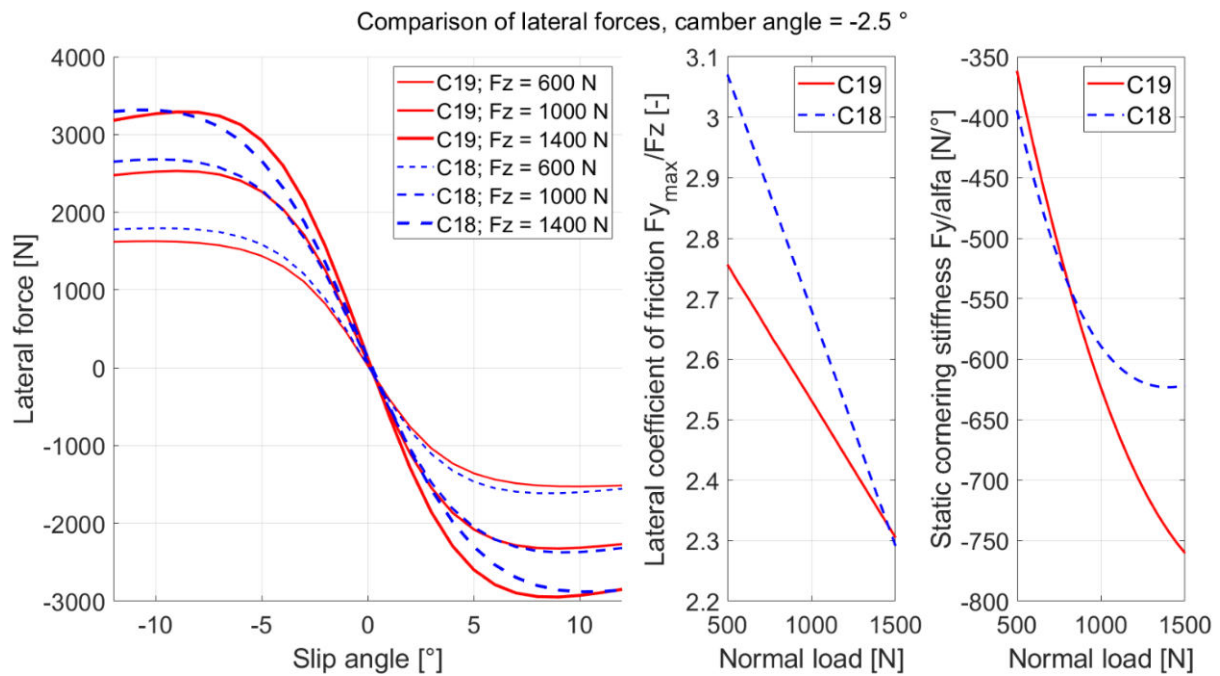


Figure 18 Comparison of lateral forces between C18 and C19 from the tire model

To get a better idea of the limit tire behavior in cornering, maximal forces from inner and outer wheels are summed while the load transfer effect is added. Weight distribution and load transfer distribution are considered to be equal for each axle and total downforce of 850 N is equally distributed. The lateral acceleration used in this calculation only influences the load transfer and normal load of the tires, the maximal lateral forces are then calculated for this static lateral acceleration and do not represent real lateral forces as in driving under such acceleration.

$$F_{Z_{outer}} = F_{Z_{static}} + \frac{LT}{2} + F_{Z_{aero}} \quad (1)$$

$$LT = \frac{m \cdot A_{y\_static} \cdot g \cdot h_{CG}}{T} \quad (2)$$

Where  $F_{Z_{outer}}$  is the normal load of the outer wheel during cornering,  $F_{Z_{static}}$  is a quarter of the vehicle's weight,  $LT$  is load transfer,  $F_{Z_{aero}}$  is a quarter of the total aerodynamic downforce,  $m$  is mass,  $A_y$  is static lateral acceleration (in Gs),  $g$  is the gravitational acceleration,  $h_{CG}$  is the center of gravity height and  $T$  is the average track. For the inner wheel, load transfer is subtracted and the tire model is mirrored around both X and Y axes. No camber change is considered. [7]

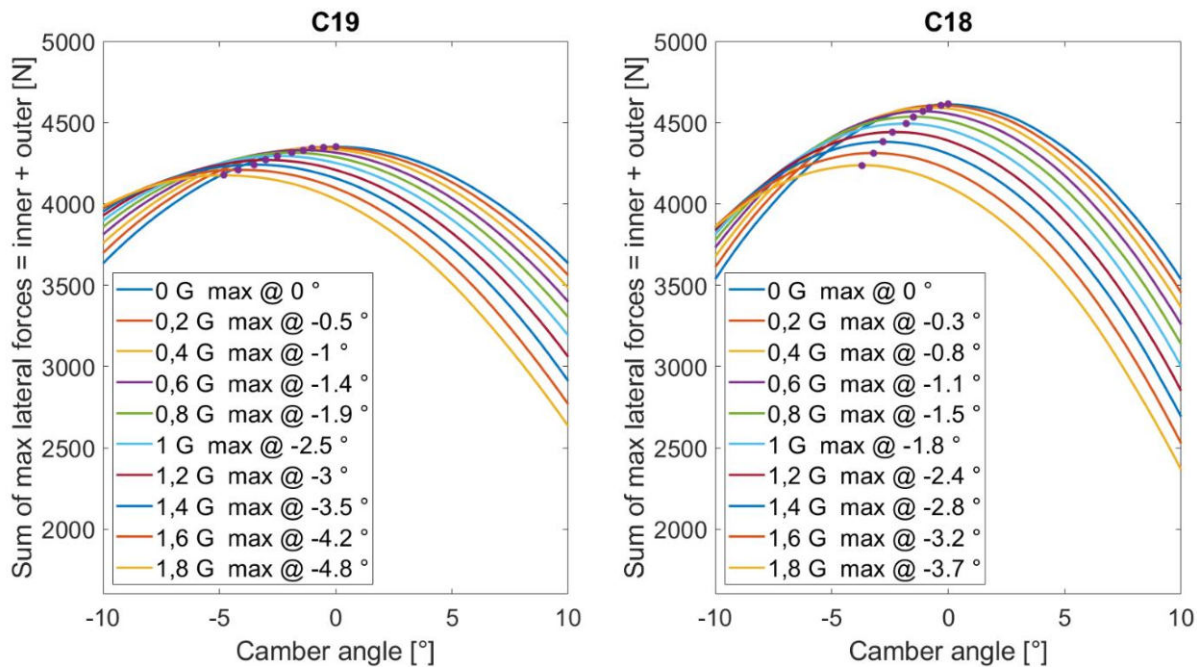


Figure 19 Comparison of the tire's lateral forces for load transfer variation and camber variation

In Figure 19 is shown the sensitivity of the tire to load transfer and camber. C19 is less sensitive to camber and significantly less sensitive to load variation. Secondly, the C19 tires need more camber angle. The higher coefficient of friction of C18 seen in Figure 18 applies only for lower loads and therefore for lower load transfer which can be seen in Figure 19 as well.

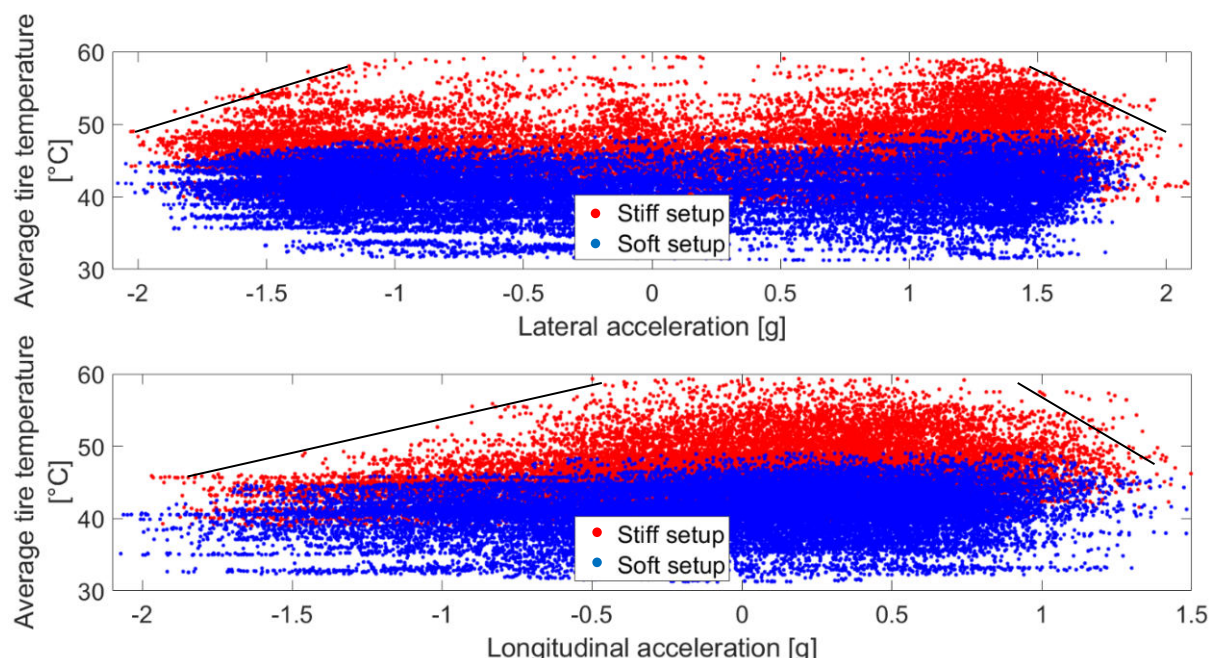


Figure 20 Comparison of the average temperature of front right tire vs lateral and longitudinal acceleration for different setups

### 1.2.2 COMPARISON OF SOFT AND STIFF SUSPENSION SETUPS

Dragon 9 suspension was designed with a strong emphasis on the aerodynamics and its sensitivity which resulted in very stiff suspension rates. During testing, the setup was softened as the tires were overheating. With lower wheel and roll rates than planned for also came lower damping coefficients and besides, even lower damping ratios were used during testing and competition. These were the cornerstones of changes in motion ratios that will be addressed later in this thesis.

As seen in Figure 20, with a stiffer suspension setup, the tires reached much higher temperatures. As depicted by the black lines, with higher temperature than approximately 50 °C there is a decrease in the tire's capability of force transmission (for braking the limit is approximately 45 °C). Understeer and a loss of braking performance were perceived by the driver.

*Table 2 Suspension rates related to Figure 20*

		Spring Rate Heave [N/mm]	Wheel Center Rate [N/mm]	Spring Rate Roll [N/mm]	Roll Rate [Nm/°]
Front	Stiff	55	58.6	95	1452
	Soft	45	48	55	841
Rear	Stiff	55	75.8	95	1380
	Soft	45	62	55	799

In Table 2 is shown the setup change between the two runs in Figure 20, Table 3 shows the percentage difference. Significantly larger influence on the temperature change has a change in the roll rate.

*Table 3 Percentage difference in suspension rates*

	Spring Rate Heave	Wheel Center Rate	Spring Rate Roll	Roll Rate
Front [Δ %]	-18,2	-17,9	<b>-42,1</b>	<b>-42,1</b>
Rear [Δ %]	-18,2	-18,4	<b>-42,1</b>	<b>-42,1</b>

Very important factor that causes the temperature rise in the tires is the slip. The frictional power of the tires is dependent on the slip velocity of the tires in both longitudinal ( $V_{sx}$ ) and lateral ( $V_{sy}$ ) direction. The rise of temperature with the stiffer setup is possibly caused by larger tire load variation (worse mechanical grip) and thus a need for larger slip angles. Larger slip angles create larger slip velocities and thus larger frictional power that is dissipated into heat: [9]

$$P_y = F_y \cdot V_{sy} \quad (3)$$

$$P_x = F_x \cdot V_{sx} \quad (4)$$

Where  $P_y$  is frictional power due to lateral force  $F_y$  and  $P_x$  is frictional power due to longitudinal force  $F_x$ . Unfortunately, slip angle sensor such as Correvit is needed for a precise signal of slip

angles and slip ratios. It would be interesting to measure the tire temperature and slip angles while changing the suspension setup to see this dependency.

Another source of heat of the tire is the energy dissipated in the damping of the tire while compressing and while rolling (tire rolling resistance). This factor could be seen directly if a ride height sensor was used to isolate the tire vertical deformation. [9]



## 2 DESIGN CHANGES OF THE SUSPENSION

Based on the comparison of different suspension designs, lap time analysis in Chapter 1.1 and the tire analysis in Chapter 1.2, several changes in the design were made. Some wheel geometry changes were based on steering forces.

- Installation ratio, dampers position
- Wheel geometry
- Wishbone layout

Analytic calculations in Mathcad, Matlab as well as kinematic and force analysis of the suspension assembly in Adams Car software, were made in the process.

New Matlab simulations were created and some are based on the work of previous team members and are further improved:

- Cooperation of Matlab vertical model with Adams to obtain equal values.
  - Calculation of helper spring pretension to achieve desired chassis position (modeling position) under the static load.
  - Calculation of wheel rates, ride rates, damping ratios, and frequencies in the whole wheel travel range.
- Steering torque calculation is used and improved
- New Matlab scripts are made to:
  - display the wheel inclination angle during a lap
  - calculate steady-state tire forces in various acceleration combinations

In Adams, the suspension assemblies of each axle were created in previous years and were improved as part of this thesis:

- Non-linear spring characteristics are added (including helper spring)
- Addition of bump stops with measured F-x characteristics, rebound stops
- Correction of the reduction gear in the steering system
- Addition of flexible elements (bushings) in the suspension links and a hub compliance bushings. Switching between kinematic and compliant mode is now available.

Also, a full vehicle model was made for the first time together with other team members, various parameters were improved. As part of this thesis, these improvements were done on the full vehicle model:

- Adjusting communicators to connect all the subsystems correctly
- Aerodynamic forces dependant on the ride heights are added according to our aero maps from CFD
- Adjusting of some engine, transmission, and differential parameters

All of these models and simulations were done for Dragon X and Dragon 9 as the interest is to compare the design changes of the two vehicles.

## 2.1 SPRINGS AND DAMPERS

As shown in Chapter 1.1, springs and dampers of the front axle have taken a larger amount of space to accommodate in comparison to the previous cars. As the system has proven to be ideal for the aerodynamic-dependent formula student car, the Dragon X continues to use this concept. Therefore, a process of optimization of the concept is sought after.

### 2.1.1 DEFINITION OF STATIC SUSPENSION RATES FOR THE ROLL-HEAVE SYSTEM

There is a need for a slight alteration of the common equations for Wheel Center Rate, and Roll Rate for the roll-heave system because both wheels of each axle are connected via the springs and dampers. For an initial estimation, these simplified formulas are used.

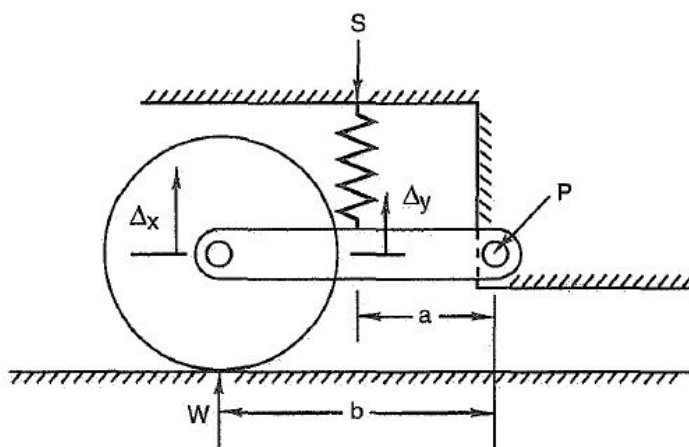


Figure 21 Installation ratio for simple suspension [10]

The standard equation for the wheel rate is [10]:

$$K_W = K_S \cdot (IR)^2 \quad (5)$$

Where  $K_W$  is wheel rate,  $K_S$  is spring rate,  $IR$  is installation ratio which is calculated as [10]:

$$IR = \frac{\Delta_y}{\Delta_x} \quad (6)$$

Where  $\Delta y$  is the displacement of one end of the spring which is connected to the wheel and  $\Delta x$  is the displacement of the wheel center, Figure 21.

From the equality of work of the wheel and the spring [7]:

$$W \cdot \Delta_x = S \cdot \Delta_y \quad (7)$$

Where  $W$  is the force acting at the wheel center and  $S$  is a force acting on one side of the spring. As seen in Figure 22, the system is symmetrical. As the symmetry axis goes through the heave spring it can be divided into two springs that are in series.

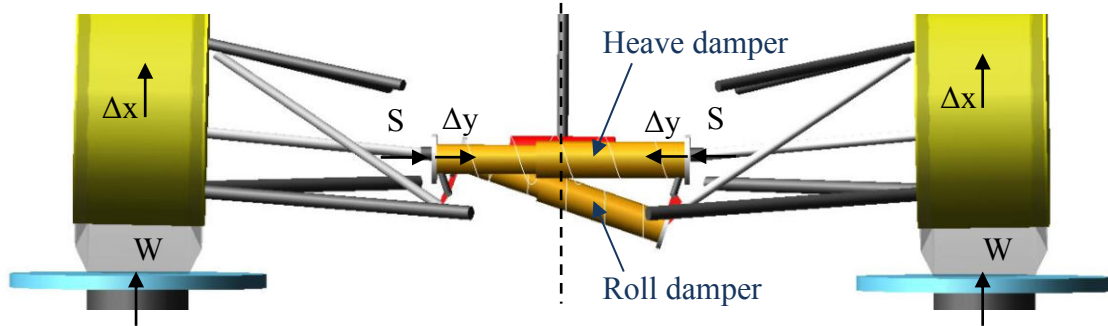


Figure 22 Installation ratio of heave spring for the roll-heave suspension

$$K_{S\_Heave} = \frac{K_{S\_Heave\_half}}{2} \quad (8)$$

Where  $K_{S\_Heave}$  is the stiffness of heave spring and  $K_{S\_Heave\_half}$  is the stiffness of half of the heave spring. Then from Equation 7 and 8:

$$K_{W\_Heave} \cdot \Delta_x^2 = K_{S\_Heave} \cdot 2 \cdot \Delta_y^2 \quad (9)$$

Where  $K_{W\_Heave}$  is wheel rate in heave. This can be simplified with Equation 6:

$$K_{W\_Heave} = K_{S\_Heave} \cdot (IR_{Heave})^2 \cdot 2 \quad (10)$$

Where  $IR_{Heave}$  is the installation ratio for heave motion. So for the roll-heave suspension, wheel rate is actually double in comparison with the standard suspension. A different way to think about this is that while the spring is not attached to the chassis but rather to the other wheel, the reaction forces from the other wheel will influence the first wheel with the extra force. Or since the heave spring is, in fact, an axle spring, it is clear that the work done by each wheel will be half of the spring's work. Because there is only one spring for both wheels. The wheel rate calculated in Equation 10 applies only for the heave motion of the vehicle. For the standard independent suspension to reach the same wheel rate, springs of twice as high stiffness would have to be used. Therefore, with roll-heave, the weight of the springs can be saved. The travel of the heave spring is twice as much, which can be problematic for the damper if high installation ratios are used. In fact, a need for longer damper occurred when switching from corner dampers to the roll-heave system, during the design of Dragon 9.

In practice, the installation ratio is obtained from Adams Car simulation, where it is given as:

$$IR_{ADAMS\_Heave} = \frac{\text{Total deflection of the heave spring}}{\text{Displacement of the wheel}} \quad (11)$$

$$IR_{ADAMS\_Heave} = IR_{Heave} \cdot 2 \quad (12)$$

Then  $IR_{ADAMS\_Heave}$  is an installation ratio for the heave movement of the whole axle. Using this installation ratio, the wheel rate is calculated as half of the axle rate.

$$K_{W\_Heave} = K_{S\_Heave} \cdot (IR_{ADAMS\_Heave})^2 / 2 \quad (13)$$

For the roll rate, the situation is very similar and the effect of the roll spring can be calculated at the wheel. To move from translational movement to rotational,  $1^\circ$  of roll angle is imposed and the anti-roll moment that follows is calculated as [7]:

$$M_{Anti-roll} = K_{W,Roll} \cdot \Delta_x \cdot \frac{t}{2} \cdot 2 \quad (14)$$

$M_{Anti-roll}$  is an anti-roll moment of one axle,  $K_{W,Roll}$  is a wheel rate due to the rolling motion of the car and  $t$  is the track. The wheel displacement is calculated from the roll angle  $\phi$  which is in degrees:

$$\Delta_x = \frac{t}{2} \cdot \operatorname{tg}(\phi) \quad (15)$$

Equation 10 can be used with the roll spring stiffness  $K_{S,Roll}$  and installation ratio of the roll spring  $IR_{Roll}$  (roll IR is obtained analogically to heave using Equation 6, and considering the roll spring in Figure 22):

$$M_{Anti-roll} = K_{S,Roll} \cdot (IR_{Roll})^2 \cdot t^2 \cdot \operatorname{tg}(\phi) \quad (16)$$

For the roll angle being  $1^\circ$  as mentioned earlier, the  $M_{Anti-roll}$  is the roll rate of one axle. The total roll rate of the vehicle  $K_\phi$  is the sum of the front  $K_{\phi,Front}$  and rear  $K_{\phi,Rear}$  roll rates.

$$K_{\phi,Front} = K_{S,Roll,Front} \cdot (IR_{Roll,Front})^2 \cdot t_{Front}^2 \cdot \operatorname{tg}(1^\circ) \quad (17)$$

$$K_\phi = K_{\phi,Front} + K_{\phi,Rear} \quad (18)$$

Where  $K_{S,Roll,Front}$  is the front roll spring rate,  $IR_{Roll,Front}$  is the installation ratio for the front roll spring. For the calculation of damping forces at the wheel, equivalent equations are used to obtain damping coefficients at the wheel where instead of spring rates, damping coefficients of the dampers are used.

## 2.1.2 ANALYSIS OF THE DRAGON 9 SUSPENSION SETUP

### HEAVE SPRING AND AERODYNAMICS

Following the suspension setup influence on the tire discussed in Chapter 1.2.2, here is a comparison of the same setup change and its influence on the aerodynamic balance of the car (see Figure 23). These simulations are based on the work of Ing. Martin Hlaváč which is applied for Dragon 9 and Dragon X, the issue is further dealt with in his master's thesis ref. [10]. It is clear that a softer suspension setup causes higher variation in the center of pressure and thus a variation of the vehicle's balance.

The relationship of the aerodynamics and suspension has been the basis of the heave spring design. "Bump stops" become very important as they limit the chassis movement beyond a certain point and prevent the bottoming of the car (especially the front wing). Bump stops cause a sudden rise of a spring rate beyond a certain point of the damper's displacement, which is

equivalent to a progressive spring rate. This can be beneficial because a combination of softer spring and a bump stop can limit the extreme chassis movement (such as hard braking) and remain the softer characteristics for the rest of the lap (straights). The space between the bump stop and the damper can be adjusted via the “*bump stop washers*”. [10]

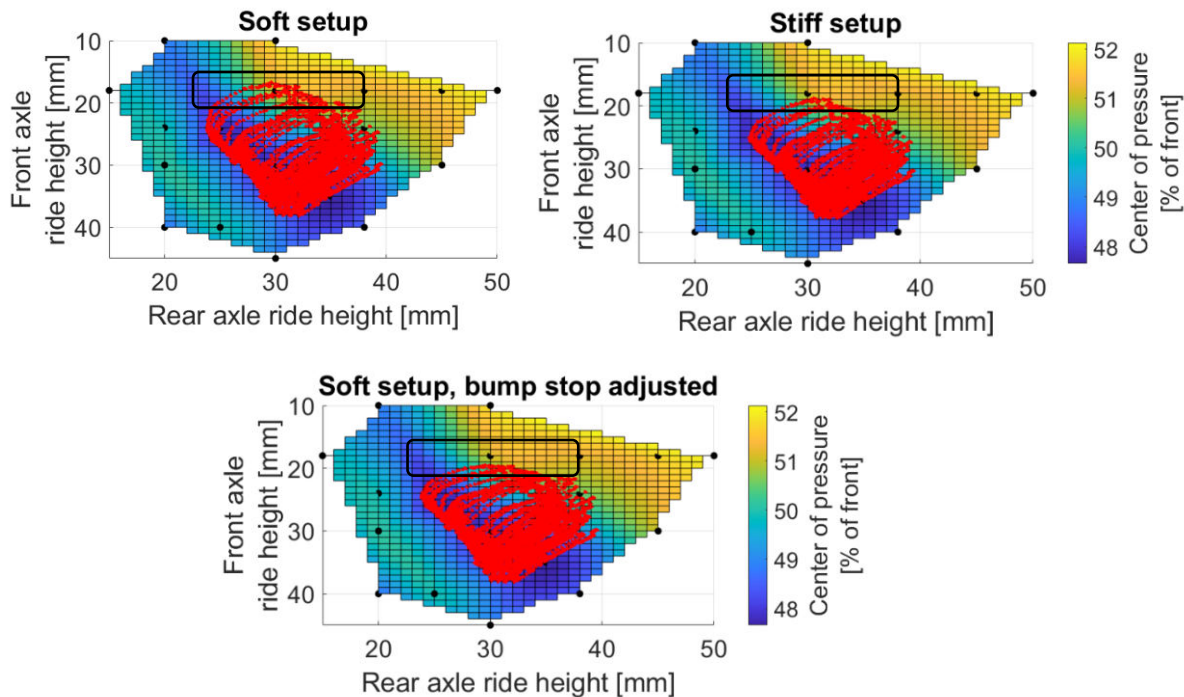


Figure 23 Comparison of suspension setups of Dragon 9 with respect to aerodynamic balance.

The combination of softer setup and a higher amount of bump stop washers which cause the bump stop to work earlier can be seen in Figure 23 in the lower figure. However, tire temperature might prove to be an issue yet again as earlier working bump stop is essentially a stiffer suspension rate. To validate this, a different bump stop setups can be made during testing while the tire temperature will be monitored to see this relationship. The problem which occurred with Dragon 7 was oversteer due to loss of rear downforce, or in other words, a shift of the center of pressure to the front. This was one of the reasons why a heave spring was implemented. In Table 4 can be seen how stiffer springs influence the mean value of the aerodynamic balance and bump stops reduce the maximal values.

Table 4 Mean and maximum values of the Center of Pressure in Figure 21, and Figure 22

	Center of Pressure [% front]	
	Mean value	Maximum value
Stiff	48.39	51.19
Soft	48.49	51.44
Soft, earlier bump stop	48.47	51.04

## ROLL SPRINGS

Unfortunately, the CFD analyses for rolling and yawing movements of the vehicle were not yet made due to high computational complexity and so aero maps in roll and yaw are not available.

Thus the aforementioned heave spring analysis can not be applied for the roll spring at this moment. Assuming the vehicle is aerodynamically sensitive to roll as it is to heave and pitch motions, an effort to make the roll rates very stiff was made. The reason for this was also to reduce the rolling movements of the chassis and to increase the load transfer speed and so the response in the entry of a corner. As discussed earlier in Chapter 1.2.2, the overheating of the tires occurred during testing, and softer roll rates were used.

Ultimately, it comes down to a compromise between the tires and aerodynamics. Aerodynamic packet requires stiffer suspension and tires require softer suspension. This compromise was met by reducing the stiffness to the point where tires were not overheating.

## DAMPERS

For the sake of testing the roll-heave system possibilities, a wide range of damping ratios were desired. Dampers Öhlins TTX25 MkII with the valve kit number 13 purchased from Kaz Technologies were chosen due to the ability to adjust both low and high-speed (LS and HS) of both compression and rebound, and because the valve kit number 13 reached the highest damping forces. Dynamometer testing of the dampers took place to obtain the F-v characteristics (Figure 24). For simplicity, these curves were reduced into polylines each consisting of two straight lines which are representing the low-speed and high-speed damping see Figure 25. The slope of low-speed and high-speed curves are the damping coefficients.

*Table 5 Damper speed range [12]*

Speed range	Influence
Below 5 mm/s	Friction
5-25 mm/s	Inertial chassis motions (low-speed)
25-200 mm/s	Road inputs (high-speed)
Above 200 mm/s	Curbs (high-speed)

For simplicity, compression and rebound coefficients are considered equal because the F-v characteristic of the Öhlins damper is nearly symmetrical about the X-axis. It is problematic to locate the bend of the curvature, as it is often not visible. According to literature, the low-speed motion of the damper occurs approximately up to 25 mm/s, see Table 5. [12]

In Table 6 is a list of damping coefficients that represent each setup of the damper.

*Table 6 Damping coefficients from the dynamometer testing*

Setup [number of rotations]		Damping coefficients [Ns/mm]	
Low-speed	High-speed	Low-speed	High-speed
4.5	4.5	10.54	4.23
3.5	3.5	6.1	2.13
3	3	2.63	1.35
2	2	1.43	0.66
1	1	0.73	0.37

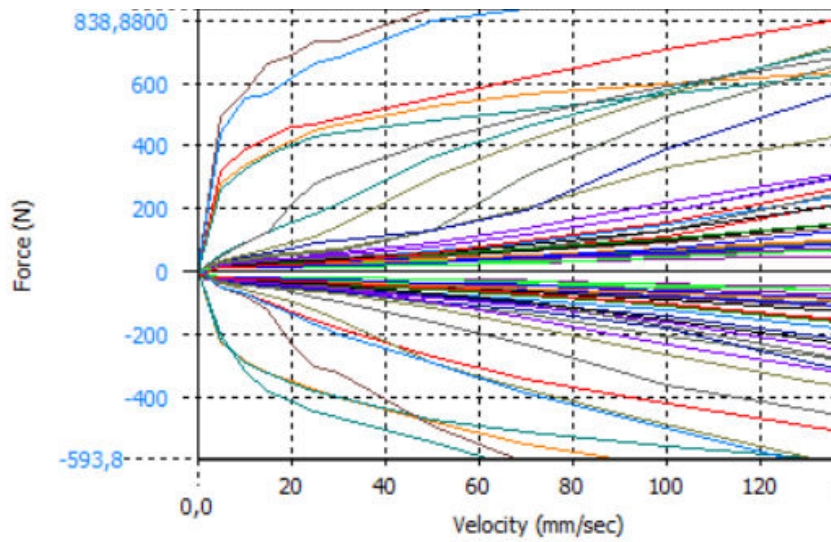


Figure 24 Dynamometer measured  $F$ - $v$  characteristics of the damper for multiple settings

To calculate the damping ratios, critical damping  $C_{crit}$  is needed. The basic equation is [10]:

$$C_{crit} = 2 \cdot \sqrt{k \cdot m} \quad (19)$$

Where  $k$  is stiffness and  $m$  is mass. For the suspended mass characteristics, if the stiffness of the tire is neglected,  $k$  is equal to the wheel rate. With the tire included,  $k$  is equal to the ride rate. Mass in the equation is the suspended mass. Rather than single wheel damping characteristics, the suspension of TU Brno racing has been designed based on heave and roll vibration modes, each mode has its independent spring and damper for each axle. The resulting pitch vibration mode characteristics are accepted as a compromise. The critical damping for heave of the front wheels  $C_{Crit\_Heave\_Front}$  with neglected tires is calculated as [10]:

$$C_{Crit\_Heave\_Front} = 2 \cdot \sqrt{K_{W\_Heave\_Front} \cdot SM_{Front\_Left}} \quad (20)$$

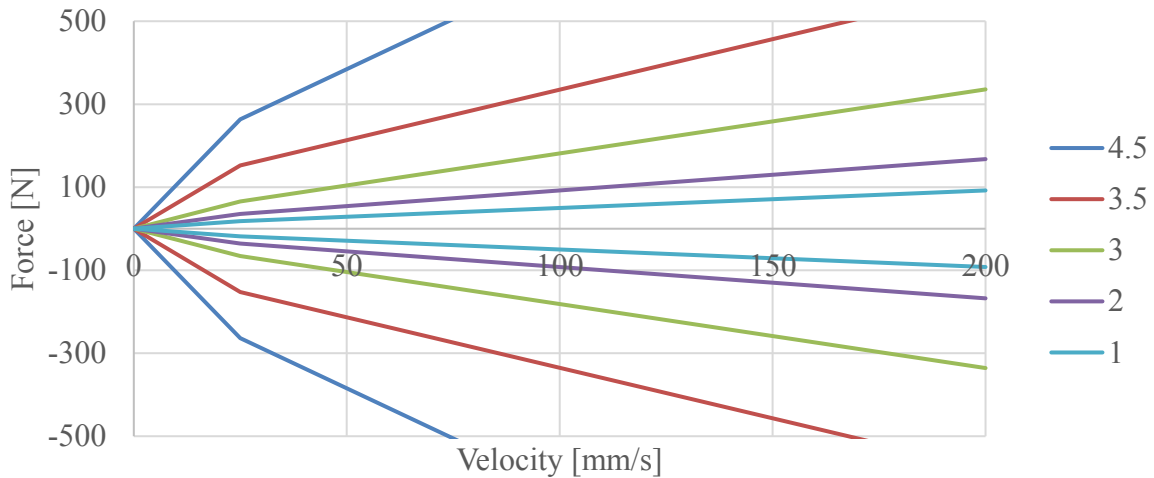


Figure 25 Simplified model of a damper with multiple setups

Where  $K_{W\_Heave\_Front}$  is the wheel rate of the front wheel in heave,  $SM_{Front\_Left}$  is half of the front suspended mass. As mentioned earlier, if the tires are included, ride rate is used instead which it is the tire rate and wheel rate in series. For the critical damping in roll  $C_{Crit\_Roll}$ , the variables are rotational instead of translational [10]:

$$C_{Crit\_Roll} = 2 \cdot \sqrt{K_\phi \cdot I_{Roll\_Axis}} \quad (21)$$

Where  $I_{Roll\_Axis}$  is the inertia of the suspended mass around the roll axis. Then damping ratios in heave (Eq. 22) and roll (Eq. 23) can be calculated [10]:

$$\zeta_{Heave} = \frac{C_{Heave\_Front}}{C_{Crit\_Heave\_Front}} \quad (22)$$

$$\zeta_{Roll} = \frac{C_{Roll}}{C_{Crit\_Roll}} \quad (23)$$

Where  $C_{Heave\_Front}$  is the damping coefficient in heave at the wheel calculated equivalently to wheel rate in Equation 10, instead of spring rate a damping coefficient of the heave damper is used.  $C_{Roll}$  is damping coefficient acting in roll and is calculated equivalently to roll rate in Equations 17 and 18.

Table 7 Damping ratios

		Damping ratio [-] (neglecting tire)			
		Low-speed		High-speed	
		Front	Rear	Front	Rear
Heave	Original design (setup = 3)	0.77	0.84	0.39	0.43
	FSG setup (setup)	0.76 (2.75)	0.76 (2.5)	0.38 (2.75)	0.44 (2.75)
Roll	Original design (setup = 3)	0.81		0.41	
	FSG setup (setup)	0.99 (2.75)		0.43 (2.5)	

Table 7 is a list of damping ratios of the original design and the specific setup used in Formula Student Germany (FSG) 2019. Table 8 is a list of suspension parameters and a comparison between the original stiffer design and actual used softer design during the competition FSG. The parameters of the softer setup are chosen as the default values for the Dragon X design.

### 2.1.3 DRAGON X DESIGN

The main idea behind the change of the Dragon X design is to reduce the installation ratio, use stiffer springs, and use higher damping coefficients. As discussed in Chapter 1.1.1, the space requirements of the roll-heave system are not negligible. The main parameter that decides the size of bellcranks and thus positions of dampers is the installation ratio. The limitation of this reduction is in the damping coefficient of the damper. When lower installation ratio and higher spring rates are used to remain the wheel rate, the damping ratio decreases if the damping coefficient of the damper remains unchanged.

Table 8 Comparison of suspension rates and frequencies of Dragon 9 between the original design and the setup at Formula Student Germany

Heave	Installation ratio [-]		Spring rate [N/mm]		Wheel rate [N/mm]		Ride rate [N/mm]		Wheel frequency [Hz]		Ride frequency [Hz]	
	Front	Rear	Front	Rear	Front	Rear	Front	Rear	Front	Rear	Front	Rear
Original design	0.73	0.83	55	55	58.6	75.8	36.8	42.9	5.13	5.61	4.07	4.22
FSG setup	0.73	0.83	45	40	48.0	55.1	32.3	35.4	4.64	4.78	3.81	3.83
Roll	Installation ratio [-]		Spring rate [N/mm]		Roll rate neglecting tires [Nm/°]		Roll rate including tires [Nm/°]		Roll frequency neglecting tires [Hz]		Roll frequency including tires [Hz]	
	Front	Rear	Front	Rear	Front	Rear	Front	Rear	Front	Rear	Front	Rear
Original design	0.78	0.78	95	95	1452	1380	670	637	9.27		6.30	
FSG setup	0.78	0.78	50	50	764	726	474	450	6.73		5.30	

It is seen when Equation 22 is broken down using Equation 20 and Equation 10:

$$\zeta_{Heave} = \frac{2 \cdot C_{D\_Heave\_F} \cdot (IR_{Heave\_F})^2}{2\sqrt{2 \cdot K_{S\_Heave\_F} \cdot (IR_{Heave\_F})^2 \cdot \frac{SM_F}{2}}} = \frac{C_{D\_Heave\_F} \cdot IR_{Heave\_F}}{\sqrt{K_{S\_Heave\_F} \cdot SM_F}} \quad (24)$$

Where  $C_{D\_Heave\_F}$  is the damping coefficient of the front heave damper,  $SM_F$  is the front suspended mass. The decrease of damping ratio is linear to the installation ratio and as the spring rate is in the denominator, the damping ratio will also decrease with increasing spring rate. An iteration process is needed to find the final installation ratios (Figure 26). In Creo Parametric (3D CAD software) are constructed sketches in the plane of roll damper and heave

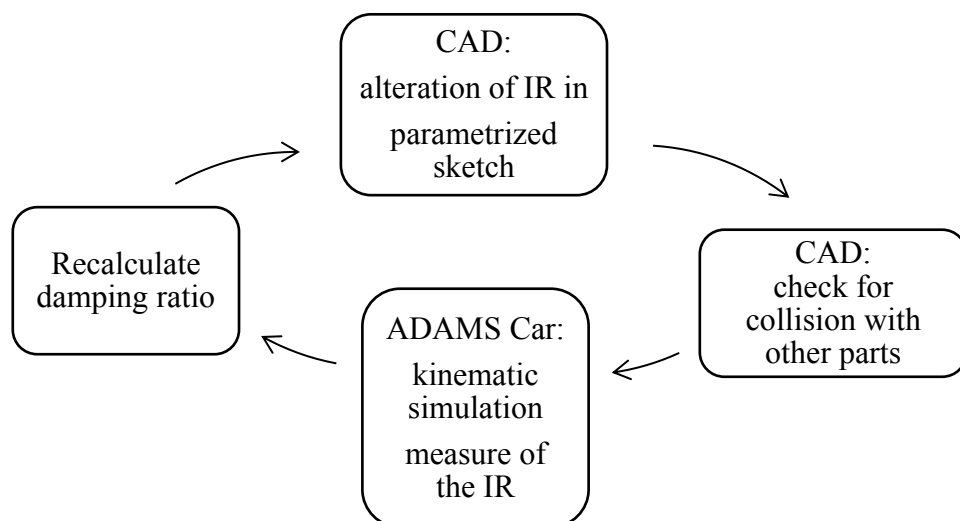
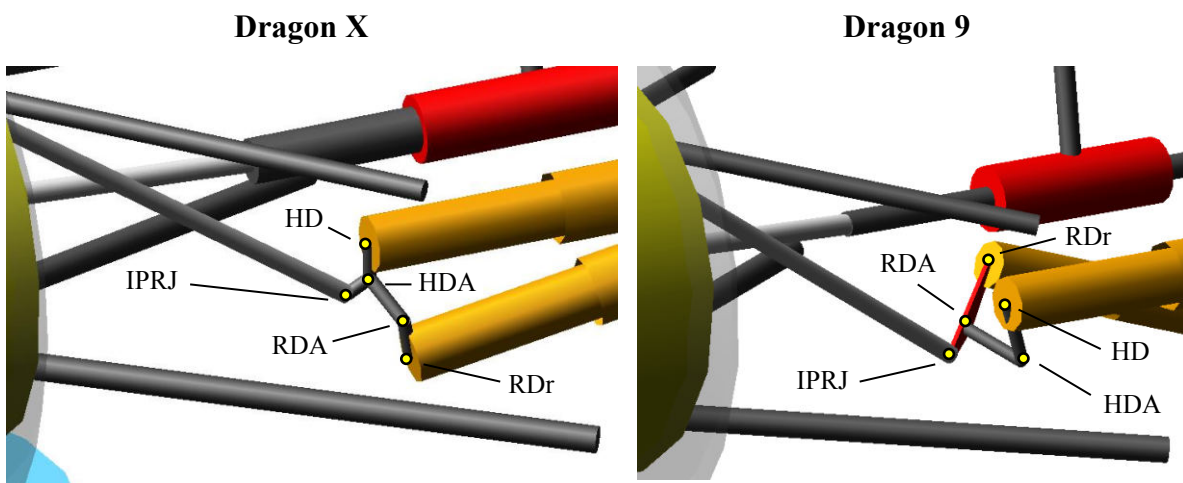


Figure 26 Iteration process of the reduction of installation ratio in bellcranks

damper, where the ground clearance is controlled and leverages of the bellcrank are parametrized via angles and lengths. The leverage is changed here, this sketch influences the kinematic skeleton of the model which changes the position of the dampers. Then a check of interference with other parts is made.

After that, the hardpoints in Adams are altered and kinematic simulation of “parallel wheel travel” or “roll & vertical force” is made. Then a measurement of installation ratio is done as a derivative of spring displacement over wheel displacement. If the resulting installation ratio does not match the desired result, it is needed to go back to the sketch in CAD and change the leverage in the desired direction. The damping ratio is then recalculated with the actual installation ratio.

In Figure 27 is shown the final design of the bellcrank skeleton and its comparison with Dragon 9. From experience with the Dragon 9 bellcranks design (Figure 1), the dampers were switched



*Figure 27 Comparison of the bellcranks of Dragon X and Dragon 9 from the kinematic point of view*

for the force transmission during a two-wheel bump (heave) to be direct. The heave spring and damper is loaded with higher forces. This enables the bellcrank to be lighter.

*Table 9 Explanation of the hardpoint labels*

Hardpoint abbreviation	Full name (explanation)
IPRJ	Inner pull/pushrod joint
OPRJ	Outer pull/pushrod joint
HD	Heave damper (attachment point of the damper)
HDA	Heave damper axis (point on the bellcrank axis in the plane of the heave damper)
RDr	Roll damper right (attachment point of the damper on the right side)
RDA	Roll damper axis (point on the bellcrank axis in the plane of the roll damper)
PRA	Pushrod axis (point on the bellcrank axis in the plant of the pushrod; at rear only)



Concerning the leverage arms of the bellcrank, the important length is not the absolute distance between the points (e.g. IPRJ and HDA) but rather the minimal (orthogonal) distance between the axis of the member (pullrod or damper, e.g. axis passing through IPRJ and OPRJ in case of pullrod) and the rocker axis (HDA), see Figure 28.

- If the leverage of the pullrod **decreases**, the IR **increases**
- If the leverage of the heave damper **increases**, the IR **increases**

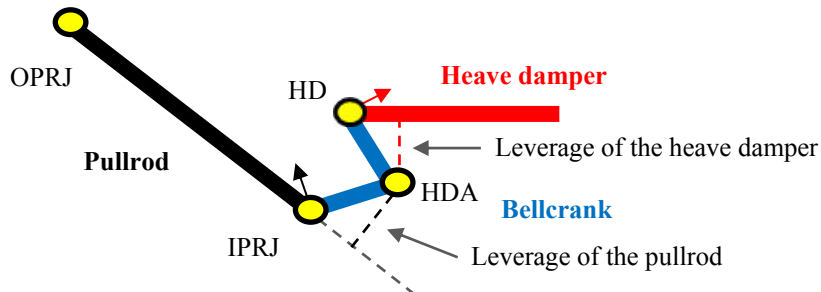


Figure 28 Leverage of the bellcrank defined

While the points move on a circular trajectory around the HDA, the leverages are constantly changing. The layout displayed in Figure 28 achieves high progressivity of the IR in heave, as pointed out with the red and black arrows, the points will move and leverage of the pullrod will decrease, the leverage of heave damper will increase, thus increasing the IR. From Figure 27, it is visible that the bellcrank arm of the pullrod on Dragon 9 was perpendicular to the pullrod axis in the static position, thus creating negligible progressivity. However, the heave damper bellcrank arm was angled the same way on Dragon 9 as shown in Figure 28, which caused progressivity in bump. On Dragon X, the source of progressivity in heave was switched, the heave damper arm is perpendicular to the heave damper axis in a static position, while the pullrod arm is angled to create progressivity. This was beneficial because the angled heave damper required a large amount of space in the bellcrank, which complicated the design. This creates negligible progressivity in roll because the rise of IR on one side is canceled with a decrease of IR on the other. With the bellcrank arm of the heave damper angled on Dragon 9, the heave damper was rising vertically in bump (required additional space) - this is also eliminated on Dragon X.

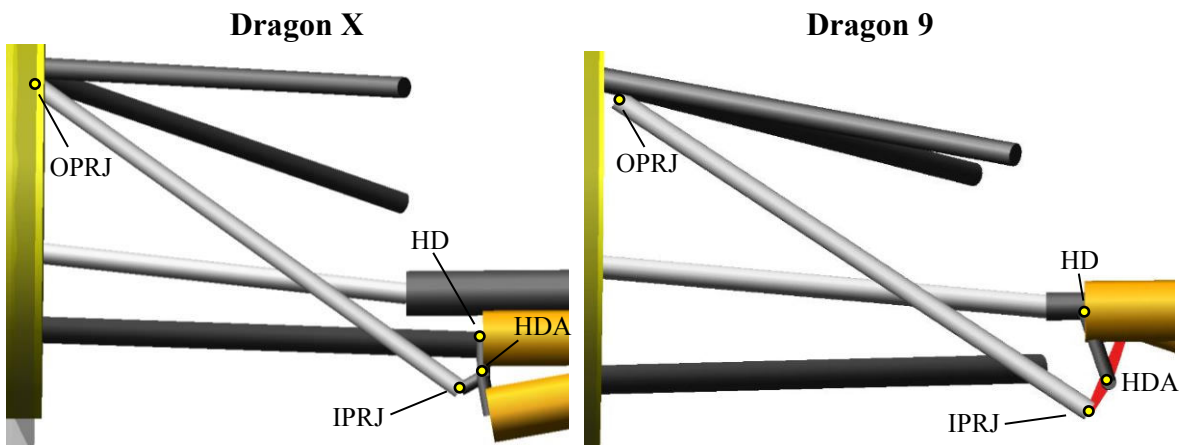


Figure 29 View of the front suspension in the plane of heave damper

Because the project of magnetorheological dampers (MR) is developed simultaneously by colleague Jiří Miša, there is a need to accommodate these dampers as well as standard dampers. As the project has been ongoing already and the dampers were made, the length of the heave dampers (distance between HD\_left and HD\_right) needed to remain the same because the MR dampers are the same length as the Öhlins dampers from Dragon 9 (custom heads of the dampers were made). Combining this with the discussed change of the source of progressivity, the bellcranks were moved further away from the center plane of the vehicle. This change helped to increase the IR while remaining the bellcrank size because it changed the angle of the pullrod. The higher angle of the pullrod (more vertical), the better transmission of the vertical force from the wheel to the pullrod and damper. Furthermore, as the bellcrank is smaller, the axis (HDA) is moved lower, which increases the slope of the pullrod and increases the IR. In Figure 29, the difference in the layout can be seen, the angle between the heave damper axis and heave damper arm (HD, HDA) is changed and the angle OPRJ-IPRJ-HDA is also changed. It is also visible that the OPRJ is moved towards the inside of the wheel, due to a scrub radius change discussed in Chapter 2.2.3. It reduced the slope of the pullrod, thus reducing the IR and another set of iterations was needed. The layout of wishbones influences the wheel trajectory, which also influences the IR – iterations and compromise are needed.

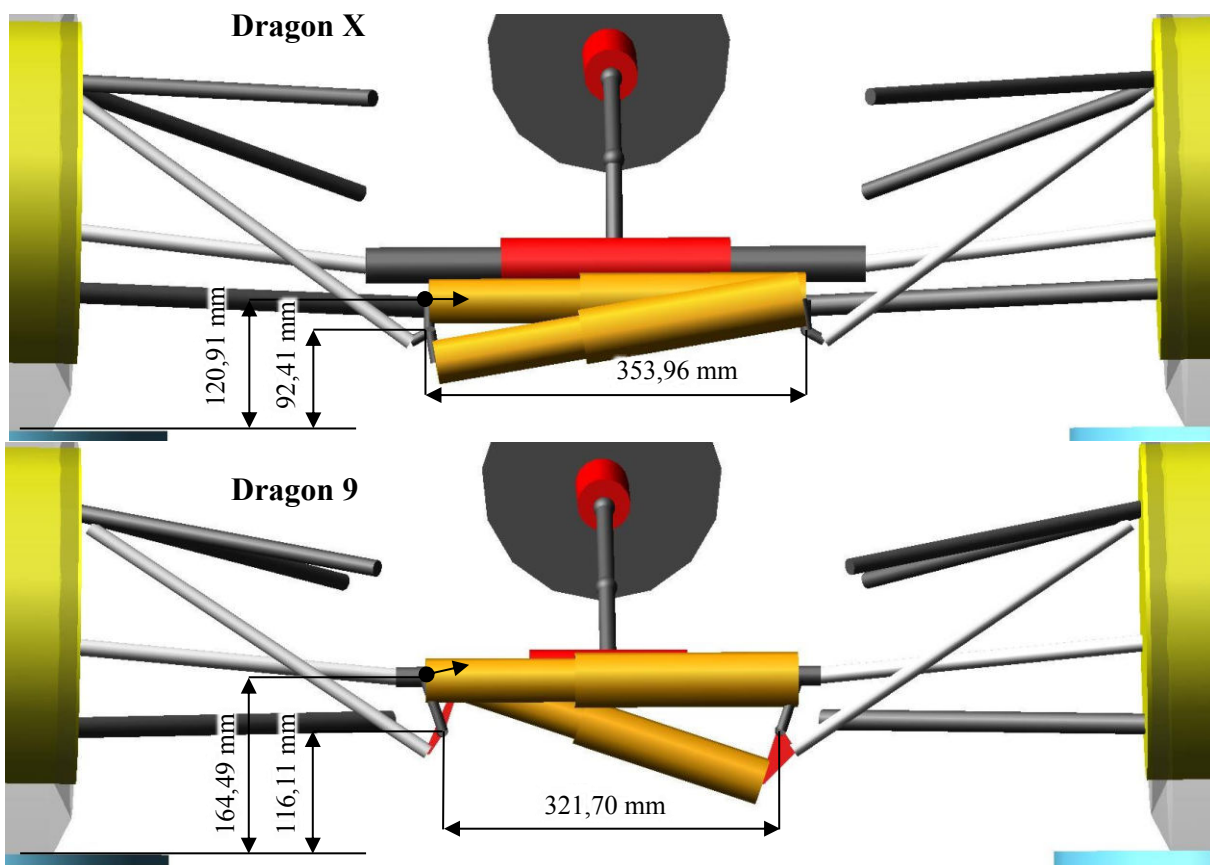


Figure 30 Comparison of Dragon X and Dragon 9 location of front dampers

A summary of the changes that influence the IR:

- Change of the bellcrank leverage arms – reduces the leverage of heave and roll dampers
  - Reduces the IR
  - Allows to lower the bellcrank, which increased the slope of the pullrod

- Increases the IR
- Change of the source of progressivity by changing the angles of bellcrank arms
  - Causes the bellcranks to move further to the sides
    - Increases the slope of pullrod
      - Increases the IR
- Changes of the wheel geometry (mostly OPRJ) influence the slope of the pullrod
- Change of the upper wishbone
  - Changes movement of the OPRJ
    - Influences the amount of translational displacement along the axis of the pullrod per unit of wheel travel

The main goal was to lower the maximal vertical coordinates of the front dampers. As seen in Figure 30, the heave damper was lowered by 43,58 mm in the static position. In bump, the heave damper on Dragon 9 would travel higher with respect to the static position in the vertical direction, due to the progressivity on the bellcrank. On Dragon X, the static position is the highest in all dynamic conditions. As mentioned earlier, the bellcrank axes were moved further apart by 32,26, which improved the slope of pullrod, but the aerodynamics could be slightly negatively affected by this change. It also allowed the roll damper to be in a more horizontal position which decreased the amount of space required in the vertical direction when the roll damper moves.

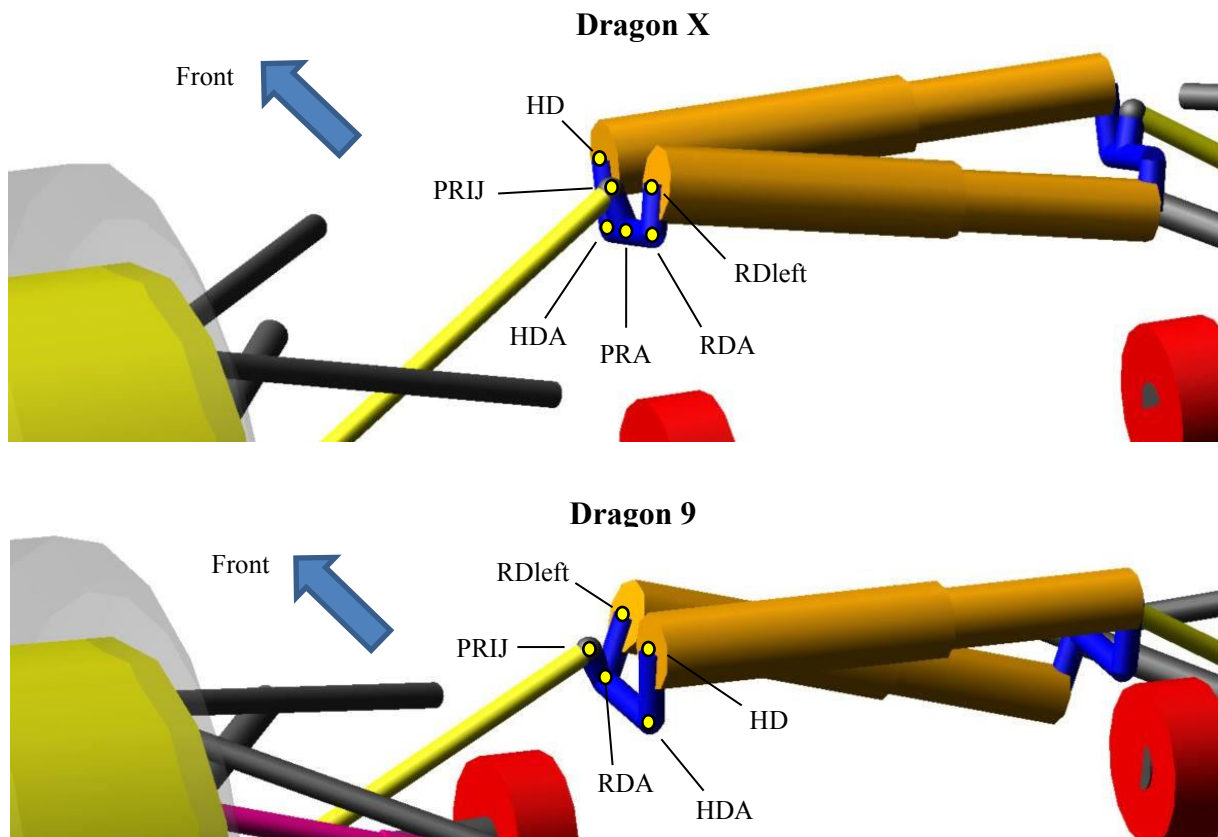


Figure 31 Rear springs and dampers comparison between Dragon X and Dragon 9 (respectively)

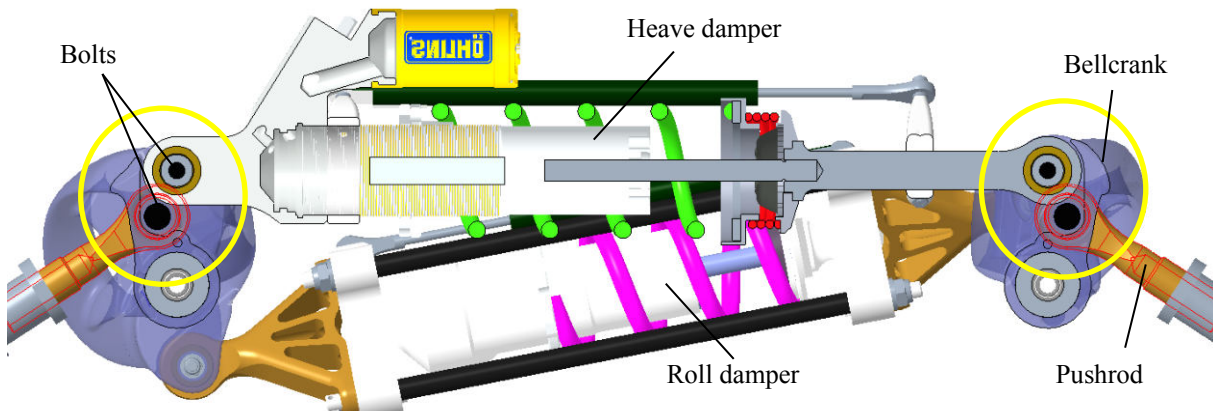


Figure 32 Problematic region of the rear bellcrank skeleton design

At the rear axle, the position of the roll-heave system is moved due to the change of the rear wishbones and chassis discussed in Chapter 2.3.5 and 2.4. The roll installation ratio is desired to be equal to the front for simplicity of the roll stiffness distribution setup. As the rear suspension is a pushrod system and heave dampers were moved to be in plane with the pushrod, a problem arose.

Both dampers and pushrods are connected via the spherical bearings, these consume space that is needed around the HD hardpoint as well as PRIJ. Due to this fact, the plane of the pushrod and heave damper were offset for the spherical bearing housings to not interfere. It is shown in Figure 31 – PRA stands for “Pushrod, axis”, which refers to point on the bellcrank axis which is closest to the PRIJ, there is a distance between PRA and HDA. In Dragon 9, the PRA is coincident with RDA. Even with this offset, it was a problematic part of the IR design at the rear axle, because of the bolts that are needed to fasten each connection, see Figure 32. The pushrod inserts would interfere with the heave damper heads. The bolts (black colored) are also needed to have sufficient clearance from the heave damper heads, as they are necessary to disassemble easily. This becomes problematic when progressivity of the IR is desired and is also the main reason for the difference of heave IR in front and rear – the heave damper was needed to be placed further away from the bellcrank axis.

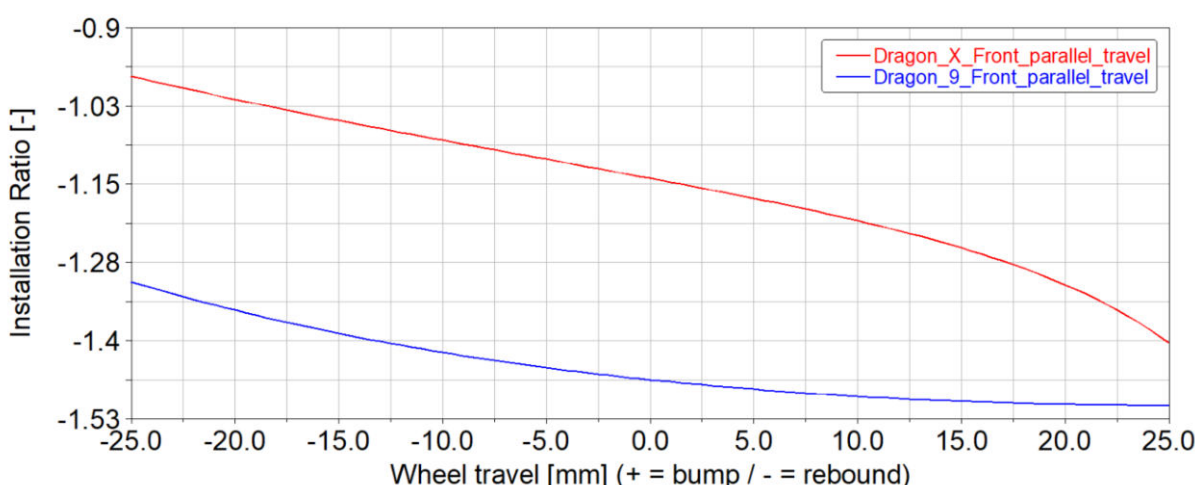


Figure 33 Comparison of **heave** installation ratio between Dragon X and Dragon 9 at the **front** axle

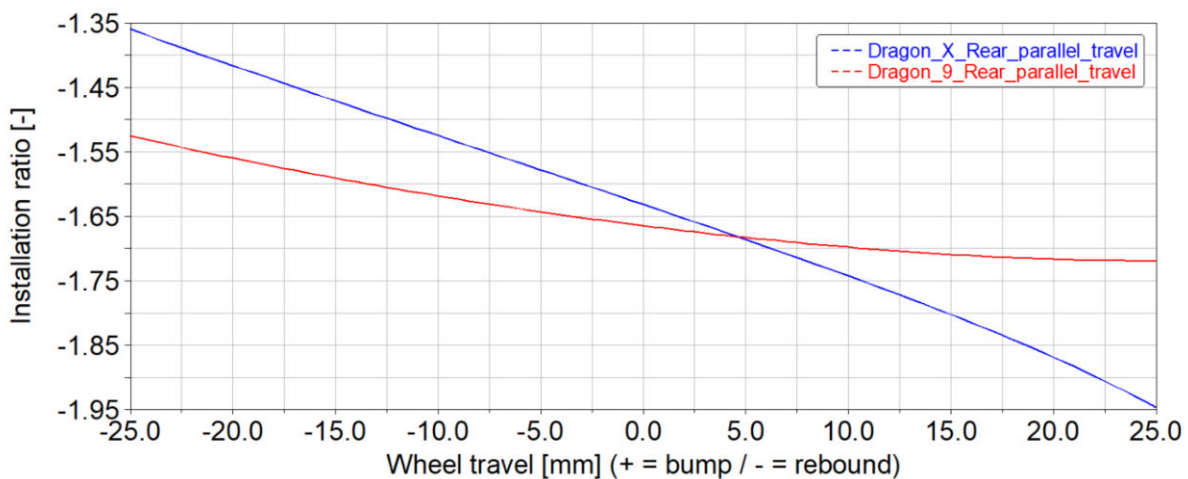


Figure 34 Comparison of **heave** installation ratio between Dragon X and Dragon 9 at the **rear** axle

The final heave installation ratio characteristic of the **front** axle over the whole suspension travel can be seen in Figure 33. The reduction in installation ratio in a static position (Wheel travel = 0) is obvious as well as the increased progressivity in bump. This progressivity is chosen for better cooperation with the aerodynamic system, which is ride height sensitive. It creates progressivity of the wheel rate but its influence is much lower than of a bump stop. The benefit of progressive motion ratio is its increase in damping forces as well as suspension rates, the damping ratio will increase according to Equation 24 – that is if the bump stop rate is neglected. The increase of damping forces could lead to an overdamped system, but as soon as the bump stop starts to act, the suspension rate rises quickly then also the critical damping rises. The increased damping forces are therefore used to help remain the damping ratio (which is decreasing in the bump stop range).

The rear characteristics can be seen in Figure 34, the graphs are obtained from “parallel wheel travel” kinematic simulations in Adams Car of each suspension assembly independently. The installation ratios displayed refer to IR<sub>ADAMS</sub> in Equation 12, it is double the IR of each wheel

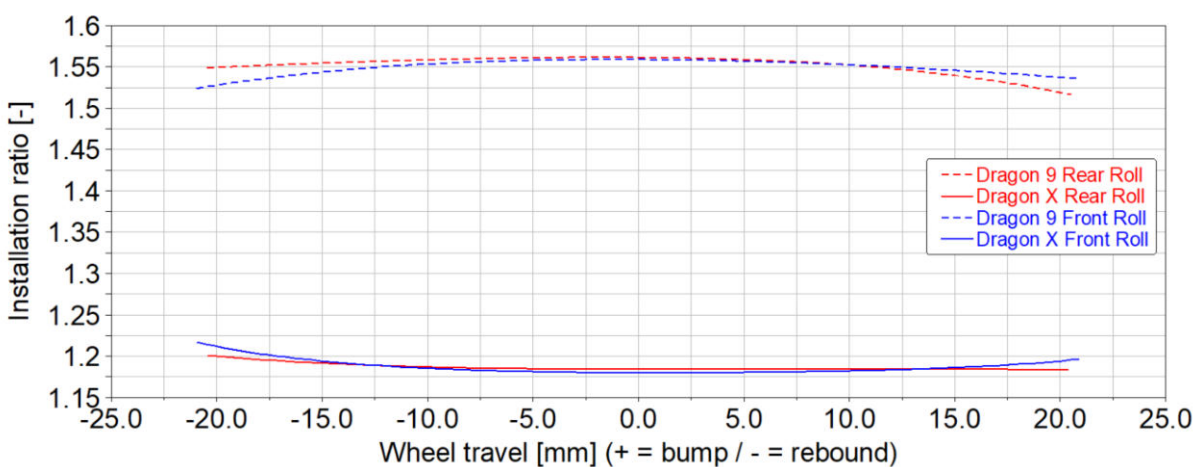
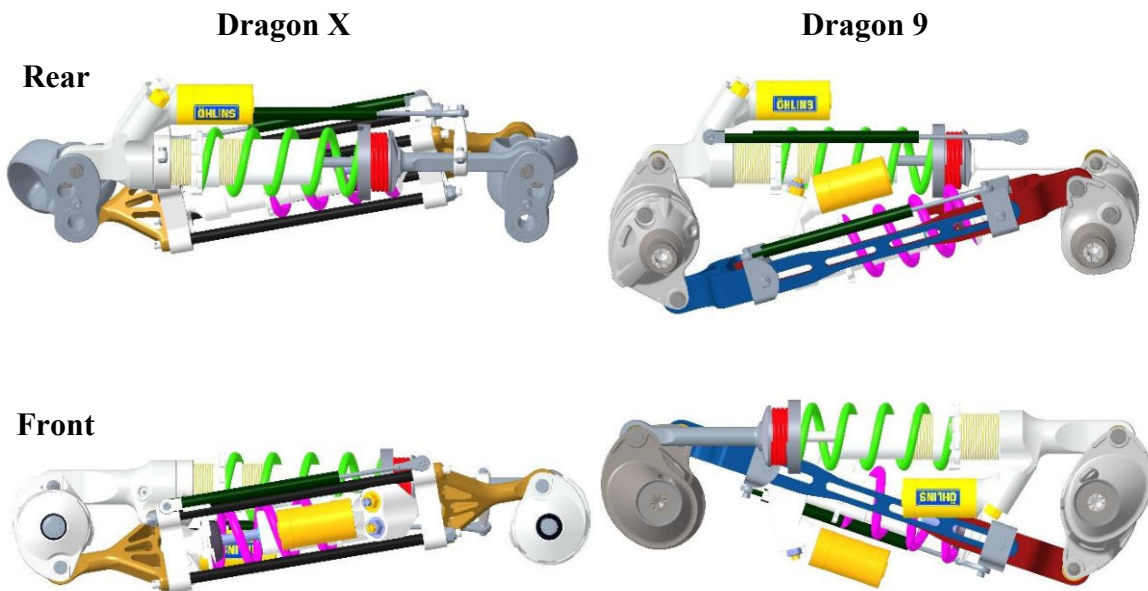


Figure 35 Comparison of **roll** installation ratio between Dragon 9 and Dragon X

independently or it can be described as an IR of the axle. It is calculated in Adams as a derivative of heave spring travel with respect to wheel travel.



*Figure 36 Comparison of the springs and dampers position and the bellcranks between Dragon X and Dragon 9 (displayed in scale 1:1 including the position)*

In Figure 35 is shown how the roll installation ratios were reduced and how the pull/pushrod arm progressivity influenced the characteristics. Although, the change (progressivity on Dragon X) in the installation ratio in roll is negligible.

In Figure 36 can be seen how the packaging of the dampers and rockers was improved. The picture is taken from the front of the car. Due to the changes in rear suspension and chassis, the roll-heave system was moved slightly higher while the front system was placed lower. The effect on chassis will be discussed later. In front, the roll damper was needed to be rotated by  $90^\circ$  around its axis because of the external reservoir of the damper.

Thanks to the change in the roll damper “anti-tension” construction (ensures the roll spring is always in compression both righthand and lefthand corner), the roll and heave dampers could be placed closer to each other, which further decreased the size of the bellcranks. The new construction itself is lighter as well.

## STATIC CHARACTERISTICS

In Table 10 are static values of suspension rates. Heave values were designed to be equal to the Dragon 9 FSG setup, the roll values were chosen slightly higher as the roll spring rates in other events were used slightly higher as well. As will be shown later, several different spring rates (softer and stiffer) are made as well for the setup tuning during testing. Therefore, it is possible to obtain various setups. Of course, there is a limit in changing springs to stiffer rates, as the damping ratio could become insufficient.

*Table 10 Comparison of Dragon X design and Dragon 9 FSG suspension rates and frequencies*

Heave	Installation ratio [-]		Spring rate [N/mm]		Wheel rate [N/mm]		Ride rate [N/mm]		Wheel frequency [Hz]		Ride frequency [Hz]	
	Front	Rear	Front	Rear	Front	Rear	Front	Rear	Front	Rear	Front	Rear
DX	0.57	0.81	75	42	47.9	55.5	32.3	35.6	4.64	4.80	3.81	3.84
D9 FSG	0.73	0.83	45	40	48.0	55.1	32.3	35.4	4.64	4.78	3.81	3.83
Roll	Installation ratio [-]		Spring rate [N/mm]		Roll rate neglecting tires [Nm/°]		Roll rate including tires [Nm/°]		Roll frequency neglecting tires [Hz]	Roll frequency including tires [Hz]	Roll frequency neglecting tires [Hz]	Roll frequency including tires [Hz]
	Front	Rear	Front	Rear	Front	Rear	Front	Rear				
DX	0.59	0.59	95	95	831	790	498	473	7.02	5.43		
D9 FSG	0.78	0.78	50	50	764	726	474	450	6.73	5.30		

*Table 11 Comparison of Dragon X and Dragon 9 roll gradients*

		Roll gradient [°/G]	
		Neglecting tires	Including tires
D9	Original	0.204	0.443
	FSG	0.388	0.626
DX		0.357	0.595

Roll rates were important as they are individual for each axle, therefore represent the roll stiffness distribution as well, but roll gradients were also important informatively as they are easier to visualize. Shown in Table 11.

Finally, the damping ratio which was partially the limitation of the installation ratio change is displayed in Table 12. Where a large reduction of installation ratio took place, the damping ratio decreased, therefore higher damping coefficients (setups) had to be used to obtain equal damping ratio. The drawback is that the damping coefficient rises exponentially as the low-speed valve is closing. Thus, tuning in the vicinity of the closed low-speed valve will be more difficult to achieve. The damping coefficients were obtained by linear interpolation between the coefficients of measured data.

*Table 12 Comparison of Dragon X and Dragon 9 damping ratios*

		Damping ratio [-] (neglecting tire)			
		Low-speed		High-speed	
		Front	Rear	Front	Rear
Heave	DX (setup)	0.76 (3.19)	0.76 (2.56)	0.38 (3.38)	0.44 (2.80)
	D9 FSG (setup)	0.76 (2.75)	0.76 (2.5)	0.38 (2.75)	0.44 (2.75)
Roll	DX (setup)	0.99 (3.23)		0.43 (3.31)	
	D9 FSG (setup)	0.99 (2.75)		0.43 (2.5)	

### 2.1.4 KINEMATIC SIMULATIONS IN ADAMS AND MATLAB

All these values displayed above are only static. As the spring rate with bump stop and progressive IR create a progressive wheel rate, it is desirable to display characteristics in the whole suspension travel region. Matlab scripts are written based on the work of Ing. Martin Hlaváč [10] and supplemented with emphasis on the comparison and development of the Adams Car model. As the static position of the vehicle is also the modeling position, the helper spring has to always be preloaded with a specific force for this to be true. In reality, the difference in static wheel rate caused by an offset of static positions might not be significant. However, part of this thesis is focused on improving the Adams Car model, therefore it is desirable to unite the Matlab and Adams simulations. For this, an iterative loop was written in Matlab to adjust the helper spring precisely, see Figure 37. Installation ratios displayed above

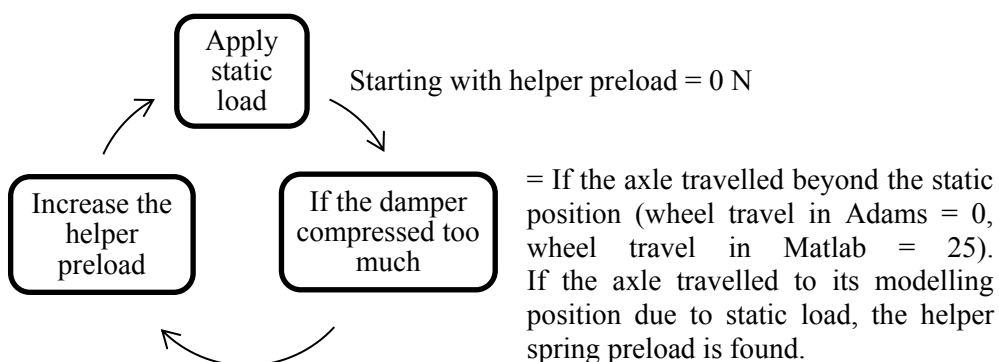


Figure 37 Helper preload iterative loop

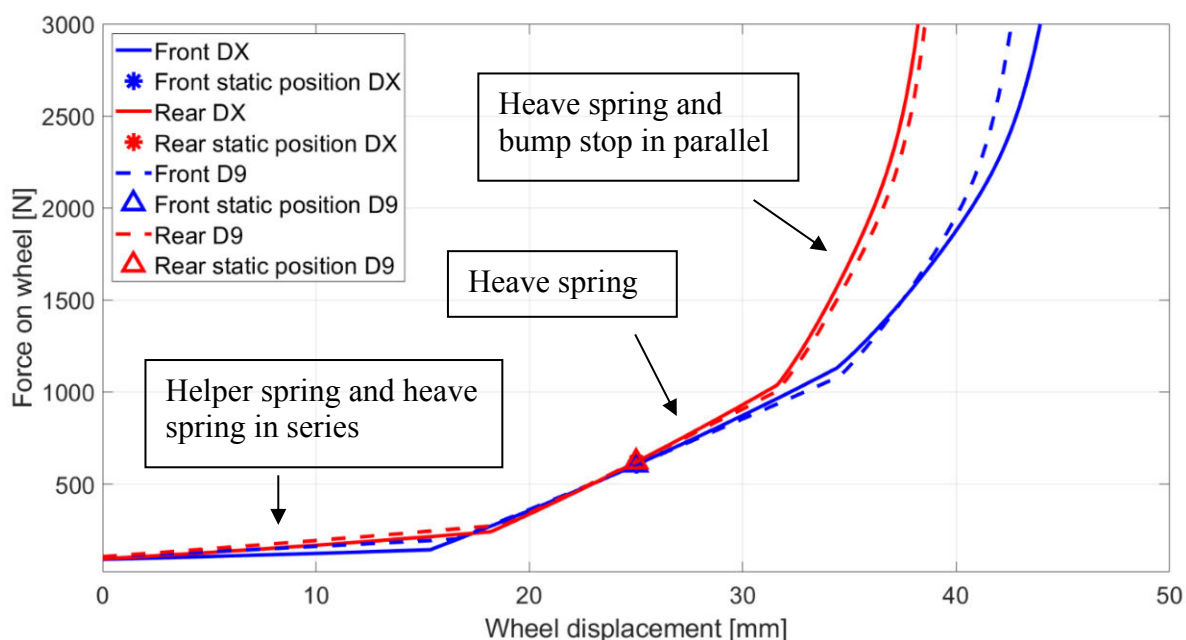


Figure 38 Force on wheel vs wheel travel

\* wheel displacement = 25 mm in Matlab is equal to wheel travel = 0 mm in Adams, which is the modelling and static position

are exported from Adams Car into Matlab where it is used to display all the characteristics of the vertical dynamics in the entire suspension travel.

If the damper compressed too little with helper preload = 0, the helper spring needs to be longer or the gap between the helper spring and damper seat with fully extended damper needs to increase.

Using this tool, Dragon 9 characteristics are recalculated. Although, in reality, the static position on Dragon 9 did not equal the modeling position because this issue was not dealt with before. In Figure 38 is shown how very similar F-x characteristics of the wheel were achieved with different installation ratios. The static position is highlighted with a marker.

The force in spring is calculated using the kinematic characteristics from parallel wheel travel simulation in Adams, then it is recalculated to the wheel using installation ratio. The spring deflection is multiplied by the corresponding immediate stiffness and the force is summing up in the system. The calculation of force on wheel from spring is based on the equality of works done, see Equation 7.

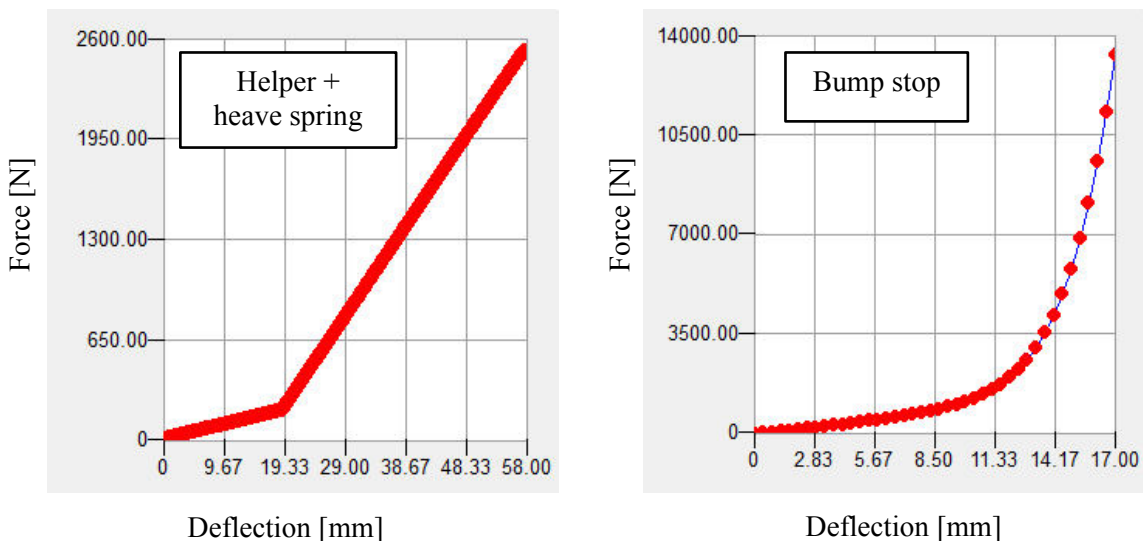


Figure 39 Spring nonlinear characteristics and bump stop curve in Adams

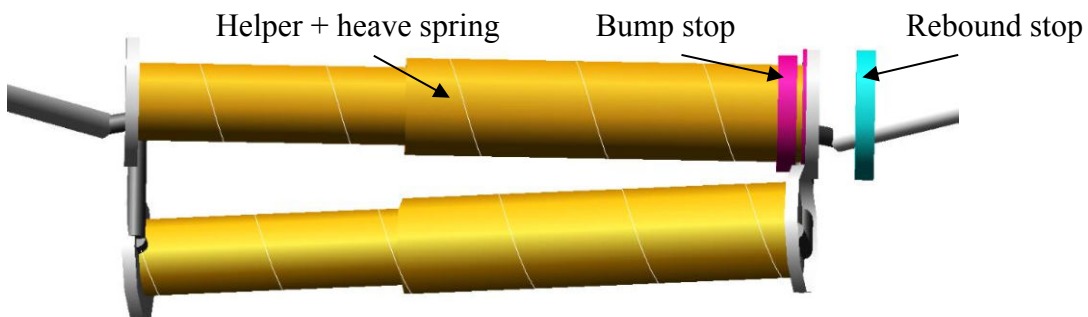


Figure 40 Bump stops and rebound stops were added to the Adams model

The Matlab script is a tool to improve the Adams model. The force-deflection curve of the spring without the bump stop is imported to Adams (Figure 39). The bump stop is independent as it is available as another element in Adams. Bump stop and rebound stops are added into the Adams model. The measured F-x characteristics of bump stops are also imported to Adams – Figure 40. In previous years, the Adams model only had default linear springs. These are still used for roll springs. To have a static position in a modeling position in Adams, preload is needed, it is calculated in Matlab and imported in Adams as force preload of the nonlinear spring. Bump stop clearance is also calculated in Matlab and is dependent on the number of used bump stop washers. For initial setup, bump stop washers were chosen to achieve similar F-x characteristics as seen in Figure 38.

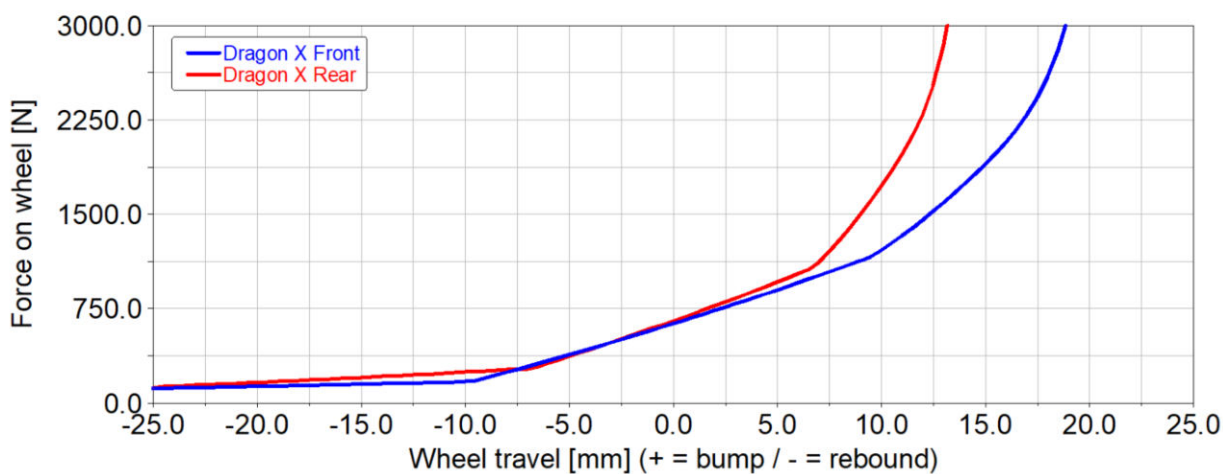


Figure 41 Force on wheel vs wheel travel from Adams parallel wheel travel simulation

In Figure 41 is shown F-x characteristics of the wheel from Adams Car simulation. There is a 0,5 mm error of wheel position between the Adams simulation and Matlab. This error can be caused by a numerical error of the Matlab recalculation and can be neglected. The real helper's pretension will never be so accurate and the mass will differ.

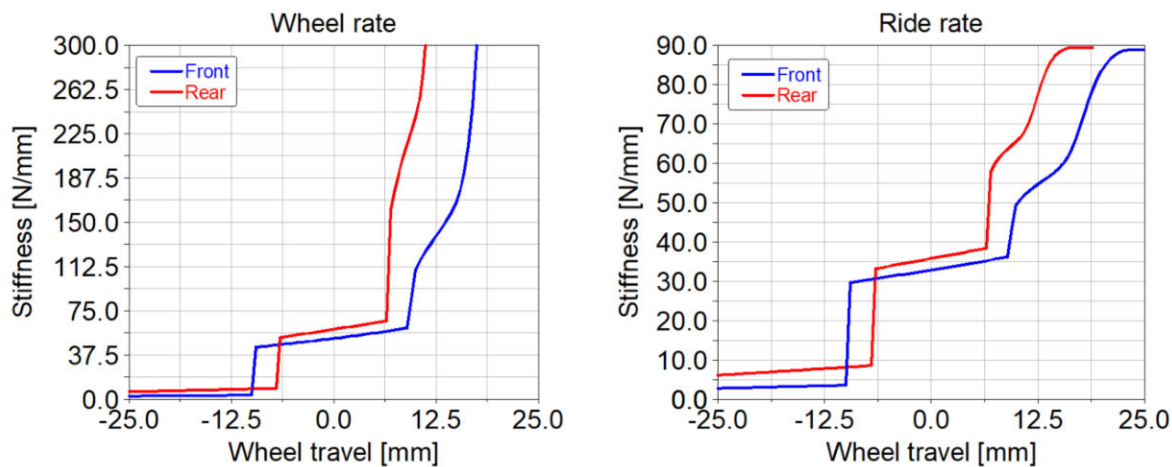


Figure 42 Wheel rate and ride rate of DX from Adams parallel wheel travel simulation

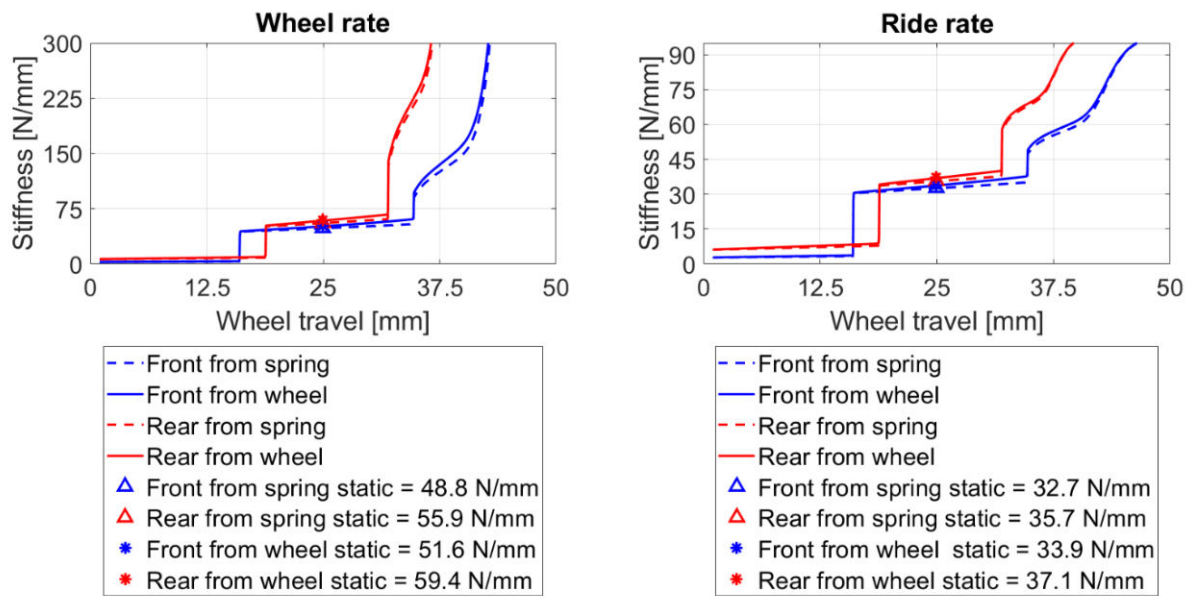


Figure 43 Wheel rate and ride rate of DX from Matlab

In Figures 42 and 43 is a comparison between calculation in Adams and Matlab. The static values from Adams:

Table 13 Static values of WR and RR from Adams

	Wheel rate [N/mm]	Ride rate [N/mm]
Front	51.54	33.90
Rear	59.23	37.07

The values from Matlab equal to Adams when the rates are calculated from the wheel. Wheel rate is a derivative of the F-x characteristic of the wheel.

$$WR_{From-wheel} = \frac{\partial(F_{Wheel})}{\partial(x_{Wheel})} \quad (25)$$

The spring values are calculated analytically the same way as the static values and are also much closer to the static values displayed above in Table 10. Wheel rate from spring is calculated according to Equation 10. The difference between calculation from spring and wheel

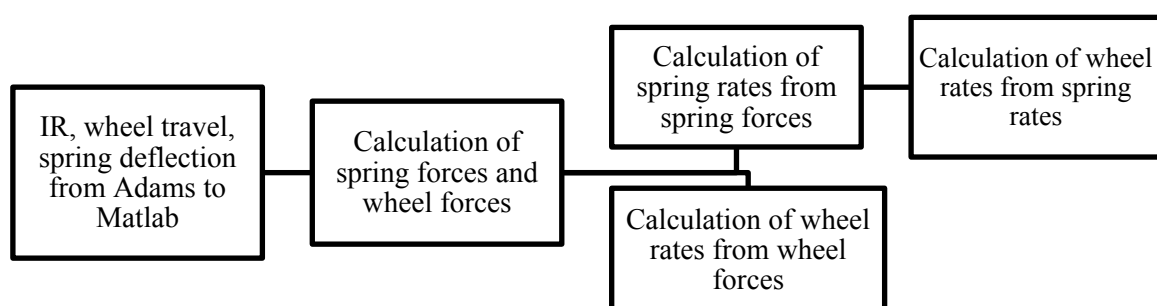


Figure 44 Diagram of different wheel rate calculations in Matlab

is probably caused by multiple usages of installation ratio, which is also a numerical derivation from Adams. The values obtained from Adams are considered more accurate. Further Matlab simulations calculate with the wheel rate calculated from the wheel force. The Diagram of the different wheel rate calculation approaches is displayed in Figure 44. Ride rate is then simply calculated as wheel rate and tire rate in series.

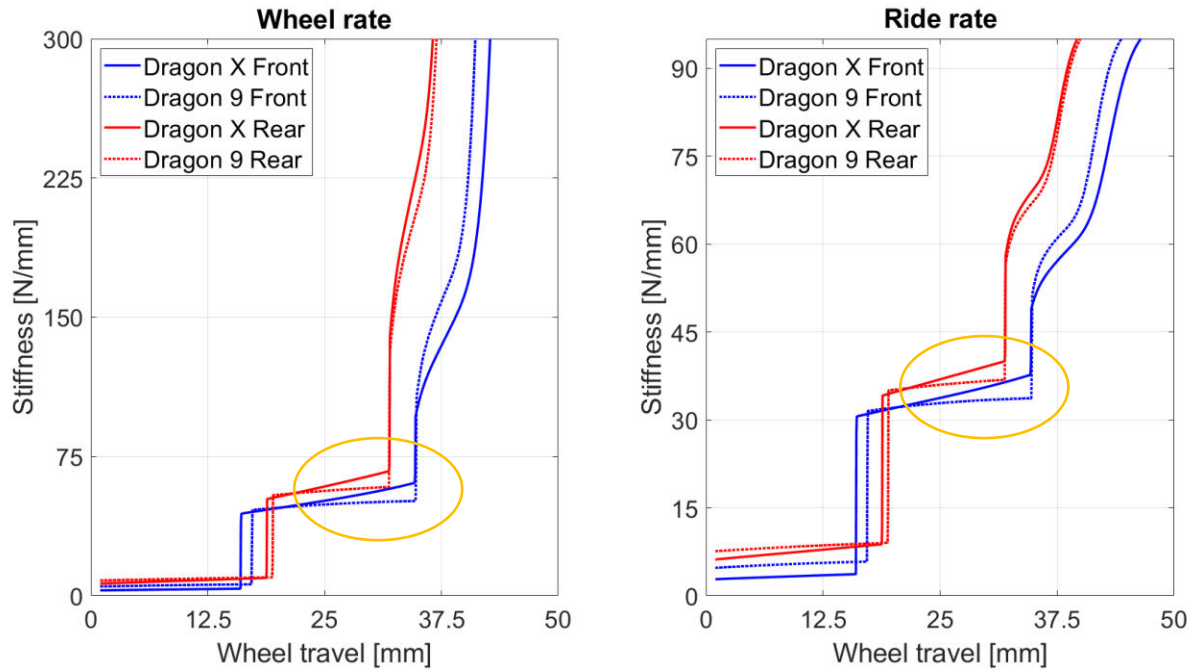


Figure 45 Comparison of Dragon X and Dragon 9 wheel and ride rates from Matlab

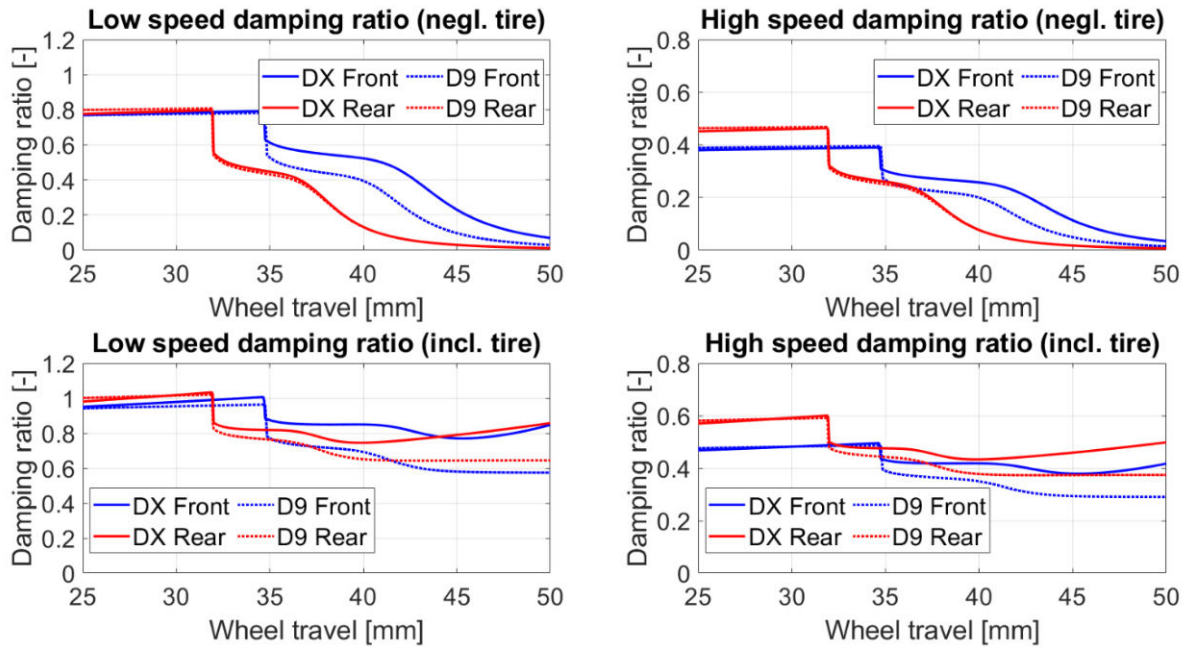


Figure 46 Damping ratios comparison of Dragon X and Dragon 9 from Matlab. Setups according to

In Figures 38 and 41, the influence of IR progressivity is hard to see, but in wheel and ride rates it is more visible, see Figure 45. Still, the bump stop has a much larger impact.

According to Equation 24, with rising (progressive) IR, the damping ratio should rise as well. Although the effect is not large, it is visible in Figure 46. An underdamped suspension has been problematic during testing at high speeds when the downforce increased and the bump stops were acting. The progressivity in installation ratio could be an improvement for these situations. The higher progressivity is most visible at the front axle. Both IR progressivities were chosen to be proportional (gain approx. 118 % of static value), so according to rising IR, the damping ratio should also rise, but at the rear axle this effect can be barely seen. This could be caused by a larger wheel rate at the rear, especially in bump stop (which is caused by higher rear IR). Then the difference in damping ratio caused by the installation ratio is reduced by wheel rate. Therefore, larger progressivity should be ideally used at the rear to have an equal effect on the damping ratio (front and rear). When the tire is included, the progressive IR is seen more clearly in the damping ratio, as the total stiffness is decreased.

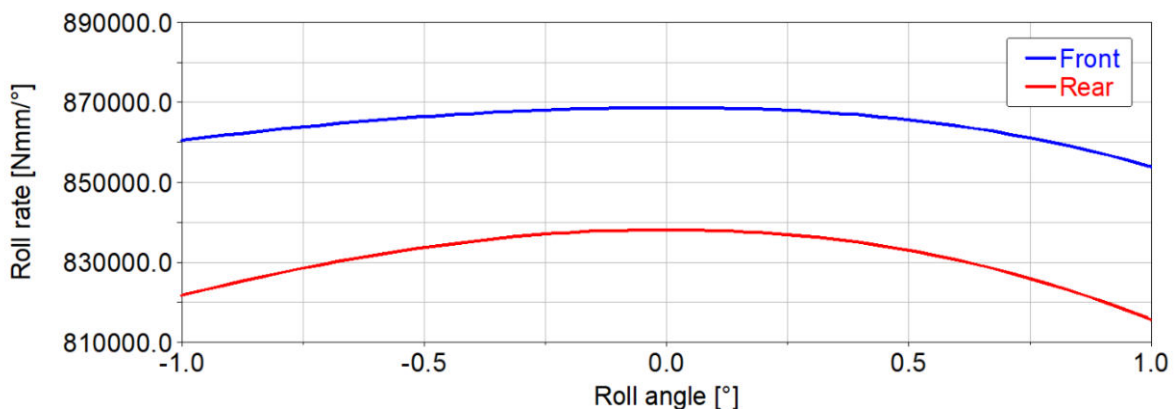


Figure 47 Roll rates from Adams

In Figure 47, the roll rate kinematic characteristic is given from Adams roll and vertical force analyses. The curvature is given by the nonlinearity of the mechanism (rotational movements). Interestingly there seems to be a slight difference in roll rate between left and right roll angle. This was not yet clearly understood as the roll system is point-symmetrical, the point of symmetry lies on the roll damper axis and in the middle plane of the vehicle.

### 2.1.5 ALGORITHM FOR AN AUTOMATIC OPTIMAL COIL SPRING CONSTRUCTION DESIGN

Different spring rates were chosen around the above-mentioned default values to give sufficient freedom in the setup. The values were chosen while taking into consideration the original (stiffer) suspension design. Drawback of completely different front and rear heave spring rates (due to different IRs) is that more different spring rates are needed. Unfortunately, no coil spring manufacturer is interested in sponsoring our team at the moment, therefore the number of springs is reduced due to the costs. A list of heave springs is displayed in Table 14, green rows are the chosen ones after the cost reduction. Our drivers are non-professionals so the setup change is sufficient anyway. The heave spring rates were chosen by wheel rates. One of the important values needed for the coil spring design is the maximal deflection of the spring. For

heave springs it corresponds to 25 mm of wheel bump travel from a static position, which is obligatory by the rules. These values were calculated using the Matlab parallel wheel travel script discussed above.

*Table 14 Heave spring rates options*

Front			Rear		
Spring rate $k$ [N/mm]	Wheel rate [N/mm]	Max spring deflection $x$ [mm]	Spring rate $k$ [N/mm]	Wheel rate [N/mm]	Max spring deflection $x$ [mm]
60.5	38.5	46.1	34	45	63.7
63.5	40.65	45.4	36	47.5	62.6
67	42.8	44.6	38	50	61.7
70.5	44.95	44	39.7	52.5	60.9
75	47.85	43.2	42	55.5	60
77	49.2	42.9	43.5	57.5	59.5
80	51.35	42.4	45.5	60	58.8
84	53.5	41.9	47	62.5	58.4
87	55.65	41.5	49	65	58
92	58.5	41	52	68.5	57.8

For roll springs, the options were also chosen according to the previous stiffer setup (to achieve approx. 0,2 °/G with the stiffest rates). The spring deflections correspond to 2,5 G of lateral acceleration, but due to their small values, they do not affect the coil spring design.

Spring rate [N/mm]	Roll gradient neglecting tire [°/G]	Max spring deflection front for 2.5 G [mm]	
		Front	Rear
75	0.45	12.86	12.73
85	0.4	11.38	11.22
95	0.36	10.21	10.07
110	0.31	8.8	8.67
125	0.27	7.75	7.64
140	0.24	6.95	6.86

The basic equation for the calculation of coil spring stiffness is given as [13]

$$k = \frac{d^4 \cdot G}{8 \cdot D^3 \cdot n_a} \quad (26)$$

Where  $k$  is the coil spring stiffness,  $d$  is the wire diameter,  $G$  is the modulus of elasticity in torsion,  $D$  is the mean diameter of the spring,  $n_a$  is the number of active coils. This was used in previous years. By a manual iterative method, different stiffnesses were obtained by changing the spring dimensions. This could lead to overweight spring coils designs as the weight of the spring was not considered. The stress calculation was also not considered, therefore the calculated springs could have low safety factor. Mainly because of the weight of the coil (steel wire), this Matlab iterative calculation was created. Several conditions need to be met in the coil spring design:

- Coil spring stiffness meets the desired options (within limits)
- Wire diameter meets the manufacturer's options (5,6; 6; 6,3; 7,1; 8 mm)
- Spring diameter is in desired boundaries (given by the damper and related components in CAD)
  - $D_{inner}$  minimal 36,6 mm
  - $D_{outer}$  maximal 52,1 mm
- Minimal number of active coils  $n_a = 2$
- Pitch less than 25,4 mm
  - Given by the manufacturer
- Safety factor of 1,05
  - Chosen low, because the load case is very extreme
- Minimal weight available

Pitch of the spring with closed and machined ends is calculated as [13]:

$$p = \frac{L_0 - 2 \cdot d}{n_a} \quad (27)$$

Where  $p$  is pitch, and  $L_0$  is the free length, which is calculated from the minimal needed deflection:

$$L_0 = x_{min} + d \cdot (n_t) \quad (28)$$

Where  $n_t$  is the total number of coils,  $x_{min}$  is the maximal possible spring deflection (Table 14). To obtain safety factor, stress needs to be calculated [13]:

$$\tau = K_W \frac{8 \cdot F \cdot D}{\pi \cdot d^3} \quad (29)$$

Where  $\tau$  is the maximal shear stress in the wire,  $F$  is the maximal acting force, and  $K_W$  is Wahl's coefficient. Maximal force is given by the equation of spring force, which is spring stiffness times the maximal deflection. Safety factor is then [13]:

$$k_k = \frac{R_{se}}{\tau} \quad (30)$$

Where  $k_k$  is the safety factor and  $R_{se}$  is the yield strength in shear, which is chosen according to literature as the least conservative value [13]:

$$R_{se} = 0,7 \cdot R_m \quad (31)$$

Where  $R_m$  is the ultimate shear strength. As the material is chosen a cold drawn patented wire of class SH,  $R_m = 2330$  MPa. [13]

Both  $R_{se}$  and safety factor are chosen very non-conservative, as the values from literature are for general mechanical engineering use, while Formula student is designed to last only one

season and weight limits are pushed. If the conservative values were chosen, the coil springs would not even fit the dimension limitation and would be very heavy. For control, the stresses in springs used in previous seasons were recalculated and some were even below safety factor of 0,75.

The weight of the coil spring is calculated simply as the weight of the wire [13]:

$$m = \frac{\pi^2 \cdot d^2 \cdot D \cdot n_t \cdot \rho}{4} \quad (32)$$

Where  $m$  is the mass of the coil spring and  $\rho$  is the density. The algorithm is shown in Figure 48.

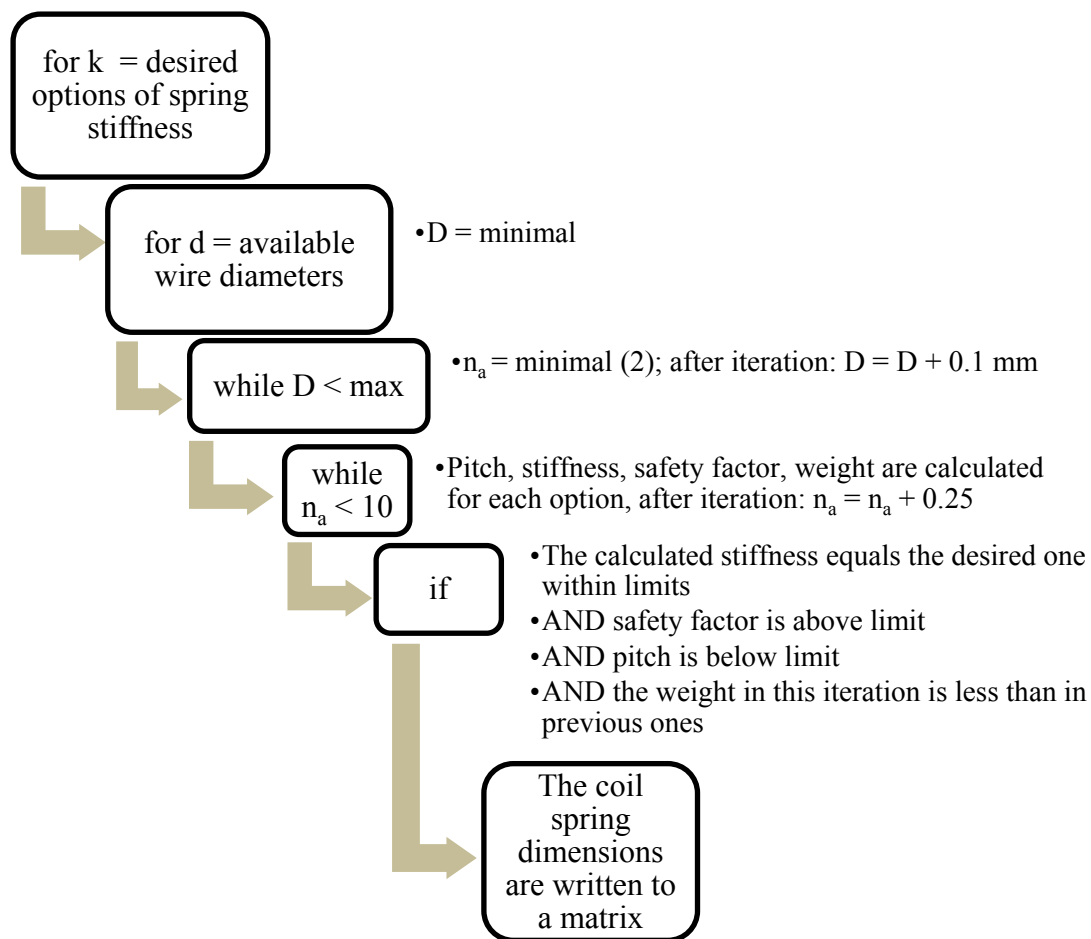


Figure 48 Coil spring design algorithm

To visualize the selection procedure, the coil spring options were plotted throughout different stages of the selection process from all options to the final one in Figure 49.

The comparison with last year's spring design in terms of weight is unfair because the stress calculation of the coil springs has not been dealt with before in our team. If an actual deflection of the spring occurred up to the maximal necessary point - which is mandatory by the rules,

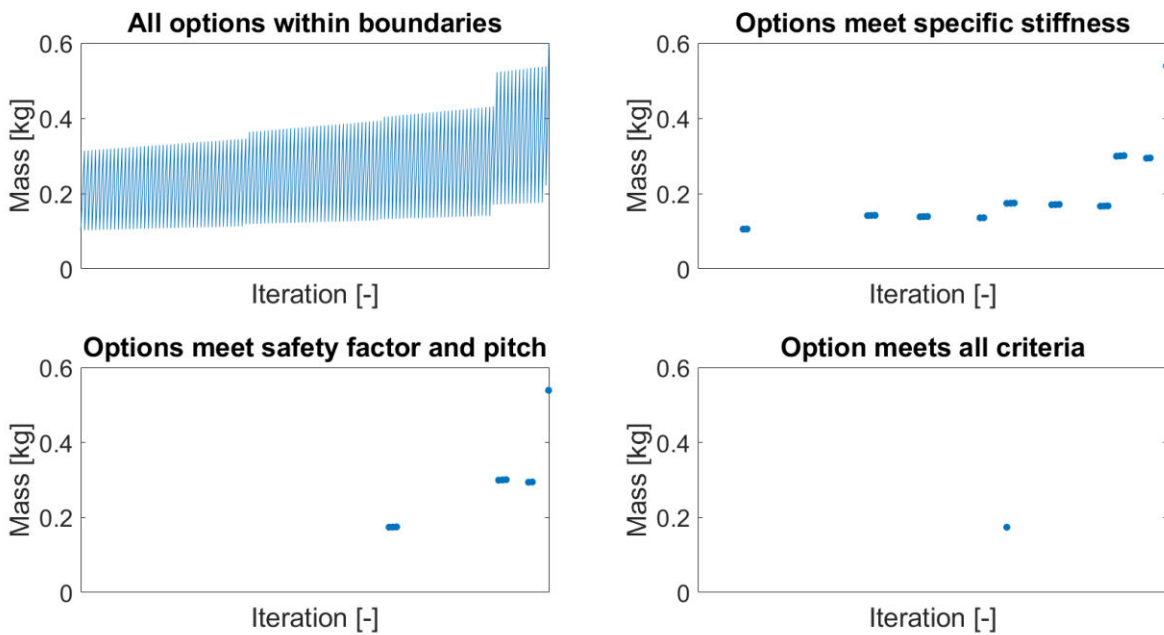


Figure 49 Selection of the coil spring design

some plastic deformation would probably occur. This could not be risked, therefore a safety factor of 1,05 was established. Where the real limit lies is not known but it could be measured in the future to reduce the weight of the coil springs and the desired safety factor would be under control. The comparison can be seen in Figure 50 and the weight of Dragon X springs is higher. This script can be used in the future to obtain the optimal dimensions of the springs without the need to iterate manually, plus provides control over safety via the analytic stress calculations.

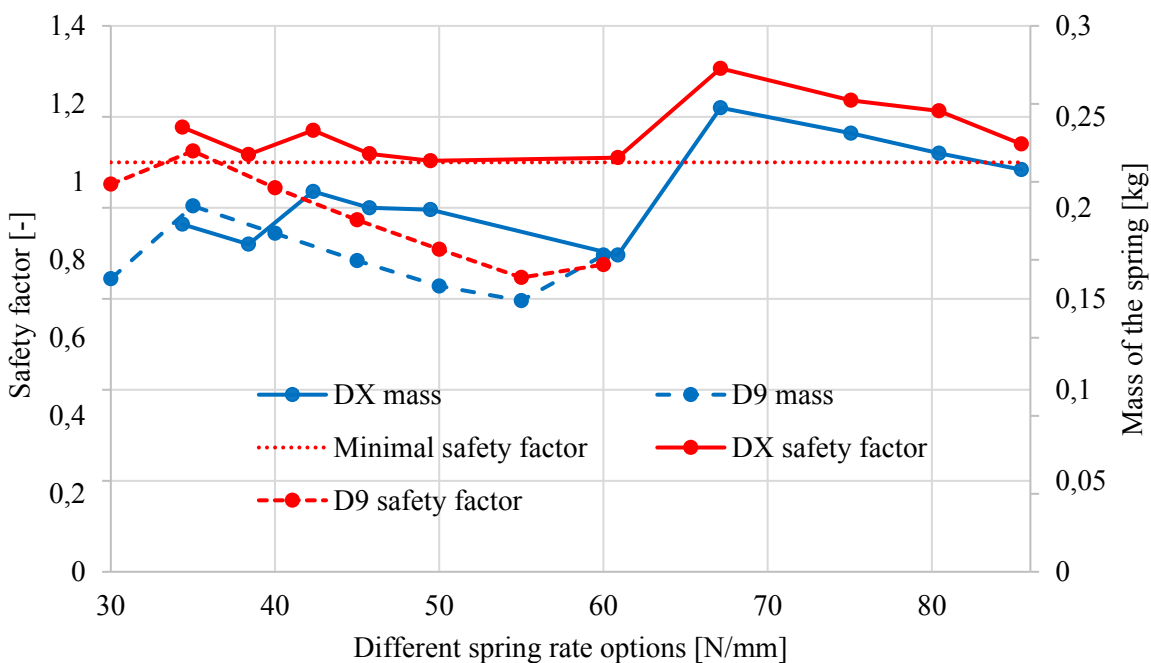


Figure 50 Comparison of weights and safety factors of DX and D9 spring options

## 2.2 WHEEL GEOMETRY

Concerning wheel geometry, two main issues are dealt with at the front axle, these are camber change due to steering and steering forces at the entry of a corner in braking-in-turn situation. The camber change is altered via the caster angle and steering forces in braking via scrub radius. The Ackermann geometry calculation is not part of this thesis and was done by another team member.

### 2.2.1 WHEEL INCLINATION ANGLE ANALYSIS

This chapter continues to deal with the issue discussed in Chapter 1.2.1, where the problem of unequally distributed temperature on the tire surface was seen in the data. From the comparison of the inner and outer temperature, it is obvious that a change in the inclination angle (IA) of the wheel is needed. The inclination of the wheel discussed in this thesis is the angle between the wheel plane and a normal to the road plane. The signs of the inclination angle are mirrored left to right, unlike the convention in Adams Car (SAE). The term “camber” is not used because in Adams Car it is the angle of the wheel from the front view in relation to chassis, not the road. The inclination angle discussed here might be also called “camber in relation to the road”. Negative inclination angle always means that the wheel (top of the wheel) is inclined inward to the chassis (like camber), zero inclination angle means that the wheel is perpendicular to the road surface. [7]

To study the wheel IA during testing, a reconstruction of the wheel position is done from the test data. From Adams Car suspension simulations, the IA for each situation on the track is calculated. To improve the accuracy of the simulations, non-linear spring and bump stop characteristics are imported to the Dragon 9 Adams Car model as well. Tires are also included,

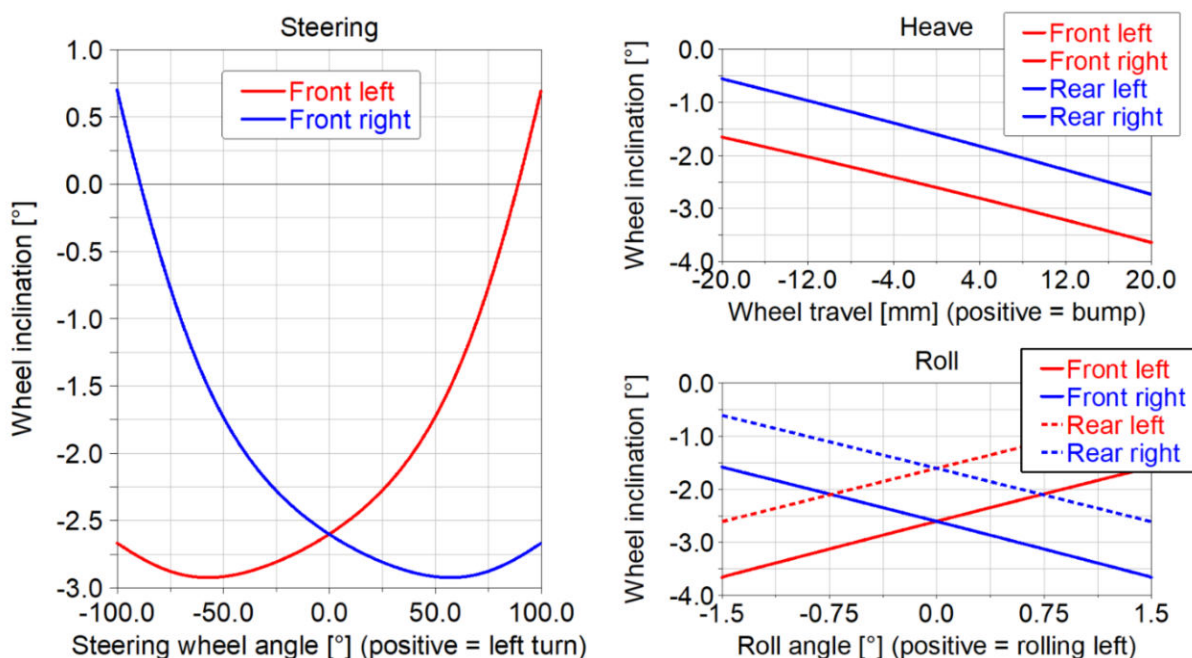


Figure 51 Wheel inclination angle change due to steering, heave and roll of Dragon 9.  
Tires are included. Static camber front =  $-2.6^\circ$ , rear =  $-1.6^\circ$

while the vertical stiffness of the tire is a constant of 99 N/mm. Compliances are not included in these simulations. The effects of steering, heave motions, and roll motions of the body on the wheel IA can be seen in Figure 51.

Camber change in roll should ideally level the rolling of the car and thus prevent a positive inclination angle at the outer wheel. Figure 51 shows that as the car rolls to the left in a right-hand turn, the outer wheel (left) is losing the negative inclination angle and gains more positive IA. This is not desirable, but to level the camber loss in roll, vast change in wishbones, roll-centers, and inboard pickup points would have to be made. In Figure 52 is shown a comparison of IA to the road (including tires) and to the wheel centers (WC) plane (neglecting tires). The camber change in roll with neglected tires is the one that can be controlled by the kinematics, it is only a portion of the total IA.

$$IA \text{ to } WC \text{ plane} = IA - (RA \text{ to the road} - RA \text{ to the WC plane}) \quad (33)$$

Where  $RA$  is the roll angle.

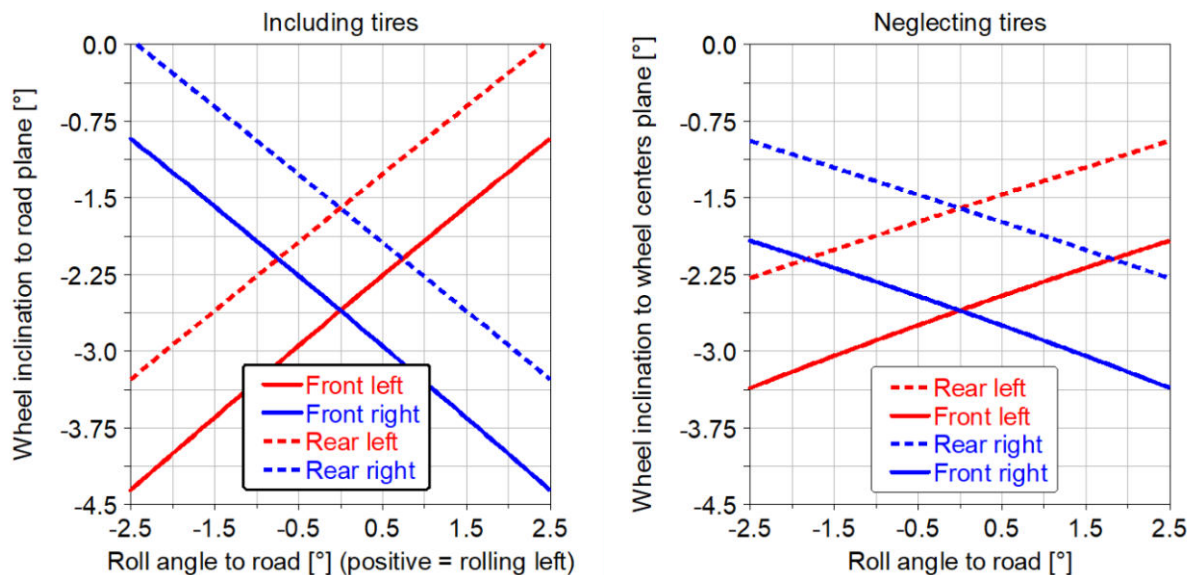


*Figure 52 Comparison of wheel inclination angle between simulations where tires are included (on the left) and where tires are neglected (on the right). Wheel centers plane is a plane constructed from the wheel center points. X-axis corresponds to the roll angle of the chassis to the road, including tires.*

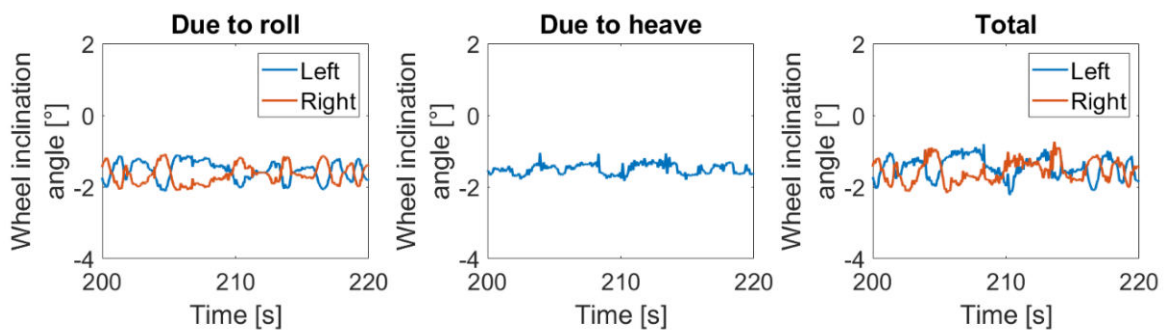


*Figure 53 Change of the rear wheel inclination angle calculated from data, tires included*

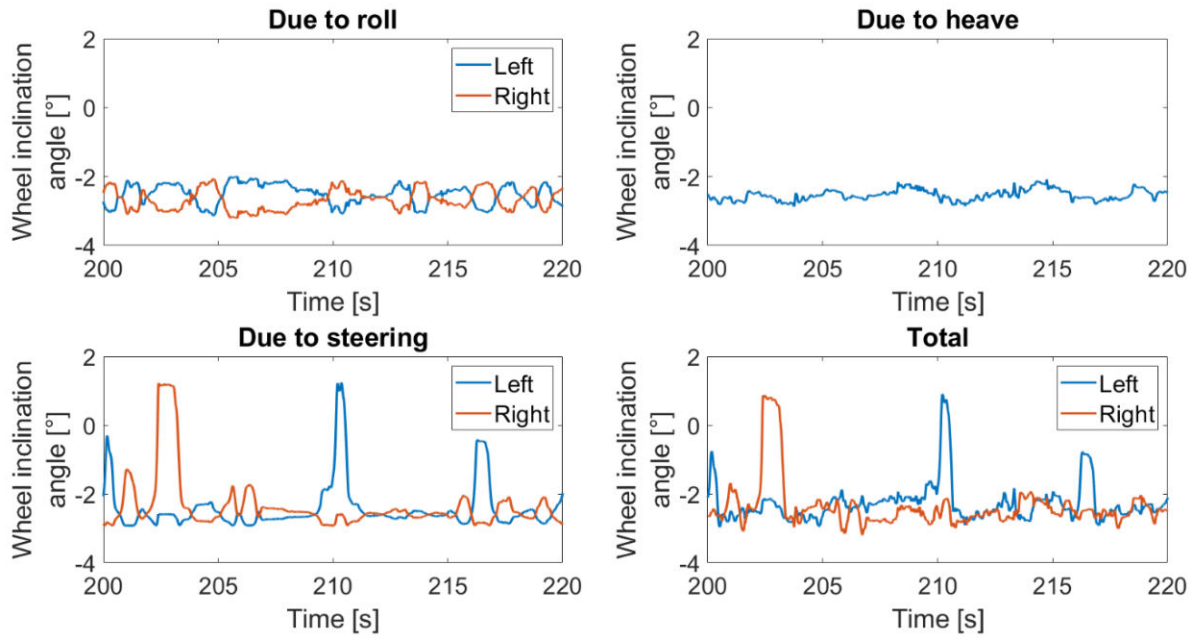


Figure 54 Change of the **front** wheel inclination angle calculated from data, tires included

Combining the Adams simulations with the measured on-track data is done via the deflection of the springs, which is logged using linear potentiometers and via the steering wheel angle, logged with an angle sensor. Kinematic simulations from Adams and measured data are exported to Matlab. Then a certain heave damper deflection from the track can be related to a certain wheel inclination (which is caused by heave), similarly with roll dampers and steering wheel angle. This is of course a simplified approach used for an estimation of the wheel IA. To obtain precise values, more sensors would be needed. For instance, a bellcrank angle position would help to obtain the precise position of the wheels in relation to chassis and a ride height

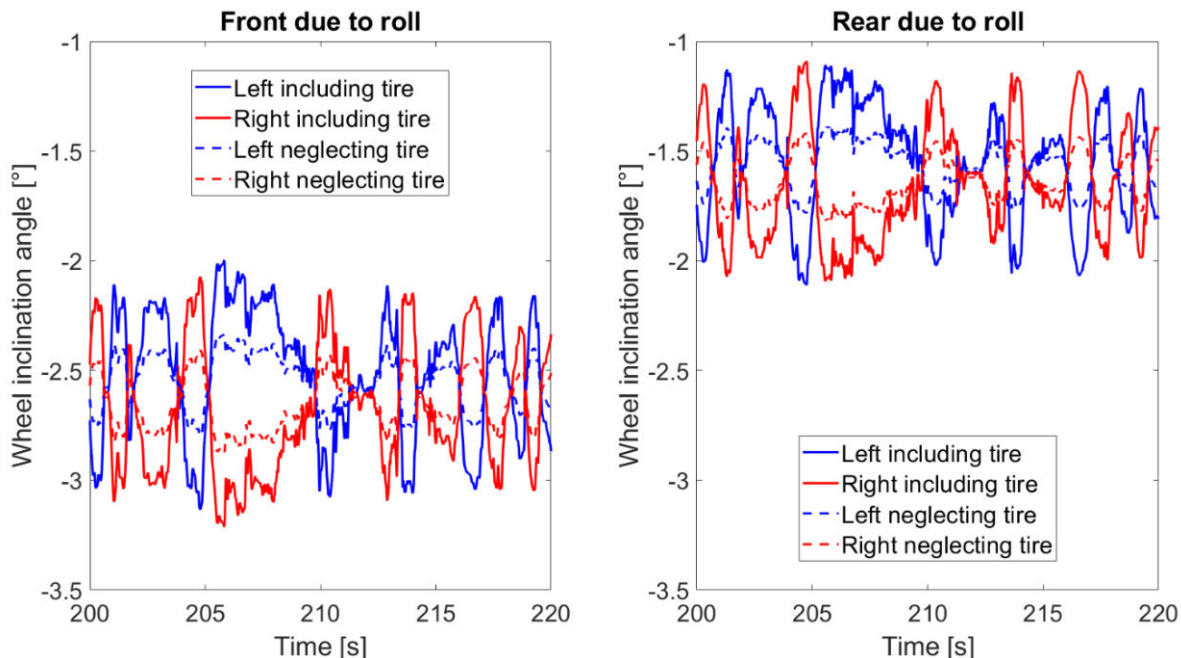


Figure 55 Comparison of the camber change due to both tires and kinematics and due to kinematics only.

sensor would provide the tire deflection. This would improve the accuracy of the computed values, but compliance would still not be contained. To get a true wheel inclination angle at all times during testing, a wheel inclination angle sensor would have to be used.

In Figures 53 and 54 are displayed wheel inclination angles which are obtained from the measured data and calculated using the Adams Car kinematic simulations. The data used are from the same testing session as the tire temperature data in Chapter 1.2.1. The effect of roll, heave, and steering are shown individually and a summary of all these as well.

The steering has the greatest influence, but mainly in the positive IA direction on the inner wheel, the negative camber gain on the outer wheel is little as seen in Figure 51. According to Chapter 1.2.1, higher negative IA on the front axle is needed and that can be done by increasing the caster angle. A different approach is to increase the camber gain in roll, for example by shortening the upper wishbones or by decreasing the front view swing arm length. But the effect of roll displayed in Figures 53 and 54 are with the tires included. The kinematic roll camber gain will only improve a certain portion of this camber change as seen in Figure 52. The difference between the camber change caused by tires and kinematics can be seen in the data as well in Figure 55. In other words, because the suspension is stiff due to aerodynamics, there is low potential in gaining a lot of camber from wheel travel.

## 2.2.2 CASTER ANGLE DESIGN

To understand the influence of both kingpin inclination angle (KPI) and caster angle on Dragon 9, the kinematic points were adjusted to give  $0^\circ$  of KPI and  $0^\circ$  of caster to isolate their

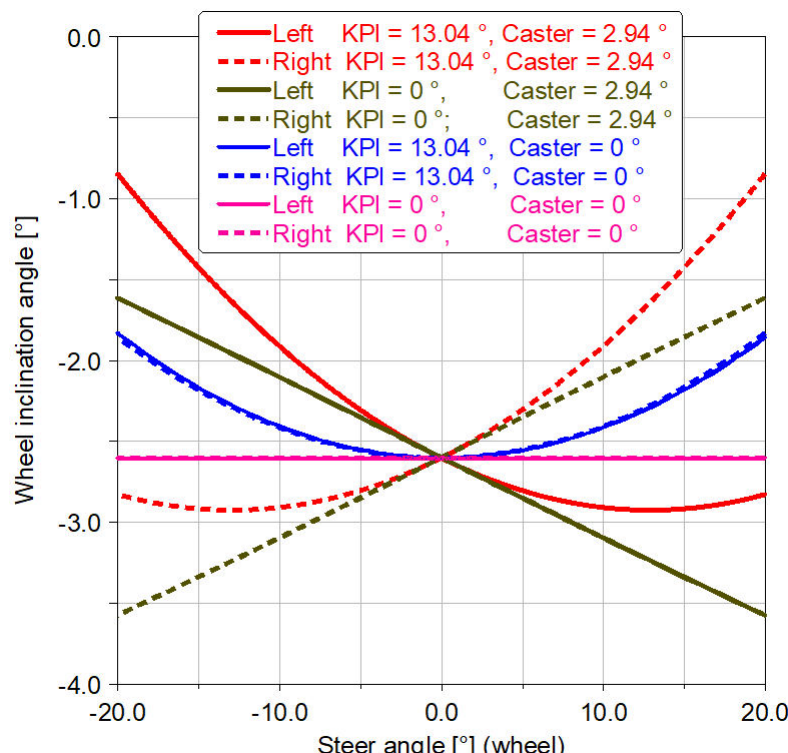


*Figure 56 Influence of kingpin inclination angle and caster angle on the camber change in steering.  
Red color = Dragon 9 values.*

influences independently, see Figure 56. It is clear how KPI only creates a positive camber change in steering and caster creates linear dependency, creating desirable negative camber at the outer wheel and positive camber at the inner wheel in a corner. Also noticeable is the dominant influence of the caster angle which in proportion to its value creates much higher camber change than KPI angle.

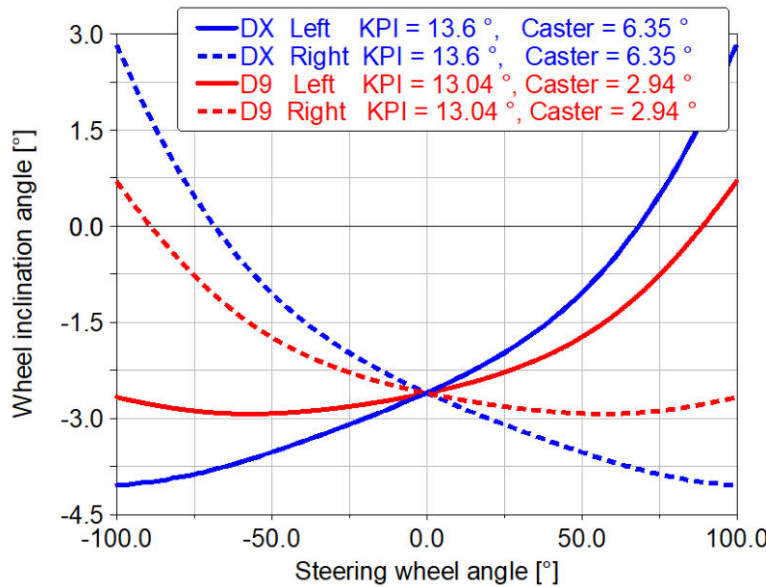


Figure 57 Comparison of camber change in steering between DX and D9

From analyses displayed above, caster angle is increased to increase camber change on the front wheels. On the other hand, this also means that the steering torque due to vertical load will increase and the cross load transfer will also increase. Another issue is the entry of the corner, which was rated by the drivers as better in terms of response in comparison with previous cars which used higher caster angle values. A large camber angle that is created at the corner entry might not be usable before the full roll angle of the car happens at the apex. A compromise is needed. The caster angle was not adjustable so different caster angle could not be tested to solve the tire temperature problem and to still be well perceived by the driver at the entry of the corner. A choice of caster angle is made based on the Adams Car suspension simulations, tire model, and on the values that were used on previous cars. The chosen caster angle is 6,35 °. According to the tire model analyses in Chapter 1.2.1, Figure 19, at 1,8 lateral G, larger camber by 1,1 ° is needed with C19 in comparison with C18 tires. C18 tires are used as a guideline as they had sufficient wheel IA angle according to the tire temperature data. The emphasis is to create a higher negative inclination angle on the outer wheel in a corner. As seen in Table 15, the difference is -1,38 ° at full steering angle.

Table 15 Comparison of wheel inclination angle at maximal steering wheel angle between D9 and DX

			D9	DX	Design change
Static camber			-2.6	-2.6	
Wheel inclination angle at 100 ° steering wheel angle	Outer wheel	Absolute value	-2.67	-4.05	-1.38
		Camber change	-0.07	-1.45	
	Inner wheel	Absolute value	0.68	2.83	2.15
		Camber change	3.28	5.43	

In Table 16 are values of KPI and caster of the previous cars. The chosen caster angle is close to the Dragon 8 value which was generally well perceived by the driver. The KPI angle remained close to the Dragon 9 value mostly due to a scrub radius change discussed later in this thesis.

*Table 16 Comparison of caster and KPI angles between previous cars and DX at  $\delta_{SW} = 0^\circ$*

	D7	D8	D9	DX
Caster angle [°]	7.71	6.23	2.94	6.35
KPI angle [°]	8.54	8.62	13.04	13.6

To see the effect of the different caster during racing, Dragon X steering characteristics are exported from Adams and combined again with the data. A comparison of total inclination angle during a part of a lap is shown in Figure 58. The tire is used in larger inclination angles which was desired.

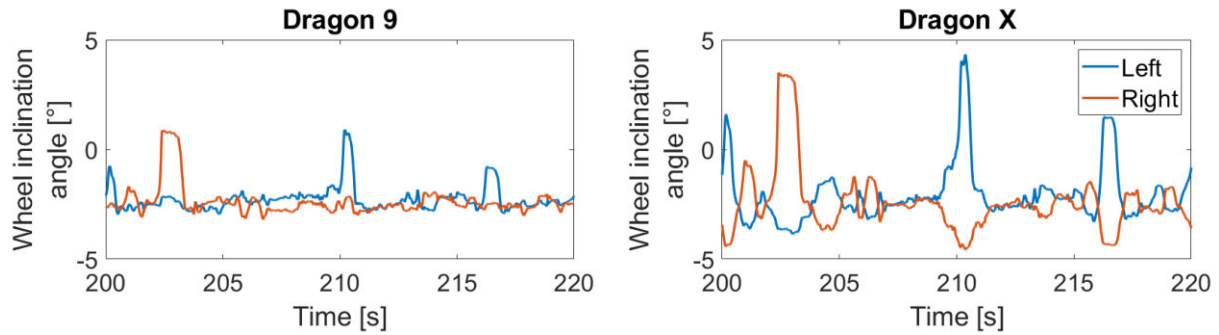


*Figure 58 Comparison of inclination angles of Dragon 9 and Dragon X in data*

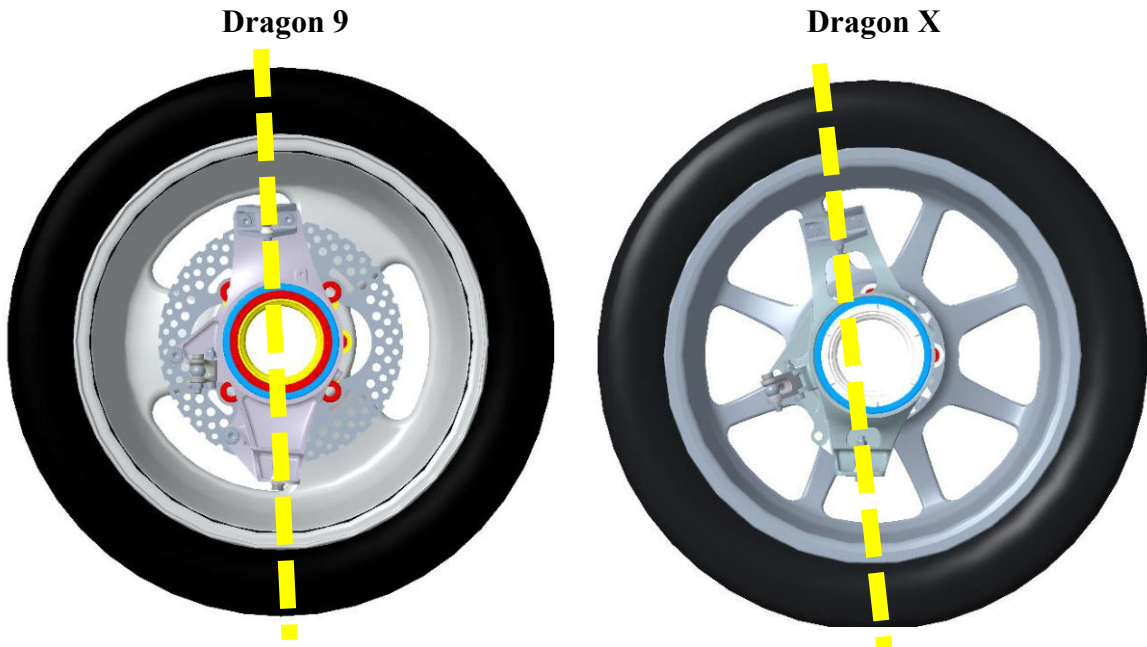


*Figure 59 Comparison of the front wheel geometry viewed from the side*

### 2.2.3 STEERING FORCES AND SCRUB RADIUS DESIGN

With the change of caster angle comes a change in steering forces due to vertical load according to the equation [14]:

$$M_V = -(F_{zl} + F_{zr}) \cdot d \cdot \sin \lambda \cdot \sin \delta + (F_{zl} - F_{zr}) \cdot d \cdot \sin \nu \cdot \cos \delta \quad (34)$$

Where  $M_V$  is the total moment from left and right wheels,  $F_{zl}$  and  $F_{zr}$  are the vertical loads on left and right wheels,  $d$  is the scrub radius,  $\lambda$  is the kingpin inclination angle,  $\nu$  is the caster angle and  $\delta$  is the steering angle. These effects are low because the sinus functions of the KPI and caster are used.

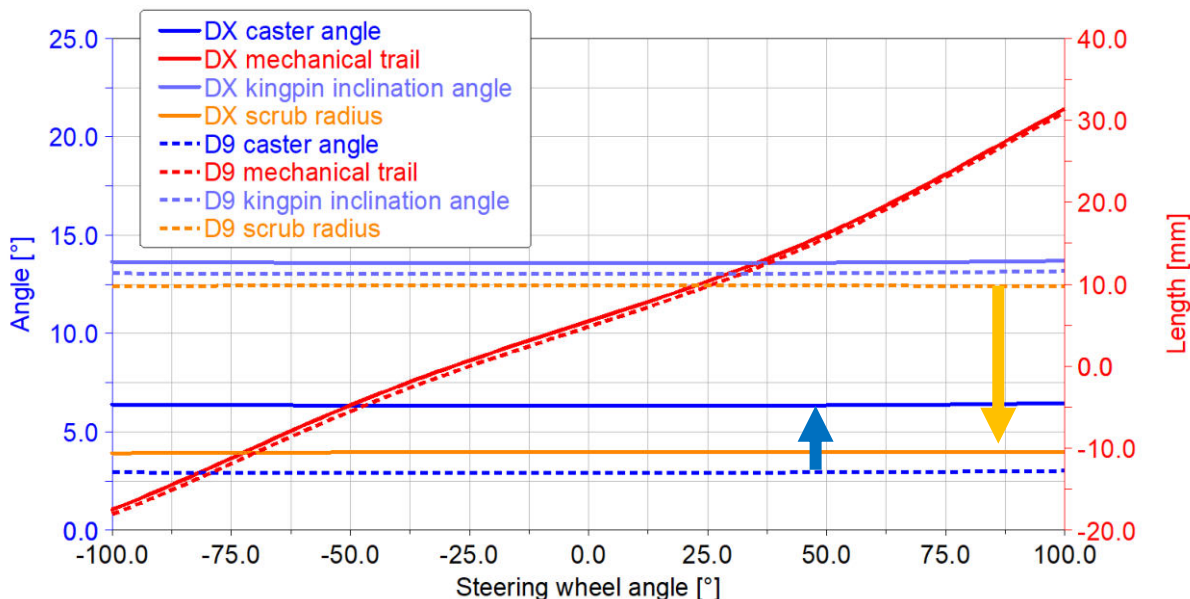


Figure 60 Left front wheel comparison of wheel geometry characteristics for camber angle = 0°

Scrub radius was changed because of the potential of decreasing steering wheel torque at the entry of the corner where a combination of cornering and braking occurs. For a positive scrub radius, due to longitudinal braking force, there will be torque which steers the outer wheel out of the corner and the inner wheel into the corner. If the scrub radius is negative, the torques will have the opposite signs and since the outer wheel is loaded more than the inner wheel, the torque that steers the wheel into the corner will be higher than the one steering out.

In Figure 60 is an overview of the important characteristics of the front wheel geometry. The scrub radius change is dominant, values are listed in Table 17.

Table 17 Characteristic values of front wheel geometry

		Mechanical trail		Scrub radius for camber = 0 ° ( $d_0$ )	Max steer angle
		Zero steer	Full steer		
DX	inner	5.48	-17.49	-10.42	31.7
	outer	5.48	31.42		22.6
D9	inner	4.816	-18.06	9.94	30.6
	outer	4.816	30.96		24.4

The values of scrub radius above apply for zero static camber angle, but there is a difference between the way the camber angle is changed on the vehicle physically and the way Adams Car changes it. Adams rotates the wheel around the wheel center, while in reality the camber is changed via distance washers that are inserted at the upper ball joint (upper outboard wishbone joint). That means the wheel is in reality rotated around an axis that goes through the lower ball joint (LBJ, lower outboard wishbone joint) and the steering outboard joint. This creates a difference between the real scrub radius and the one in Adams. The real approximate scrub radius for a certain static camber angle (neglecting the shift of tire contact patch and the steering joint) can be calculated as:

$$d = d_0 - LBJ_z \cdot \tan(\gamma_{static}) \quad (35)$$

Where  $d_0$  is the scrub radius at zero camber angle,  $LBJ_z$  is the vertical coordinate of the lower ball joint from the road ( $z = 0$  is the road) and  $\gamma_{static}$  is the static camber angle. Thus increasing the negative camber will increase positive scrub radius (and decrease a static negative scrub radius). An overview of the scrub radius change due to static camber and camber change due to steering is shown in Table 18. The camber change listed here is taken from Table 15. The camber change due to steering does not influence the scrub radius (clear from Figure 60).

*Table 18 Camber and scrub radiiuses for the steering torque calculations*

		Camber [°]		Scrub radius [mm]	
		Left	Right	Left	Right
Zero steer	Dragon 9	-2.6	-2.6	15.4	15.4
	Dragon X	-2.6	-2.6	-4.4	-4.4
Full steer to the left	Dragon 9	0.68	-2.67	15.4	15.4
	Dragon X	2.83	-4.05	-4.4	-4.4

A Matlab script to calculate steering forces has been created in previous years by other team members, this script has been used and improved as a part of this thesis. The script first calculates the vertical load of each wheel based on static load transfer and the roll stiffness distribution, this was improved by calculating the elastic and geometric load transfer of suspended mass and the load transfer of non-suspended mass. Then, using a scaled tire model (Flat Track tire model scaled based on on-track data), the lateral, longitudinal forces, and the aligning torque are calculated. The scaling of the tire model is not part of this thesis and was done by other team members. The camber is also an input to the tire model and is dependent on the current combination of vehicle and steering angle, the values used in the calculation are listed in Table 18. Camber change in roll and heave are neglected here. From the tire forces and torque, the wheel torques from vertical, lateral, longitudinal forces and the self-aligning torque are calculated according to Eq. 34 and the equations [14]:

$$M_L = (F_{yl} + F_{yr}) \cdot (\text{mechanical trail}) \quad (36)$$

$$M_T = (F_{xl} - F_{xr}) \cdot d \quad (37)$$

$$M_{AT} = (M_{zl} + M_{zr}) \cdot \cos \sqrt{\lambda^2 + v^2} \quad (38)$$

Where  $M_L$  is the  $M_z$  moment of the wheel due to lateral force,  $F_{yl}$  and  $F_{yr}$  are left and right lateral tire forces,  $M_T$  is the  $M_z$  moment of the wheel due to longitudinal force,  $F_{xl}$  and  $F_{xr}$  are left and right longitudinal tire forces,  $d$  is the scrub radius,  $\lambda$  is the kingpin inclination angle and  $v$  is the caster angle.

Then the forces in steering rods are calculated. The steering rods force component acting parallel to the steering rack (the vehicle's Y-axis) times the radii of the steering pinion gives the torque acting on the steering wheel. The focus of this thesis is on the design changes of the suspension and as the main change that influences the steering torque is the change of scrub radius, only a combined cornering and braking state will be calculated here. The vertical loads are calculated from load transfers, longitudinal force is calculated as a maximal braking force for a given load (therefore is constant). This approach is simplified and only an approximation, because a combined tire model must be used to account for the loss of lateral force due to longitudinal force and give more precise values. Nevertheless, the influence of the design change of kinematics can be seen here. The lateral and longitudinal accelerations are taken from the g-g diagram in Figure 17.

Having the positive scrub radius on Dragon 9, the more loaded outer wheel will produce more longitudinal force, which will, in this case, produce higher understeering torque on the outer wheel and oversteering torque on the inner wheel (which will be lower). Thus the total wheel torque from the scrub radius will have an understeering effect. On the other hand, with a negative scrub radius, the total torque obtained from scrub radius will have an oversteering effect. This will reduce the total understeering torque in the steering wheel in the braking-in-turn event.

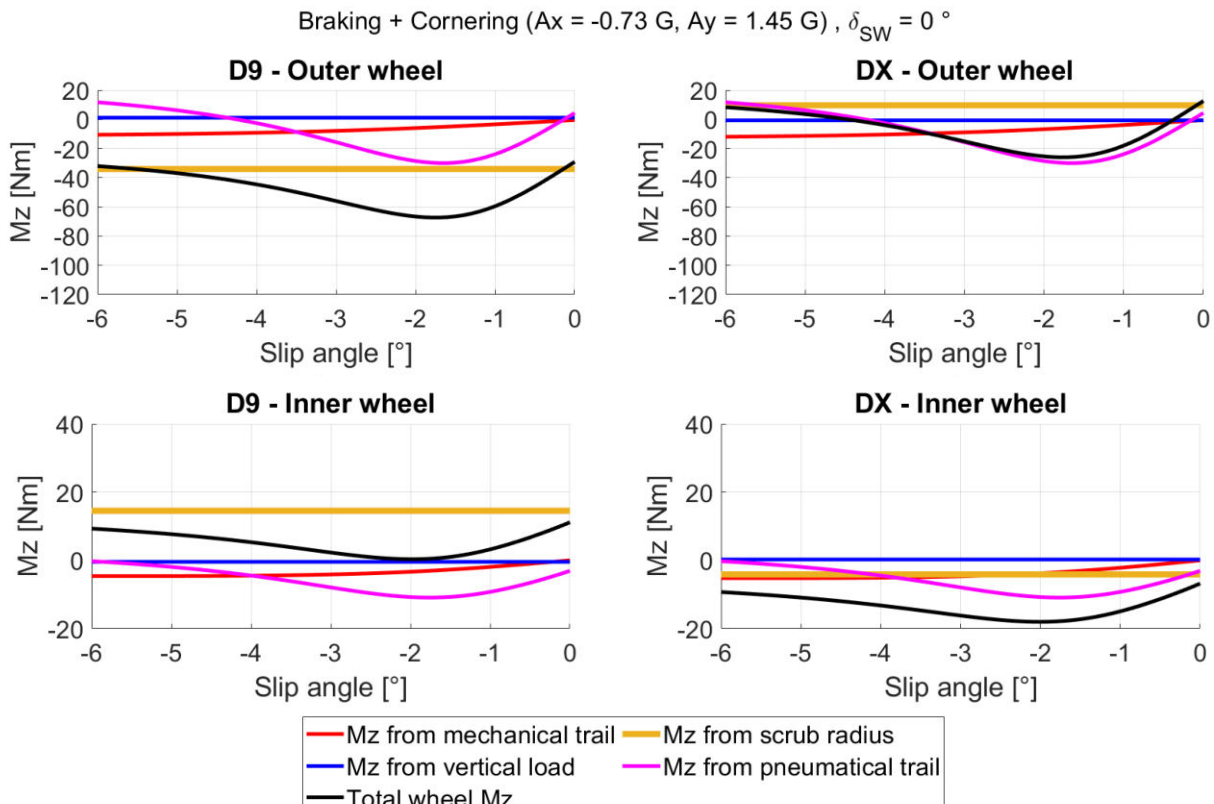


Figure 61 Aligning wheel torque comparison in zero steering angle in combined cornering and braking (braking-in-turn)

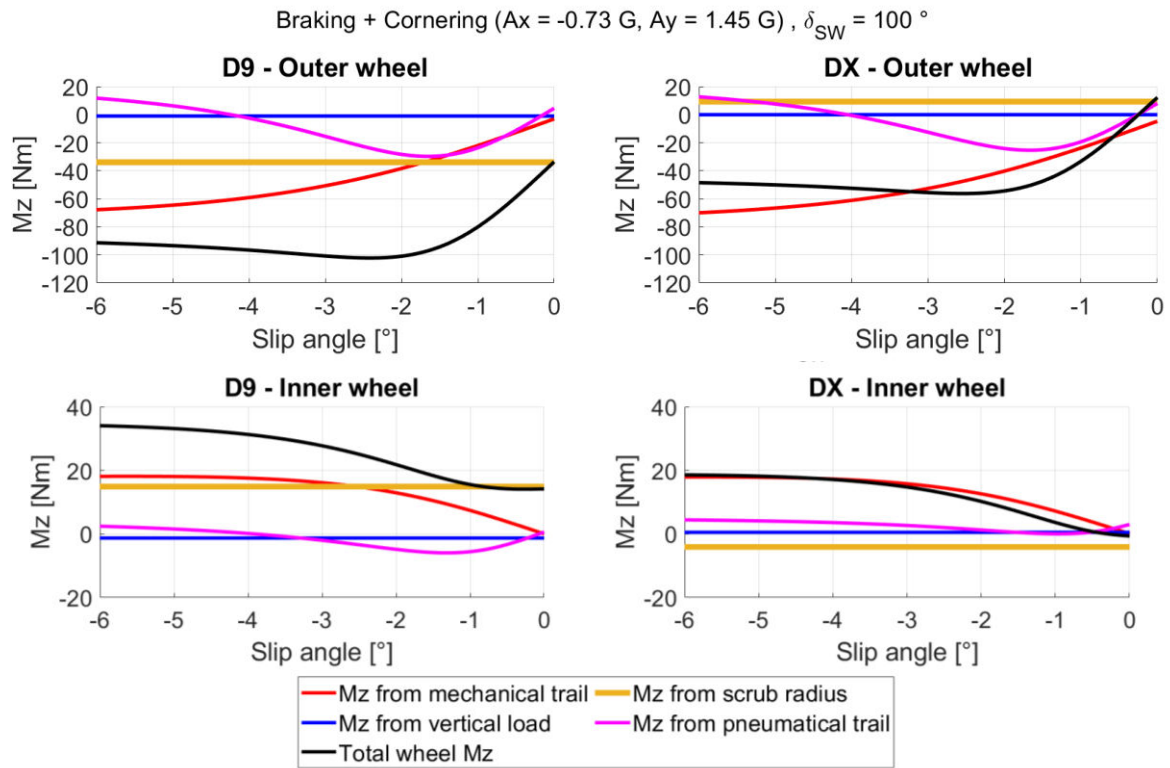


Figure 62 Aligning wheel torque comparison in maximal steering angle in combined cornering and braking (braking-in-turn)

In Figure 61 and Figure 62 are shown the results of the wheel aligning torque calculation. In both zero and full steer angle, the Mz torque due to scrub radius offsets the total torque. The effect of the outer wheel is always higher than the inner wheel. The negative value of the torque is an understeering moment. The lateral force of the tire has a positive sign, the slip angle is negative and the self-aligning torque is negative. The situation with a full steering angle is displayed because the wheel torque coming from the vertical load is influenced by the steering angle. But as can be seen in the figures, the torque from Fz is negligible.

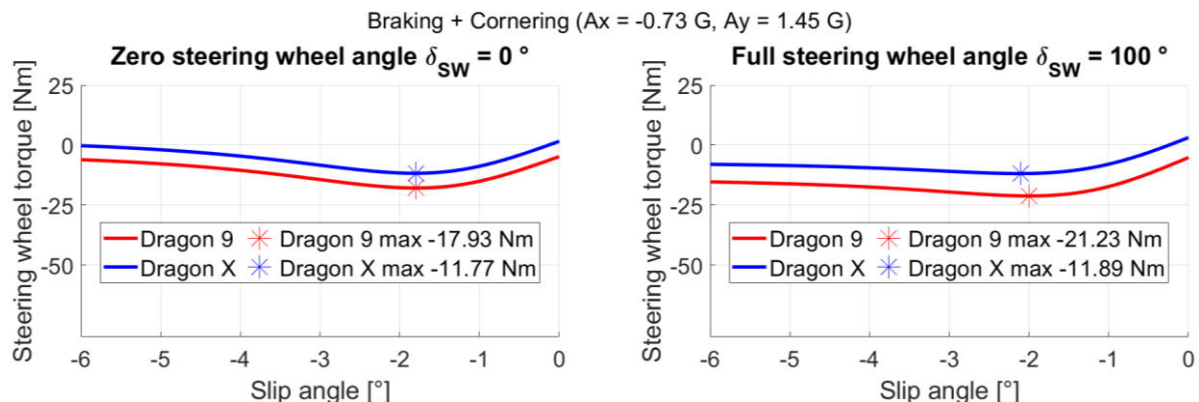


Figure 63 Comparison of the total steering wheel torque

These simulations do not account for the lateral shift of the contact patch which will increase the negative scrub radius on the outer wheel and decrease the negative scrub on the inner wheel which will create a more oversteering moment.

The total effect of the design change on the steering torque can be seen in Figure 63.

### SIMULATION OF TIRE REACTIONS IN ADAMS DYNAMIC SUSPENSION ANALYSIS

For a double-check of the analytic calculations, tire forces and moments at the maximal steering wheel torque from the Matlab simulation are inputs to the Adams Suspension Dynamic Analysis. The tire forces and moment are listed in Table 19. Higher camber angles due to caster also decrease the self-aligning torque.

*Table 19 Tire forces at maximal steering wheel torque*

	$\delta_{sw} [^{\circ}]$	Fy [N]		Fx [N]		Fz [N]		Mz [Nm]	
		Left	Right	Left	Right	Left	Right	Left	Right
Dragon 9	0	643	1143	-801	-2137	532	1436	-10.888	-29.706
	100	718	1241	-848	-2176	532	1436	-4.848	-28.336
Dragon X	0	643	1143	-801	-2137	532	1436	-10.888	-29.706
	100	749	1334	-847	-2124	532	1436	1.402	-23.406

The different scrub radius (due to different camber setup) between reality and Adams will influence the results, the scrub radius – static camber angle dependency is seen in Figure 64. The dynamic camber angle is used in Matlab to calculate the tire reactions and the static angle

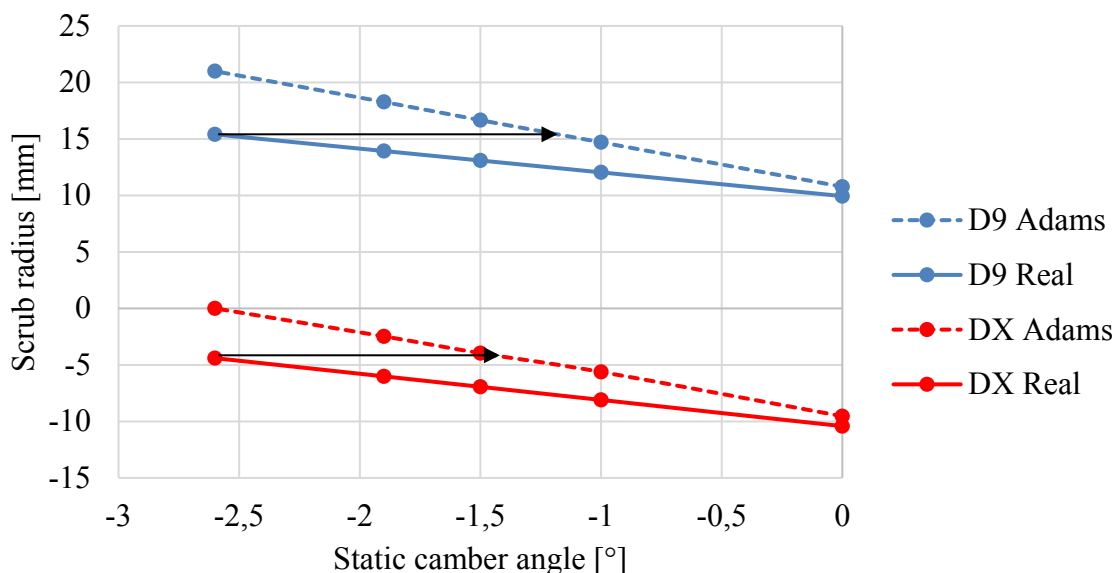


*Figure 64 Difference of scrub radius between reality and Adams for different static camber angles.  
To simulate equivalently in Adams camber angle has to be smaller for the scrub radiiuses to be equal between Matlab and Adams. The arrows describe the change from Matlab to Adams.*

is used for the scrub radius calculation. Using the dynamic simulation in Adams, the tire reactions are inputs and do not influence tire forces, therefore the camber angle is changed to obtain equal scrub radiiuses.

The corrected camber angle for Adams is seen in Table 20. This correction is only used for this double-check analysis. The difference between the slopes of D9 and DX in Figure 62 is caused by different wheel center heights.

*Table 20 Correction of Adams camber for the analysis*

	Matlab		Adams	
	D9	DX	D9	DX
Scrub [mm]	15.4	-4.4	15.4	-4.4
Camber [°]	-2.6	-2.6	-1.18	-1.30

“Parallel wheel travel” and “roll & vertical force” analyses are made to check the suspension rates are approximately equal, see Figure 65. These also influence the amount of steering torque needed to steer in a standing still situation. [14]

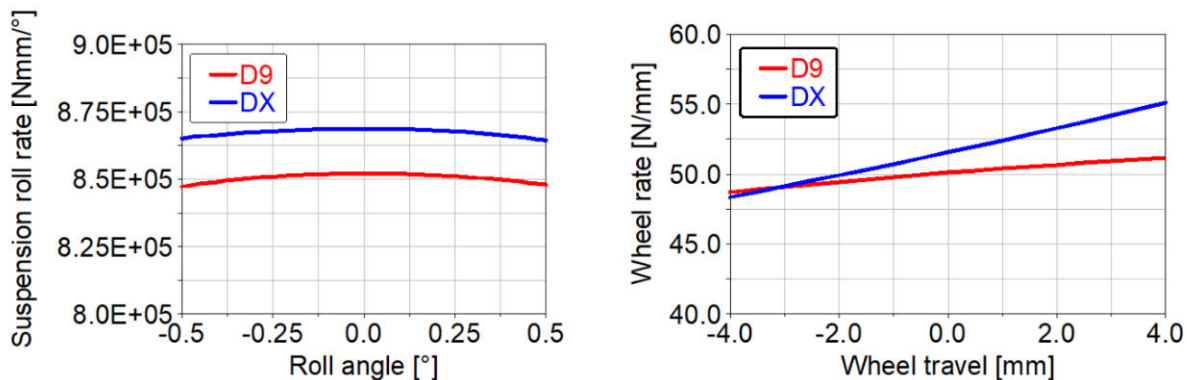


*Figure 65 Dragon 9 and Dragon X suspension rates at static position in Adams*

In Table 21 is seen a consistency of the results within 5 % except for the case of Dragon X with a full steering angle.

*Table 21 Comparison of steering wheel torque calculated in Matlab and Adams*

		Dragon 9		Dragon X	
Steer angle [°]		0	100	0	100
Steering wheel torque [Nm]	Matlab	17.93	21.23	11.77	11.89
	Adams	18.2	20.31	11.51	15.71
Difference [%]		1.51	-4.33	-2.21	32.13

The difference might be caused by a different steering rod position at the full steering angle (in Matlab it does not change), due to track differences (contact patch is dependent on camber), or by other differences in the kinematics. Adams Car approach is surely more accurate as it considers all the kinematics of the car. The difference between Adams and reality will greatly

depend on the accuracy of the tire model and compliances. These simulations are done in a kinematic mode, therefore compliances are not included.

Table 22 Dragon X steering torque reduction in % according to different approaches

	Dragon X steering torque [%]	
	Zero steer	Full steer
Matlab	-34.3558	-43.9943
Adams	-36.7582	-22.6489

### STATIC STEERING TORQUE AND CROSS LOAD TRANSFER DUE TO STEERING ANGLE

Adams Car suspension steering analyses of the front axle are made to display the influence of the different wheel geometry on static steering torque. The camber angle in these analyses is  $0^\circ$ .

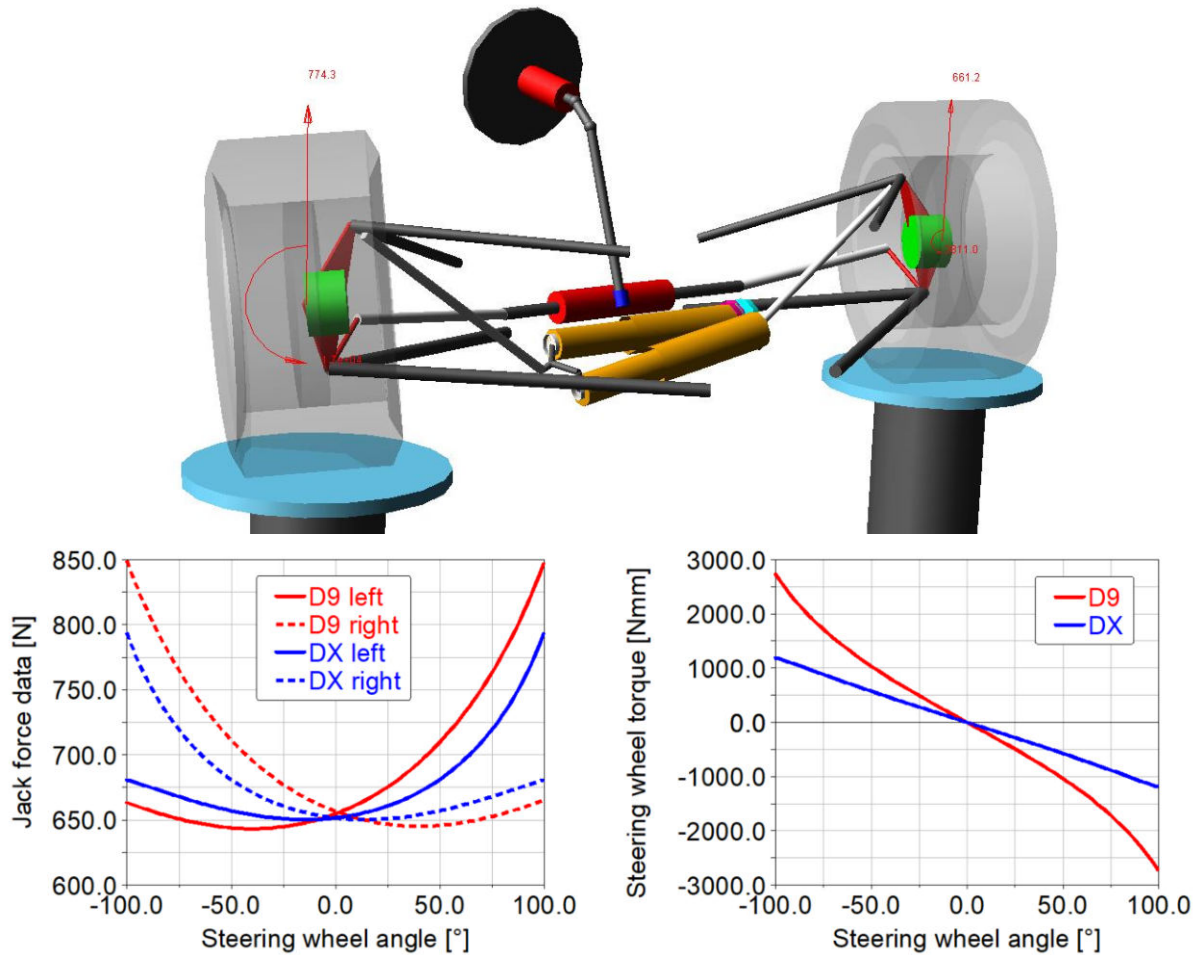
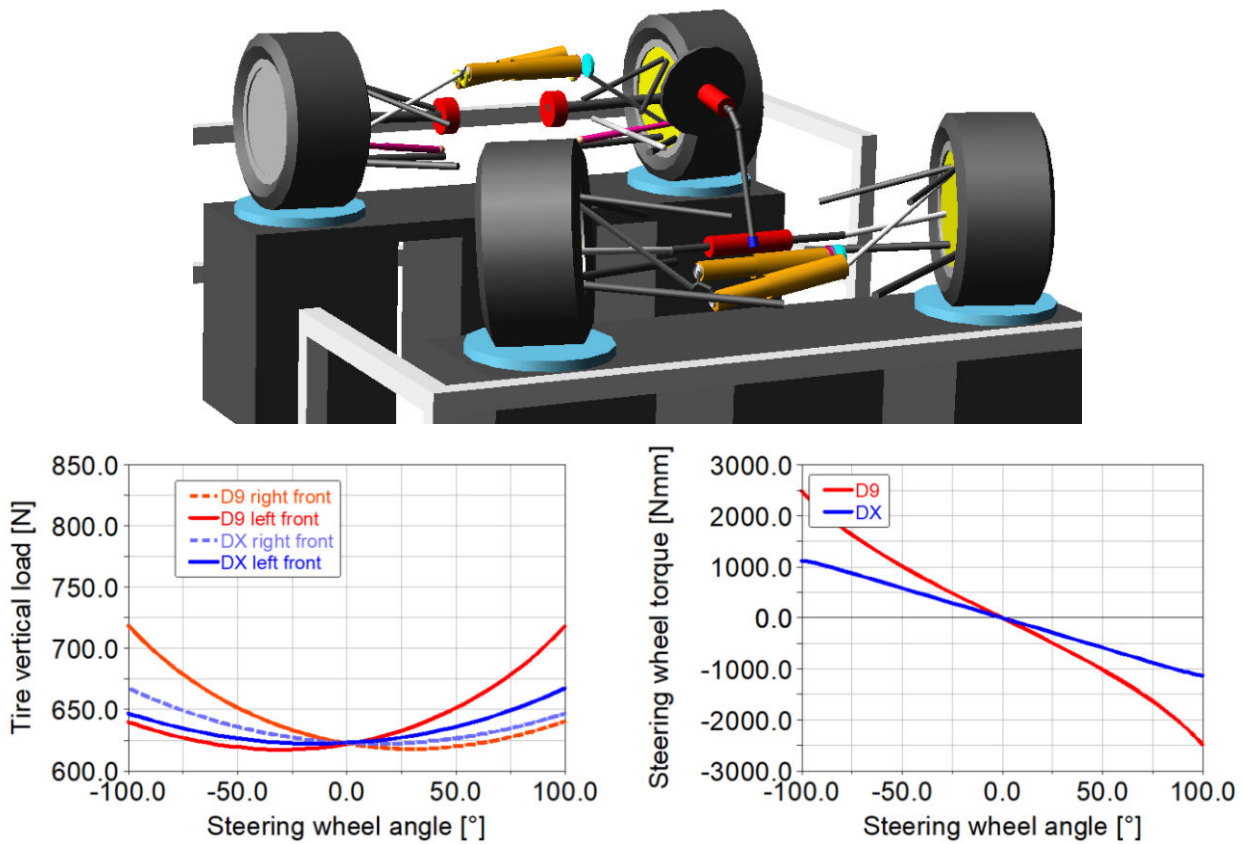


Figure 66 Cross load transfer and steering wheel torque do to steering from Adams suspension simulation. Static camber angle =  $0^\circ$ .

In Figure 66, a cross load transfer and a steering wheel torque induced by steering are displayed. Even though the caster angle was increased, the decrease of scrub radius has a larger influence. The forces in Figure 66 seem to be too large, analyses with full vehicle models are conducted. Using the SPMM testrig, the full vehicle model is placed on 4 cylinders and steering analyses are conducted. Figure 67 shows the results from full vehicle analysis which are much lower in comparison with only front suspension analyses. The values at the maximal steering angle are listed in Table 23. The load difference of 21 N seems more realistic. Unfortunately, the rear wheel load has not changed as the chassis is also fixed to the ground.

*Table 23 Comparison of suspension assembly and full vehicle analyses in Adams*

		Wheel vertical load [N]			Steering wheel torque [Nm]
		Left	Right	difference	
Suspension simulation	Dragon 9	847	665	182	2.739
	Dragon X	793	680	113	1.192
	difference	-54	15	-69	-1.547
Full vehicle simulation	Dragon 9	718	640	78	2.485
	Dragon X	667	646	21	1.128
	difference	-51	6	-57	-1.357



*Figure 67 Static steering analysis with full vehicle model in Adams*

According to Equation 33, the steering wheel torque due to vertical load is calculated. A zero camber angle and vertical load from the Adams SPMM simulation is considered. The results are very low as seen in Table 24. The resulting calculated torque has an opposite sign due to the opposite scrub radius. The resulting calculated SW torque from vertical load has an oversteering effect on Dragon X. The effect of camber change is not considered here and that is probably the main source of difference between the analytical calculation and Adams simulation and also the reason why there is always an “understeering” (or stabilizing) torque in Adams when steered.

*Table 24 Calculated torques due to vertical load*

	Total Mz due to vertical load [Nm]			SW torque [Nm]
	From KPI	From Caster	Total	
D9	-1.51	0.01	-1.5	-0.36
DX	0.96	0.01	0.97	0.23

The cross load transfer will increase the load under the front inner wheel and rear outer wheel. As the vehicle is equipped with a limited-slip differential one of the issues of the last cars was an undesirably common locking of the differential due to the insufficient rear inner wheel load. Reduction of the cross load transfer due to steering will decrease the unloading of the interested wheel and prevent slippage of the wheel.

The cross load transfer caused by steering can be easily measured on scales. Dragon 9 is placed on scales, a paper is put under the tires to enable easy steering, both maximal steering inputs

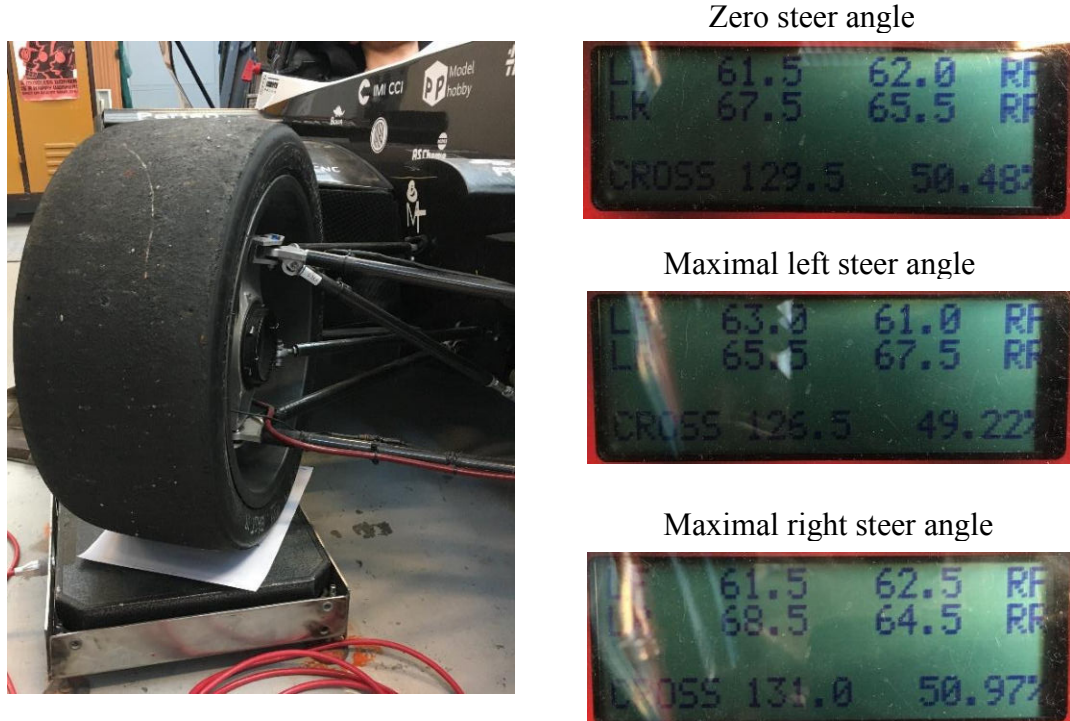


*Figure 68 Measurement of wheel load change due to steering*

are executed while the scales are being monitored. The suspension rates are equal to the FSG setup and are the same as in simulations.

*Table 25 Measured wheel load values in different steering angles and calculated cross load transfer*

		Measured loads [kg]		Corrected load distribution [kg]		
Steer angle		Left	Right	Left	Right	
Zero	Front	61.5	62	62	62	
	Rear	67.5	65.5	66.5	66.5	
			Difference [kg]		Cross LT [kg]	
Max left	Front	63	61	1	-1	
	Rear	65.5	67.5	-1	1	2
Max right	Front	61.5	62.5	-0.5	0.5	
	Rear	68.5	64.5	2	-2	2.5

As seen in Figure 68 and Table 25, the real cross load transfer is much lower. The simulation is quite different from the real measurement procedure. To validate the simulation, equal conditions (fixed chassis) should be met. Or a custom simulation procedure might be created in Adams to obtain equal conditions as in the measurement. The value of interest is the one measured on scales. The reduction of cross load transfer is nevertheless expected with Dragon X, although the values will probably be much smaller as well.

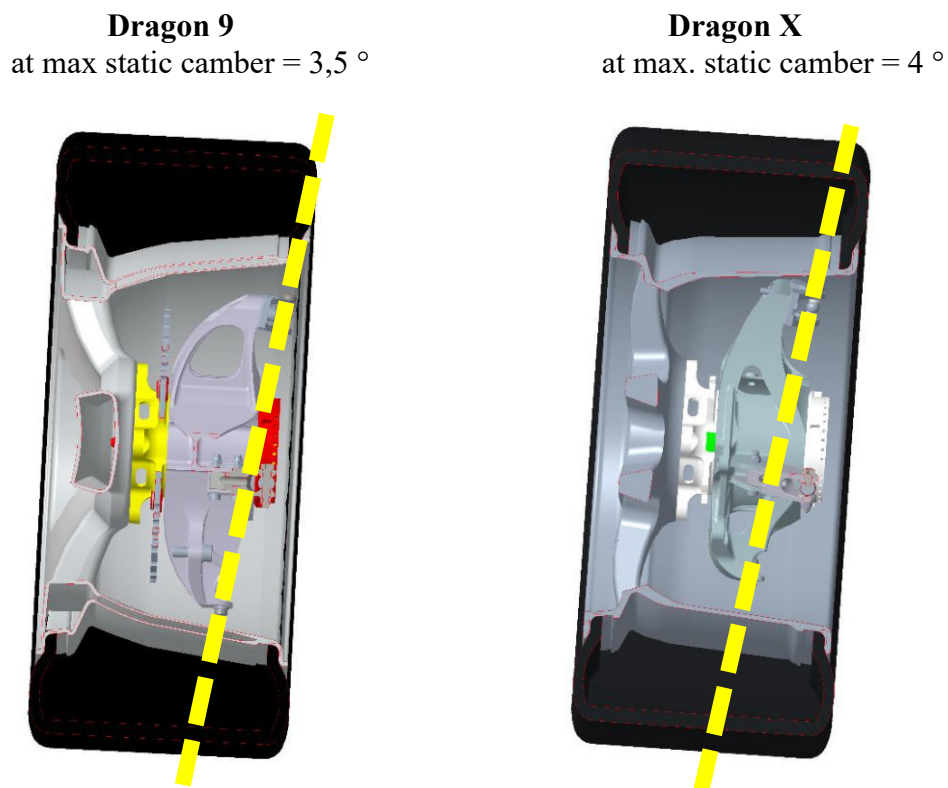


*Figure 69 Front geometry comparison between Dragon 9 and Dragon X viewed from the front in section. As displayed, the maximal static camber value has been also increased.*

## 2.2.4 REAR WHEEL GEOMETRY

Due to a vast change of rear wishbone layout discussed in Chapter 2.3.5, and due to a four-wheel steer project, rear wheel geometry is changed completely. These characteristics were controlled:

- Caster angle = 0 °
  - Mainly because the rear wheel steering will be turning the wheels both inside and outside of the turn depending on the current speed. Caster angle would in one of these cases create a positive camber angle on the outer wheel which is undesirable.
- Spindle length reduced from 65 mm to 48 mm
  - To reduce Mz torque from the tractive force
- Scrub remains minimized (is dependent on current camber angle)
- The tie rod base length remains the same

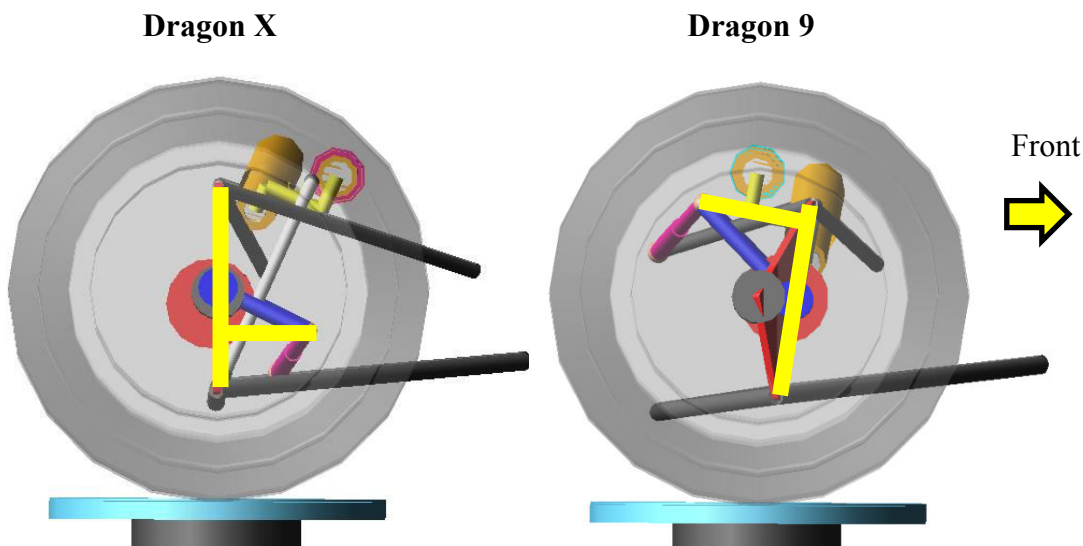


Figure 70 Comparison of tie rod base length between Dragon X and Dragon 9

The assumption used here was to mirror the original position around the wheel center to remain the original roll steer behavior. But according to literature, the position of the tie link should be either in front of the steering axis and placed higher vertically, or should be behind the steering axis and lower vertically. The situation at the front axle should be exactly opposite (left rear wheel layout applies to the right front wheel). [10]

This issue will be addressed later in this thesis when kinematics and compliance are studied.

Collision with the rim, anti-features, roll centers, and forces in the suspension links were the limiting factors of the rear wheel geometry.

## 2.3 SUSPENSION LINKS

In this chapter are discussed the design changes of wishbone arms, pull/pushrods, tie rods, load cases, and force distribution among the suspension links.

### 2.3.1 THE GEOMETRY OF SUSPENSION WISHBONE ARMS

During the design of the wishbone's layout, several kinematic characteristics are observed and controlled, these can be designed by altering the inboard pickup points. The outboard pickup points are set according to the wheel geometry design, but these influence the kinematic characteristics as well, therefore there is always an iterative loop and compromises. Also, as mentioned earlier, there is a relation between the installation ratio and the wishbone arm geometry (the one that is the pull/pushrod connected to). But not only the kinematic characteristics take part in the design of the suspension layout, force distribution among the suspension links, and compliances need to be considered as well. Some simulation tools such as the compliant mode in Adams Car model were not yet made during the design of the suspension kinematics, these were added after. Therefore, in the initial design of Dragon X suspension, compliance was not simulated and only force distribution was checked. The design iterative loop of this stage is shown in Figure 71.

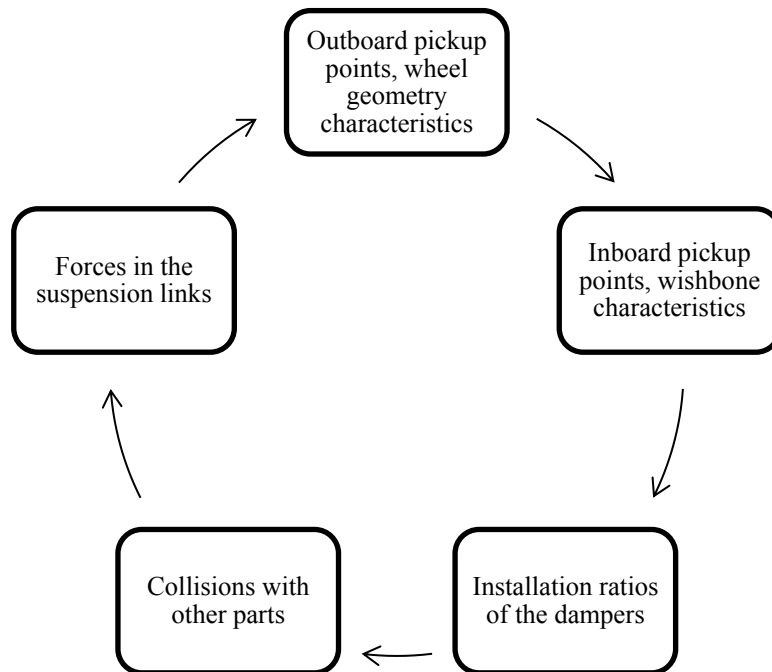


Figure 71 Iterative loop of the kinematic design with the emphasis on wishbones

Concerning the “wishbone characteristics”, these were the ones with key interest:

- Front view swing arms
  - Location of front and rear roll centers
  - Camber change in heave and roll
  - Track variation

- Side view swing arms
  - Anti-features
    - Front anti-dive
    - Rear anti-lift
    - Rear anti-squat

Heights of front and rear roll centers influence the amount and speed of roll of the suspended mass, therefore they are related to the velocity of load transfer and response of the car. The rolling motion of the car also influences the side ride heights, thus aerodynamics. The vehicles of TU Brno Racing have always had roll centers located above the ground and under the center of gravity. The amount of jacking forces is also related to the roll center height (jacking forces due to  $F_y$  are directly connected to the angle of the side swing arm to be exact). Another characteristic checked is the migration of the roll center. [7]

Camber change in heave and roll are interconnected and rely mostly on the location of the instantaneous center. The length of the side view swing arm is the main factor influencing the camber change. Short swing arm length (located on the inside of the particular wheel) will produce higher negative heave camber change and less positive roll camber change. It will also produce more track variation. Concerning camber change, another important effect is caused by having a shorter upper wishbone and a longer lower wishbone. The instantaneous center will then migrate, reducing the length of the side view swing arm in bump, which will create a progressive camber change in heave and roll. Heave and roll camber change are connected because the roll camber change is calculated by deducting the heave camber change from the vehicle's roll angle. Shorter upper wishbones would then require the chassis to get wider, thus increase mass and limit the space for aerodynamic devices. [10]

Anti-features are important for suspension cooperation with aerodynamics. The advantage of anti-features is that they reduce the suspension travel, thus limit the ride height variation, but only in braking and acceleration. For example, stiffer springs will reduce the ride height variation in every part of the lap - straights, entry, apex, and exit of a corner, but anti-features will only have a significant effect in sections, where longitudinal forces are transmitted. As discussed earlier, there is a direct relationship between the stiffness of the suspension, mechanical grip, and the tire temperature. Therefore anti features provide basically a stiffer suspension in the most needed sections of the lap, while during the straights and bumps, the suspension is softer, reducing the heating of the tire and producing a higher mechanical grip. [7][10]

The goal was to remain all of these characteristics identical to the Dragon 9 (in reasonable limits). These characteristics were in general considered satisfactory and no immediate problem seemed to arise from them therefore were not meant to be changed. Although with the new simulation tools such as the full vehicle model in Adams, analyses can be conducted to optimize these parameters, this is not dealt with in this thesis.

### 2.3.2 TIRE FORCES

An important part of the designing process of the wishbone layout are the forces in suspension links. Force reactions in the suspension are obtained from Adams suspension dynamic simulation, where tire forces and moments are the inputs. The forces are calculated for steady-

state situations. Some load cases from previous years are altered and a case of braking + acceleration is added. The load cases are based on the g-g diagram from data, there is an additional safety as seen in Figure 72.

- Braking (2,5 G)
- Acceleration (2 G)
- Cornering (2,5 G)
- Braking + cornering ( $1,6 \text{ G} + 1,6 \text{ G} = 2,26 \text{ G}$ )
  - Used to be 2,5 G + 2,5 G in the past (too conservative)
- Acceleration + cornering ( $1,4 \text{ G} + 1,4 \text{ G} = 1,98 \text{ G}$ )
  - Was not simulated in the previous years

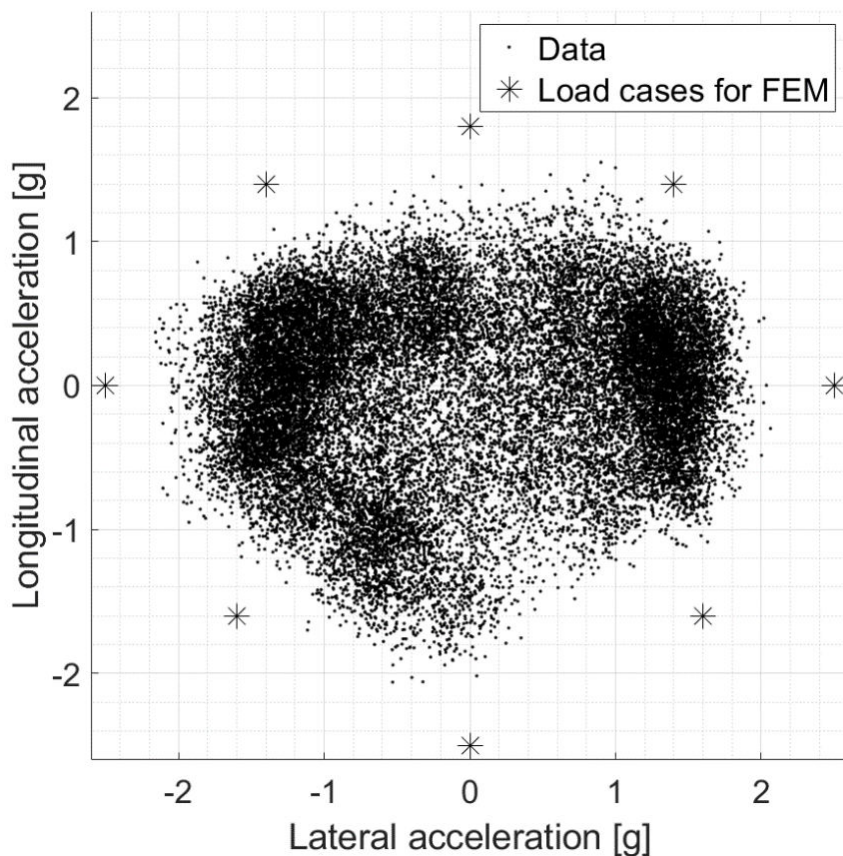


Figure 72 Load cases for FEM analysis in g-g diagram with unfiltered measured data

The forces that are used for structural analysis of the suspension parts are calculated for the acceleration of 2,5 G in cornering and braking. Other load cases are chosen for similar additional safety as seen in Figure 72. These values are based on experience and they give good reliability of the parts. The fatigue analyses are not simulated at the moment in our team, therefore experience is important in terms of the lifespan of the parts and load cases used in static FEM. The tire models used for standard calculations of vehicle dynamics are scaled down to a limit of approximately 2 G. Therefore to calculate these higher load cases, the tire model has to be rescaled. To push the weight of the car even lower, experiments with parts designed

for only 2 or 2,1 G could be made, because only approximately 1,8 G of filtered lateral acceleration is achieved during driving on the formula student tracks. Forces in transient events can be higher than in steady-state. Strain gauge measurement can give an equivalent steady-state acceleration to cover both the transient and steady-state situations.

In the combined states, the vertical loads of the wheels are calculated for combined load transfer, then the tire forces are calculated independently for lateral and longitudinal forces. A combined tire model should be used to obtain more accurate values.

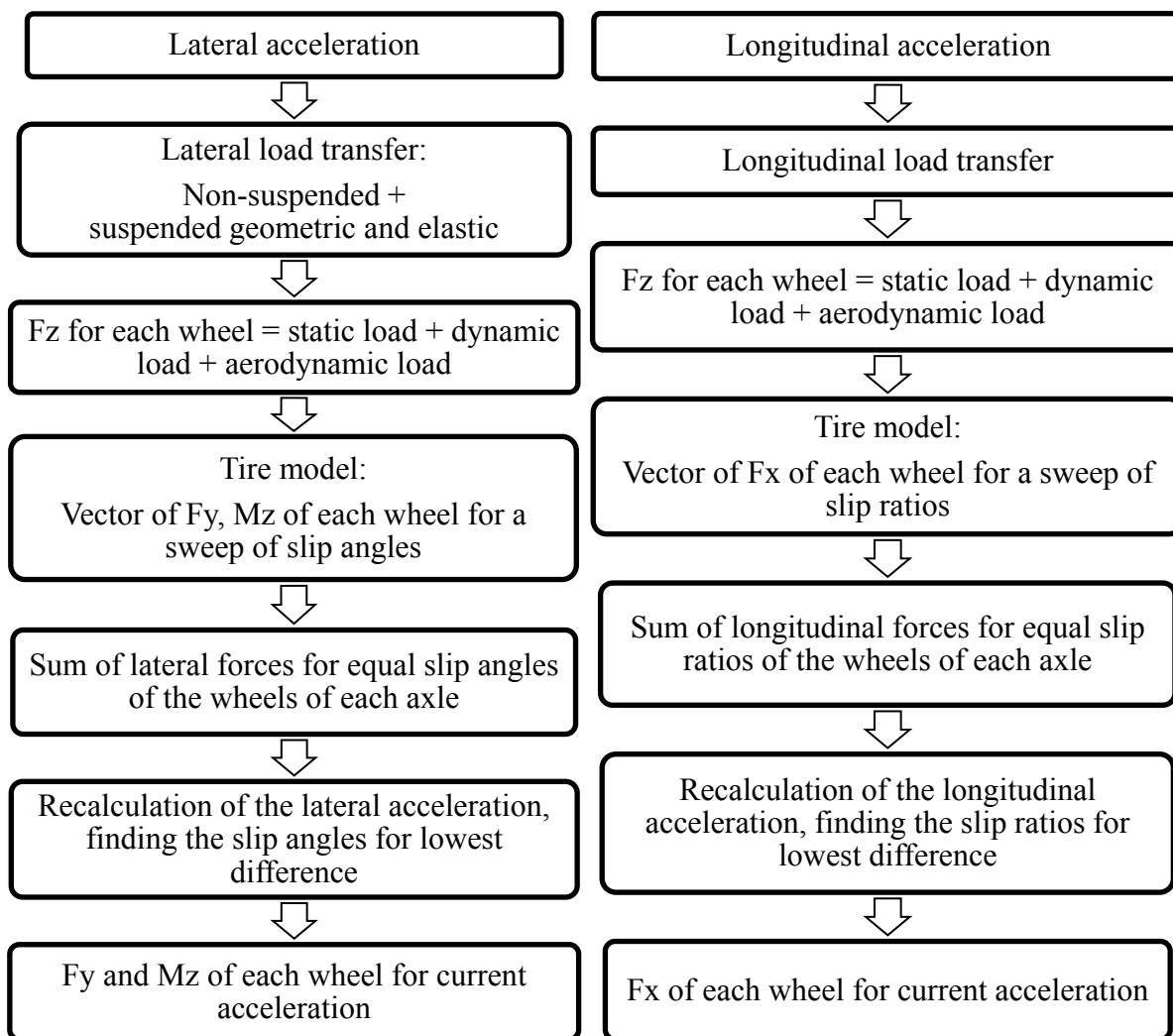


Figure 73 Calculation of steady-state tire reactions from the tire model

The steady-state load cases are calculated with a downforce of 850 N. The aerodynamic balance includes the drag induced moment  $M_Y$  which loads the wheels. This is obtained from CFD simulations.

The  $M_Z$  influence is considered in the calculation of steering forces, where a peak of steering force is observed, not the peak acceleration. There are also calculated the forces in tie rods, the values are very low.

The coordinate system for the inner wheel is mirrored by flipping the sign of both lateral force and slip angle (mirrored around X and Y-axis).

The tire forces are calculated in Matlab from the tire model, load of each tire is calculated from the static load, dynamic load and aerodynamic load. The static load is a portion of the vehicle's weight per current wheel (dependent on weight distribution), dynamic load is calculated from load transfer and aerodynamic load is a portion of aerodynamic downforce per current wheel (dependent on aero balance). The inputs for the tire model are vertical load, inclination angle, and slip angle (or slip ratio for longitudinal LT). Initially, a sweep of slip angles (slip ratios) are inputs to the tire model, then an assumption of equal slip angles (ratios) per each axle is made (Ackermann geometry is neglected). All lateral (longitudinal) forces are summed and the acceleration is recalculated. Then the slip angles (ratios) which give the lowest difference between the calculated and initial acceleration are the resulting tire forces and moments for current acceleration. (Figure 73).

To find the limit of the tire, slip angles are chosen to obtain maximal lateral (longitudinal) forces for a given load. The sum of these forces gives a larger acceleration of the vehicle than the initial acceleration condition. Therefore a bisection method is used to recalculate the next input acceleration condition from the result of the previous iteration, until the error between the result and input is less than limit. An iterative loop used to find the acceleration limit of the vehicle is displayed in Figure 74.

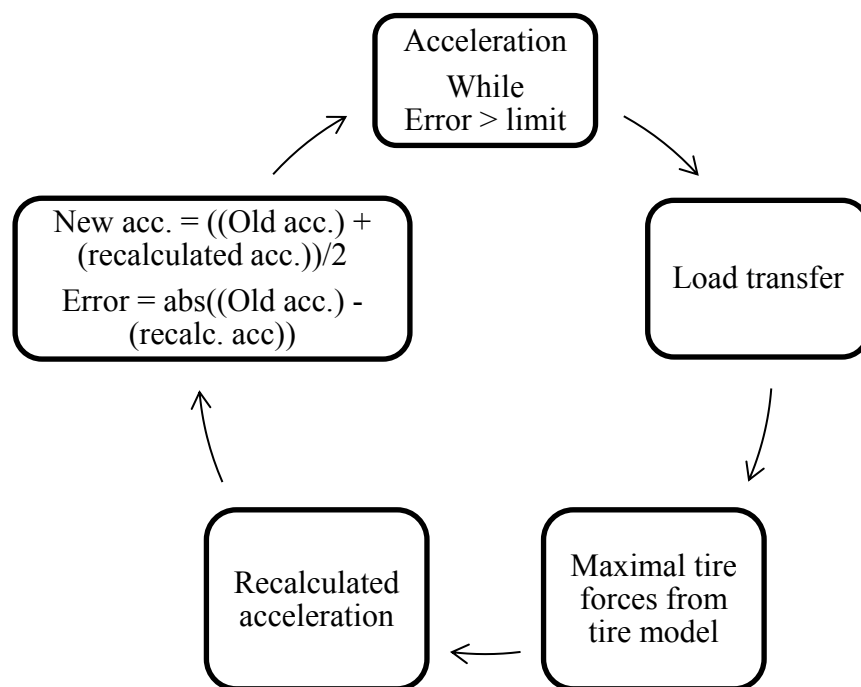


Figure 74 Finding the acceleration limit

### 2.3.3 DYNAMIC WHEEL BUMP

Two dynamic load cases were studied in the design process of the suspension in previous years: single and double wheel bump. Tires were neglected and bump stops were not contained in the model. Dynamic vertical bump of the wheel has been simulated as time-dependent vertical displacement in the Dynamic suspension simulation in Adams Car. The characteristic of this displacement is shown in Figure 75. As the sweep is 1.2 s long, damper forces induced by this

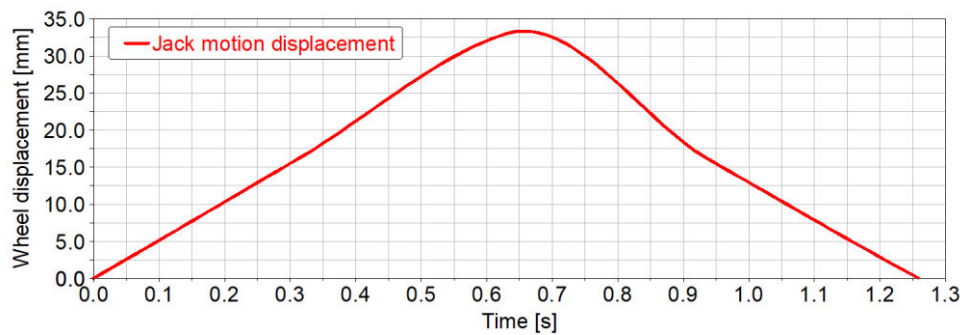


Figure 75 Wheel displacement – time spline previously used for the dynamic bump analyses

motion are very little. Real bump is quicker. With the neglected tires and bump stop in the model, the wheel travel was large to obtain sufficient forces in pull/pushrods (according to data). These inconsistencies were the reason for a revision of this dynamic simulation and its inputs. From data acquisition, signals from strain gauges on pull/pushrods were observed for the highest occurring forces. In Figure 76 is shown the peak force which occurred during the endurance race in FSG and Table 26 shows a list of the individual maximal forces from two competitions.

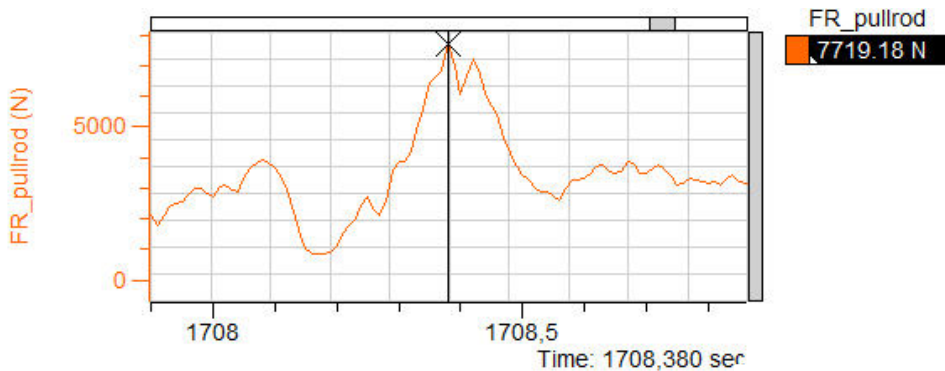


Figure 76 Maximal force from strain gauge of front right pullrod, Formula Student Germany 2019

As seen, the force in pull/pushrod due to bump during a race lasts approximately 0,2 s.

Table 26 Maximal occurred forces in pull/pushrods in competitions

	FS Germany		FS East	
	Left	Right	Left	Right
Front [N]	5423	7719	3917	4089
Rear [N]	-5136	-6860	-3407	-3545

The forces in Table 26 are individual and do not represent a single event. In Table 27, the forces in all pull/pushrods are displayed in the event of the two maximal bumps (yellow highlighted in Table 26). In this simulation, only the vertical load is considered even though the real load case included certain lateral and longitudinal acceleration, while a bump was ridden over. This is a simplification that is based purely on the strain gauge measurement of the pull/pushrods.

Force excitation in the pull/pushrods is caused only by a time-dependent vertical displacement of the testrig.

*Table 27 Data of pull/pushrod forces of each wheel in the 2 maximal load cases from competition*

	Front maximal bump		Rear maximal bump	
	Left	Right	Left	Right
Front [N]	4424	7719	4076	6318
Rear [N]	-3174	-4729	-4432	-6860

By the displacement excitation, the forces in Table 27 (white background) are sought to be measured in the simulation. By an iteration process, approximate heights of the road bumps are found.

*Table 28 Maximal testrig vertical displacement which causes desired forces in pull/pushrods, found by an iteration process*

	Height of the bump [mm]	
	Left	Right
Front	21	41.5
Rear	25	44

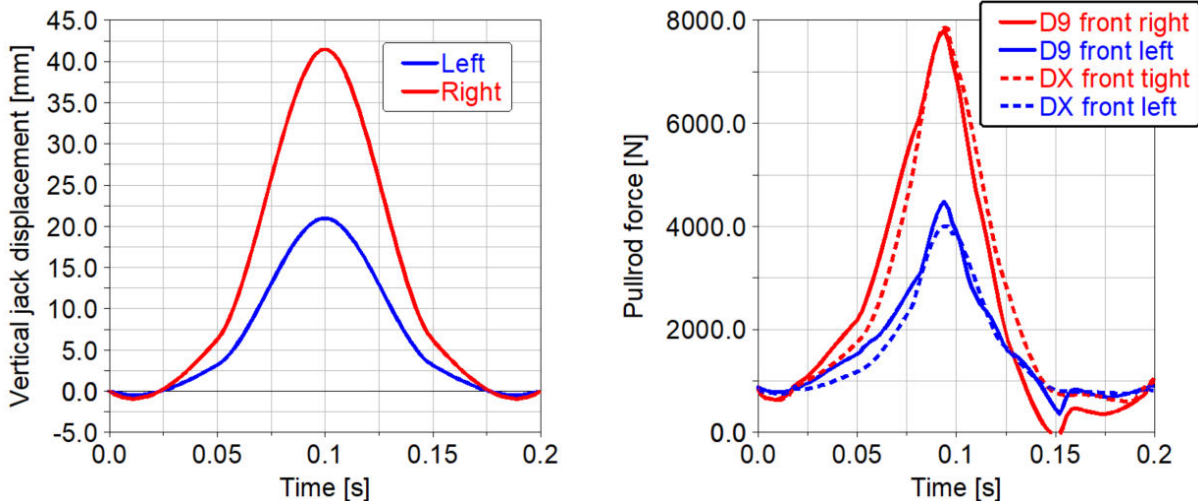


*Figure 77 Vertical displacement of the front testrig (on the left) and resulting pullrod forces (on the right)*

As expected, the resulting forces in pull/pushrods are almost equal (between D9 and DX) due to equal ride rates and the slope of the pull/pushrods which remained almost unchanged. See Figures 77 and 78.

Since similar forces (7,7 kN in the pullrod and 6,8 kN in the pushrod) were used in previous years for the FEM analyses of parts that proved to be reliable, there is no need to increase the safety of this load cases as it would only increase mass.

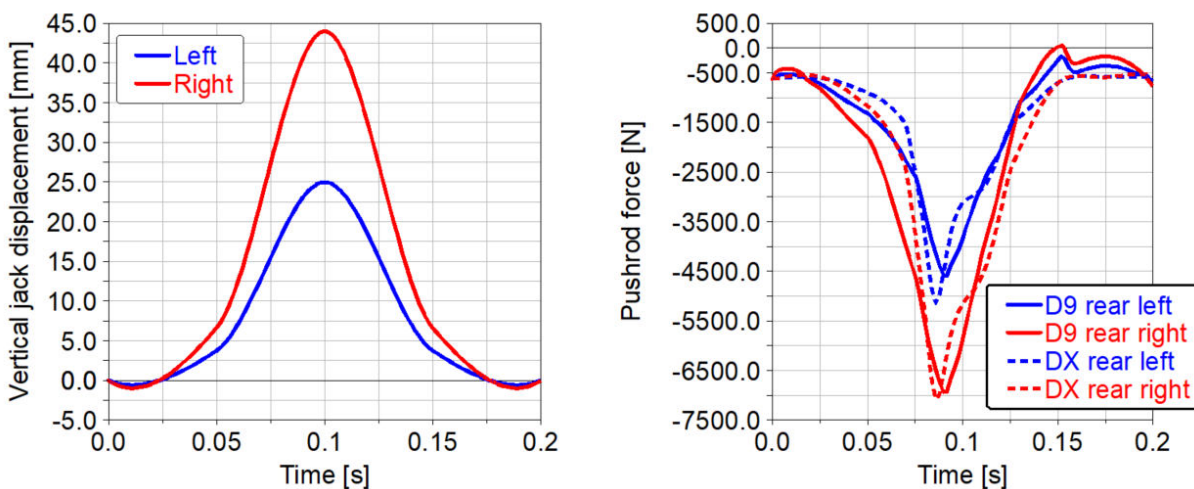


Figure 78 Displacement of rear wheels (on the left) and pushrod forces (on the right)

In Table 29 is a comparison of the resulting force reactions in suspension links. As seen, the force has shifted to the rear wishbone links in all cases. This is due to the caster change and reduced rear chassis.

Table 29 Comparison of forces in suspension links due to a dynamic bump

	D9 [N]				DX [N]			
	Front upper	Rear upper	Pullrod	Front upper	Rear upper	Pullrod	7853	Pushrod
Front axle	-5239	-4421		-3493	-5791			
	Front lower	Rear lower		Front lower	Rear lower			
	387	702	7796	-90	1045			
Rear axle	Front upper	Rear upper	Pushrod	Front upper	Rear upper	Pushrod	-7080	Pushrod
	-597	188		200	-660			
	Front lower	Rear lower		Front lower	Rear lower			
	3260	4321	-6934	2039	5009			

### 2.3.4 FRONT SUSPENSION

The changes in the front wishbone layout were mainly caused by the change of wheel geometry, requirements of aerodynamics, installation ratio, while “wishbone kinematic characteristics” remained.

Viewed from the top (Figure 79), the main difference is caused by wheel geometry, because negative scrub radius puts the outboard kinematic points further into the wheel envelope and caster moves the upper outboard point rearward, this caused the rear wishbone links to collide with the wheel rim and thus were the inboard kinematic points moved forward. For the force distribution to remain ideally equal, the wishbones were meant to remain the original span angle.

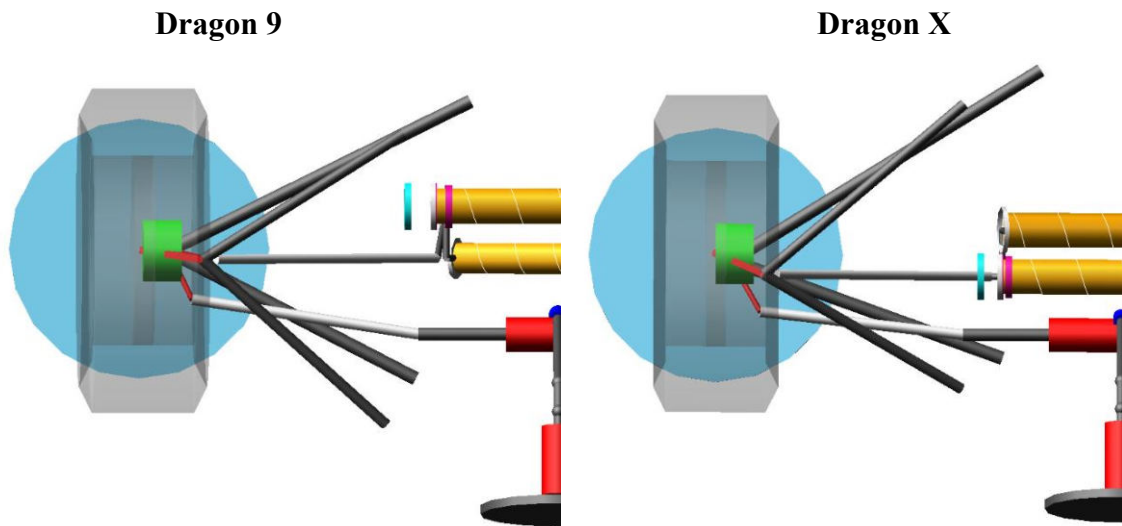


*Figure 79 Top view comparison of front suspension*

Viewed from the side (Figure 80), the changes in wishbone layout are mainly caused by the aerodynamic requirement to move the front lower inboard pickup point upward. To remain the desired anti-dive, roll center height and installation ratio, other points had to be relocated.

The side view swing arm length was reduced because of the anti-dive, which produced the caster angle change in wheel travel (Figure 81). The more loaded wheel will have more caster angle and vice versa, this is desirable as seen from the tire model discussed in Chapter 1.2.

Collisions with the rim were controlled primarily in the Adams model where a rim envelope is modeled. As seen in Figure 82, a combination of extreme wheel travel and maximal steering wheel angle is simulated. For the control of the lower wishbone, a wheel bump of 25 mm and maximal steering angle is simulated, for rear upper wishbone link is used rebound of 25 mm (both from static position). Different camber angles also influence the clearance between the rim and wishbones, therefore minimal camber angle of  $-1^\circ$  is tested for the lower arms and maximal camber  $-4^\circ$  is tested for upper arms.

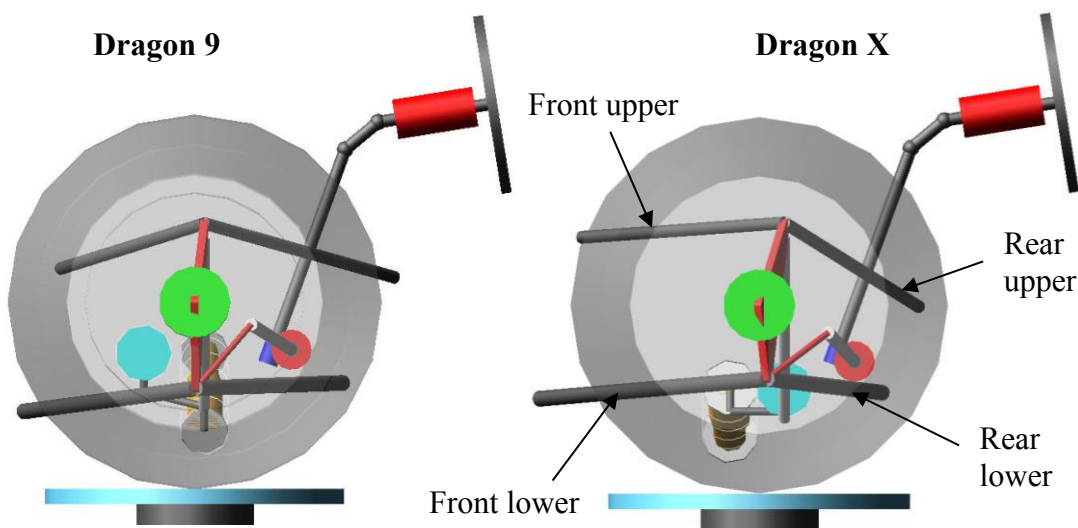


*Figure 80 Side view comparison of front suspension*

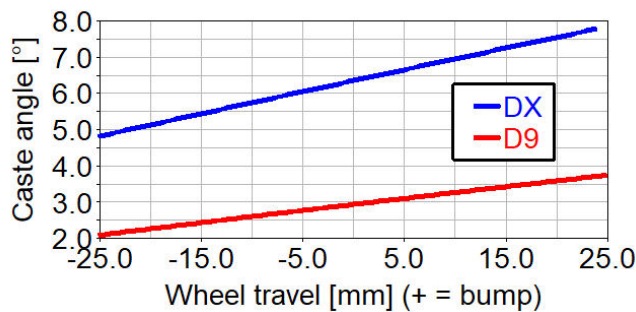


Figure 81 Caster angle change in wheel travel

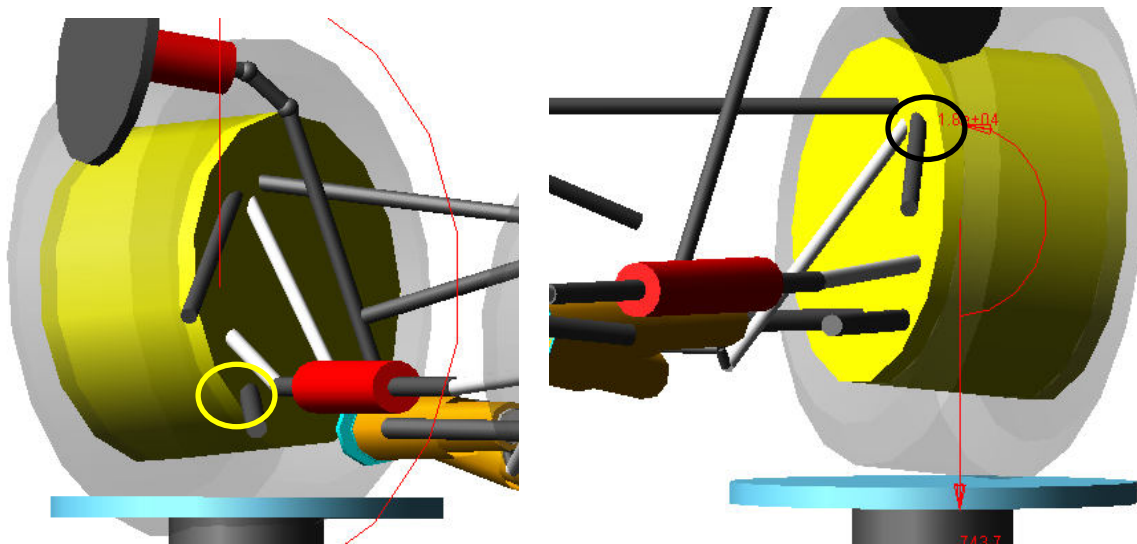


Figure 82 Dragon X collision check in Adams, combination of 25 bump on the left, and 25 mm of rebound on the right with maximal steering angle.

The collision check is also done in CAD by other team members. As discussed earlier, there is a difference between the camber setup in Adams and in reality which also influences the collisions.

## FORCES IN FRONT SUSPENSION LINKS

The force reactions under the wheel obtained from load transfers and tire model are inputs in the Dynamic suspension analysis in Adams (Table 30).

Table 30 Input tire forces for the front suspension steady-state analysis

	Cornering 2.5G		Braking 2.5G		Cornering + Braking 2.26 G	
	Left	Right	Left	Right	Left	Right
Fy	62.82	2941	0	0	945	1761
Fx	0	0	-2554	-2554	-660	-2131
Fz	24.72	1585	1403	1403	637	1737

Dragon 9 and Dragon X are compared under equal conditions, tires of 99 N/mm vertical stiffness, and suspension rates are approximately equal.

*Table 31 Comparison of result forces in front wishbones and pullrods on the right side*

	D9 [N]			DX [N]		
Cornering	Front upper	Rear upper	Pullrod	Front upper	Rear upper	Pullrod
	-1545	-1351		<b>-637</b>	-1411	
	Front lower	Rear lower	3919	Front lower	Rear lower	3803
	-2262	-1911		-2124	<b>-2456</b>	
Braking	Front upper	Rear upper	Pullrod	Front upper	Rear upper	Pullrod
	-2828	-164		-2756	<b>-687</b>	
	Front lower	Rear lower	2676	Front lower	Rear lower	2608
	4731	-3796		4981	<b>-4253</b>	
Cornering + Braking	Front upper	Rear upper	Pullrod	Front upper	Rear upper	Pullrod
	-2641	-456		<b>-2262</b>	<b>-816</b>	
	Front lower	Rear lower	3676	Front lower	Rear lower	3584
	2490	-4356		<b>2858</b>	<b>-5092</b>	

As seen in Table 31, the forces have increased in general but the increase is not considered dramatic in terms of safety but will surely cause higher compliance. The forces were measured in the joints according to the work of Ing. Gabriel Stariak, ref. [15]. Reactions in wishbones were the main limitation of the front wheel geometry, otherwise lower kingpin inclination angle would be set.

### 2.3.5 REAR SUSPENSION

Rear wishbone inboard pickup points were changed dramatically, this chapter follows the issue discussed in Chapter 1.1. The pursuit for lower mass, lower yawing moment of inertia, and larger diffusor were the reasons for this design change which was inspired by the competition.

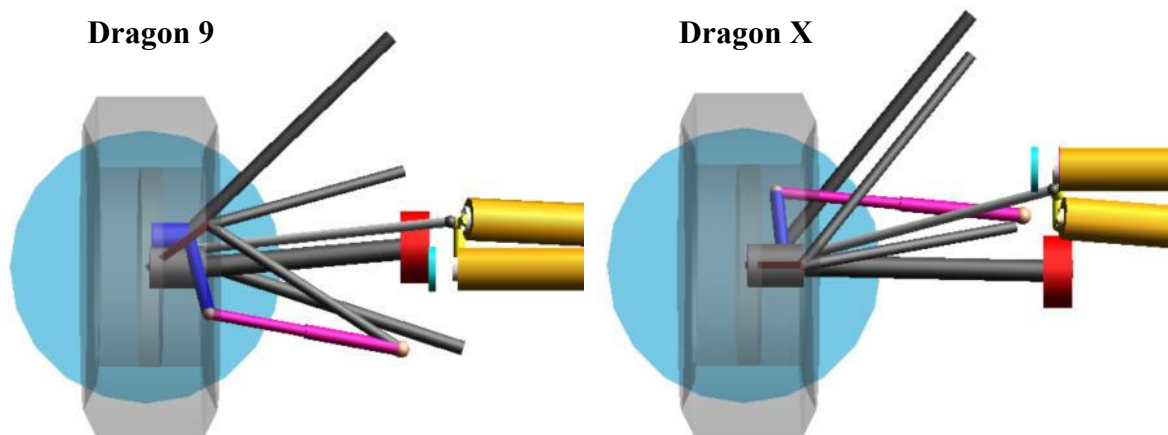


*Figure 83 Top view comparison of rear suspension*

The inboard pickup points are moved to the front, before the drive shaft which is currently blocking the view of the rear lower wishbone link, which was designed to be approximately perpendicular to the longitudinal axis. The tie rod is moved in front of the wheel center as discussed earlier because there is no longer a chassis in the back to attach it to. The fact that a full carbon fiber monocoque chassis is done for the first time this year (previously was monocoque only in the front part, while at the rear was a steel tubular frame) has made it much easier for the choice of inboard pickup points. There is no need for compromises between the chassis nodes and kinematic pickup points.

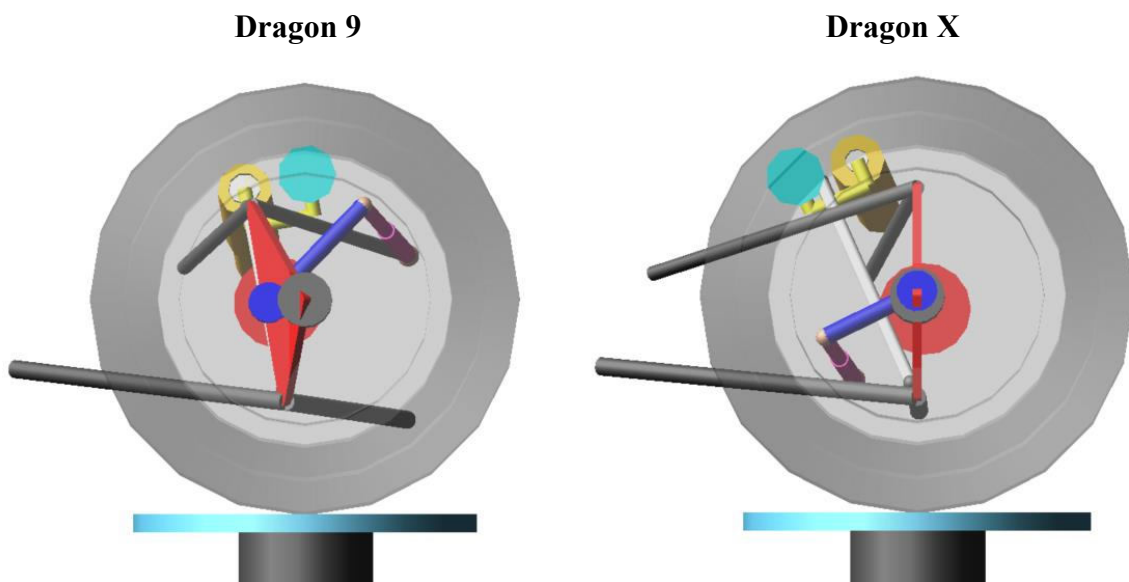
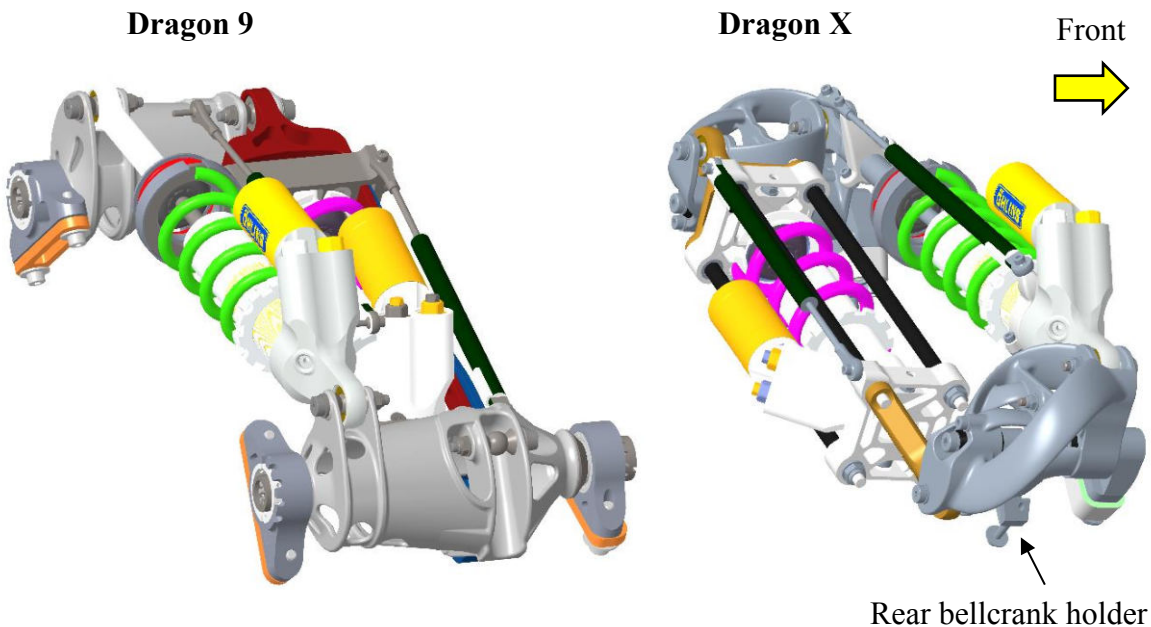


Figure 84 Side view comparison of rear suspension

The final shape of the wishbones was a result of compromises and a large number of iterations. Simulation script with Adams Insight was used to try to find a compromise automatically but due to a large number of kinematic characteristics and mechanical limitations was the iteration process primarily done manually. Knowledge of the kinematic characteristics and the way they can be achieved is crucial for an effective iteration process.

In the top view in Figure 83 can be seen that another limitation was the collision of rear upper wishbone link with the pushrod and a collision of the tie rod with the pushrod.

As will be shown later in the figures of CAD assembly, another limitation was the end of the monocoque which ended before the driveshafts. It had to have sufficient clearance with the driveshafts (in all positions) while, in order to minimize the moment of inertia, the differential was not to be moved further to the back. Also, to have sufficient stiffness of the monocoque which is ended with a square tubular hoop, there was a need for the rear upper and rear lower pickup points to be connectable with a straight line (in an ideal case). This caused the rear upper wishbone to be headed further to the front.



*Figure 85 Comparison of the rear roll heave suspension systems*

The main issue when this design change was first considered was the mounting of the bell cranks of the roll heave system. This is related to Figure 9 in Chapter 1.1, where a problematic area of the rear chassis (consequence of the roll damper placed slantwise) is displayed. The roll heave suspension system is wide in the longitudinal direction and as the rear part of the chassis was reduced, there was no space for mounting the bellcranks in the original way.

As seen in Figure 85, the rear bellcrank holder was moved forward and is attached to the very end of the monocoque, while the roll damper was moved backward and is now behind the monocoque. This solved the original problematic area discussed in Chapter 1.1. As the roll damper is in an overhang behind the monocoque, it is a source of compliance which was reduced as much as possible by the FEM optimization methods. This issue is dealt with in detail in the bachelor thesis “Rocker for formula student vehicle” of Petr Šprta. The possibility of such constructional solution and its sufficient stiffness enabled the reduced chassis implementation.

The collisions were checked similarly as at the front axle, the rear-wheel steering of  $3^\circ$  was also considered for the new four-wheel steering project.

The main drawback of the reduced rear chassis is undeniably the increased compliance of the wishbones. At the time the kinematics were designed, the flexible bodies were not yet implemented into the Adams model, therefore the design was based on the force distribution among the suspension links.

## FORCES IN THE REAR SUSPENSION LINKS

For the rear axle force analysis, cornering, acceleration, and a combination of these were considered.

*Table 32 Input tire forces for the rear suspension steady-state analysis*

	Cornering at 2.5G		Acceleration at 2G		Cornering + Acceleration at 2G	
	Left	Right	Left	Right	Left	Right
Fy	108	3018	0	0	889	1423
Fx	0	0	2452	2452	1018	2459
Fz	43	1650	1325	1325	731	1631

The forces in the rear suspension links have increased in general. But when comparing these forces with the ones in the front suspension, they are still lower, therefore there should not be an issue with the safety of this new geometry.

*Table 33 Comparison of result forces in rear wishbones and pushrods on the right side*

	D9 [N]			DX [N]		
Cornering	Front upper	Rear upper	Pushrod	Front upper	Rear upper	Pushrod
	670	722		-319	1452	
	Front lower	Rear lower		Front lower	Rear lower	
	-80	-1763		769	-2370	
Acceleration	Front upper	Rear upper	Pushrod	Front upper	Rear upper	Pushrod
	-2105	945		-1823	1362	
	Front lower	Rear lower		Front lower	Rear lower	
	-254	2601		-1149	3652	
Cornering + Acceleration	Front upper	Rear upper	Pushrod	Front upper	Rear upper	Pushrod
	-1697	1253		-1991	2123	
	Front lower	Rear lower		Front lower	Rear lower	
	-735	1208		-1039	1932	

### 2.3.6 TIE RODS AND BUMP STEER

Design of the exact position of tie rod is changed at the end to minimize bump steer. This is done primarily by changing the vertical coordinate of the inboard tie rod kinematic point. Design of Experiments (DOE) simulation script in Adams Insight can be used to automatically find the ideal position. See Figure 86.

Forces in tie rods are very small and are calculated based on the steering forces script in Matlab and verified in Adams.

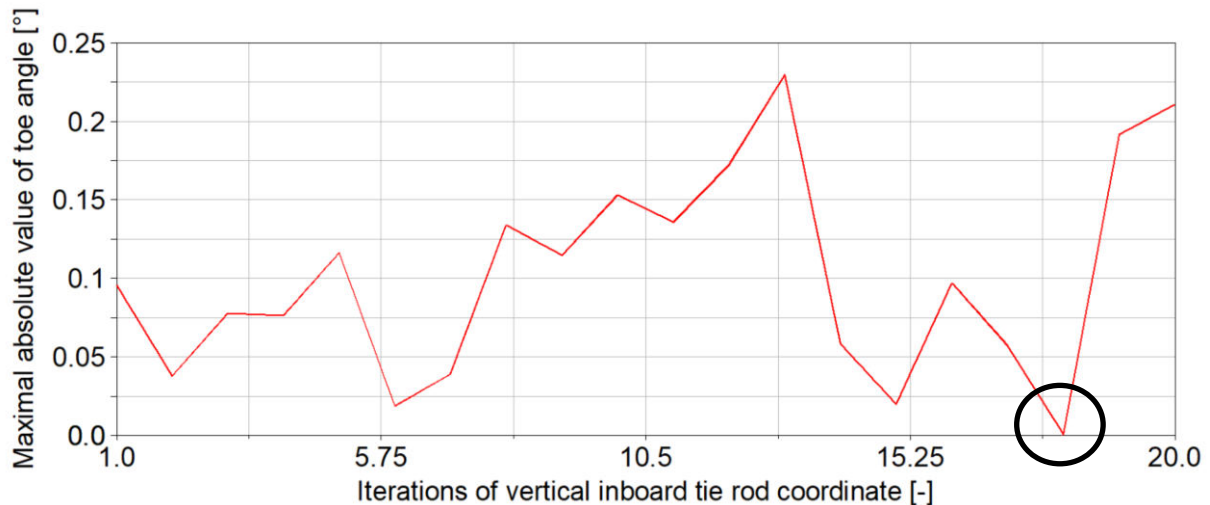


Figure 86 Simulation script of parallel wheel travel for tie rod location optimization

## 2.4 EFFECT OF KINEMATIC DESIGN CHANGES ON THE VEHICLE PARAMETERS

Some changes in kinematics were implemented solely for the reduction of the vehicle's weight, center of gravity height, or yawing moments of inertia. In this chapter, the impact of these changes will be discussed and quantified.

As seen in Figure 87 the monocoque at the front axle was reduced significantly. The monocoque is thinner as the upper wall is lowered and the lower wall is moved up for the aerodynamics.

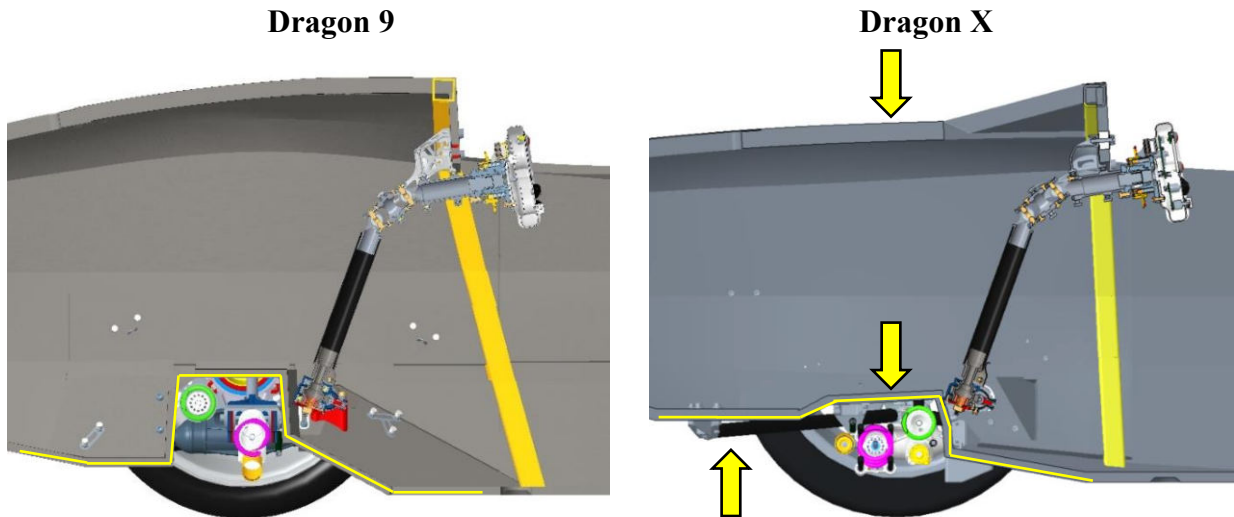
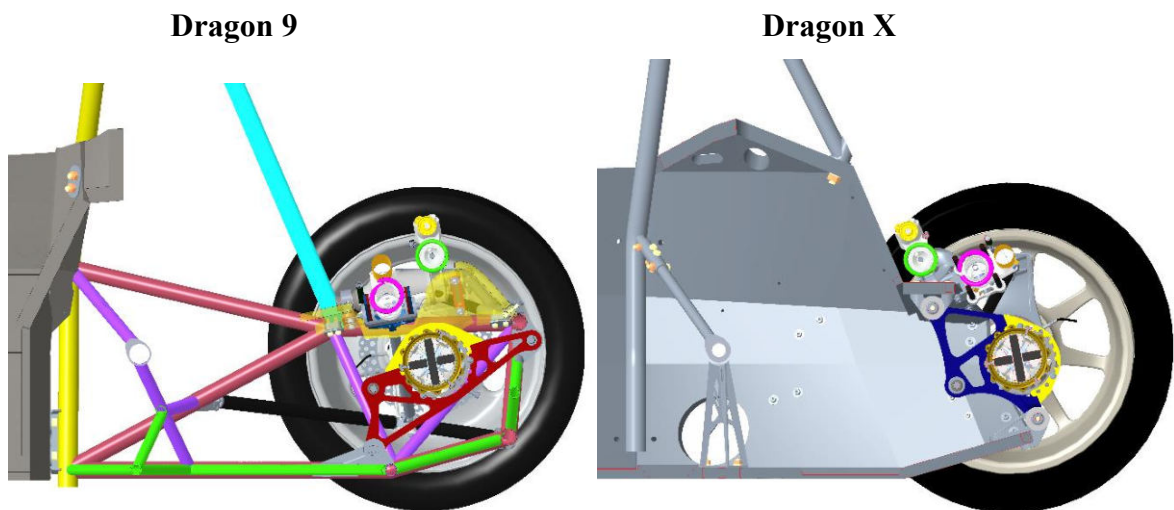


Figure 87 Reduction of the front part of the monocoque due to kinematics

The bellcranks were reduced as well, as shown in Figure 36.



*Figure 88 Reduction of the rear part of the chassis due to kinematics*

Viewed from the side in a section, the reduction of the rear end of the chassis is shown in Figure 88, not only has the chassis end moved forward, but also it remained higher, leaving more space for the diffusor.

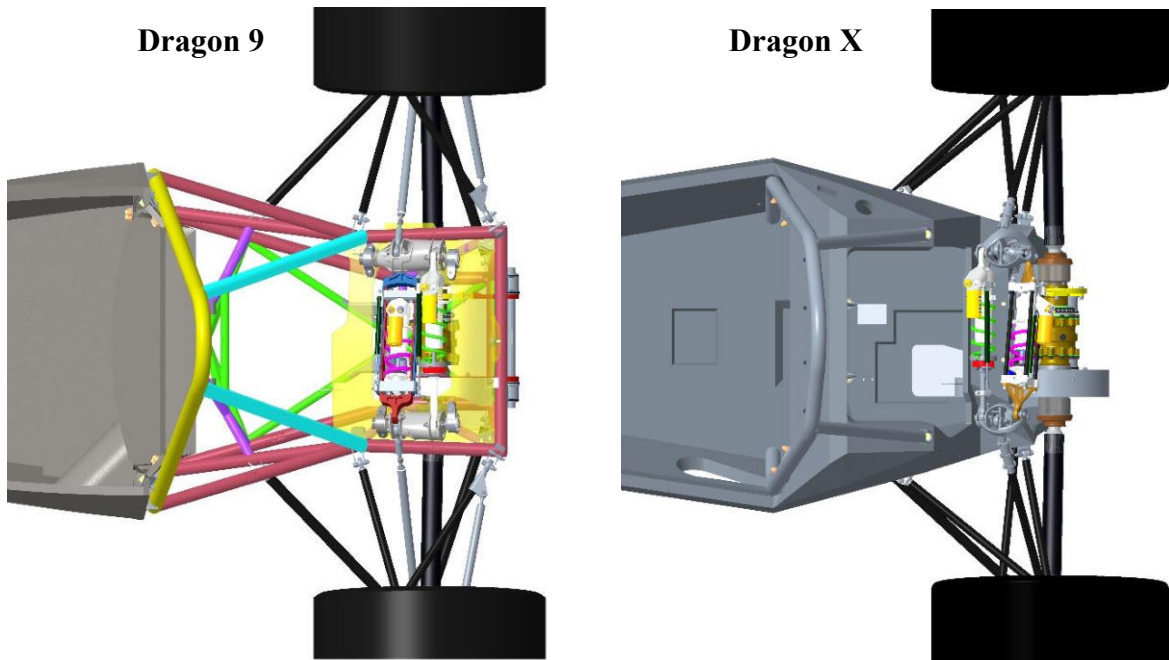


*Figure 89 Top view comparison of the rear axle*

Viewed from the top, in Figure 89, the layout of the wishbones and drivetrain is seen. The differential is now placed behind the chassis as well as the rear roll damper.

To display the rear part of the chassis and suspension more clearly, a 3D view of the rear is shown in Figure 90.

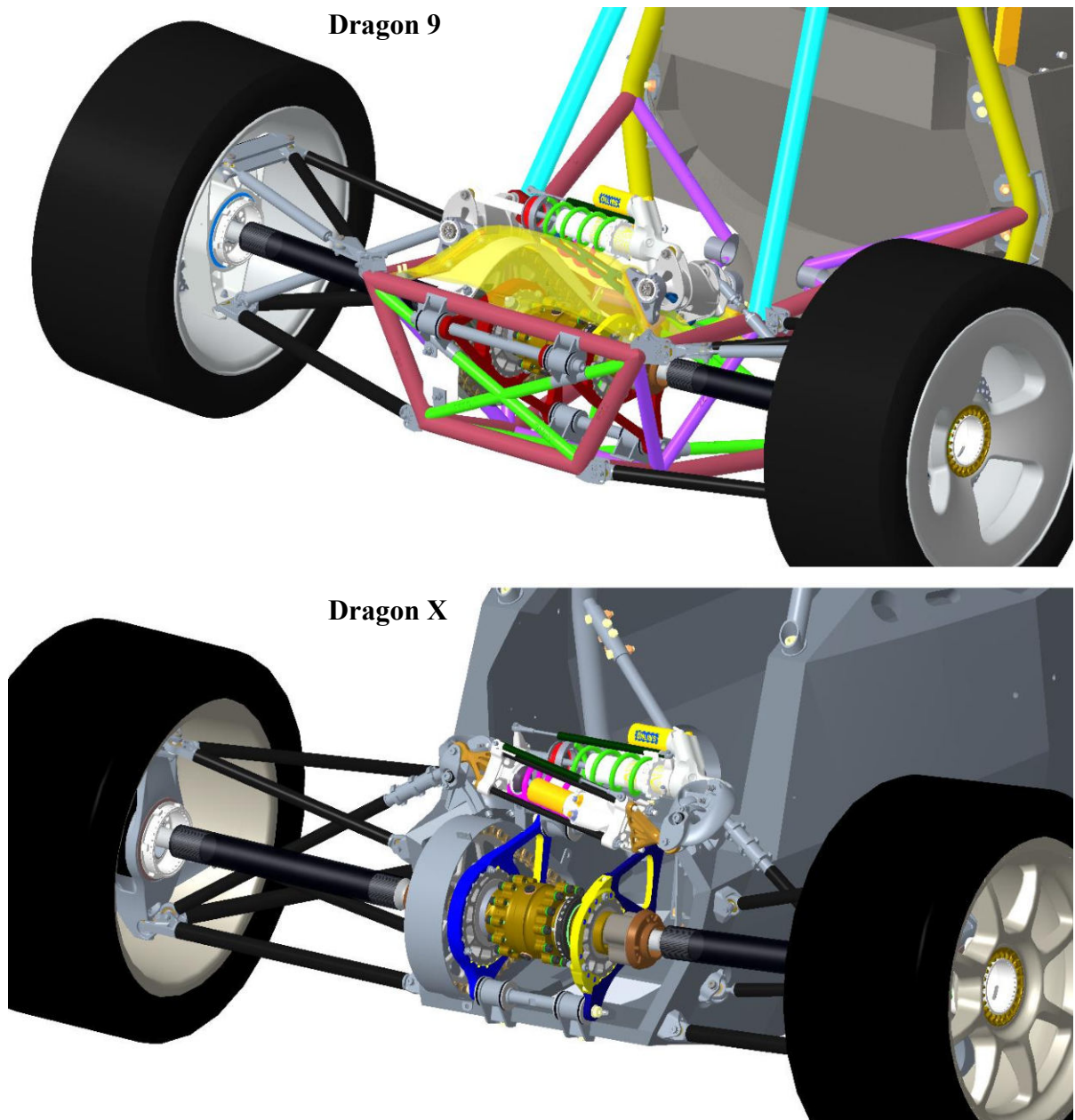


*Figure 90 3D view of the rear end of the vehicle*

To quantify the effect of kinematics, only the influenced parts are measured and compared. These are the monocoque and the roll-heave suspension system. As Dragon 9 chassis consisted of front carbon fiber monocoque and rear steel tubular frame, the chassis is divided into front and rear parts. Also, the tubular frame can not be compared to the full monocoque, therefore an approximate full monocoque of the Dragon 9 is constructed, consisting of the front monocoque of Dragon 9, rear part of the Dragon X monocoque and then an extra part at the rear to compensate the reduced chassis. See Figure 91.

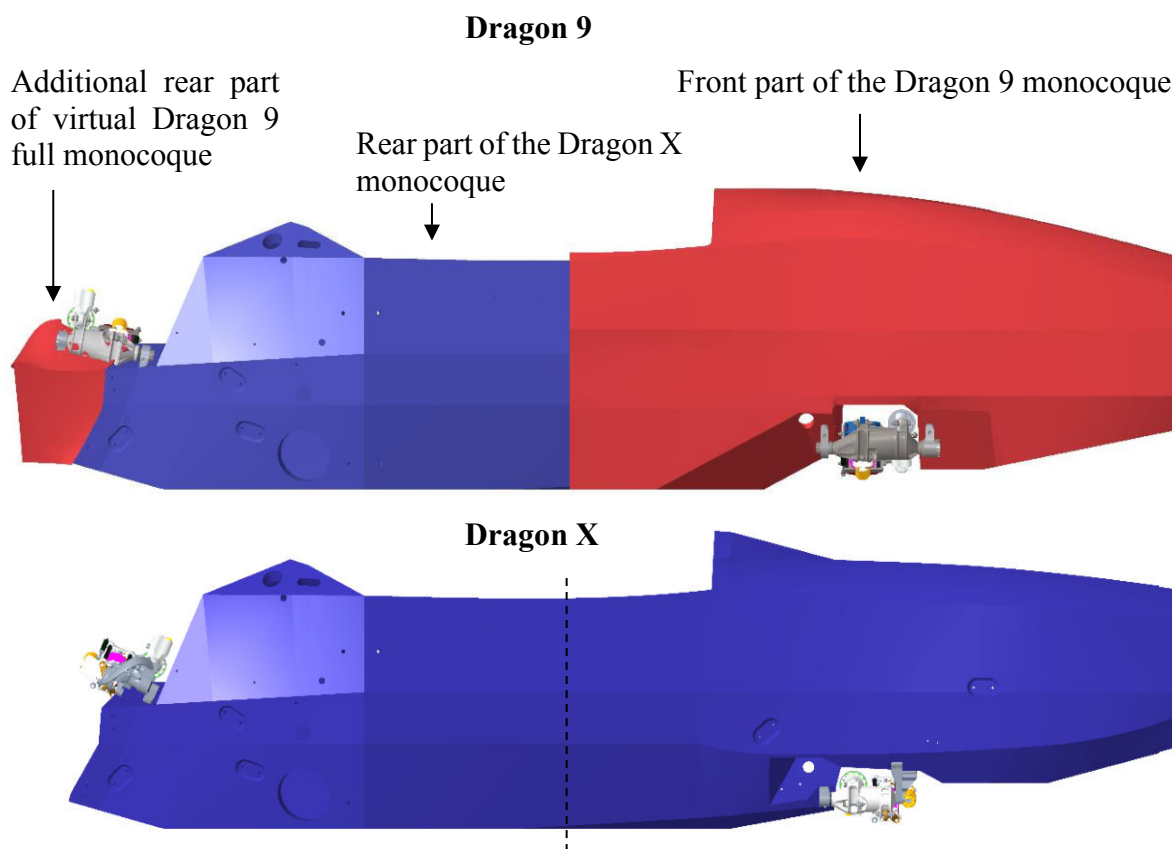


*Figure 91 Comparison models of the monocoques and roll-heave systems. Virtual Dragon 9 full monocoque is constructed to obtain comparable model.*

The models shown in Figure 91 are made of assemblies that are considered to be most affected by the kinematic changes. It is only an approximation because a direct comparison of the two vehicles would be non-objective, as it would also include the transition from tubular frame to the monocoque. The changes in the monocoque structure are also considered and subtracted in this comparison. The weight of the monocoque is only roughly estimated in the model, it is a solid body with a certain density which reflects the actual composite material.

*Table 34 Comparison of the chassis between Dragon X and virtual full monocoque of Dragon 9*

	Full monocoque				Front part			Rear monocoque excess
	D9	DX	Difference		D9	DX	Difference	D9
			Values	Percentage of D9 [%]				
Mass [kg]	15.72	14.48	-1.24	-7.89	9.12	8.82	-0.30	0.96
CoG_z [mm]	292.80	287.60	-5.20	-1.78	335.50	321.50	-14.00	
Mol_z [kg.m <sup>2</sup> ]	7.22	5.72	-1.50	-20.78				

The Dragon X monocoque is divided into two parts to see the influence of the front and rear independently, the plane of this division is shown in Figure 91.

In Table 34 is shown the comparison of the chassis, the percentage difference shows that the greatest impact has been on the yawing moment of inertia, which has reduced nearly 21 %. In table 35 is shown the comparison of roll-heave systems, due to limited space at the rear, the roll-heave system was placed slightly higher, thus the total  $CoG_Z$  of the systems is increased a little. The mass reduction is around 11 % and  $MoI_Z$  is also almost 20 %.

*Table 35 Comparison of the roll-heave systems*

	Both roll-heave systems including holders				Front assembly		Rear assembly	
	D9	DX	Difference		D9	DX	D9	DX
			Values	Percentage of D9 [%]				
Mass [kg]	6.56	5.82	-0.74	-11.28	2.96	2.86	3.65	2.92
$CoG_Z$ [mm]	219.00	220.26	1.26	0.58	106.45	134.40	326.01	340.15
$MoI_Z$ [kg.m <sup>2</sup> ]	3.87	3.12	-0.76	-19.68				

The moments of inertia of the subsystems are not measured for simplicity, certainly, the rear end is the main contributor to this reduction. The weight reduction is always a team effort and consists of the work of many team members, each responsible for the constructional design of their assembly. Therefore the displayed weight reduction is not only on account of kinematics.

To compare the impact of these changes on the whole vehicle, a model of Dragon X is assembled with the Dragon 9 virtual full monocoque and Dragon 9 roll-heave system. Then the percentage differences drop greatly.

*Table 36 Comparison of full vehicle assemblies including the driver*

	DX with virtual D9 full monocoque and D9 roll-heave system	DX full vehicle assembly	Difference	
			Values	Percentage of D9 [%]
Mass [kg]	248.73	246.75	-1.98	-0.80
$CoG_Z$ [mm]	298.83	298.82	-0.01	-0.00334
$MoI_Z$ [kg.m <sup>2</sup> ]	156.95	155.08	-1.87	-1.19

The impact of kinematics on the aerodynamics is not clear. There has been a vast change in the aerodynamic package, and due to a change in the rules, it is now legal to extract air under the car by fans. The shorter chassis enabled this system to be closer to the vehicle's CoG.

### 3 KINEMATICS AND COMPLIANCE

The geometry of the rear suspension has changed and a reduction of stiffness is expected. As mentioned earlier, in the design phase of the car, compliance analyses were not yet available in our team and thus it has been studied after the design deadline. The topic of kinematics and compliance has not been dealt with before in our team.

One option is to simulate the whole suspension assembly using FEM analyses, which is a vastly complicated simulation with a large number of elements, and long simulation time. Also, this analysis will only give a certain camber or toe stiffnesses, the complex simulation would have to be repeated for every design change. These numbers could be used for analytical vehicle dynamics simulations in Matlab. To simulate the compliance in Adams, flexible bodies could be imported into the model from Ansys, but the complexity would remain.

Instead, a simplified approach is taken. Each suspension link is connected with a spherical joint and therefore there is primarily tension or compression in each of them. Due to manufacturing inaccuracies and the way wishbones are connected to the pull/pushrod, there is a residual bending moment in the wishbones, which is neglected here. The normal stiffness of each suspension link (except for pull/pushrods which are not dealt with here), including their holders and connections, are represented by a bushing, which only has certain flexibility (stiffness) in the normal direction (axis of the link), while other translational stiffnesses are very high and the rotational stiffnesses are zero. Therefore, a flexible joint is created which has a certain amount of flexibility in the axis of a particular suspension link, while other degrees of freedom remain equal to the spherical joint. For example, a wishbone arm stiffness is represented by two bushings located at the inboard connection points to the chassis. The flexible translational degree of freedom is the Z-axis of the bushing. For consistency, only spherical joints are replaced, therefore the tie rod stiffness is represented by the bushing at the upright because the inboard tie rod joint is a hook joint. Adams offers two modes of simulation – kinematic or compliant mode, thus bushings are only active in the compliant mode and spherical joints are only active in the kinematic mode. Both joints are present in the model and can be easily switched between each other.

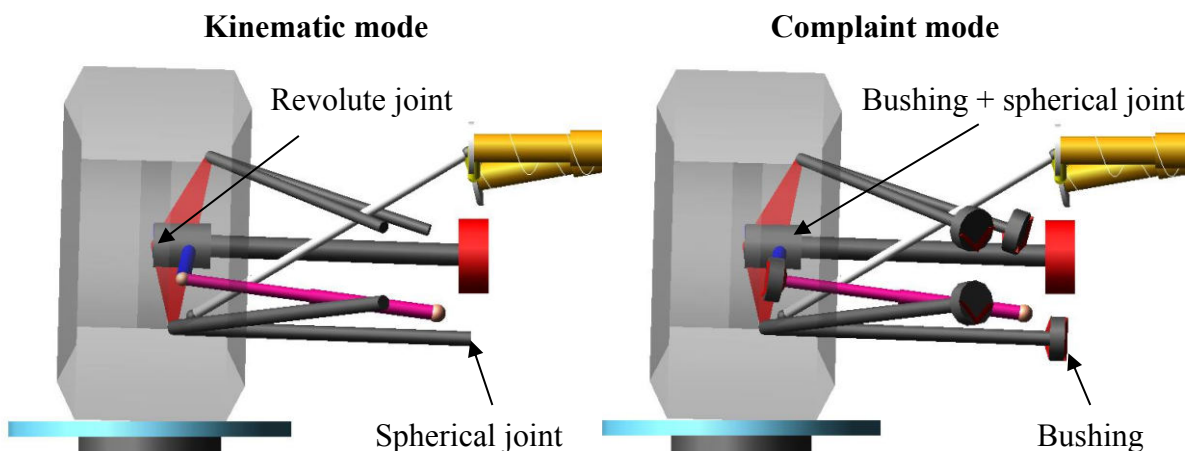
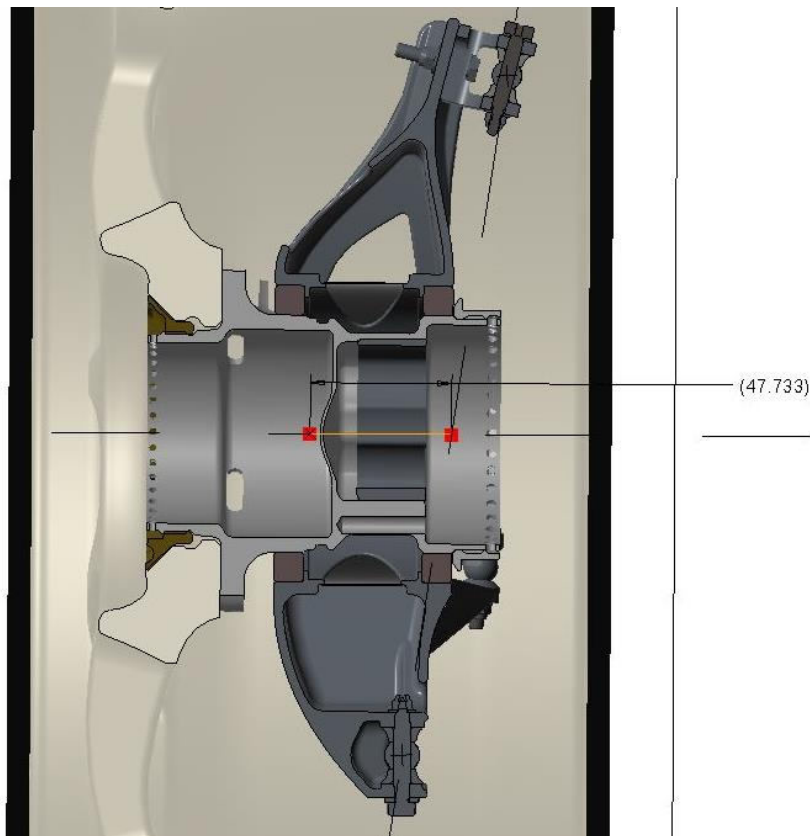


Figure 92 Kinematic and compliant mode of rear suspension in Adams

To represent the stiffness of the wheel assembly (hub, upright, wheel), hub compliance is built according to the Adams Help guidelines. It replaces the revolute joint between the hub and the upright with a bushing and a spherical joint. The location of the revolute joint is at the wheel center, but the hub compliance is offset using the “hub compliance offset” parameter variable. The offset is obtained from CAD as a distance between wheel center and a point of intersection of a plane constructed from outboard points (upper, lower outboard wishbone points, and the outboard tie rod point) and the wheel axis (Figure 93). Therefore, hub compliance represents the stiffness of the wheel assembly up to the connection points of suspension links.



*Figure 93 Rear hub compliance offset measured from CAD*

### 3.1 BUSHING STIFFNESS SENSITIVITY STUDY

The stiffnesses of the bushings should be based on a measurement. Each link should be either loaded with a normal force and the deflection measured or the whole suspension compliance should be measured and then distributed among the individual bushings to obtain equal results. The actual measurement is not part of this thesis but a measurement device will be presented later.

As there are no measured values, to begin with, FEM analyses are conducted to obtain initial values, but the real deflection is expected to differ due to simplifications in FEM simulations and due to chassis deflection. To get an overview of the bushing stiffness influence on the

camber and toe compliance, a sensitivity study is conducted. Boundary conditions in these simulations:

- All bushings have equal, **linear** stiffnesses
- Hub compliance is deactivated

*Table 37 Load cases for bushing stiffness sensitivity study of compliance*

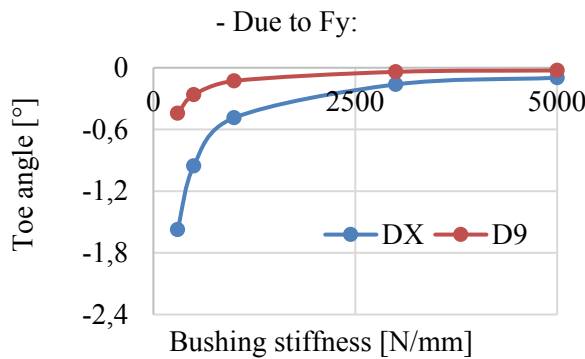
	Lateral			Longitudinal		
	Acceleration [G]	1	1.5	2	Acceleration [G]	-2
Fy [N]	788.73	1472	2059	Fx [N]	-576	1472
Mz [Nm]	-19.83	-23.41	-6.21			

*Table 38 Bushing linear stiffnesses used in the sensitivity study*

Bushing stiffnesses [N/mm]	300	500	1000	3000	5000

The bushing stiffness is represented by a property file in Adams, which can be easily changed in a text editor, all the bushings then change simultaneously. This gives a good time efficiency in adjusting the simulations for multiple bushing stiffnesses. Simulations of different load cases

#### Rear toe compliance, 1 G lateral



#### Rear camber compliance, 1 G lateral

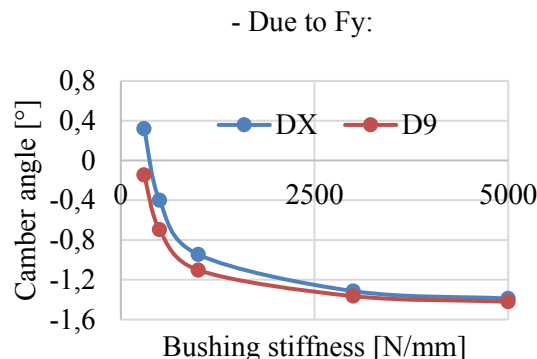


*Figure 94 Toe and camber compliance for different bushing stiffnesses due to 1G lateral acceleration. Static toe = 0 °, static camber = -1.5 °*

and different bushing stiffnesses are conducted. These simulations are done using suspension dynamic analyses, where static forces are inputs at the contact patch. Only the rear axle changed dramatically, therefore this sensitivity study is only done at the rear in this thesis.

The tire forces are calculated from the tire model for different accelerations as discussed before, Mz of the tire is also included. Vertical load is not applied, because the main purpose of these simulations is the comparison with real measurement, where the vertical load will not be applied, this will be discussed later. In this study, loads from lateral, longitudinal forces and the aligning torque are studied only. Fy and Mz are applied together. The load cases are displayed in Table 37.

In Table 38 are displayed different bushing stiffnesses used for the sensitivity analysis. There are 5 different bushing stiffnesses for 5 different load cases, for Dragon 9 and for Dragon X (Dragon 9 compliant model is also created in Adams only by changing the hardpoints), that is a total of 50 simulations only for the rear axle. Besides, Fy and Mz were also simulated individually to see their contribution, there will be even more simulations later in this thesis.

The springs are replaced with extremely stiff linear springs with no preload to simulate the damper solid replacements, which will be used during the real measurement. The gravity is switched off, as there was an offset at the start of the simulation at zero horizontal load, when the gravity was on. This is done to isolate the horizontal load influence. The real measurement will monitor the change of toe and camber due to horizontal load, not vertical.

In Figure 94 are 2D graphs of toe and camber compliances due to both Fy and Mz and also each of them individually. Camber stiffness loss was expected and the values seem reasonably small.

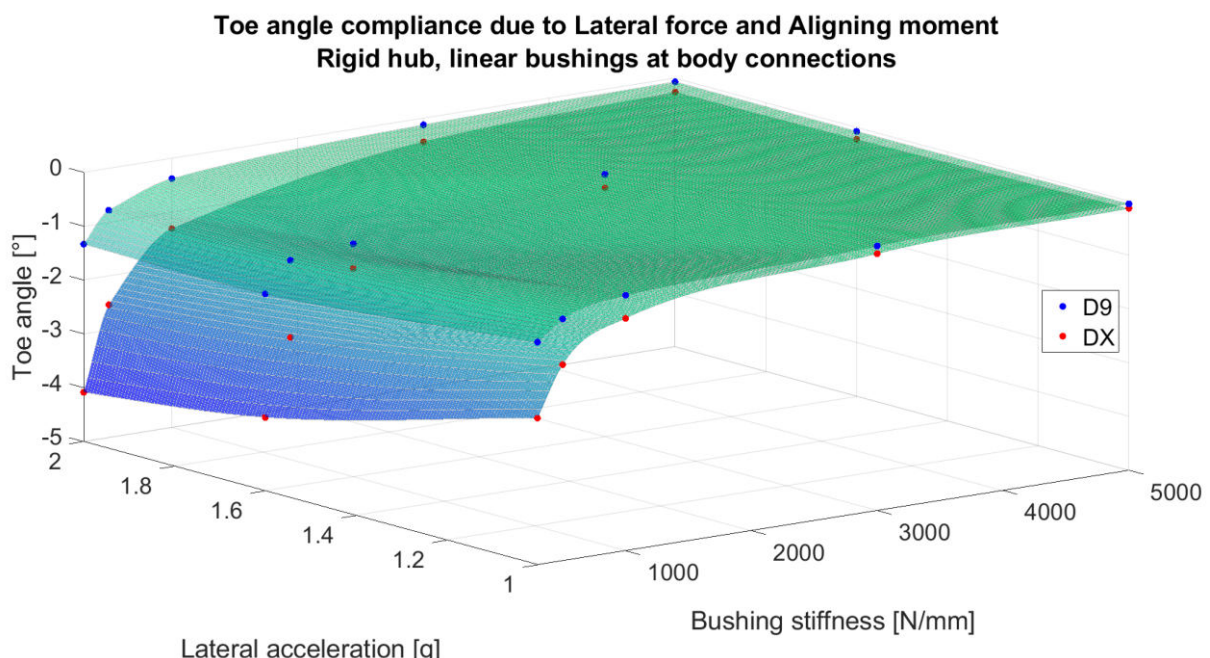


Figure 95 3D graph of rear toe angle compliance for various lateral accelerations and bushing stiffnesses. Static toe = 0 °, negative is toe-out.

But toe angle stiffness due to  $F_y$  is reduced significantly with Dragon X. The difference of  $M_z$  influence on toe angle is not large, which was expected due to the equal tie rod bases.

In Figure 95 is 3D map of toe compliance due to lateral acceleration. The difference between Dragon 9 and Dragon X is large. It is seen that toe compliance rises exponentially with insufficient suspension stiffness. Using these analyses, the actual value of stiffness needed for each component can be estimated, from this graph a minimum of 3000 N/mm could be set for instance. Compromise between mass and compliance can be also found using these simulations, too high stiffness will provide only little improvement and will add mass.

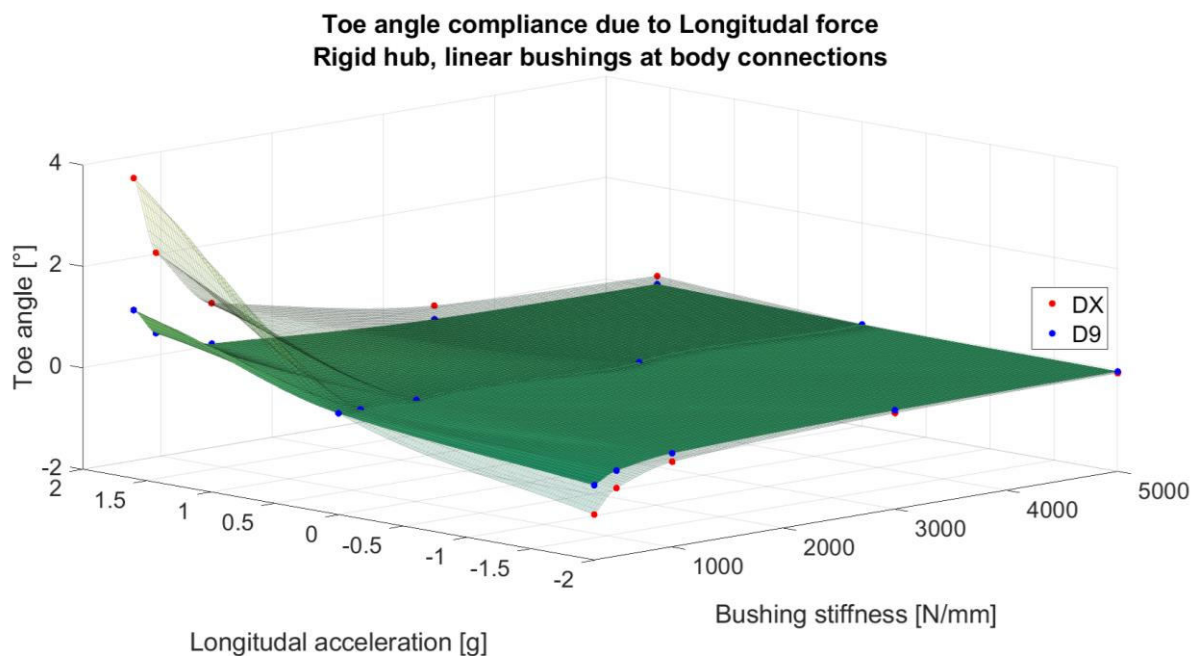


Figure 96 3D graph of rear toe angle compliance for various longitudinal accelerations and bushing stiffnesses. Static toe = 0 °, negative is toe-out.

In Figure 96 is seen the toe compliance due to longitudinal accelerations, here is also observed loss of toe stiffness. In Attachment I are 3D maps of **camber** compliances due to lateral and longitudinal forces. Camber angle compliance is higher with DX than with D9 mainly due to higher forces in wishbones, but toe angle compliance is higher mainly because of tie rod location in relation to wishbones. This issue will be addressed later.

The 3D maps are used to give an idea of the suspension stiffness influence on toe and camber compliance and to give an approximate value of bushing stiffnesses corresponding to certain suspension compliance, which will be measured in the future.

### 3.2 COMPLIANCE ANALYSIS BASED ON FEM VALUES

Each link has different stiffness due to either different dimensions, attachment holder, or due to chassis compliance. Stiffness distribution among the suspension link will greatly influence the value and direction of the compliance. For instance, as seen from force analyses in Chapter

2.3.5, the largest force is acting on the lower wishbone in cornering, therefore the lower outboard kinematic point deflects the most – if all suspension links have equal stiffnesses (this was estimated for the sensitivity stiffness analyses in previous chapter). In reality, lower wishbones are made of tubes of larger diameters and therefore should be stiffer. If the joint will produce large compliance, the tube dimensions will probably not make any difference as carbon fiber tubes are very stiff. This needs to be measured to obtain trustworthy values.

To get approximate values of the stiffness distribution among the suspension links, FEM analyses are conducted by other team members.

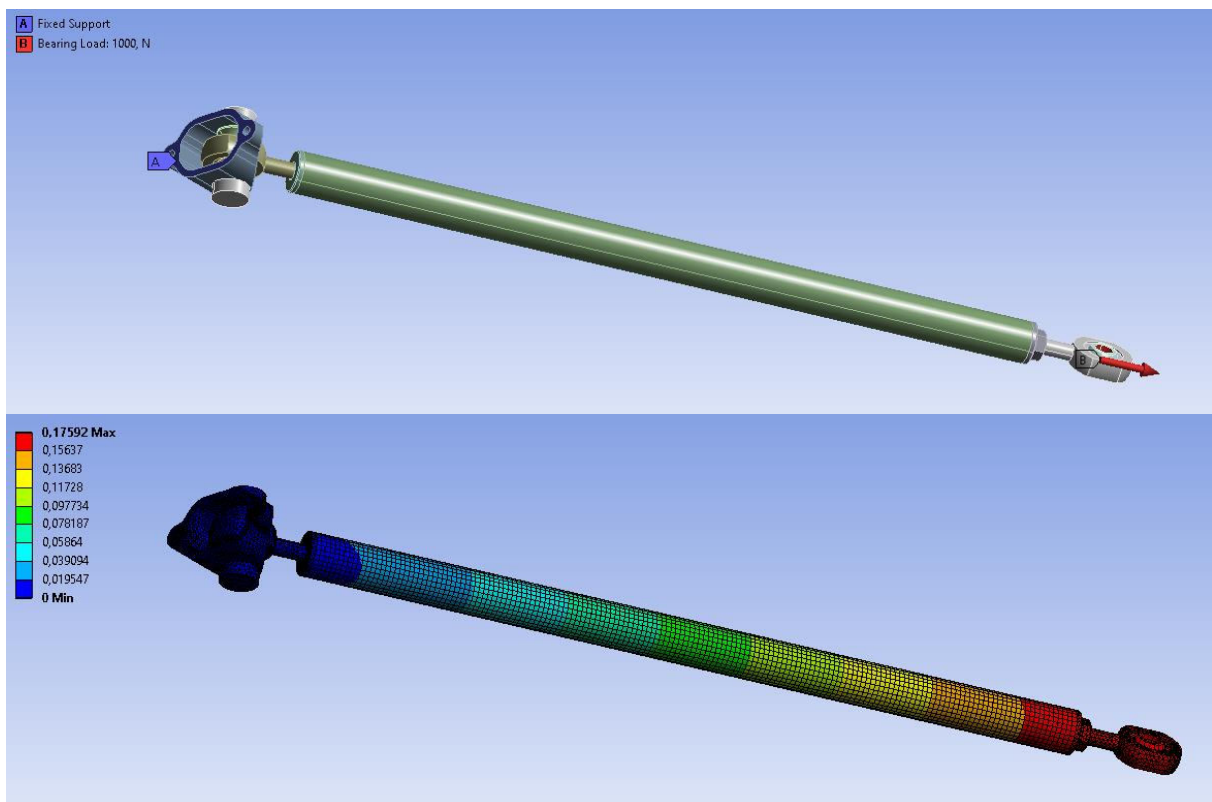


*Figure 97 Tension analysis of rear tie rod using FEM.  
Boundary conditions (upper) and total deformation (lower).*

As seen in Figure 100, a basic FEM analyses are conducted, including the holders. Other suspension link FEM analyses are shown in Attachment II. Cylindrical support was used in some cases to limit the deformation to translational only, although this is not strictly correct, it is sufficient for this usage.

*Table 39 Normal stiffnesses of suspension links from FEM*

	Rear tie rod	Upper wishbone link	Lower wishbone link	Front tie rod
Normal force [N]	1000			
Deformation [mm]	0.17592	0.12833	0.07559	0.07154
Stiffness [N/mm]	5684.402	7792.410	13229.613	13978.780

In Table 39 are calculated stiffnesses according to the FEM results. The front tie rod shows the highest stiffness, which does not seem realistic. The front tie rod has the same diameter as rear tie rod and is attached to the steering rack, thus is expected to have equal or lower stiffness than the rear tie rod. Consequently, the rear tie rod stiffness from FEM is applied for the front tie rod. Then the stiffnesses correspond to expectations and dimensions, tie rod being most flexible, and lower wishbones being the stiffest.

For these analyses, hub compliance is activated and the rotational stiffnesses are obtained from FEM as well. In hub compliance, all the translational stiffnesses are zero, because the spherical joint takes care of the translational degrees of freedom, only the rotational stiffnesses around the vehicle's X and Z axes have a certain flexibility, according to the FEM. In Attachment III are shown FEM analyses of the wheel assembly which are used for hub compliance estimation.

*Table 40 Hub compliance stiffness calculation from FEM (Attachment III)*

	Force [N]	Moment [Nm]	Deformation			Camber/toe stiffness [Nm/deg]
			Rim lower/front [mm]	Rim upper/rear [mm]	Camber/toe angle [deg]	
Fy	100	22.5	0.0360	-0.0289	0.0104	2173.529
Mz		0.1	0.0002733	-0.0003566	0.0001	995.550

The camber (toe) angle in Table 40 is calculated as:

$$\text{Camber angle} = \tan^{-1}\left(\frac{\text{Rim lower} - \text{Rim upper}}{\text{Rim diameter}}\right) \quad (39)$$

Rim diameter is 359,3 mm.

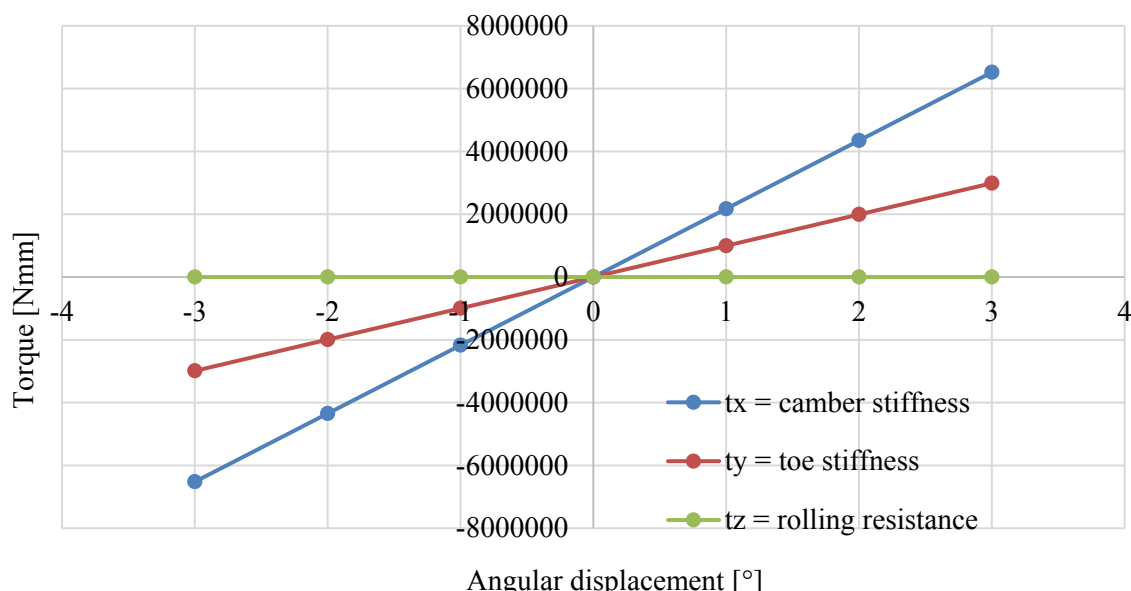


*Figure 98 Hub compliance rotational stiffnesses according to FEM analyses*

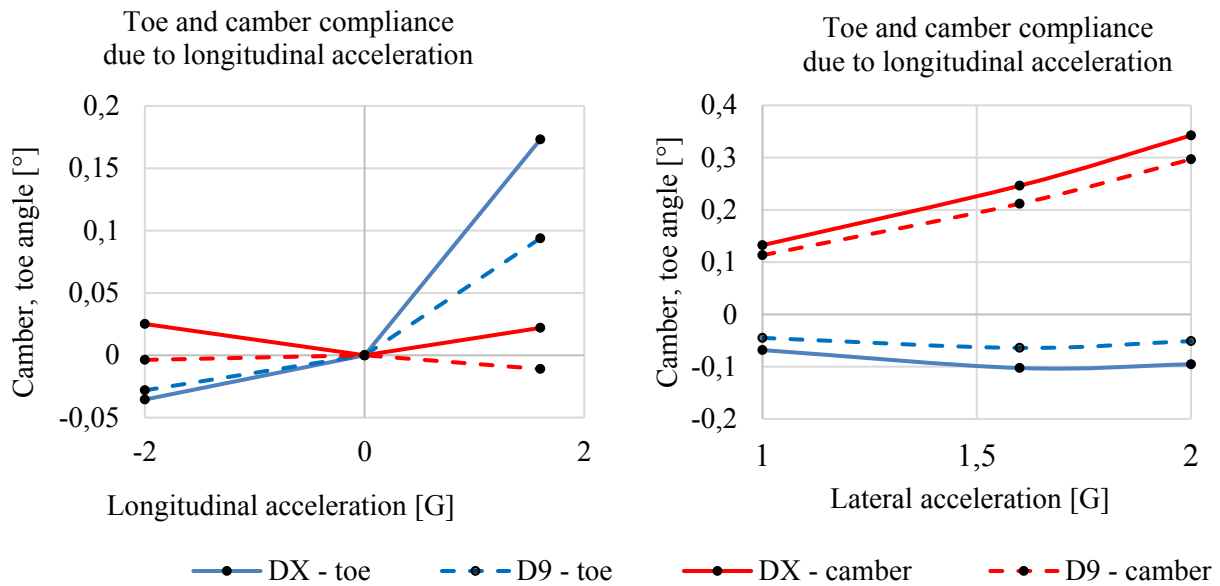


Figure 99 Results of compliance analyses in Adams with stiffnesses according to FEM analyses.  
Toe-out is a negative toe angle.

As the bushings have linear stiffness rates, the compliances are also linear if they are decomposed to each  $F_y$ ,  $F_x$  and  $M_z$ . Then normalized compliance can be estimated, see Table 41. Here is seen a large increase in suspension compliances. The values of camber angle compliance seem to be small when the effect of the camber angle on the  $F_y - \alpha$  is considered, although the values are presumed to be larger in reality. Concerning camber angle compliance in braking, there is a large increase of 678 % in the direction of positive camber angle, but the braking forces at the rear are small and the decrease of negative camber would improve the longitudinal force transition. However, in combined braking and cornering, this loss of camber would be undesirable. Similarly, camber loss due to  $M_z$  is high in percentage, but the actual values are very negligible.

Table 41 Normalized compliances and percentage comparison,  
bushing stiffnesses used from FEM analyses

	DX				D9	
	Toe		Camber		Toe	Camber
	Compliance [°/kN], [°/100 Nm]	Percentage of D9 [%]	Compliance [°/kN], [°/100 Nm]	Percentage of D9 [%]	Compliance [°/kN], [°/100 Nm]	Compliance [°/kN], [°/100 Nm]
F <sub>x</sub> braking	-0.062	<b>126.335</b>	0.044	<b>-678.378</b>	-0.049	-0.006
F <sub>x</sub> traction	0.118	<b>184.542</b>	0.015	<b>-200</b>	0.064	-0.007
F <sub>y</sub>	-0.041	<b>200.269</b>	0.166	<b>115.241</b>	-0.02	0.144
M <sub>z</sub>	-0.1807	<b>-124.4118</b>	0.0073	<b>-425</b>	-0.1452	-0.0017

Toe compliance is considered to be the most problematic, because of the slip angle influence on the lateral force.

It is clear from the simulation results, that hub compliance only offsets the total compliance value, but does not change the differences between the designs. The hub compliance will be important, for the measured data and simulation to be unified.

### 3.3 NEW REAR TIE ROD POSITION DESIGN

Because of the large increase of toe compliance, improvement is sought after. The wishbones are partially in an overhang, which is due to the shortened chassis, this causes an increase of forces in the wishbones and could be improved only, by going back to the previous design of Dragon 9. But in case of tie rod, there are still degrees of freedom in terms of its position, while the concept remains.

In the design phase of rear wheel geometry, a mistake was made by mirroring the tie rod original position around the wheel center for the new position. This approach was based on ref. [10], but it was not known that according to the same literature, the position of tie rod on Dragon 9 was in an unrecommended position. Therefore, if it has been in the recommended region, the mirroring would probably not produce such bad results. Unfortunately, the recommended regions for placing the tie rod by the literature were misunderstood in the original design phase of Dragon X.

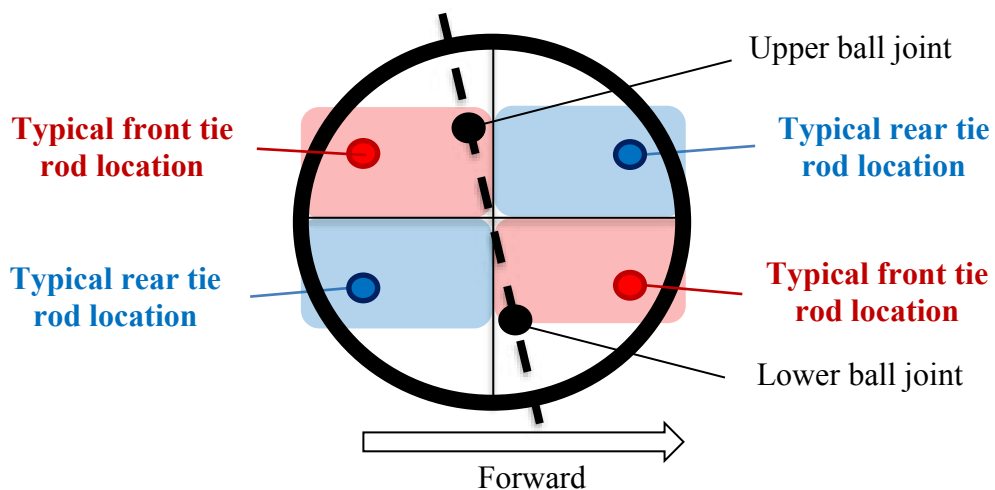


Figure 100 Typical (recommended) tie rod locations according to ref. [10]

From the animations of compliant simulations in Adams, the reason why this layout is recommended became obvious. In cornering at the outer wheel, the lateral force is acting on the lower ball joint, compressing the lower wishbone, while the upper wishbone is in tension (See Table 33). If the Mz and Fy are separated, in kinematic mode, the tie rod load coming from Fy is caused by mechanical trail, that creates an Mz moment of the wheel. The mechanical trail on the formula student car is small, thus the main load of the tie rod is due to the tire's Mz. In the

compliant mode, the load on the tie rod increases, as some load from the wishbone is transferred to the tie rod. But the stiffness differences of lower (or upper) wishbone and tie rod are much lower than the load differences. Therefore, with the suspension link's stiffness distributed as displayed above, the wishbones are deflecting much more than the tie rod. At the rear axle the mechanical trail is zero, if  $M_z$  of the tire is neglected and only  $F_y$  is applied at the tire, tie rod is loaded very negligibly, while wishbones deflect. Therefore the tie rod outer ball joint acts as a pivot around which the wheel rotates. Upper wishbone is in tension and lower in compression, thus the upper ball joint will deflect to the outside and lower ball joint will deflect to the inside. Depending on the vertical position of the tie rod, which is the “pivot point”, the wheel will deflect either toe-in or toe-out. If the tie rod will be high, the main influence will come from the upper ball joint and vice versa for the lower position. Therefore, with the current position of tie rod (which is outside of the recommended region – before the wishbone joints and lower), the lower ball joint will have the main influence on the direction of toe compliance and will cause toe-out. If the tie rod would be placed behind the wishbone outboard joints, remaining the vertical coordinates, toe-in compliant behavior under the  $F_y$  load would be obtained. To obtain stable compliant behavior in cornering, rear toe-in and front toe-out compliance is sought after.

These observations for steady-state **cornering** situations, concerning **toe** compliance, are made based on the compliant simulations:

- Tie rod is loaded by the  $M_z$ 
  - $M_z$  of the wheel consists of the tire's  $M_z$  and  $F_y$  acting on the mechanical trail arm
  - Large tie rod base decreases the tie rod load and thus toe compliance due to  $M_z$
- $F_y$  mainly loads the wishbones
  - Compliance due to lateral force comes mainly from the deflection of wishbones around the tie rod outboard joint
    - Lower wishbone arm deflects more
      - If the tie rod is placed lower, the toe compliance will be higher than in the upper position
      - Depending on the fore-aft position of tie rod to the lower ball joint the compliance will have a toe-out or toe-in character
    - Upper wishbone arm deflects less
      - If the tie rod is placed higher, the toe compliance will be lower than in the lower position
      - Depending on the fore-aft position of tie rod to the upper ball joint the compliance will have a toe-out or toe-in character
  - There is a theoretical point on the steering axis that does not move
    - This is a vertical coordinate of the tie rod for the lowest toe compliance

- Large tie rod base will decrease the amount of toe compliance due to  $F_y$

To improve the compliant behavior of the rear wheel, the tie rod is moved upward, as it is the only possibility (the change is mainly based on  $F_y$ , the situation differs for  $F_x$ ).

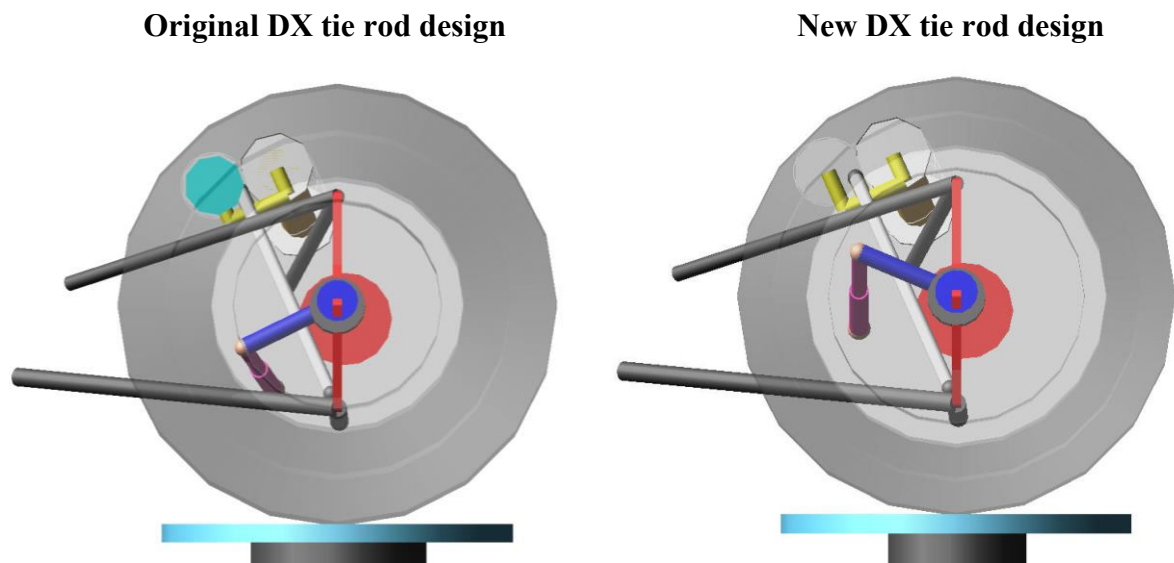


Figure 101 Comparison between the original and the new rear tie rod design

This kinematic change was made after the design freeze of the vehicle, including the design of rear uprights, but at least an insert for tie rod holder was implemented into the monocoque. Therefore, if the compliance will be problematic, either new upright or a flange to attach the new tie rod to the upright could be made. Otherwise, it can be used for the next vehicle design.

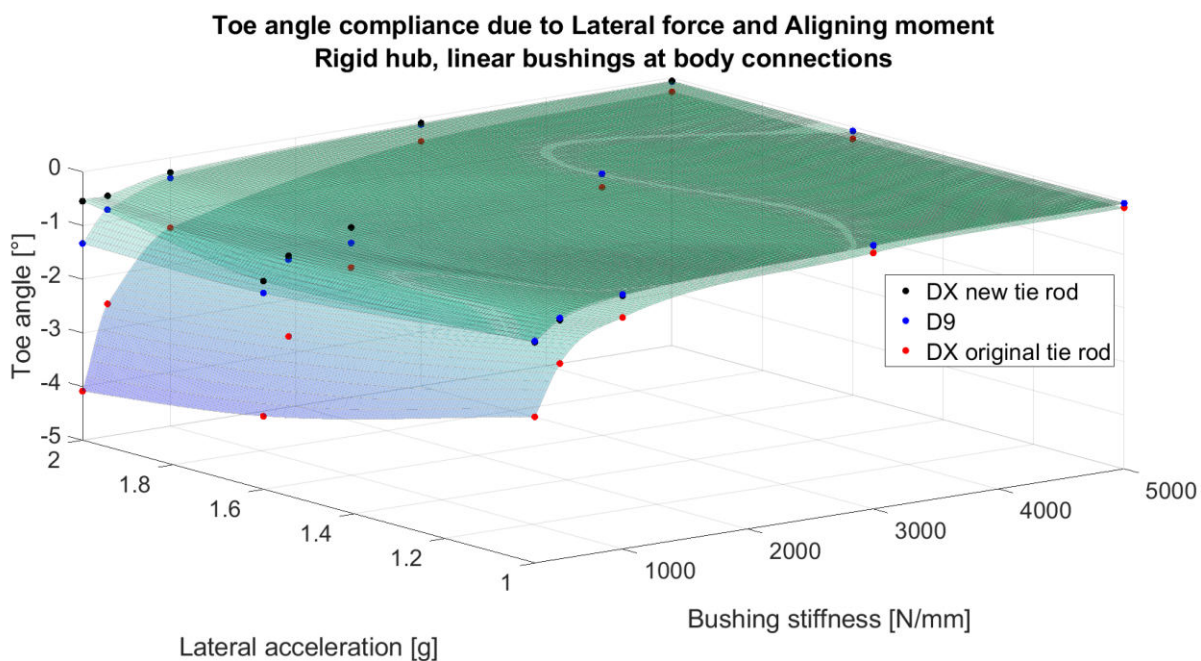


Figure 102 Comparison of rear toe compliance due to lateral acceleration for different designs.  
All bushings have equal stiffness, hub compliance is deactivated.

The new tie rod was designed to have minimal bump steer as well.

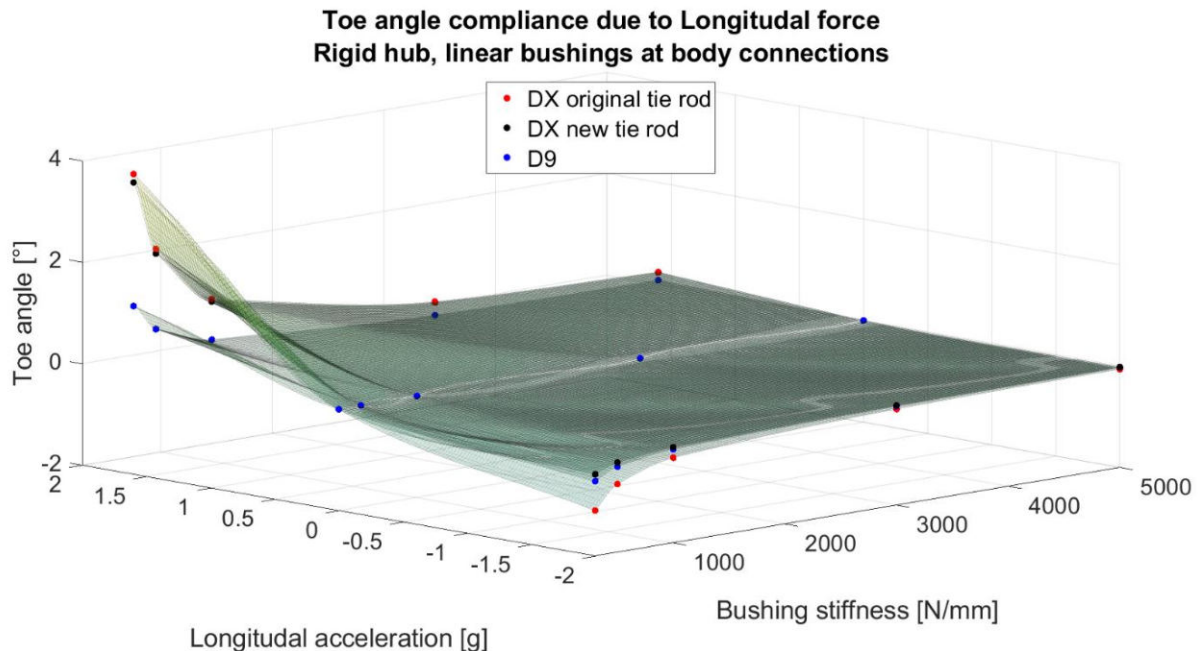


Figure 103 Comparison of rear toe compliance due to longitudinal acceleration for different designs.  
All bushings have equal stiffness, hub compliance is deactivated.

As seen in Figure 104, the change in tie rod vertical position has largely decreased the toe compliance due to lateral force and it is even lower than the D9 design.

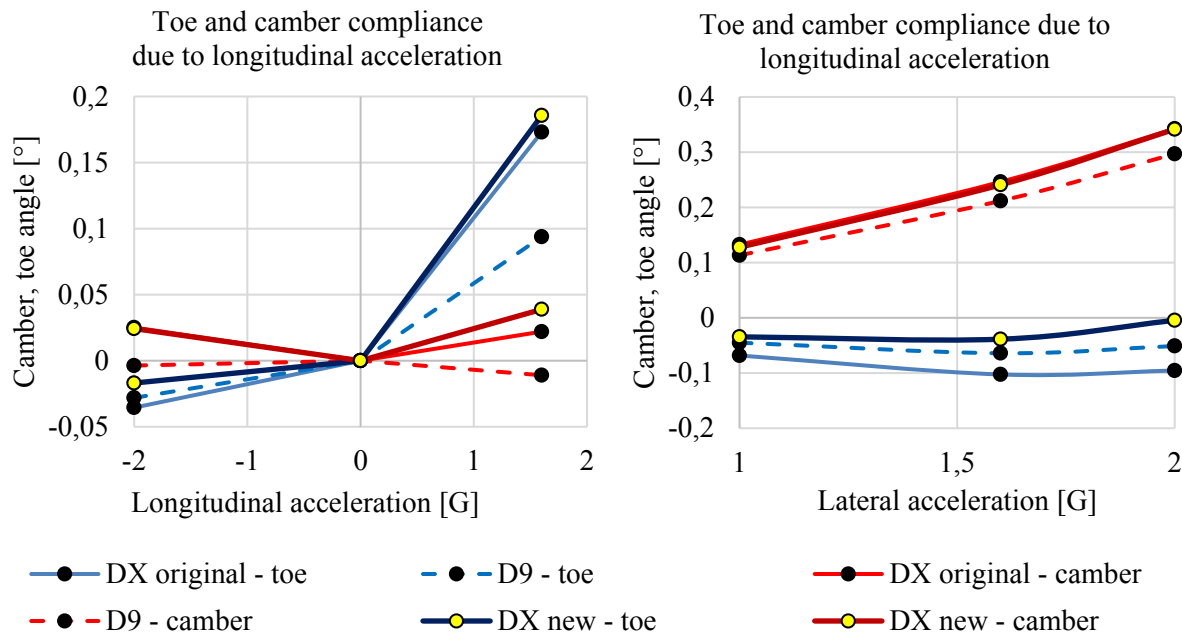


Figure 104 Comparison of rear suspension compliances for different designs with the bushing stiffnesses according to FEM analyses and with the hub compliance active

The reason for toe compliance is different under the longitudinal load, changing the longitudinal position of the inboard tie rod point could improve the compliance. Changing the lateral position of the outboard tie rod point could also make a difference.

The camber characteristics can be seen in Attachment IV, these have not improved, and in case of traction force, the camber compliance has even increased. Camber is mainly dependent on the wishbone layout but the tie rod placed lower is loaded more in comparison with the upper position. The more it is loaded by the lateral force, the more it helps to reduce the camber compliance.

*Table 42 Normalized compliances and percentage comparison of different designs. Results from Adams compliant analysis with FEM bushing stiffnesses.*

		DX original tie rod		D9		DX new tie rod	
		toe	camber	toe	camber	toe	camber
Values [°/kN], [°/100 Nm]	Fx braking	-0.0616	0.0436	-0.0488	-0.0064	-0.0293	0.0422
	Fx traction	0.1176	0.0149	0.0637	-0.0075	0.1262	0.0264
	Fy	-0.041	0.1661	-0.0205	0.1441	0.0032	0.1663
	Mz	-0.1807	0.0073	-0.1452	-0.0017	-0.1858	-0.0167
Percentage of D9 [%]	Fx braking	<b>126</b>	-678	100	100	<b>60</b>	-657
	Fx traction	185	-200	100	100	198	-354
	Fy	<b>200</b>	115	100	100	<b>-16</b>	115
	Mz	124	-425	100	100	128	975

As seen in Table 42, the toe compliance due to lateral force has decreased and even changed its direction. Rear toe compliance due to pure Fy will create toe-in, thus stable behavior.

With this new simulation tool, all the suspension links can be designed with respect to compliance, not only force distribution. Wishbones are dependent on several kinematic characteristics and are not easily changed if everything else is to remain, but tie rod can be changed quite easily. A DOE (design of experiments) in Adams Insight can be used to find the best position of the tie rod to obtain the desired toe compliances in all the load conditions.

### 3.4 DESIGN OF SUSPENSION COMPLIANCE MEASURING DEVICE

To obtain more accurate values of suspension compliances, they need to be measured on the car. A basic device to measure the effect of horizontal forces and the effect of aligning torque is designed. The idea is to mount this device on the rims and induce forces at the road distance. Another option was to design very stiff custom rim, which would be connected to the rods, but

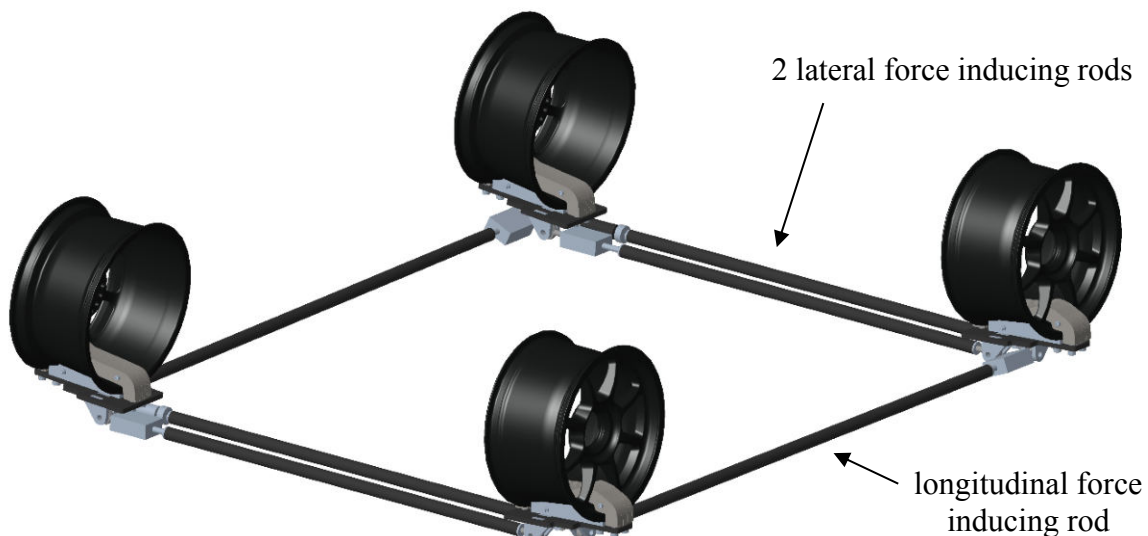


*Figure 105 The compliance measuring device*

the manufacturability would decrease in this case. The device consists of tubes, laser-cut plates, lathe milled small parts, fasteners, and 2 force transducers. Only lateral or longitudinal load case can be applied at a time.

As seen in Figure 107, the rods are connected with opposite threads, therefore the force will be induced by shortening (or prolonging) the length of the rod, while the induced force will be measured by the force transducers. Two lateral rods are present to induce the aligning torque.

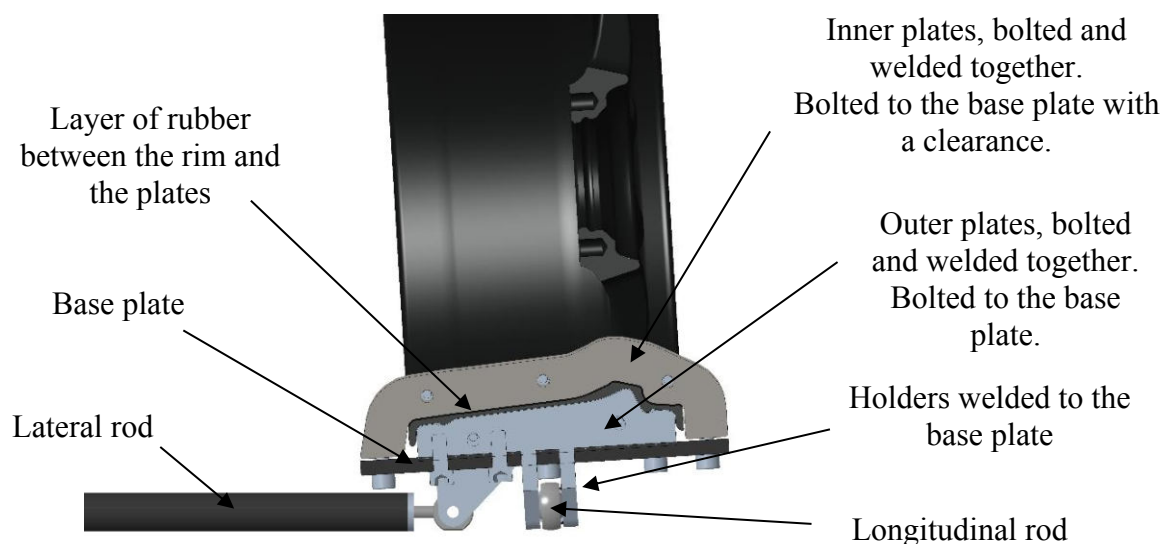


*Figure 106 Mounting of the compliant measuring device to the rim viewed in section*

The car will be lifted, lying on the bottom side of the monocoque. Dampers will be replaced by solid damper replacements.

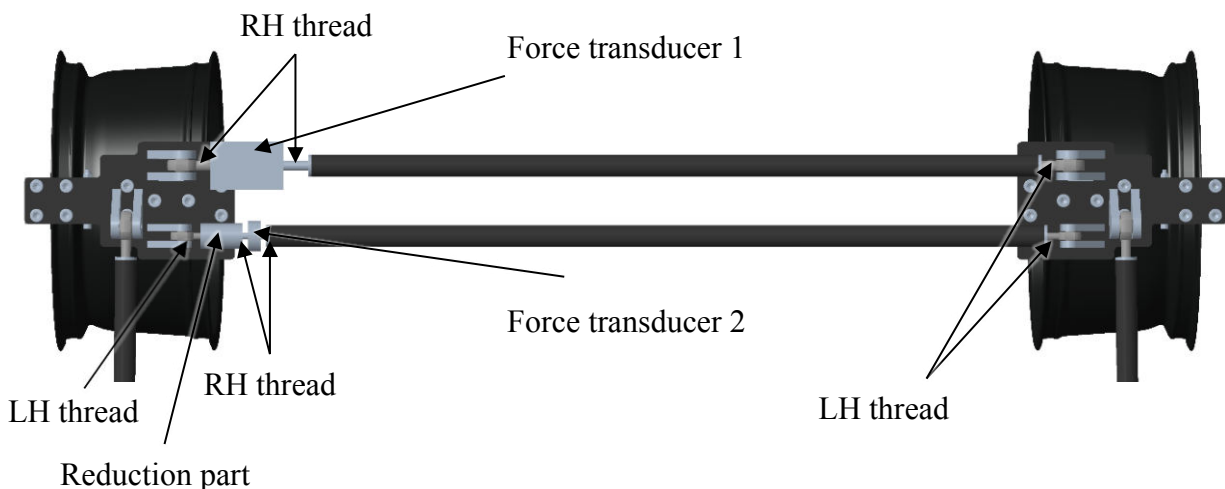


*Figure 107 Bottom view of the measuring device*

For the measurement of the toe angle and camber angle, line-lasers will be used. These lasers will be mounted on a toe angle setup device, which is regularly used to set the static toe angle. These devices are mounted to the wheel hub. The lasers will point in the longitudinal direction and project a vertical plane. In an exact distance from the laser, two rods will be placed. Both rods will be parallel to the lateral axis of the vehicle, one will be placed on the ground and the second one in a certain vertical height. On these rods, lines will be marked and then measured.

- Difference between the upper and lower rod mark shows camber angle
- Lateral displacement of the marks on both rods shows toe angle

The actual toe and camber angle is then calculated using goniometric functions. Change of the track will not be recorded. Another approach is to use at least 3 dial indicators on the rim, each will measure the lateral displacement of the point on the rim. Then the absolute position of the rim can be reconstructed, including the lateral translation. The actual measurement is not part of this thesis.

When the toe and camber compliances are measured, a unification between the measurement and simulation is sought after. For this, the Design of Experiments can be used in Adams, while the scaling factors of the bushings will be promoted to Inclusions of Factors. Adams will execute several simulations, with different bushing stiffnesses (each individual). Then a combination of bushing stiffnesses that matches the actual measured values will be chosen.

This measuring device can be also used for a control measurement of the forces under the tire, which will be recalculated from the strain gauge signals in wishbones, this is a master's thesis project of colleague Pavel Gellner.

Another source of instability or control loss might be caused by free play which is surely present on the car in each suspension connection. Fitted bolts are used to minimize the free play but bearings have certain play as well, this free play increases in mileage and when summed in the whole system, it could be non-negligible (or even significant). To measure the free-play, short length potentiometers could be mounted between the wishbone insert and the chassis to monitor

the free-play during racing, although vibrations from the engine could be problematic. The aforementioned measuring device will not monitor free plays, as the suspension will be preloaded by the weight of the measuring device itself.

This device will measure the total toe and camber compliances, another approach is to measure each link in the same way as simulated using the FEM analyses (including holders). A sweep of load from tension to compression would be ideal to obtain the nonlinear Force - deflection characteristic of each link. These characteristics can be then easily implemented into the Adams model.

## 4 EFFECT OF KINEMATIC DESIGN CHANGES ON VEHICLE DYNAMICS

Some effects of the design changes were already discussed, here is a summary of the design changes and their influence on the vehicle dynamics:

- Lower steering forces in braking-in-turn state
  - Have positive effect on the “control” of the driver
    - In terms of force needed for a turn
  - Have a positive effect on the driver’s stamina during a race
  - This effect will be quantified by the subjective rating of the driver during testing and objective measurement of the steering rod forces by strain gauges
- Higher steering camber change should utilize the usage of the tire and provide more lateral acceleration
  - The usage of the tire will be measured by infrared sensors during testing
  - Tire model can be used to quantify the impact, but due to a vast tire model inaccuracy, the result is mainly informative
- Lower mass
  - Provides more translational acceleration with the same total acting force, according to Newton’s Second Law of Motion
  - Decreases the load transfer
    - Increases the coefficient of friction
- Lower yawing moment of inertia
  - Provides more yawing acceleration with the same total acting yaw moment, according to Newton’s Second Law of Motion
    - More yawing acceleration of the car decreases the time needed for the rear slip angle to be created and thus decreases the time for the maximal lateral force to be produced
- Compliances will influence the control and stability of the vehicle
  - The steady state characteristics will be discussed later in this chapter, but compliances can have large effect (if not much larger) on transient states.
    - For instance yaw acceleration will probably be reduced due to compliance

This year, the full vehicle model in Adams was assembled, it provides new opportunities for vehicle dynamic simulations. The skidpad event can be tested directly in the constant radius cornering simulation, acceleration event can be simulated as well. The opportunities are almost endless, even the whole track can be simulated.

In this chapter, the Force-Moment Method is chosen to monitor the influences of chosen parameters.

#### 4.1 FULL VEHICLE MODEL IN ADAMS

It has been a team effort to produce a usable full vehicle model, but there are still many features to be improved. For instance, the differential and engine parameters do not precisely match the real values. To have a model which corresponds with the reality, the tires need to be measured directly on the car while driving. The tire model which is used in the Adams model is a Flat Track tire model, only basically scaled to obtain a reasonable coefficient of friction. Series of tests with identical boundary conditions as in the simulations can be made to validate the model.

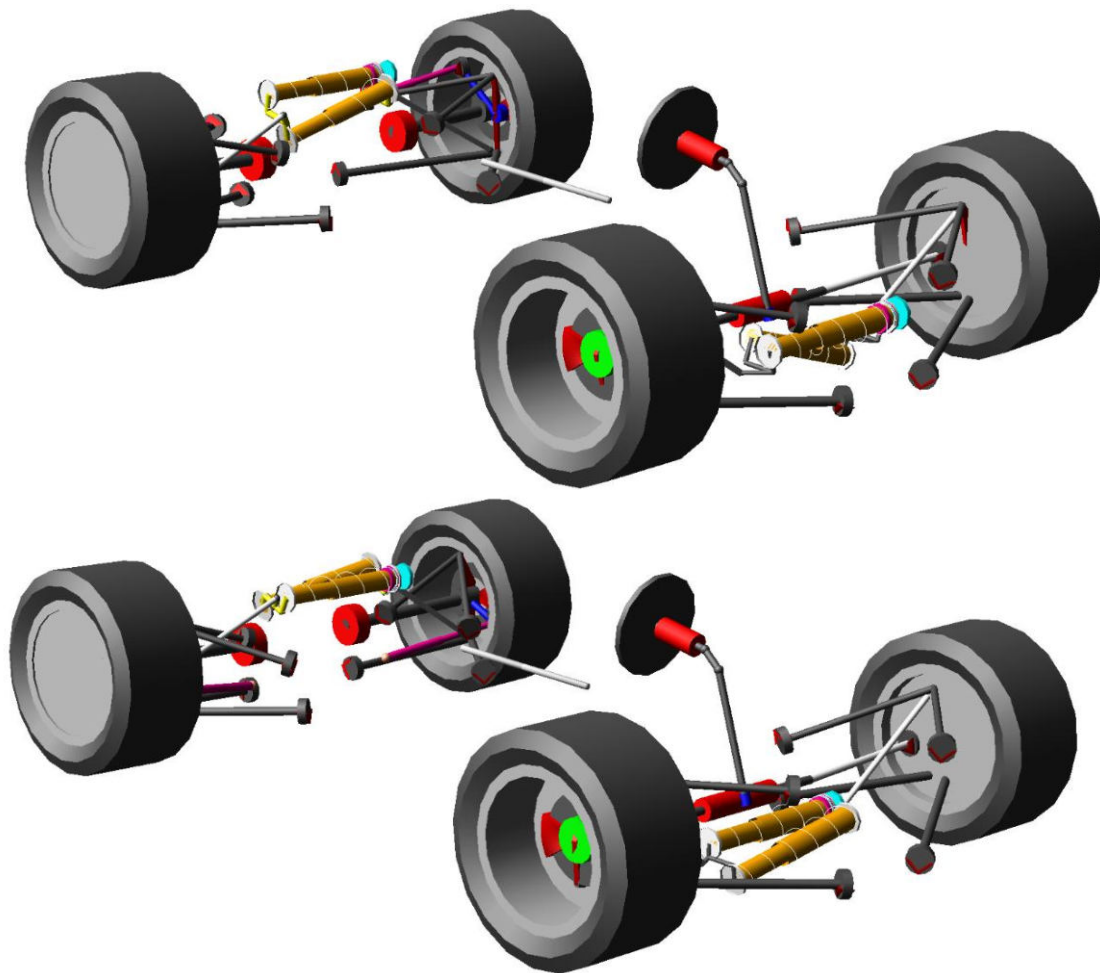


*Figure 108 Full vehicle model of Dragon 9 (upper) and Dragon X (lower) in Adams Car*

As part of this thesis, as already mentioned:

- Dragon 9 full vehicle model was made from the Dragon X model, including the spring and bump stop characteristics, see Figure 111.
- Compliance bushings were added to the front axle as well.
- Aerodynamic forces were added to the chassis subsystem

### IMPLEMENTATION OF RIDE HEIGHT DEPENDENT AERODYNAMIC FORCES

As the roll or yaw aero maps are not available at the moment, the aerodynamic forces were modeled according to the Matlab vertical model. The aerodynamic load is divided into 3 components:

- Downforce at the front axle
- Downforce at the rear axle
- Drag force acting on the ground

The drag induced moment  $M_d$  is included in the two downforces.

Each force is represented as point-force acting on the chassis subsystem.

$$F_{Aero} = \frac{1}{2} \cdot \rho \cdot A \cdot C \cdot v^2 \cdot ucf \cdot scale \quad (40)$$

Where  $F_{Aero}$  is the aerodynamic point-force,  $\rho$  is air density represented as a parameter variable and is constant,  $A$  is the frontal area,  $C$  is the corresponding aerodynamic coefficient, both  $A$  and  $C$  are ride height dependent, they are inserted to the model as Data Element 3D splines (surfaces), where  $X$  is the front ride height,  $Z$  is the rear ride height and  $Y$  is the parameter. The  $v$  is the longitudinal velocity, which is a built-in System Element. The  $ucf$  is a built-in variable that only controls the units of the force and  $scale$  is a parameter variable used for easy scaling of the aerodynamic forces.

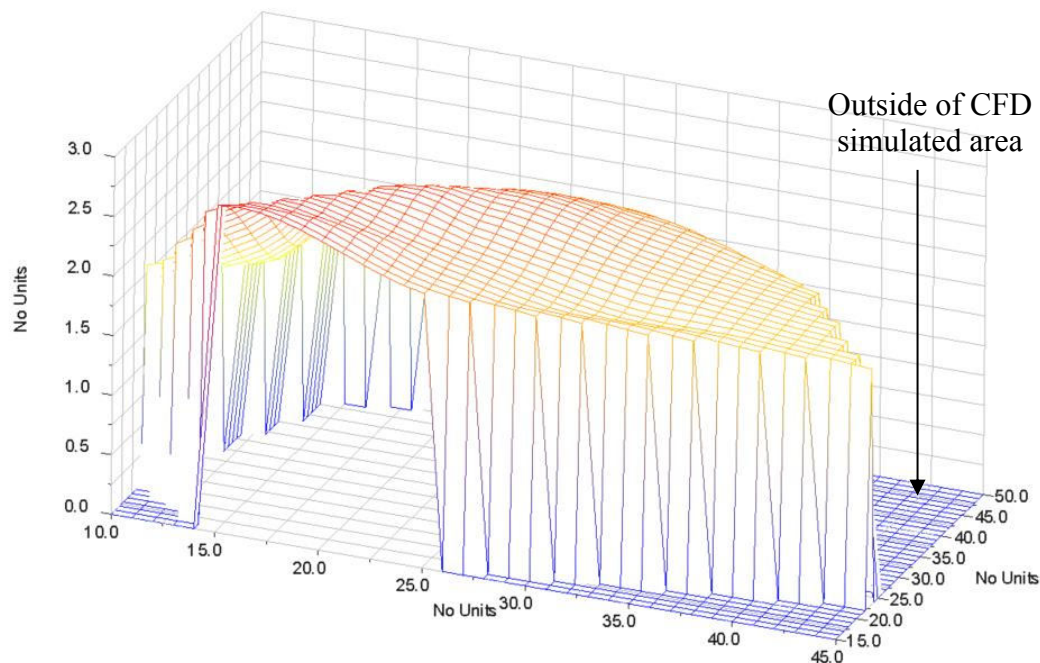


Figure 109 3D spline of rear downforce coefficient



The ride height measurements are System Elements that measure the distance between the “ground.origo” marker and a new hardpoint, which is created in the height of 35 mm above ground (modeling position), at the longitudinal coordinate of each axle and in the middle plane. The helper spring pretension calculation ensures that the modeling position is equal to the static position. In the static equilibrium simulation is done a double-check, to ensure that in the static position, the ride height measurement equals approximately 35 mm.

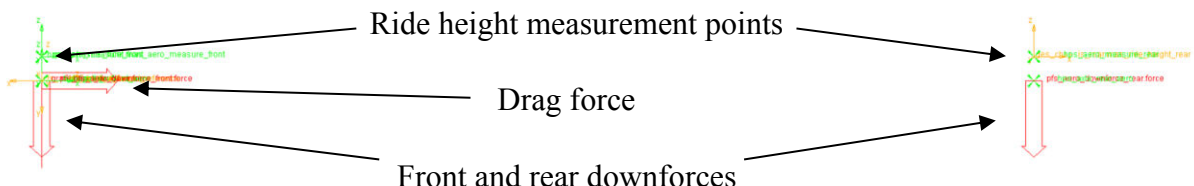


Figure 110 Custom ride height dependent aerodynamic forces in Adams

There is a built-in feature for aerodynamic forces and moments, but this approach was chosen to correspond with the Matlab vertical model.

Several simulations were conducted to double-check the resulting aerodynamic forces in the Maintain Straight-line event simulation.

## 4.2 FORCE-MOMENT DIAGRAM (YAW MOMENT DIAGRAM)

Force-Moment Method was chosen to monitor several vehicle dynamic characteristics of the car. In previous years, a Matlab script to calculate the Force-moment diagram was done, while the kinematic parameters were imported from Adams. In Adams, using the Force-Moment analysis, the whole vehicle, including all the kinematics and dynamics can be simulated without the need to export all the characteristics individually. Also, it can be used for a control of the Matlab manual calculations.

The compliance effect is also easily included and different layout of the suspension links can be studied, including its effect on control and stability. Compliance can be implemented to the Matlab script as individual normalized compliance in  $\%kN$  or  $\%Nm$  as shown previously.

The drawback of creating a Force-moment diagram from Adams is that the path is straight, thus the path radius is infinite and so the lateral force is not utilized (“unassigned”). Longitudinal force is zero, except for the aerodynamic drag. This form of Force-moment diagram is the most basic one. [10]

With infinite path radius, the yaw velocity is zero and so is the *yaw damping moment*, which is a great contributor to *control* and *stability*. Therefore, the *stability* measured in this simulation is only the *directional stability moment* which corresponds to the *understeer gradient*, it is the minimal *directional stability* of the vehicle. In a real corner, the stability will be always larger because of the *yaw damping moment*. [10]

Similarly, the *static control moment* measured in this simulation is the maximal possible, as it is not reduced by *yaw damping moment*.

These parameters can still be used for comparison of different parameters and different designs. The maximal lateral acceleration (limit) and the yawing moment at the limit should not be affected by the path curvature as they are determined by the limit lateral forces and aligning moments of the tires.

To be able to compare the influence of mass and wheelbase, the normalized version of the Force-moment diagram  $C_N$ - $A_Y$  is chosen. Although, because of neglected yaw damping moment, there will be no difference in the diagram caused by different wheelbases, while the weight distribution remains. This diagram is for constant velocity.

$$C_N = \frac{N}{W \cdot L} \quad (41)$$

$$A_Y = \frac{Y}{W} \quad (42)$$

Where  $C_N$  is the normalized yawing moment,  $N$  is the yawing moment,  $W$  is weight,  $L$  is the wheelbase,  $A_Y$  is the lateral acceleration and  $Y$  is lateral force. [10]

$$\text{Stability moment} = \frac{\partial N}{\partial \beta} \cdot \beta \quad (43)$$

Where  $\beta$  is the chassis side slip angle, for static stability  $\beta = 1^\circ$ . The static stability is the slope of the  $\delta = \text{const.}$  curve in the  $C_N = 0$  and  $A_Y = 0$ . Stability has a negative sign for stable vehicle behavior. [10]

$$\text{Control moment} = \frac{\partial N}{\partial \delta} \cdot \delta \quad (44)$$

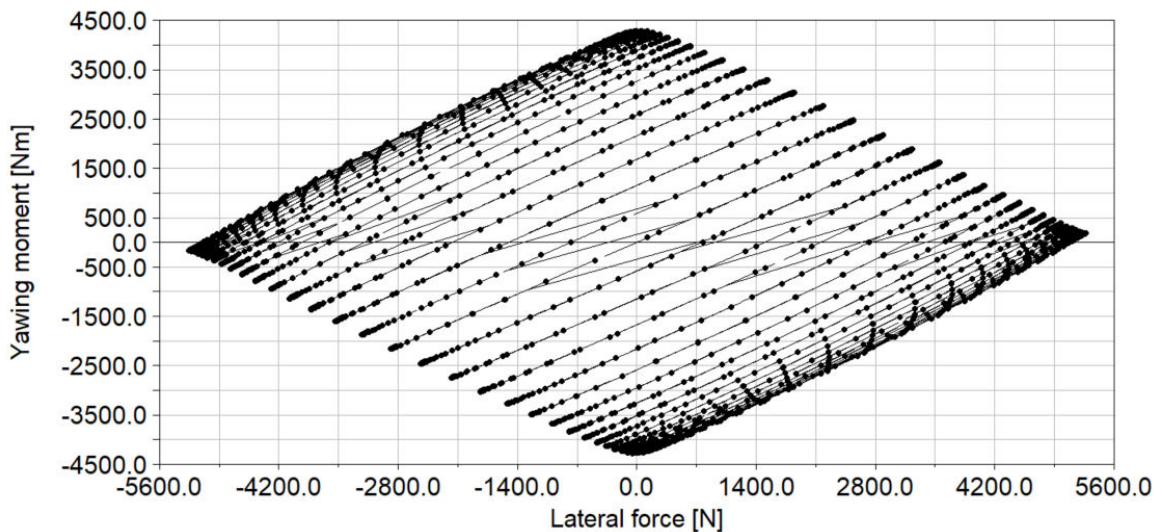


Figure 111 Force-moment diagram in Adams



Where  $\delta$  is the front wheel steer angle, for static control  $\delta = 1^\circ$ . The static control is the slope of the  $\beta = \text{const.}$  curve in the  $C_N = 0$  and  $A_Y = 0$ . [10]

Adams performs the simulation by sweeping a range of  $\delta$ s for a constant  $\beta$  as shown in Figure 111. To obtain the standard Force-moment diagram, curves of  $\delta = \text{const.}$  are needed, thus post-processing is required.

Side slip angle  $\beta$ , steering wheel angle  $\delta_{SW}$ , Yawing moment  $N$  and Lateral force  $Y$  are exported from Adams to Matlab. To obtain the steering angle of the wheel, a mean ratio of steering wheel angle to the wheel steer angle  $\delta_{SW}/\delta$  is obtained from Adams. The yawing moment and lateral force are then distributed to matrices, where each row contains constant  $\beta$  values and each column contains constant  $\delta$  values. To calculate the stability and control, derivatives of the yawing moment matrix is conducted. Stability matrix is obtained by derivating each column of the yawing moment matrix. Control is the derivation of each row of the yawing moment matrix. To plot the  $\delta$  and  $\beta$  curves, all available data is included, matrices for  $\delta$  and  $\beta$  curves are created, each column represents constant  $\delta$  ( $\beta$ ).

The steady-state acceleration limit is obtained by finding the maximal acceleration when the yawing moment is zero.

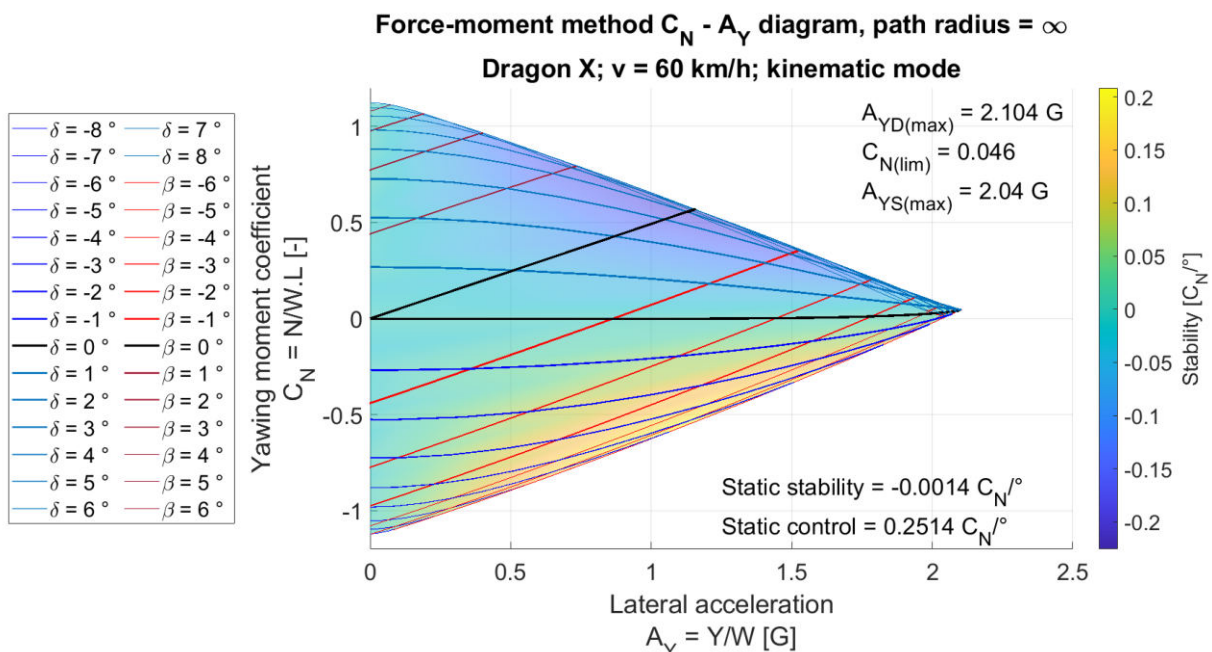


Figure 112  $C_N - A_Y$  diagram of Dragon X simulated in Adams, post-processed in Matlab.  $A_{YD(\max)}$  is limit dynamic  $A_Y$ ,  $A_{YS(\max)}$  is limit steady-state  $A_Y$ ,  $C_{N(\lim)}$  is residual  $C_N$  at the dynamic limit.

As seen in Figure 112, the diagram seems different than standard MMM diagrams, the  $\delta = 0^\circ$  curve is approximately horizontal, which would normally mean lack of stability, but in this case, where path radius is infinite, it only represents the understeer moment which is very near to zero (neutral vehicle).

The influence of mass and compliance on limit acceleration, stability and control is the main interest of these simulations. The default mass is 250 kg, the center of gravity height does not

change. Aerodynamic influence is also studied and the Dragon X vs Dragon 9 are compared as well. In Attachment I is shown enlarged Figure 112, in Attachment II is shown an extreme case of rear axle compliance and its influence on stability, in this case bushings of rear suspension links have equal stiffnesses of  $k = 300 \text{ N/mm}$  (extremely low).

### THE INFLUENCE OF MASS IN KINEMATIC AND COMPLIANT MODES

In Figure 113 is seen a comparison of limit characteristics for different masses and between kinematic and compliant modes. Data are based on Force-moment diagrams in Attachments VII and VIII, the bushing stiffnesses used in compliant mode are according to FEM analyses. It is clear, that the compliance does not influence the maximal achievable lateral acceleration, but it changes the limit under/oversteering characteristic. Since both front and rear tie rods are unfortunately positioned in unrecommended areas (see Chapter 4.3), compliance decreases stability and causes the vehicle to be more oversteering at the limit – thus the yawing moment coefficient is increased at the limit. The rear tie rod is in the original position, not in the new one.

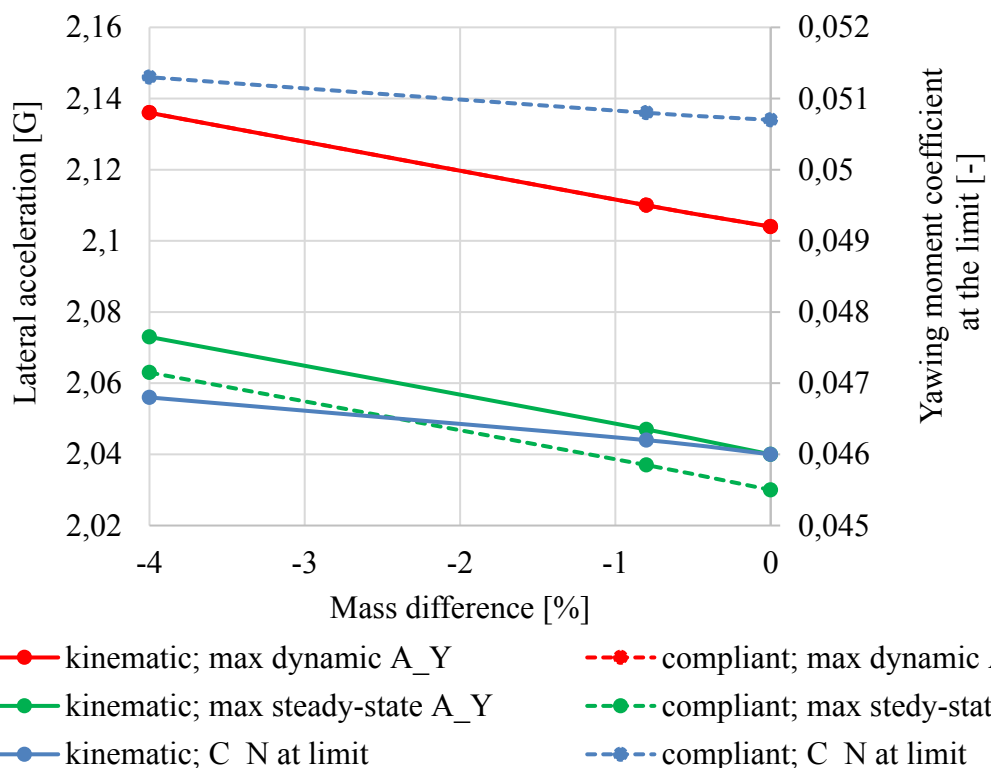


Figure 113 Comparison of limit behavior for different mass, in kinematic and compliant mode. Data based on Force-moment diagrams in Attachments VII and VIII.

In Figure 114 is visible the effect of compliance on stability and control, control decreases, which means that the front steer angle is decreased by the compliance, therefore this implies understeering front suspension compliant behavior in low lateral acceleration. Compliance



analyses of the front suspension should be made, but according to the observations based on compliant analyses of rear axle, front suspension is estimated to be oversteering under the lateral load (toe-in) – this is not verified and could be wrong. The aligning torque of the tire will always cause an understeering compliant behavior in the front (toe-out) and oversteering compliant behaviour in the rear (toe-in).

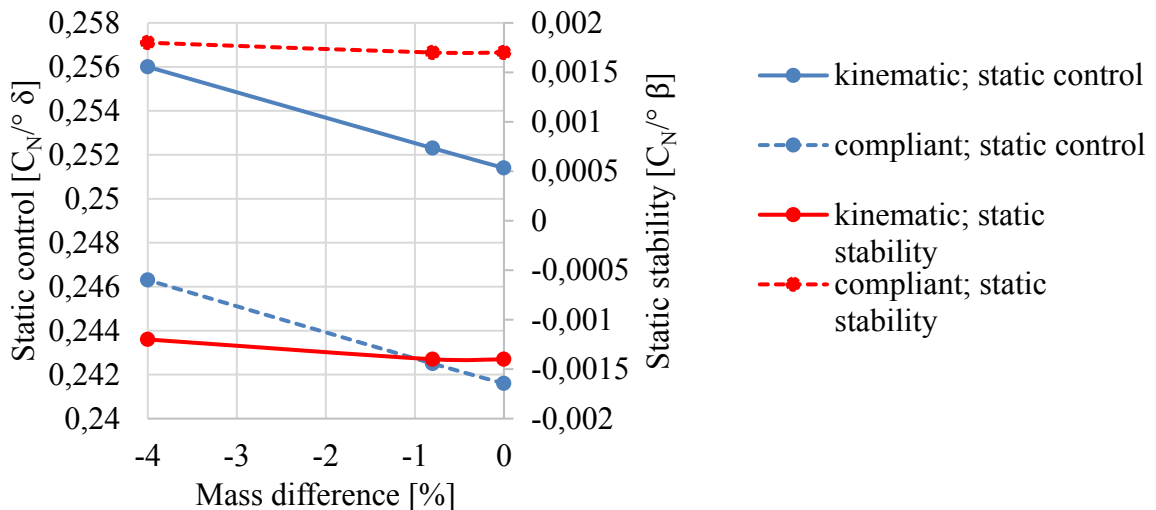


Figure 114 Comparison of static control and stability for different mass and between compliant and kinematic modes. Data based on Force-moment diagrams in Attachments VII and VIII.

### CHARACTERISTICS FOR DIFFERENT COMPLIANT MODES BETWEEN DRAGON X AND DRAGON 9

In Figure 115, it shows that Dragon 9 compliant behavior acts toward understeering at the limit. At the limit, dominant is the lateral force and aligning torque is low, therefore it appears that Dragon 9 has both front and rear axles deflecting toward understeering under pure lateral force, which is desirable. This (oversteering compliant behavior problem of Dragon X) can be solved by implementing the new tie rod position as discussed earlier, or designing the tie rod positions according to compliant simulations in the future. The Dragon 9 and Dragon X are different at the dynamic limit as well, although the mass and center of gravity were set to be equal. Even so, there could be slight difference either in the main parameters (mass) or also in the stiffnesses, roll center heights etc.. The reason for this offset is unknown, an opposite result was expected due to higher camber change in steering at the front.

In Figure 116 the static state is studied, therefore a low lateral load is applied and aligning torque of the tire probably prevails. This is observed from the behaviour between the modes 2 and 3, where front tire's M<sub>z</sub> creates an understeering moment. The poor Dragon X rear compliant behaviour (of the original design) is seen here as well. Control also decreases on Dragon X, which could mean also worse front compliant behaviour, mainly under M<sub>z</sub>, even though the steering arm length remained. Stability in kinematic mode is higher with the Dragon X.

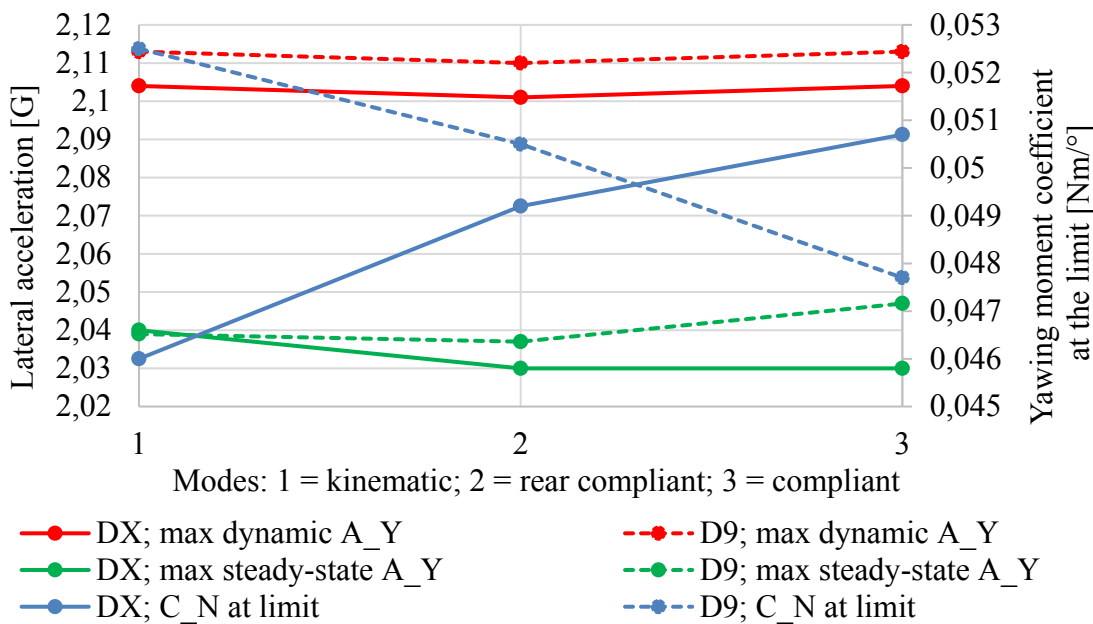


Figure 115 Comparison of limit characteristics between Dragon X and Dragon 9 in different compliant modes. Data based on Force-moment diagrams in Attachments IX and X.

A comparison between the Dragon X in compliant mode with reduced weight by 2 kg and Dragon 9 in compliant mode can be made to evaluate the advantage of the improved packaging which came with the loss of suspension stiffness. But the direct comparison of these two models is probably not objective, because in kinematic mode, the characteristics of the two cars are quite different. Therefore purely the effect of mass and compliance can not be estimated (or would be somewhat misleading). This is an issue of having too complicated model, for this

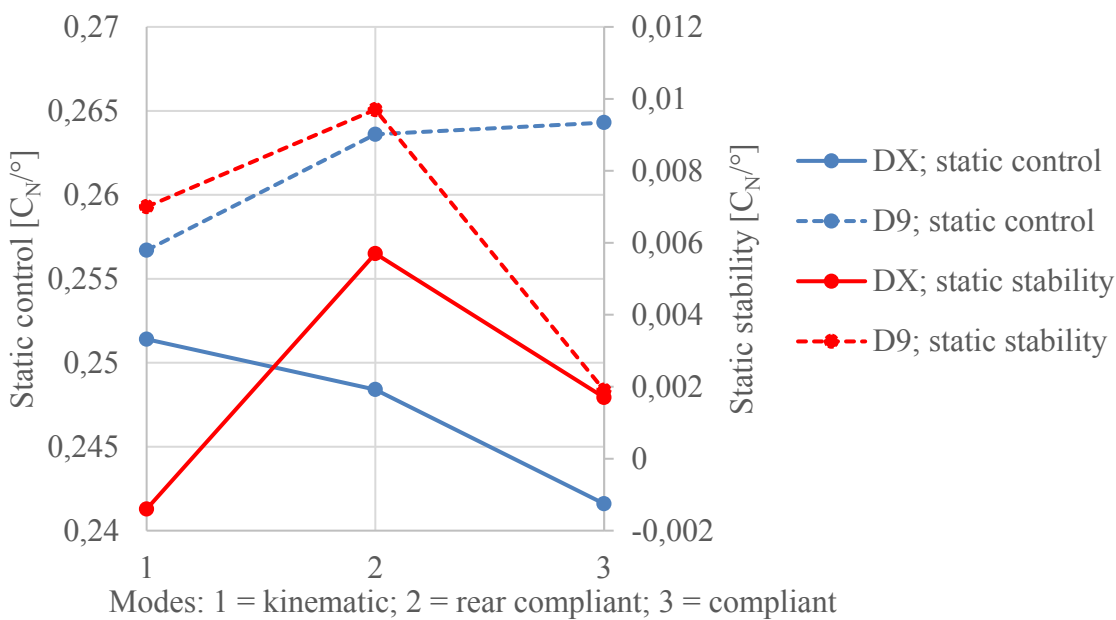


Figure 116 Comparison of static stability and control between Dragon X and Dragon 9 in different compliant modes. Data based on Force-moment diagrams in Attachments IX and X.

purpose, a calculated Force-moment diagram in Matlab would suit better. The Matlab diagram has been developed by other team members in previous years, but is not dealt with in this thesis. In Matlab, one can easily change one parameter only and see its direct influence.

Ultimately, the new vehicle design needs to be tested, data from on-track testing as well as the driver's feedback will be the very important factors in deciding, whether the concept is performing well or not. The real amount of compliance might also be very different than simulated, this could be obtained with the aforementioned compliance measuring device. The main issue of the concept is toe compliance which has been proven to be fixable by relocating the tie rod.

### INFLUENCE OF AERODYNAMICS

The influence of aerodynamic forces is displayed in Figure 117. As expected, maximal lateral accelerations are increased as well as stability and control. The limit behavior is shifting toward oversteering.

The influence of aerodynamics and mass can be normalized per 1 % of the difference, 1 % of total mass reduction improves the maximal dynamic acceleration by 0,008, while 1 % higher aerodynamic forces improve the maximal dynamic acceleration by 0,0046. Therefore, mass reduction is 1,74 times more efficient in the lateral acceleration gain.

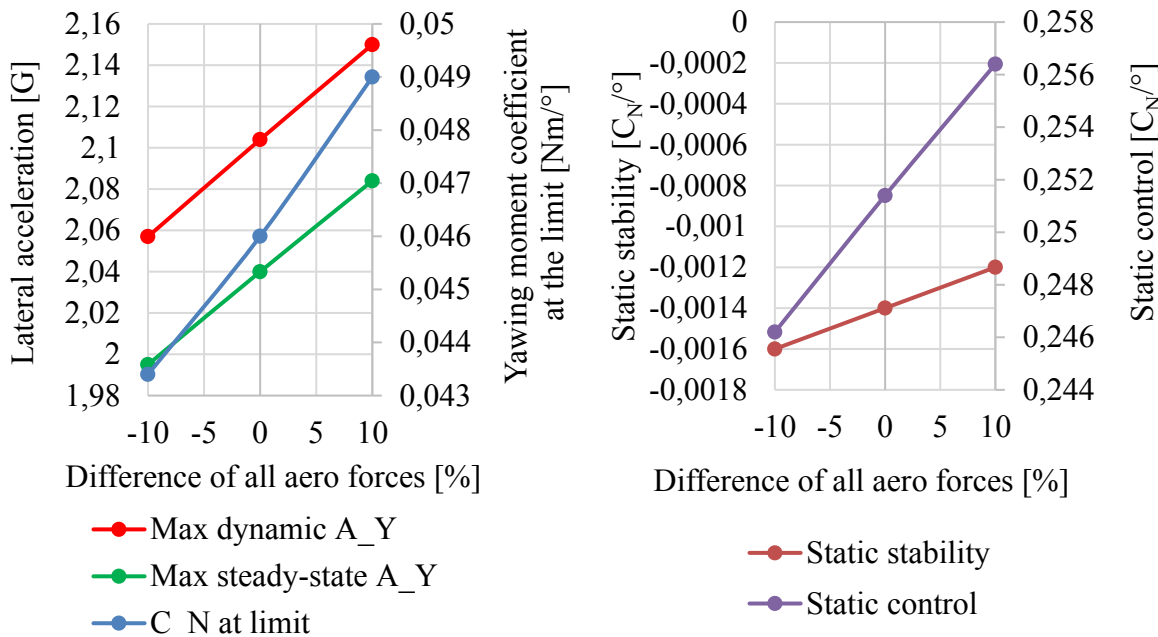


Figure 117 The influence of aerodynamic forces on vehicle dynamic characteristics of Dragon X. Data based on Force-moment diagrams in Attachment XI.

## CONCLUSION

This thesis covers the changes in the suspension kinematics and vehicle dynamics. The basis for these changes is discussed first, it concerns suspension and chassis packaging and tire analysis. As the main team goals are low mass, the center of gravity height, and yawing moment of inertia, the pursuit is to find possible ways to improve the suspension packaging. This is done by comparing the last year's design with previous cars and with the competition. In tire analysis comparison between the previous and new tires is conducted using measured on-track testing data and tire models. Data from tire temperature sensors are observed with a clear indication that a larger negative camber angle is needed on the front wheels, due to lower temperature on the inside by 3,3 °C on average and by up to almost 10 °C in peaks. The tire surface is also visually checked and it is in accordance with the measured temperature data. Tire models of the C18 and C19 Continental tires from Flat Track tire measurement are compared, a need for larger camber is seen here as well. Lastly, tire temperature data are compared between soft and stiff suspension setup, indicating overheating of the tires with too stiff suspension and therefore a need to use softer suspension rates.

Based on the tire overheating and suspension setups during competitions in the previous season, a reduction of installation ratio is conducted to improve the roll-heave suspension packaging and enable the reduction of front monocoque chassis. This installation reduction is enabled by increasing the spring rates and damping coefficients, while equivalent suspension rates and equivalent damping ratios remain. This reduction enabled the roll-heave system mass reduction which is in total (front and rear systems) 11,3 %. Apart from the installation ratio reduction, progressivity is designed to improve aerodynamic cooperation and damping.

Concerning camber change, related to the tire temperature analysis, study of wheel inclination angle during racing is conducted by combining the on-track data with Adams Car simulations. Based on this analysis, the caster angle is chosen to be changed to improve the camber change and thus utilization of the front tires. The amount of caster change is chosen based partially on experience from previous cars and the tire model analysis. The caster angle was changed from 2,94 ° to 6,35 °. The emphasis is on the outer wheel, in previous years it did not gain any negative camber in steering while the new design gains -1,45 ° in maximal steering angle.

Another change concerning front wheel geometry is conducted. A space for improvement is found in reducing the steering torque in braking-in-turn conditions which according to the driver's statement was the most strenuous state in terms of steering effort. The scrub radius is therefore changed to a negative value of -4,4 mm from last year's 15,4 mm. A calculation in Matlab is used for the steering torque calculation, the result from Matlab is a reduction of steering forces by 34,3 % in the event of combined -0,73 G longitudinal and 1,45 G lateral, which is a value obtained from data, while the steering angle is 0 °. Adams simulations are used for a control calculation of the steering torque. The tire reactions obtained from the load transfer and tire model are inputs to a simulation in Adams, and the result is a difference of 2,21 % maximum between the Adams calculation and Matlab (for a 0 ° steering wheel angle). The percentage value of reduction from Adams is 36,8 %. Maximal steering wheel angle situation is also considered in both Matlab and Adams simulations, but the difference was found to be larger, which pointed to a need to improve the Matlab calculation to be correct. Specifically, the kinematics of the front tie rod need to be included.

As the caster angle change also influences the steering wheel torque due to vertical load, simulations in Adams are conducted to monitor either the steering wheel torque but more

importantly the cross load transfer which unloads the rear inner wheel. The insufficient load of the rear inner tire was observed during a competition, as the limited-slip differential was locking undesirably often. Steering simulation with only front suspension assembly, but also with the full vehicle model on SPMM testrig are conducted. These results differ largely, but both show that the cross load transfer is reduced with the new design, which is mainly caused by the negative, and reduced scrub radius. A measurement of Dragon 9 cross load transfer is conducted on scales to obtain the real value. The differences between simulations and reality are probably caused by the fact that the chassis is fixed in the simulation, or by the compliance of the real vehicle. The steering-induced cross load transfer should decrease by 73 % according to the SPMM steering simulation and steering wheel torque caused by steering should be reduced by 55 %.

Suspension wishbone arms characteristics such as roll center height, anti-features, or camber change in heave remain unchanged, while vast changes in the wishbone layout are conducted. Front wishbones are changed only slightly to cooperate with aerodynamics and the new wheel geometry. Rear wishbone layout is changed completely, a compromise between weight and compliance is made, as the rear part of the chassis is vastly shortened. Because of the chassis reduction, a relocation and a change in rear roll-heave attachment had to be made as well as a completely new rear wheel geometry. The rear wheel geometry also cooperates with a new development project of four-wheel steering. The tie rod base remains. In the initial design, forces in all the suspension links are monitored and are the main limitation. Front wishbones are designed to be as wide as possible to reduce the braking-induced forces in the links. Rear inboard attachment points of the rear wishbones are designed to be as rearward as possible to reduce the forces in the links. Bump steer on both axles was minimized using the Design of Experiments in Adams Insight.

Due to kinematics, the packaging has improved and is estimated to save 7,9 % of the full monocoque weight, lower its center of gravity height by 1,8 % and reduce its yawing moment of inertia by 20,8 %. Furthermore, by the relocating of the rear roll-heave system, 19,7 % of the yawing moment of inertia is saved from the assembly of both front and rear roll-heave systems. In proportion to the total vehicle's weight including the driver (248,7 kg according to the CAD model), the kinematic changes should reduce the weight by 0,8 % and the yawing moment of inertia by 1,2 %.

The design process of kinematics is a large iterative circle which includes various calculations, simulations, and cooperation with the CAD model.

The thesis brings partially the design changes that will influence the vehicle's performance, but also contains a vast number of Matlab and Adams simulations, which are, as part of this thesis, improved. The most influential change is the introduction of the first functional full vehicle model in Adams, which was conducted together with colleague Jiří Miša.

As the installation ratios are changed, suspension rates and damping ratios are studied and also implemented to the Adams model. A simulation script of vertical dynamics in Matlab is vastly improved to be used as a tool for the Adams model improvement of spring non-linear characteristics, helper spring pretensions, and bump stop characteristics. Series of simulations and studies are conducted to obtain equal vertical characteristics between the Matlab and Adams model. The Matlab vertical model is extended by the damping ratio calculation and other dynamic characteristics. As the main interest of this thesis is the design change, always both Dragon 9 and Dragon X are simulated.

Concerning suspension rates, a Matlab script to automatically design an optimal coil spring with respect to stress calculation, dimensions, and weight is made.

During the front wheel geometry design, an improvement of the steering wheel torque Matlab calculation is conducted and checked with Adams simulations under equal conditions. Adams simulations and real measurement are made to monitor the cross load transfer. A completely new script to display wheel inclination angle during racing is made for the camber change analysis and design. This is a combination of on-track data, Adams suspension simulation, and Matlab post-processing.

For the analysis of forces in suspension links, new calculations of the wheel loads from tire model under braking, cornering, acceleration, and combination of these states are made. The load cases used for structural FEM analysis are revised. This includes both steady-state load cases and a dynamic wheel bump, which is remodeled entirely based on data from strain gauges in pull/pushrods. These inputs are then simulated in the vastly improved Adams model and should correspond better with reality.

In Adams, beside the first assembling of all subsystems in the full vehicle model, steering subsystem is improved to agree with reality (previously only rack displacement could be an input to a steering simulation), bump stops are added, non-linear heave spring characteristics are imported, and, most importantly, a compliant model of both axles has been implemented to the Adams by representing each suspension link with a bushing in the chassis joint. Also hub compliances were implemented and large number of simulations were conducted to monitor the suspension compliance. This is a completely new area, which has not been studied in the team before, it brings the possibility of designing the suspension links in the future not only concerning force distribution but the compliance as well. Tie rods can be placed in the most convenient position to give desirable compliant behavior. Even passive rear wheel steering (e.g. with specific link's stiffnesses), could be implemented based on a validated compliant model in Adams, in the future.

As these tools were not available in the initial design period, rear tie rod was placed in disadvantageous position, causing the rear toe compliance to increase. A new position of the tie rod was designed to give stable compliant behavior of the rear toe angle under the lateral force. The original design of the rear Dragon X tie rod caused 200 % worse toe-out compliance due to  $F_y$  than on Dragon 9, but only by placing the tie rod higher vertically, the compliance has decreased to -16 % of the Dragon 9 design (the new alternative design produces toe-in behavior).

These compliant simulations were conducted based on FEM analyses, to obtain real values, a suspension compliance measuring device was designed. This device can load the rims with longitudinal, lateral force and aligning torque.

To quantify the influence of different vehicle parameters such as mass or aerodynamics, and also to quantify the influence of compliance on steady-state control and stability of the vehicle, Force-moment method analyses are conducted with the full vehicle model in Adams Car. The diagram is constructed in Matlab and limit behavior, as well as static control and stability are monitored. At this moment, it can not be certainly stated whether the conducted mass-compliance tradeoff will improve the vehicle's performance or not. The amount of mass reduction or aerodynamic influence has been only roughly estimated and the true compliance needs to be measured. Also, the effect of compliance in transient states has not been dealt with in this thesis

---



and should be studied in the future. Also, the influence of the yawing moment of inertia (which reduced the most, in percentage) was not studied in this thesis and could prove to improve the vehicle's performance the most.

A lot of simulations were conducted using both analytical Matlab calculations and Adams. It is advantageous to be able to simulate certain changes in Matlab, such as the influence of the scrub radius on the steering torque. Based on the Matlab study, the kinematic can be changed. Some kinematic parameters are difficult to change individually as they often influence many other characteristics (scrub radius and Ackermann geometry).

## REFERENCES

- [1] *Design book of TU Brno Racing Dragon 9*. Brno, 2019.
- [2] *Calendar of TU Brno Racing for 2020*. Brno, 2019.
- [3] URBAN, Marek. *Design book of TU Brno Racing Dragon 9*. Brno, 2019.
- [4] Nb017. In: TU Fast Racing Team [online]. München: TU München, 2017 [cit. 2020-05-22]. Dostupné z: <https://tufast-racingteam.de/rennwagen/nb017/>
- [5] DP011. In: Dynamis PRC [online]. Milano: Polytechnico di Milano, 2019 [cit. 2020-05-22]. Dostupné z: <https://cutt.ly/qyI4EoG>
- [6] GELLNER, Pavel. *Design book of TU Brno Racing Dragon 9*. Brno, 2019.
- [7] ROUELLE, Claude. *OptimumG: Applied Vehicle dynamics seminar*. 6450 S. Quebec St., Ste. 5-28 Centennial, CO 80111, USA, 2018. Dostupné také z: <https://optimumg.com/our-seminars/>
- [8] *Continental Formula Student Tire: Competition Tire 2019 (C19) - Documentation*. Hannover, Germany, 2019. Dostupné také z: <https://www.continental.com/>
- [9] HALLUM, Chuck. Dynamic Traction Characteristics of Tires. JOURNAL OF PASSENGER CAR: MECHANICAL SYSTEMS JOURNAL [online]. SAE Transactions, 2002, 2002(Vol. 111, Section 6, pp. 2295-2307), 13 [cit. 2020-05-07]. Dostupné z: [https://www.jstor.org/stable/44719412?read-now=1&seq=3#page\\_scan\\_tab\\_contents](https://www.jstor.org/stable/44719412?read-now=1&seq=3#page_scan_tab_contents)
- [10] MILLIKEN, W. F., MILLIKEN, D. L.. Race car vehicle dynamics. Warrendale, PA, U.S.A.: SAE International, c1995. ISBN 15-609-1526-9.
- [11] HLAVÁČ, Martin. Návrh centrálních pružicích jednotek náprav Formule Student. Brno, 2018. Diplomová. Vysoké Učení Technické v Brně. Vedoucí práce Doc. Ing. Petr Porteš, Ph.D.
- [12] SEGERS, Jörge. Analysis Techniques for Racecar Data Acquisition [online]. Second Edition. Warrendale, Pennsylvania, USA: SAE International, 2014 [cit. 2020-05-12]. ISBN 978-0-7680-6459-9. Dostupné z: <https://www.worldcat.org/title/analysis-techniques-for-racecar-data-acquisition/oclc/885197108?referer=di&ht=edition>
- [13] BUDYNAS, Richard G. a J. Keith NISBETT. Shigley's mechanical engineering design. 10th ed. New York: McGraw-Hill Education, c2015. Series in mechanical engineering (McGraw-Hill). ISBN 0073398209.
- [14] GILLESPIE, T. D. Fundamentals of vehicle dynamics. Warrendale, PA: Society of Automotive Engineers, c1992. ISBN 15-609-1199-9.
- [15] STARIAK, Gabriel. Tenzometrické závěsy kol Formule Student. Brno, 2016. Diplomová práce. Vysoké Učení Technické v Brně, Fakulta Strojního Inženýrství. Vedoucí práce Doc. Ing. Petr Porteš, Ph.D.



## ABBREVIATIONS AND SYMBOLS

$A$	[m <sup>2</sup> ]	Frontal area
$\alpha$ , $\alpha$	[°]	Slip angle
$A_x$	[G]	Longitudinal acceleration
$A_y$	[G]	Lateral acceleration
$A_{YD(max)}$	[G]	Maximal dynamic lateral acceleration
$A_{YS(max)}$	[G]	Maximal steady-state lateral acceleration
$C$	[-]	Aerodynamic coefficient
$C18$	[-]	Continental C18 tire
$C19$	[-]	Continental C19 tire
$C_{Crit}$	[Ns/mm]	Critical damping
$C_{Crit\_Heave\_Front}$	[Ns/mm]	Critical damping of the front wheels in heave
$C_{Crit\_Roll}$	[Nms/°]	Critical damping in roll
$C_{D\_Heave\_F}$	[Ns/mm]	Damping coefficient of the front heave damper
$C_{Heave\_Front}$	[Ns/mm]	Heave damping coefficient of the front wheels in heave
$C_N$	[-]	Yawing moment coefficient
$C_{N(lim)}$	[-]	Residual yawing moment coefficient at the limit
$C_{Roll}$	[Nms/°]	Damping coefficient in roll
$d$	[mm]	Spring wire diameter; scrub radius
$D$	[mm]	Mean diameter of coil spring
$d_0$	[mm]	Scrub radius for camber angle = 0°
$D9$	[-]	Dragon 9
$D_{inner}$	[mm]	Inner diameter of coil spring
$DOE$	[-]	Design of Experiments
$D_{outer}$	[mm]	Outer diameter of coil spring
$DX$	[-]	Dragon X
$F$	[N]	Force
$F_{Aero}$	[N]	Aerodynamic force
$FEM$	[-]	Finite element method
$FSG$	[-]	Formula Student Germany
$F_{Wheel}$	[N]	Force on wheel
$F_x$	[N]	Longitudinal force
$F_{xl}$	[N]	Longitudinal force of the left wheel

$F_{xr}$	[N]	Longitudinal force of the right wheel
$F_y$	[N]	Lateral force
$F_{yl}$	[N]	Lateral force of the left wheel
$F_{yr}$	[N]	Lateral force of the right wheel
$F_{zaero}$	[N]	Normal aerodynamic load
$F_{zl}$	[N]	Normal load of the left wheel
$F_{zouter}$	[N]	Outer wheel normal load
$F_{zr}$	[N]	Normal load of the right wheel
$F_{zstatic}$	[N]	Static normal load
$g$	[m/s <sup>2</sup> ]	Gravitational acceleration
$G$	[GPa]	Modulus of elasticity in torsion
$h_{CG}$	[m]	Center of gravity height
$HD$	[ $\cdot$ ]	Heave damper attachment point
$HD\_left$	[ $\cdot$ ]	Left heave damper attachment point
$HD\_right$	[ $\cdot$ ]	Right heave damper attachment point
$HDA$	[ $\cdot$ ]	Point on the bellcrank axis in the vertical plane of heave damper
$HS$	[ $\cdot$ ]	High-speed
$IA$	[ $^{\circ}$ ]	Wheel inclination angle
$IPRJ$	[ $\cdot$ ]	Inner pull/pushrod joint
$IR$	[ $\cdot$ ]	Installation ratio
$IR_{ADAMS\_Heave}$	[ $\cdot$ ]	Heave installation ratio from Adams
$IR_{Heave}$	[ $\cdot$ ]	Installation ratio in heave
$IR_{Roll\_Front}$	[ $\cdot$ ]	Installation ratio of front roll spring/damper
$k$	[N/mm]	Stiffness
$k_k$	[ $\cdot$ ]	Safety factor
$KPI$	[ $^{\circ}$ ]	Kingpin inclination angle
$K_S$	[N/mm]	Spring rate
$K_{S\_Heave}$	[N/mm]	Heave spring rate
$K_{S\_Heave\_half}$	[N/mm]	Half of the heave spring rate
$K_{S\_Roll\_Front}$	[N/mm]	Front roll spring rate
$K_W$	[N/mm]	Wheel rate
$K_w$	[ $\cdot$ ]	Wahl's coefficient
$K_{W\_Heave}$	[N/mm]	Wheel rate in heave

$K_{W\_Heave\_Front}$	[N/mm]	Wheel rate of front wheels in heave
$K_{W\_Roll}$	[N/mm]	Wheel rate due to rolling motion of the car
$K_\phi$	[Nm/°]	Roll rate
$K_{\phi\_Front}$	[Nm/°]	Roll rate of front axle
$K_{\phi\_Rear}$	[Nm/°]	Roll rate of rear axle
$L$	[m]	Wheelbase
$L_0$	[mm]	Free length of coil spring
$LBJ_z$	[mm]	Vertical coordinate of lower ball joint from the ground
$LS$	[ $\cdot$ ]	Low-speed
$LT$	[N]	Load transfer
$m$	[kg]	Mass
$M_{Anti-roll}$	[Nm]	Anti-roll moment of one axle
$M_L$	[Nm]	$M_z$ of the wheel due to lateral force
$MoI_z$	[kg.mm <sup>2</sup> ]	Yawing moment of inertia
$MR$	[ $\cdot$ ]	Magnetorheological dampers
$M_T$	[Nm]	$M_z$ of the wheel due to longitudinal force
$M_v$	[Nm]	$M_z$ of the wheel due to vertical load
$M_z$	[Nm]	Aligning torque
$N$	[Nm]	Yawing moment
$n_a$	[ $\cdot$ ]	Number of coils
$n_t$	[ $\cdot$ ]	Total number of coils
$OPRJ$	[ $\cdot$ ]	Outer pull/pushrod joint
$p$	[mm]	Pitch of the coil spring
$PRA$	[ $\cdot$ ]	Point on the bellcrank axis in the vertical plane of pull/pushrod
$P_X$	[W]	Frictional power due to longitudinal slip
$P_Y$	[W]	Frictional power due to lateral slip
$RA$	[°]	Roll angle
$RDA$	[ $\cdot$ ]	Point on the bellcrank axis in the vertical plane of roll damper
$RDr$	[ $\cdot$ ]	Roll damper right attachment point
$R_m$	[MPa]	Ultimate shear strength
$R_{se}$	[MPa]	Yield strength in shear
$S$	[N]	Force acting on one side of the spring
$SMF$	[kg]	Front suspended mass

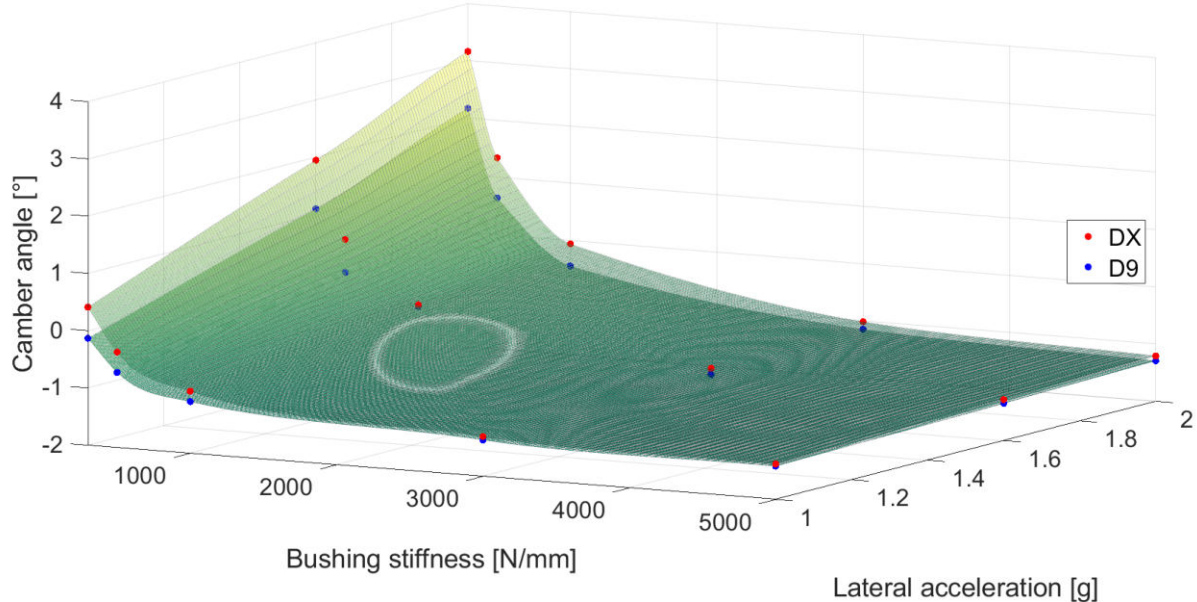
$SM_{Front\_Left}$	[kg]	Portion of suspended mass acting on the front left wheel
$SW$	[-]	Steering wheel
$T, t$	[m]	Track
$T_F$	[m]	Front track
$tx$	[Nm/°]	Rotational stiffness of the hub bushing around x axis
$ty$	[Nm/°]	Rotational stiffness of the hub bushing around y axis
$tz$	[Nm/°]	Rotational stiffness of the hub bushing around z axis
$v$	[m/s]	Velocity
$\nu$	[°]	Caster angle
$V_{SX}$	[m/s]	Longitudinal slip velocity
$V_{SY}$	[m/s]	Lateral slip velocity
$W$	[N]	Force acting at the wheel center
$W$	[N]	Weight
$WR_{From-wheel}$	[N/mm]	Wheel rate calculated from wheel force
$x$	[mm]	deflection
$x_{Wheel}$	[mm]	Wheel displacement
$Y$	[N]	Lateral force
$\beta$	[°]	Chassis slip angle
$\gamma_{static}$	[°]	Static camber angle
$\delta$	[°]	Steering angle of the front wheel
$\delta_{SW}$	[°]	Steering wheel angle
$\Delta x$	[mm]	Displacement of the wheel center
$\Delta y$	[mm]	Each spring end displacement
$\zeta_{Heave}$	[-]	Damping ratio in heave
$\zeta_{Roll}$	[-]	Damping ratio in roll
$\lambda$	[°]	Kingpin inclination angle
$\rho$	[kg/m <sup>3</sup> ]	Air density, density
$\tau$	[MPa]	Shear stress
$\phi$	[°]	Roll angle
$F_z$	[N]	Normal load



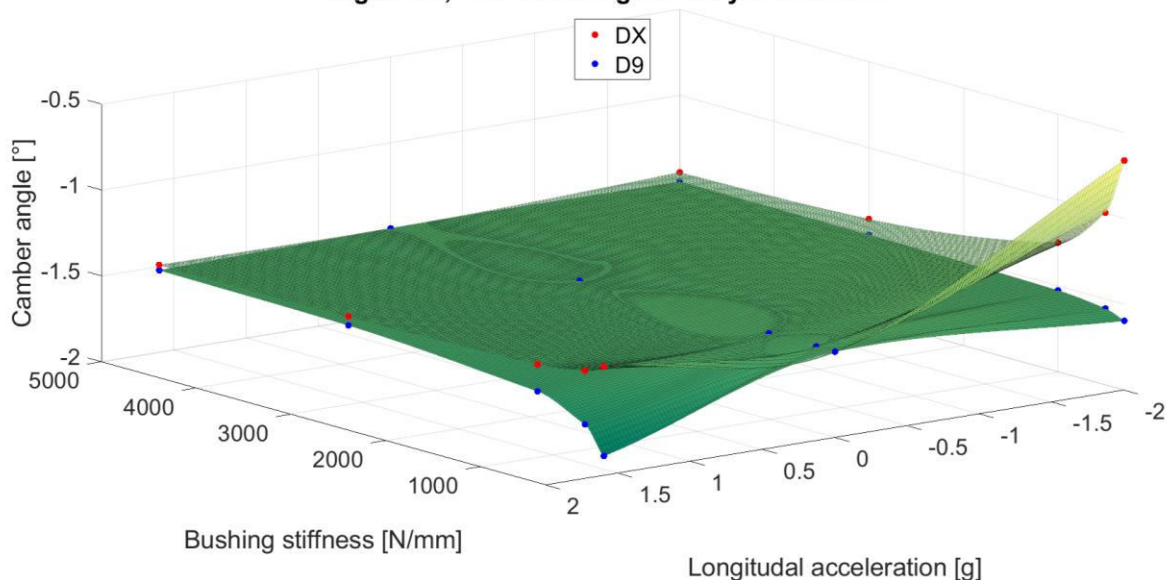
## LIST OF ATTACHMENTS

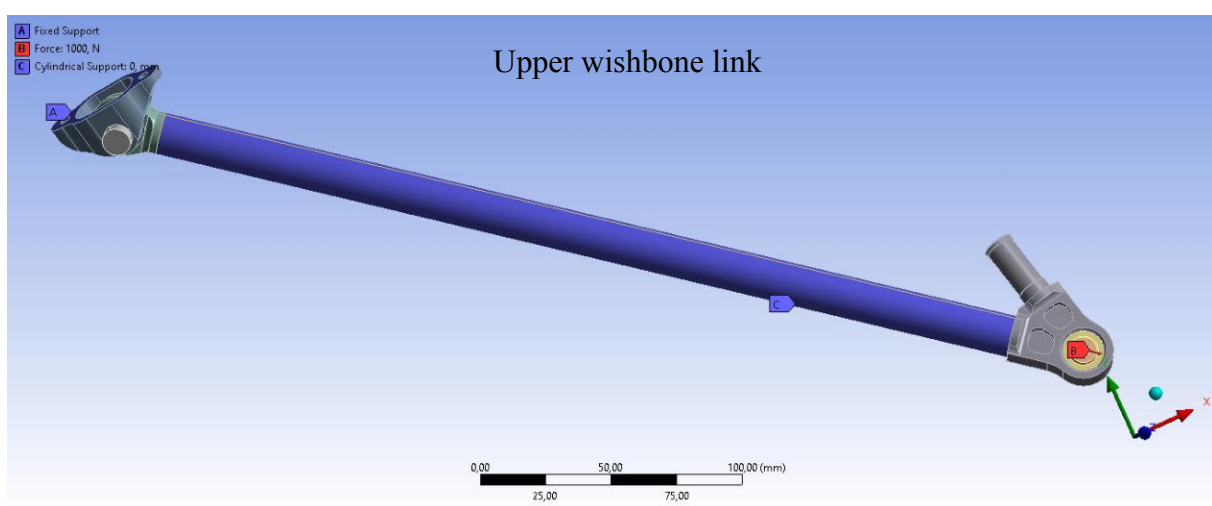
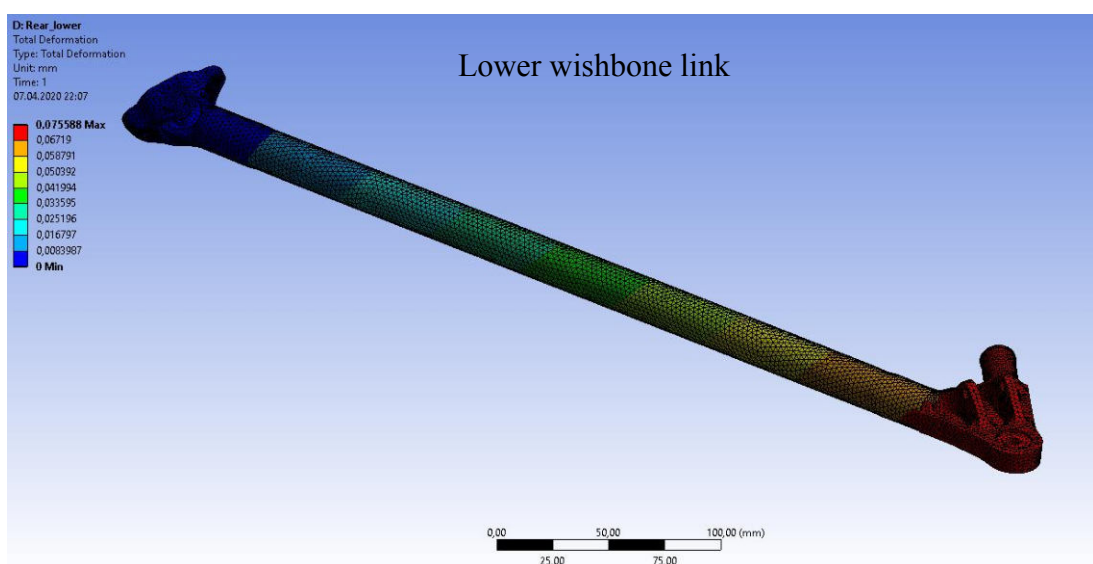
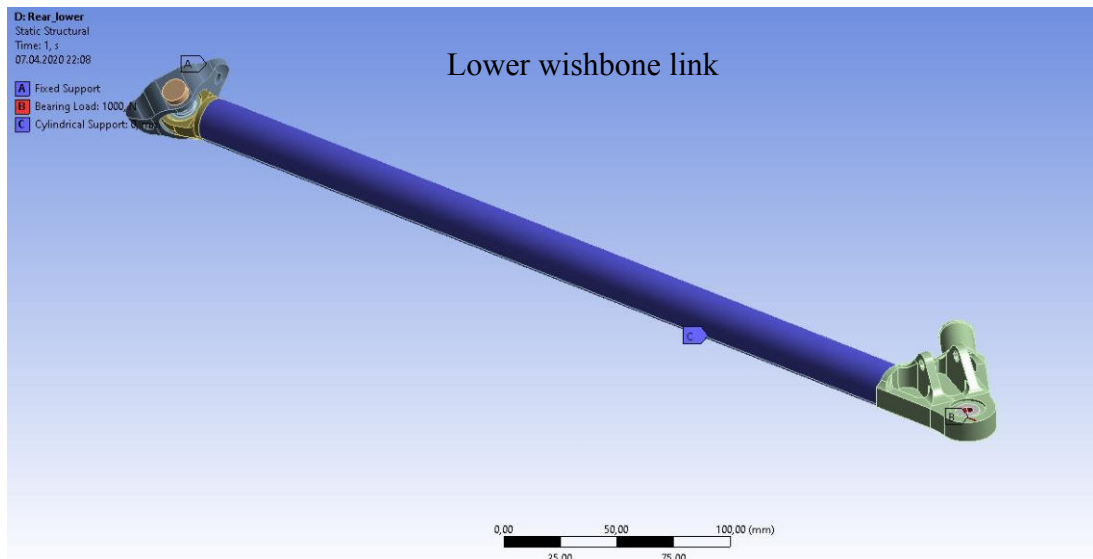
Attachment 1:	Camber compliance 3D maps for lateral and longitudinal accelerations	I
Attachment 2:	FEM tension analyses of suspension links individually	II
Attachment 3:	FEM analyses of the wheel assembly	III
Attachment 4:	Camber compliance 3D maps for lateral and longitudinal accelerations with the new tie rod design	IV
Attachment 5:	Enlarged Force-moment diagram of Dragon X in kinematic mode	V
Attachment 7:	Enlarged Force-moment diagram of Dragon X in compliant mode in a theoretical extreme case of poor suspension stiffness	VI
Attachment 8:	Comparison of Force-moment diagrams for different weights of Dragon X in kinematic mode	VII
Attachment 9:	Comparison of Force-moment diagrams for different weights of Dragon X in compliant mode	VIII
Attachment 10:	Comparison of Force-moment diagrams for different kinematic and compliant modes of Dragon X	IX
Attachment 11:	Comparison of Force-moment diagrams for different kinematic and compliant modes of Dragon 9	X
Attachment 12:	Comparison of Force-moment diagrams for different aerodynamic forces of Dragon X	XI

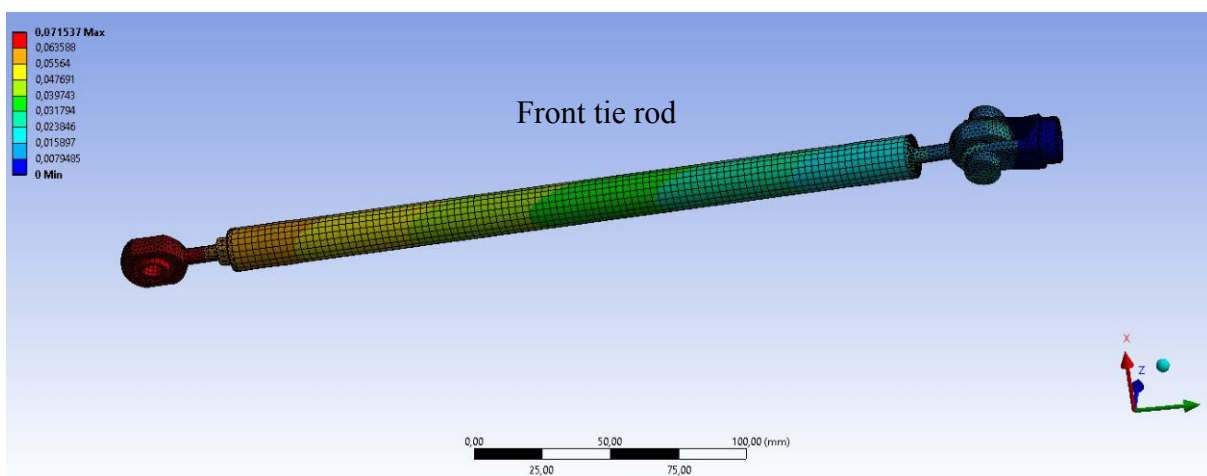
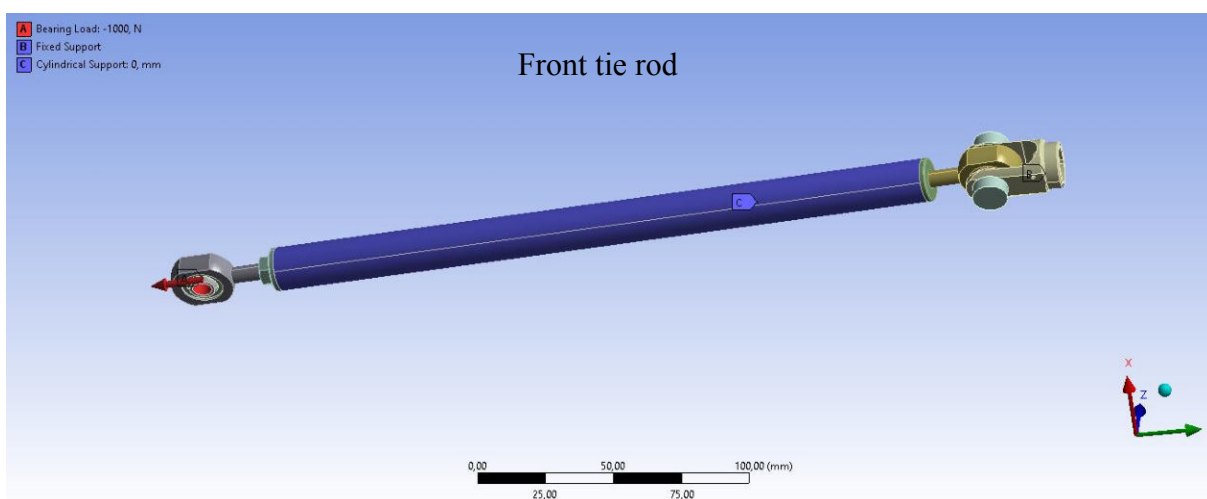
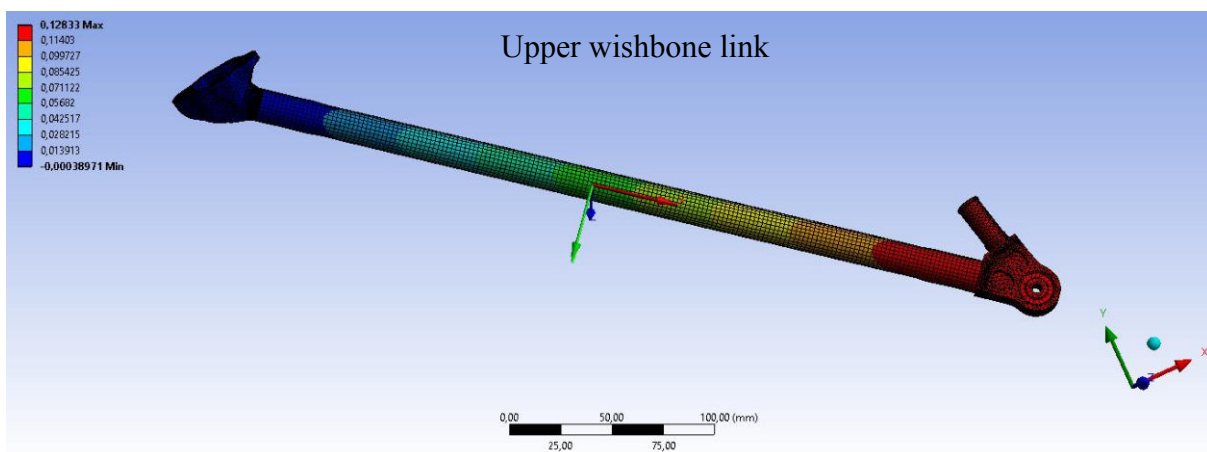
**Camber angle compliance due to Lateral force and Aligning moment**  
**Rigid hub, linear bushings at body connections**



**Camber angle compliance due to Longitudinal force**  
**Rigid hub, linear bushings at body connections**







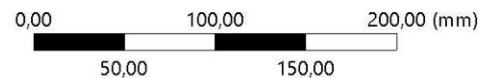
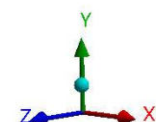
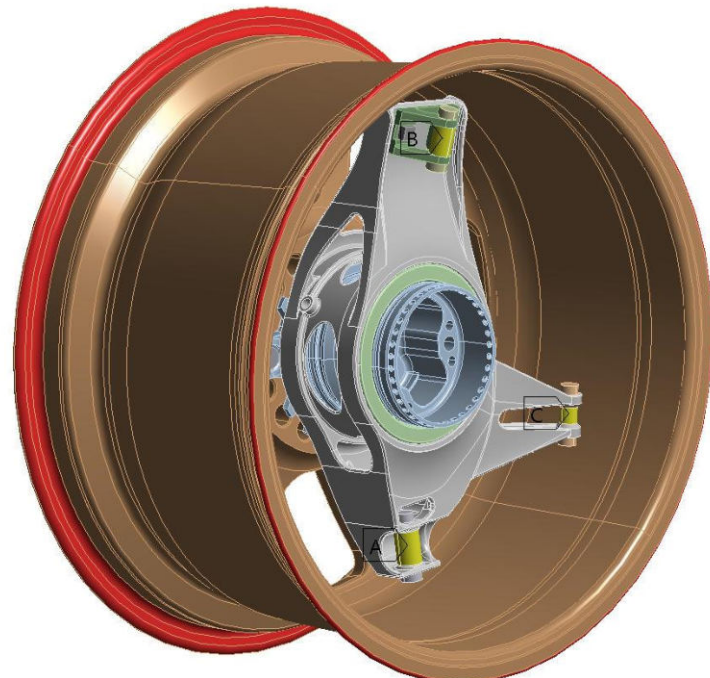
**A: Static Structural**

Static Structural

Time: 1, s

06.04.2020 18:51

- A** Remote Displacement
- B** Remote Displacement 2
- C** Remote Displacement 3
- D** Remote Force: 100, N



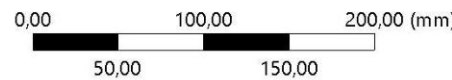
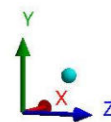
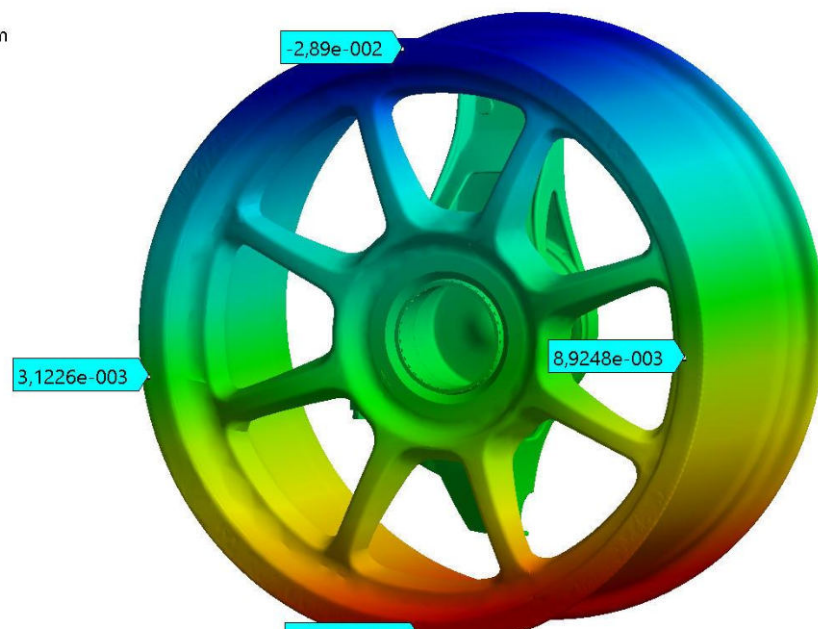
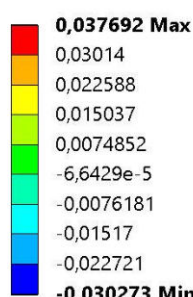
Type: Directional Deformation(X Axis)

Unit mm

Global Coordinate System

Time: 1

06.04.2020 18:55



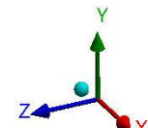
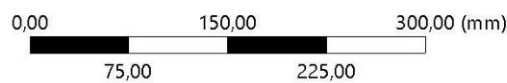
**D: Static Structural**

Static Structural 4

Time: 1, s

07.04.2020 11:21

- A** Remote Displacement
- B** Remote Displacement 2
- C** Remote Displacement 3
- D** Moment: 100, N·mm

**D: Static Structural**

Directional Deformation

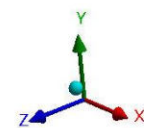
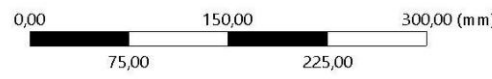
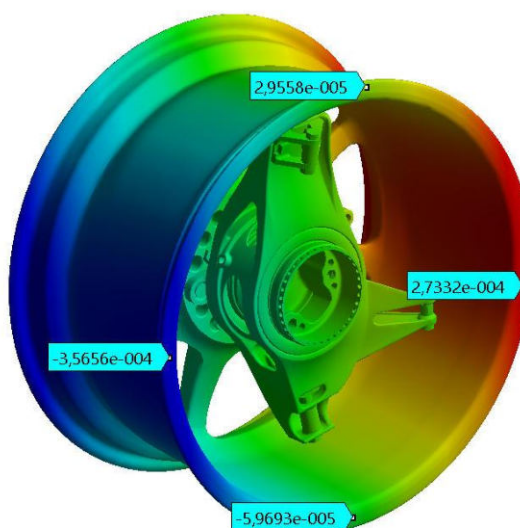
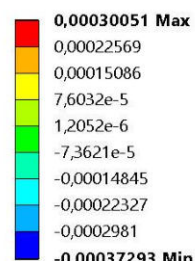
Type: Directional Deformation(X Axis)

Unit: mm

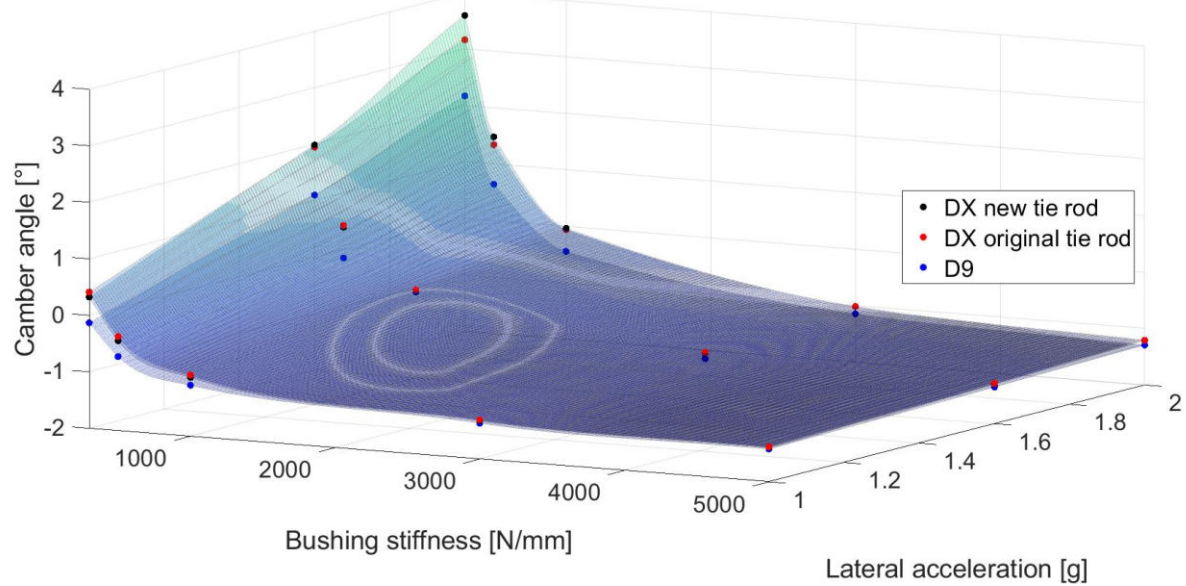
Global Coordinate System

Time: 1

18.06.2020 13:08



**Camber angle compliance due to Lateral force and Aligning moment**  
**Rigid hub, linear bushings at body connections**



**Camber angle compliance due to Longitudinal force**  
**Rigid hub, linear bushings at body connections**

